

AD633580

FLUID MECHANICS AND HEAT TRANSFER UNDER LOW GRAVITY

Edited By
H. COHAN
and
M. ROGERS

Reproduced From
Best Available Copy

Proceedings of a Symposium
Held At
PALO ALTO, CALIFORNIA
JUNE 24 and 25, 1965

1999 10/2/93

Sponsored By
UNITED STATES AIR FORCE OFFICE OF SCIENTIFIC RESEARCH
And
LOCKHEED MISSILES & SPACE COMPANY

DISTRIBUTION OF THIS DOCUMENT IS UNLIMITED

PREFACE

As a consequence of the national space program not only have many new areas of technology developed rapidly but an ever increasing emphasis is being placed on new, or hitherto neglected, facets of long established fields of research. Thus, underlying the highly visible technological successes of today is an ever growing body of knowledge on the behavior of liquids under zero or low gravity conditions.

As is so often the case in an era of intense technological activity, the scientific work has been performed by a small number of relatively isolated people or groups and their results diffusely spread throughout sundry publications directed primarily at professionals in the various scientific disciplines involved. As a means of improving the dissemination and correlation of available information and thereby providing source material for further work in the field, the Air Force Office of Scientific Research and Lockheed Missiles & Space Company joined in sponsoring a Symposium on Fluid Mechanics and Heat Transfer Under Low Gravitational Conditions. The symposium was held in Palo Alto, California June 24 and 25, 1965. This volume contains the proceedings of the Symposium.

The emphasis of the Symposium was on research and fundamental knowledge. While our motivation in organizing the conference was to further the understanding of the problems involved in fluid containment, transfer, and control under low gravity conditions, it was not our objective to cover in a detailed way every complexion of these topics. Rather we hoped that in choosing special items of basic interest and treating them in some detail that the Symposium would better serve to acquaint specialists in a given discipline with the foundations, concepts, and techniques of other disciplines concerned with the problem area. Thus, although man in orbital flight is not of explicit concern to the material selected for this Symposium, the technological problems introduced by the requirement to maintain and employ a useful man under a perpetual low gravity environment underlie many of the papers selected.

Many of the problems of fluid behavior under low gravity conditions have become apparent only recently. Much of the work in the field has been of a pragmatic nature, albeit most analytical rather than experimental. Experimentation is difficult and often unsatisfactory with the present state of the art. Supplementing one g_0 experiments extrapolated by theory to low gravity, only two techniques exist today for earthbound fluid mechanical experiments at zero or low gravity. The first is the use of the free fall drop tower with, or without, ancillary means for applying small accelerations. The other technique in present use is that of zero-g trajectories in aircraft or sounding rockets.

Drop towers are limited in the time for experiment to the order of 1 to 3 seconds at present. The size of experiments which can be accommodated by current drop towers also is severely limited. Thus scaling of low gravity experiments (a topic which is almost unexplored) becomes of paramount importance. Also, with such short times available in drop tower tests, heat transfer experiments involving boiling or thermal stratification become very difficult or impracticable. The use of aircraft allows times in the neighborhood of 15 to 20 seconds in zero-g flight but presents other problems from the standpoint of the large accelerations experienced by the models just prior to the zero-g condition, as well as the unpredictable drag forces created by random air currents in the cabin. It is also very difficult to provide small directed acceleration forces to a model in free fall in an aircraft cabin. Many of the same limitations apply to sounding rockets, complicated by the difficulties of retrieving data and the severe limitation on experiment size.

In a sense then we are confronted by a chicken and egg situation with regard to fluid mechanical experiments at low-g. As in so many fields of endeavor, it is necessary to combine analytical techniques with experiments designed to test the validity of theory or to prove, or improve, computational methods. These may then be used, when confidence in their applicability has been gained, to make predictions of fluid behavior under conditions impossible to test today until a space vehicle has been designed, constructed and flown, yet it is the very integrity of the space vehicle and its subsystems that one would wish to verify before a design has been frozen and hardware produced. It may very well be that the eventual hope for workers in the field will be to design experiments for orbital evaluation in a space vehicle. However, very little has been accomplished to this end thus far.

As will be seen in the following pages, the 16 papers comprising the Symposium represent a mixture of analytical and experimental work covering a wide spectrum of the present state of the art. Sufficient time was allowed for each presentation to make attendance at the Symposium meaningful to the participants. The speakers were able to discuss their work and elaborate on those areas they wished to high-light. Sufficient time was also allocated for discussion from the floor so that any attendee with a specific interest could satisfy his curiosity and obtain additional information and references. These lively discussions were recorded, edited, and are included in this volume, each immediately after the pertinent paper. To aid in the discussions, the evening before the first session, each registrant was given preprints of all the papers to be presented at the four sessions which made up the Symposium.

We are indebted to many members of the staff of Lockheed Missiles & Space Company who helped to make the meeting a success. Among the many who assisted the editors, special mention must be given to Myron P. Hollister, James G. Seebold, and Hugh M. Satterlee who carried out the formidable task of reading and evaluating the submitted papers. We wish to express our appreciation to Marian Staupp and Linda De Moss for their intelligent and cheerful attention to the numerous small details of greeting and registering the attendees smoothly and with a minimum of confusion. We also wish to thank Roy Dreisbach for his assistance in processing the manuscripts and illustrations, and for his careful planning and execution of the many tasks that contributed so heavily to the success of the symposium.

It is the hope of the editors that these proceedings will prove to be a useful tool in charting the paths for future research and development in the field of Fluid Mechanics and Heat Transfer Under Low Gravitational Conditions.

M. Rogers

H. Cohan

BLANK PAGE

CONTENTS

	Page
Preface	v
WELCOMING ADDRESS – E. P. Wheaton, Vice President and General Manager, R&D Division, Lockheed Missiles and Space Company	xiii
WELCOMING ADDRESS – Brig. Gen. E. A. Pinson, USAF, Deputy Commander, Office of Aerospace Research	xvii
KEYNOTE ADDRESS – Major Edward Westlake, USAF, Chief, Environmental Control and Life Support, MOL Program Office	xix

Session I

Chairman: W. E. Jahsman
Senior Member of the Research Laboratory
Lockheed Missiles and Space Company

SATURN V LOW-GRAVITY FLUID MECHANICS PROBLEMS AND THEIR INVESTIGATION BY FULL-SCALE ORBITAL EXPERIMENT F. E. Swalley, G. K. Platt, and L. J. Hastings Marshall Space Flight Center, NASA	1-1
AN EXPERIMENTAL INVESTIGATION OF THE DYNAMIC BEHAVIOR OF THE LIQUID-VAPOR INTERFACE UNDER ADVERSE LOW-GRAVITATIONAL CONDITIONS W. J. Masica and J. A. Salzman Lewis Research Center, NASA	2-1
INVISCID FLUID FLOW IN AN ACCELERATING AXISYMMETRIC CONTAINER P. Concus, G. E. Crane, and L. M. Perko Lockheed Missiles and Space Company	3-1

Session II

Chairman: Lt. Col. W. S. Gibson, USAF
Deputy Air Force Plant Representative – Sunnyvale

SOME THERMAL ASPECTS OF A CONTAINED FLUID IN A REDUCED- GRAVITY ENVIRONMENT S. H. Schwartz and M. Adelman Douglas Aircraft Company	4-1
---------------------------------------------------------------------------------------------------------------------------------------------	-----

Session II, Cont.

Page

DISTRIBUTION OF NONCONDENSABLE GASES IN LIQUIDS UNDER LOW-g CONDITIONS N. E. Welch and E. Funk Marshall Space Flight Center, NASA	5-1
THE FLUID MECHANICS OF CONDENSING MERCURY IN A LOW-GRAVITY ENVIRONMENT R. T. Lancet and P. B. Abramson Atomics International Division, North American Aviation, Inc. R. P. Forslund, Massachusetts Institute of Technology	6-1

Session III

Chairman: Mason Charak
Program Manager, Zero Gravity Fluid Behavior & High Vacuum
Technology, Office of Advanced Research & Technology, NASA

DYNAMIC RESPONSE OF LIQUIDS IN PARTIALLY-FILLED CONTAINERS SUDDENLY EXPERIENCING WEIGHTLESSNESS F. C. W. Fung Cornell Aeronautical Laboratory, Inc.	7-1
LOW-GRAVITY LIQUID REORIENTATION M. P. Hollister and H. M. Satterlee Lockheed Missiles and Space Company	8-1
INTERFACIAL STABILITY OF LIQUID LAYERS ON ELASTIC SURFACES R. D. Smith Lockheed Missiles and Space Company	9-1
SLOSHING OF A LIQUID IN A DRAINING OR FILLING TANK UNDER VARIABLE-g CONDITIONS P. G. Bhuta and L. R. Koval TRW Space Technology Laboratories	10-1

Session IV

Chairman: M. A. Saad
Associate Professor of Mechanical Engineering
University of Santa Clara

THE EFFECT OF WALL ELASTICITY AND SURFACE TENSION ON THE FORCED OSCILLATIONS OF A LIQUID IN A CYLINDRICAL CONTAINER P. Tong and Y. C. Fung California Institute of Technology	11-1
SHAPE AND STABILITY OF THE LIQUID-GAS INTERFACE IN A ROTATING CYLINDRICAL TANK AT LOW g J. G. Seebold and W. C. Reynolds Stanford University	12-1
MENISCUS SHAPE UNDER REDUCED-GRAVITY CONDITIONS H. M. Satterlee and J. H. Chin Lockheed Missiles and Space Company	13-1
LIQUID SETTLING IN LARGE TANKS T. E. Bowman Martin Company	14-1
THE MARTIN COMPANY'S LOW-g EXPERIMENTAL FACILITY H. L. Paynter Martin Company	15-1
THE APPLICATION OF HYDROPHILIC AND HYDROPHOBIC SURFACES FOR PHASE SEPARATION IN A LOW-g ENVIRONMENT J. M. Smith, Y. S. Li, and R. M. Cima Lockheed Missiles and Space Company	16-1

BLANK PAGE

WELCOMING ADDRESS

by

Elmer P. Wheaton

Vice President and General Manager
Research and Development Division
Lockheed Missiles & Space Company

The engineering of vehicles for space travel has introduced many new problems in all technical fields. New materials and processes have been developed and it has become necessary to develop new theories for use in our engineering sciences and to greatly refine old ones. In short, engineering for space travel requires us to continually re-examine all of our techniques and methods in a continual attempt to improve the excellence of our products.

One of the most crucial parts of a space vehicle is its propulsion system. The excellence of the propulsion systems we use will determine the extent of our eventual success in conquering space. Currently, liquid rocket engines can use higher energy propellants and the vehicles employing these engines can achieve higher velocities and carry higher payloads. There are other advantages too. However, among the disadvantages associated with liquid propellant rockets is the uncertain behavior of the liquid propellants when gravitational forces are reduced by a million or more. The behavior of liquids under such conditions is quite strange to our ordinary experience. Greater knowledge of the behavior of liquids under such conditions will be essential to the design of optimum propulsion systems. Further, the collection and control of liquids in smaller devices such as boilers, condensers, and life support equipment in the absence of gravitational forces is an uncertain task at best. Our ability to obtain the necessary information about low gravity liquid behavior in all such devices, or to design around potential problem areas is very important.

Conventionally, we carry out analyses in an attempt to predict the behavior of a design or concept. We may then carry out verifying experiments to determine how accurate our predictions are, and to modify them for later use, as necessary. Analysis relative

to low-g liquid behavior can, for many problems, be couched in simple terms; that is, ideal fluid behavior may be assumed to describe liquid motion. The boundary conditions for such analysis as applied to problems of practical analysis, however, injects considerable difficulty. Numerical solution of these problems is difficult and, at this point, is providing considerable challenge to workers in the field.

Experiments are greatly limited at this time by our lack of ability to reduce body forces acting on liquids for satisfactory periods of time in experiments of reasonable scale. Drop tower test facilities, for instance, give typically 1 to 3 or 4 seconds. The aircraft test facilities now being used allow 5 to 20 seconds. Each has its advantages and disadvantages and, therefore, its own place in our current spectrum of experimental facilities. Orbital experiments will eventually answer many of the questions that are now being asked, and will be essential in some cases. Such experiments will be difficult because of the complex instrumentation required. If care is not taken we may be assured that the "instrumentation tail will wag the zero-g dog". Instrumentation for these experiments will cost far more than the experiments themselves.

At this point engineers are being asked to extrapolate 2 orders in size and 6 orders or more in g level from small scale model experiments. This points up the usefulness of analytical techniques in this field. Robert McNamara, our Secretary of Defense, has pointed out in a different connection that we need the right mix of weapons. For several years to come we will increasingly rely on mathematical analysis in this field. The purpose of this meeting is to disseminate current information. Just as importantly, however, we hope to bring together those currently involved in analysis with those doing experiments and both together with the eventual user of the information so that all may share the others' points of view. If this is achieved by tomorrow afternoon, the symposium will be a success to those speaking and to those who have come to listen.

I would now like to introduce Brig. Gen. Ernest A. Pinson, Deputy Commander of the Air Force Office of Aerospace Research. General Pinson's previous assignments have given him a wide variety of research work and technical direction responsibility. He holds an A.B. degree in physics from De Pauw University in Indiana and a Ph.D. in

Medical Physiology from the University of Rochester. He also has considerable graduate training in Nuclear Physics at the University of California. He has been decorated many times. He is a member of 9 technical societies and has written over 80 technical articles. In short, he has managed to pack into his military career more significant scientific experience than many engineers and scientists working full time in our industry. General Pinson will conclude our welcoming ceremonies this morning.

WELCOMING ADDRESS

by

Brigadier General Ernest A. Pinson

Deputy Commander*

USAF Office of Aerospace Research

During the next several days you gentlemen are going to discuss the state of the art of fluid mechanics and heat transfer under low gravity conditions. This is noteworthy because this is the first sizeable gathering of the leading research scientists and engineers concerned with these particular phenomena. A coalescence of thinking and outlook on the subject will take place here, and undoubtedly trends will be identified that will determine to a considerable extent the directions in which progress will be made in this field for some time to come.

I need not point out the importance of this field as the basis for the technological developments of space accomplishments. I do want to indicate, however, that symposia of this kind are one important aspect of a large-scale effort by the Air Force to ensure not only the timely development of critical aspects of science, but also their timely transfer into the kinds of technology that it appears this nation is going to need in the future.

As you know, this symposium is sponsored by the Air Force Office of Scientific Research, AFOSR, and by the Lockheed Missiles & Space Company, to which we are greatly indebted for being our hosts here, and for making these very fine arrangements for the sessions. AFOSR's parent command is the Office of Aerospace Research, the research agency of the Air Force. I am most pleased that our keynote speaker represents the Air Force Systems Command, one of the major "blue suit" users of the research produced by OAR. The mission of OAR is both to conduct and support research in those areas of science that offer the greatest potential for providing new

* Now Cmdr. . Office of Aerospace Research.

knowledge essential to the continued superiority of the Air Force operational capability. Within this framework, AFOSR operates in the general spectrum of science, supporting the best in research performed at colleges, universities and industrial research organizations.

A great many AFOSR conferences and symposia are geared to bringing research results directly to the attention of the users; others are designed primarily to provide timely communication between active researchers pioneering in various phases of a particular research field. This symposium appears to be serving a large portion of both functions.

I'm sure it is of interest to you to note that within OAR we recognize that for an in-house research laboratory to be successful a large amount of effort must be directed to identifying central problems of the Air Force that will depend for their solution upon increased fundamental scientific knowledge. Further, we are currently intensifying our efforts to ensure that not only are our programs planned with these problems in mind, but that the research results of these programs are rapidly disseminated.

To this end, scientists in OAR research laboratories are encouraged to devote as much as a fifth of their time to developing an awareness of Air Force problems within their technical areas, and consulting with the other Air Force elements and users of Air Force research.

In turn, the OAR headquarters plays an important role in this research process through better definition of Air Force objectives, the interpretation of Air Force objectives into scientific terms, and liaison activities with other elements of the Air Force and users of Air Force research. The active participation of the headquarters staff in these activities has been found to be highly beneficial. AFOSR conferences and symposia such as this are in every sense a parallel effort to that being carried out in our in-house laboratories.

Thus, it is with the greatest pleasure that I welcome so many of you here today, and wish you great success. I am confident that the real rewards of what we do here will be measured in terms of scientific accomplishment in the years to come.

* * *

KEYNOTE ADDRESS

by

Major Edward Westlake, USAF
Chief, Environmental Control and
Life Support, MOL Program Office

Good Morning - (Ladies) and Gentlemen.

I feel somewhat strange keynoting such a highly technical and as yet largely theoretical subject. I am a bioengineer primarily concerned with man's integration into space systems. My task in the Manned Orbiting Laboratory Program is to assure the optimum living environment in the space capsule and to measure the impact of the space environment on man's physiological and psychological performance capability. Zero or low-g is one of the primary factors affecting all aspects of this manned systems application. The latest Gemini-4 flight may cause the space planners to reconsider some of their earlier, possibly overly pessimistic, prognostications of these weightless effects, but we have a long way to go before we can write them off.

It was suggested in early discussions of this "keynote" rationale that I stress the Air Force as a "user" of your research specialty. It occurred to me at that point - in fact, I was tempted to paraphrase my subject as, "The Low Gravity State - or How I Became a User." You might also carry this humorous aside one step further to recognize us as "pushers." This might be interpreted to show that we are not addicted yet.

We, "Pushers" in Manned Space Systems Development are highly dependent on you research specialists in this new field of weightlessness. We look to you to assure that in our technological systems application we develop systems which will operate reliably in the low gravity or weightless environment of space. Ideally, we would like to have gravity independent systems; however, the present state of the art has developed very few such components so there is plenty of room for your science and art. "Zero Gravity" or "Weightlessness" is a space technology term often referred

to by most of those working space technology today. However used, it is usually only vaguely recognized as the dynamic balance of gravitational vs. acceleration forces set up in space systems in orbit around the earth or in extended planetary space flight.

In actuality, "zero gravity" or possibly more accurately "100% Gravity" (as Berenson suggested at the 2nd AAS Symposium in 1963) seldom occurs in near-Earth orbit. I will loosely define "near-Earth orbit" as space flight altitudes between 90 and 300 nm where the present manned systems have been orbited. The true force balance is dynamically established somewhere above the perfect balance or in a "Low Gravity State." This point is brought out by the theme of this symposium "Fluid Mechanics and Heat Transfer Under Low-g."

At the risk of sounding pedantic, I would like to briefly review the relationship of the significant forces creating this low gravity state of near-Earth orbital mechanics. In order to assess the relative importance of these forces, the value of one or more of the dimensionless force ratios, e.g., Bond, Froude, Weber, or Reynolds numbers should be determined.

One force may not be considered dominant over another unless the value of the pertinent number is considerably above or below the critical value at which both forces are equal (see Fig. 1). Estimates of these numbers can be made from data on fluid properties and from a knowledge of the equivalent "gravity" produced by the force under consideration. For space systems at low to moderate altitudes, aerodynamic drag due to free-molecular flow will yield values of about 10^{-5} to 10^{-7} g. Solar radiation pressure on a one-foot diameter sphere of density 10 lb/ft^3 in orbit around the Earth results in an estimated 10^{-8} g. The gravitational gradient in the vicinity of the Earth is of the order of 10^{-7} g per foot. It is obvious that for large systems in low Earth orbits, drag forces are large enough to have a substantial effect on the equilibrium configuration of the fluid in the system.

This effect is important particularly in the case of cryogenic fluids for which the surface tension is in the range of 2 to 20 dynes/cm (see Fig. 11).

DIMENSIONLESS FORCE PARAMETERS

Force Ratio	Name	Critical Value
<u>Gravitational</u> Surface Tension	Bond Number	1
<u>Inertial</u> Gravitational	Froude Number	1
<u>Inertial</u> Surface Tension	Weber Number	1
<u>Inertial</u> Viscous	Reynolds Number	1000
<u>Viscous</u> Gravitational		10 ⁻³
<u>Centrifugal</u> Gravitational		1

FROM: Berenson, P.J.; Vol 14, "Advances in Astronautical Sciences". 2nd AAS Symposium, Jan, 1963, P. 116-129

Fig. 1

ORIENTING FORCES ON FLUID IN ORBITING TANK;

Rough Order of Magnitude^a

Gravitational attractive force between liquid mass and vehicle	0.05 dynes
Inertial force due to "aerodynamic" drag, 300-naut-mile orbit	100.00 dynes
Capillary force	1,300.00 dynes
Inertial force due to "aerodynamic" drag, 90-naut-mile orbit	80,000.00 dynes

^a A sphere of liquid hydrogen of 100-cm radius (280 kg) was assumed to be in orbit in tank of 28 m² cross-sectional area. The center of mass of the hydrogen and the center of mass of the tank plus engines (220 kg) were assumed to be 300 cm apart.

FROM: Neu, J. T. and Good, R. J.,
A.I.A.A. Journal Vol. 1, No. 4, Apr 63, p. 814

Fig. 11

It has been estimated that for an orbiting 20-ft-diameter tank containing liquid hydrogen the inertial force due to aerodynamic drag at a 90-nm orbit is 60 times larger than the capillary force in view of the low surface tension of hydrogen (about 2 dynes/cm). The capillary force becomes 13 times larger than the aerodynamic drag at a 300-nm orbit.

For water with a surface tension of about 70 dynes/cm, the capillary force would be appreciable. It is obvious from what I have just said that a zero-g analysis cannot be properly used in establishing the final configuration of the fluid unless the force due to surface tension is larger than the gravitational force by an order of magnitude, in other words, with a Bond number substantially smaller than one. In addition to the above forces, the effect of mechanical disturbances (such as man himself) and heat transfer from solar radiation or other sources should be considered in determining this configuration.

You have a most difficult task since low gravity experimental conditions essential to test your theoretical calculations are (for extended duration studies) difficult and costly to acquire or utilize. I will explore this more at length a little later. Let us look at Manned System Environmental Control and Life Support for low gravity problem areas with which I am familiar. Using it as an example, I will highlight a few systems components whose operation is or may be adversely affected by low gravity conditions. In this way, I hope to give you a better appreciation of where we in applied technology need your basic research help. Let us first consider components utilizing fluid mechanics principles.

The atmosphere control system has one of the most critical gravity-sensitive components in the ECS, where liquid cryogenic gases are used to supply the breathing atmosphere. With such a liquid-gas interface, the system must assure that only gas is carried to the cabin. Present technology uses "supercritical" temperatures and pressures in a special chamber within the storage tank to create a vapor that is neither liquid nor gas but is relatively gravity-insensitive and readily evolves to gas with increasing temperature. Capillary action oxygen converters have also been built in prototype at Aeronautical Systems Division, Wright Patterson AFB, Ohio, to show feasibility of this alternate approach to supplying gas in a weightless environment.

For space missions of a year or more a closed cycle biological "regenerable" gas subsystem is being studied by many researchers. This subsystem utilizes single celled algae plants living in a water medium to absorb carbon dioxide produced by the men and then give off oxygen. The present engineering approach to this gas-liquid transfer is by way of semipermeable membranes. This gas transfer mechanism may be gravity independent but the effect of weightlessness must be verified. A prototype of such a system was successfully tested for 20 min. in an Atlas ballistic piggyback capsule at the Eastern Test Range in the summer of 1962. Wherever fluids are stored for use, such as drinking water, a positive expulsion system is utilized such as an inner bladder which can be compressed by gas pressure forced into the tank around the bladder. Atmospheric humidity control has been a problem in the Mercury manned space system as a result of the low gravity environment. It appears to have been licked in the Gemini. Humidity control, classically, is by condensation on a cold plate with gravity playing a very important role in collecting the condensate. In weightlessness one approach to this condensate collection is by differential gas pressure across a porous cold plate where capillary action and reduced pressure results in the unidirectional movement of the water into a collection reservoir where it is available for reuse. As space missions become longer than about a month, water reclamation techniques must be utilized. Membrane dialysis is a technique for purification which is being studied for space application. It will require testing in a weightless environment.

Now let us look briefly at heat transfer in the weightless state in manned space systems environmental control. Thermal transfer for man's comfort and the removal of electronic equipment heat loads is primarily performed by forced air convection, radiation and conduction while natural, gravity-oriented convection is reduced to insignificance in the weightless state.

Fire hazard is a safety problem which we are carefully studying. Ignition and combustion of spacecraft materials in pure oxygen and various two gas atmospheric mixtures of oxygen-nitrogen and oxygen-helium are being studied intensively to determine the effect of the low gravity environment of such phenomena. Thermal energy transfer without free convection, may become a most interesting problem of flame propagation to investigate the oxidative process and determine whether molecular gas diffusion

is sufficient, depending on the oxygen concentration to support combustion. The effect of the diluent gas may also be quite significant since the thermal conductive efficiency of helium is about 7 times that of nitrogen.

Now, to recapitulate, I have summarized my view of the existing low gravity state in near earth orbit (or less than 300 nm) in which our systems may normally function. I have also surveyed some of the environmental control system components where help is needed in establishing a clear understanding of the effect of the low gravity environment to assure reliable operation. As you may recall, I previously alluded to the difficult and expensive task of experimentally simulating low gravity conditions. This area of zero-g and low gravity test methodology is expanding rapidly both in size of facilities and in complexity of techniques. Various methods are available at the present for conducting experiments in zero or near zero gravity. Naturally, the best (and incidentally a most expensive) method of carrying such experiments for extended periods of time is in orbiting satellites or laboratories. So far, few such experiments have been conducted for obvious reasons. However, it is expected that the number will increase appreciably in the future. At the present time, the most useful techniques of achieving zero-g conditions for brief periods of time have consisted of drop towers, aircraft, and missiles flying zero-g trajectories, and sounding rockets. The drag forces acting on the test package in drop tower experiments can be reduced or eliminated by evacuating the tower, or by the use of an evacuated capsule in which the test packet falls freely. Zero-g test time achieved in such towers is a function of the tower height and length of cylinder. Times up to 10 seconds are now considered possible (see Fig. III).

NASA at their Lewis Research Center in Cleveland, Ohio is presently constructing a 500 foot zero gravity facility with an estimated total weightless period of about ten seconds (see Fig. IV). The basic structure is a below ground shaft 510 feet deep and about 28 feet in diameter. This shaft will contain a 20 foot diameter vacuum chamber somewhat shorter than the total shaft length. As a free fall facility it has a weightless period of 5 seconds. This period can be essentially doubled by accelerating the experiment upward from near the bottom and allowing it to free fall thereafter. Experiments up to 48 inches in diameter with lengths of 4 to 20 feet and weights to 6000 lbs can be accommodated. The facility should be operational in the spring, 1966.

DROP TOWERS

Location	Drop height (ft)	Zero-g time (sec)	Remarks
Norair Div., Northrop, Hawthorne, Calif.	87	2.3	Enclosed tower with freefall capsule partial g by counterweight, heat transfer data from thermal response, without heat input
University of Michigan, Ann Arbor, Mich.	45	1.6	
University of Colorado, Boulder, Colo.	30	1.3	tower
Stanford University, Stanford, Calif.	300-600	4.3, 6.0	mineshaft
Avco-Rad, Wilmington, Mass.	25	1.0	freefall capsule
	36	1.5	continuous acceleration measurement to ± 0.005 g
Convair Astronautics, San Diego, Calif.	9	0.75	partial g by counterweight freefall capsule evacuated tower (under construction) capsule has low-drag nose
NASA Lewis Research Center, Cleveland, Ohio	8	0.7	
	9	0.75	
	100	2.25	
	400	5.0	
University of Tokyo, Japan	16	1.0	evacuated drag shield, wheat bin arresting
NASA Marshall Space Flight Center, Huntsville, Ala.	22	1.15	
Convair, Pomona	100	2.5	pasteboard arresting streamlined body, sponge rubber arresting
Martin, Denver	75		
Wright-Patterson AFB	55	1.82	± 0.01 to ± 0.5 g relative to free fall. Pneumatic arresting (under construction)
Marine Hydrophysical Inst. Ac. of Sc.	12	.86	
Lockheed Missiles and Space Co., Sunnyvale, Calif.	103	3	encapsulated test mod. (under construction), cardboard arresting, primarily associated with Apollo, no low accel. capability 23" diam. models
North American S and I.D., Downey, Calif.	75	2.0	

Fig. III

WEIGHTLESS TEST METHODS

AIRCRAFT

Zero-G
time
(sec)

Wright Air Dev. Div., U.S. Air Force

C131B
KC135

12 to 15
30 to 32

fitted for free-floating capsule
fitted for free-floating capsule;
uses closed circuit TV for pilot
monitor

NASA
AJ2

25
10 to 12

low gravity trajectory
free floating

MISSILE, SOUNDING ROCKET, AND SATELLITES

NASA Lewis Research Center

Aerobes 150-A
Sounding rocket

5 min

gravity level below 10^{-3} g

Air Force Ballistic Missile Development Division,
TRW Systems

25 min

Atlas re-entry nose cone, data from
recoverable movies

Prepared by:
Research and Development Division
Lockheed Missiles and Space Company
7 June 1965

Fig. III (Cont.)

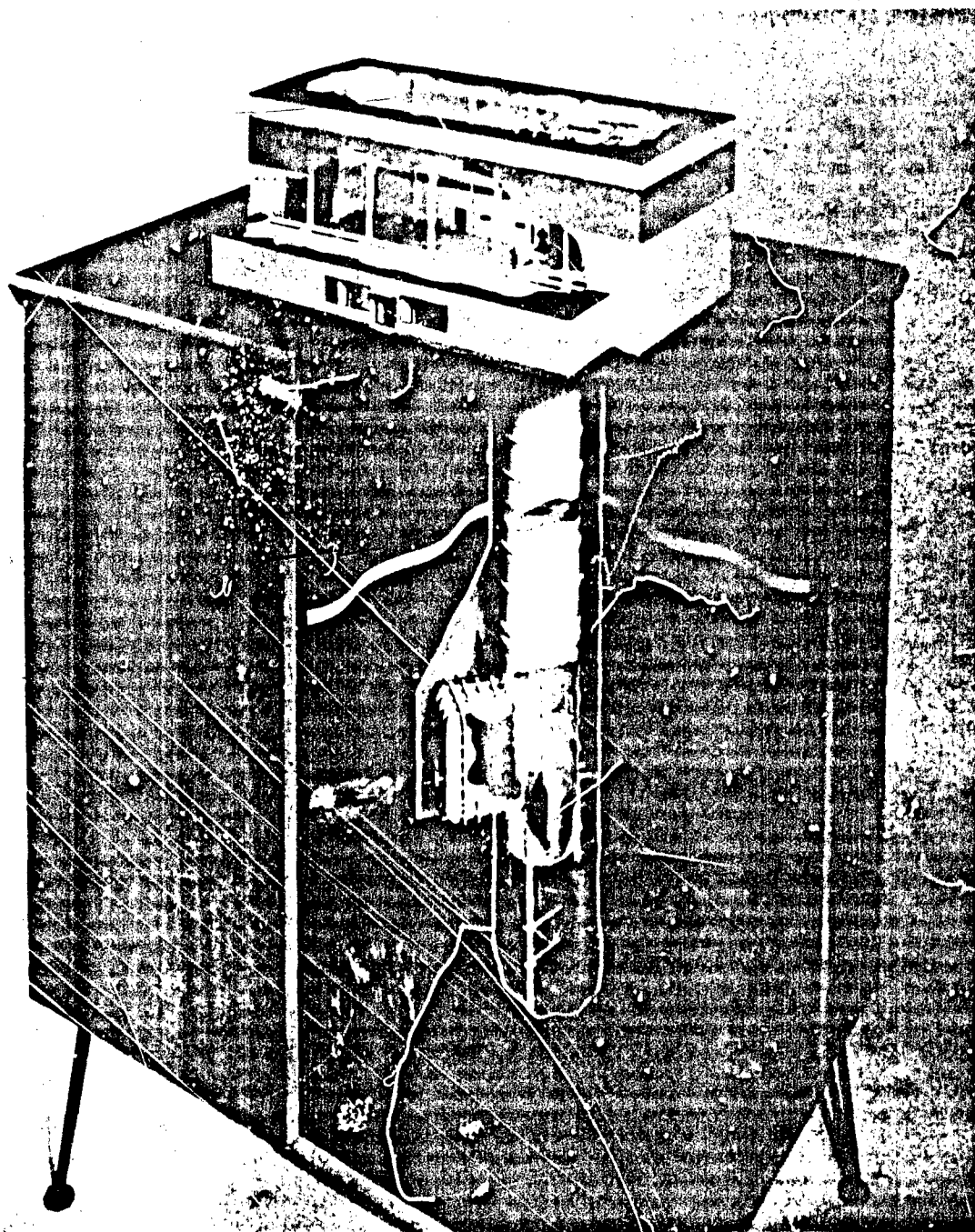


Fig. IV Drop Tower

Aircraft tests have been used extensively to obtain useful information on biological effects of weightlessness and on liquid behavior and heat transfer under zero-g conditions. The problem in this latter set of experiments has been the development of a technique of mounting the test capsule within the aircraft so that a free-floating condition could be achieved. Usable time of 9 to 15 seconds have been attained out of a possible 30 second zero-g duration of flight utilizing C-131 and KC-135 aircraft at W-PAFB. At Brooks AFB, Texas an F-100 modified fighter can achieve about 45 seconds of weightlessness carrying about a 3 cubic foot experimental payload.

As you are well aware, propulsion, power generation, and life support systems are often strongly dependent on the action of gravity for proper functioning. As I have already noted, in a zero or near zero gravity environment such systems may function poorly since the fluid flow and heat transfer processes occurring in these systems may be controlled by forces other than gravity such as surface tension, inertia, or viscous forces. Such considerations pertinent to the design of fluid systems for orbital applications, apply also to the design of terrestrial experiments on zero-g liquid behavior and convective heat transfer. In the latter case additional dimensionless parameters, among them the Grashof number, are required for a complete simulation. With a knowledge of the existing forces and of the pertinent parameters, it is possible to achieve terrestrial experiments in heat transfer and liquid settling and sloshing to be carried out under a one-g condition to gain information on the operation of the system in a near zero-g environment. Full simulation of all dimensionless parameters involved is not always possible. Moreover, for complex phenomena, the force ratios cannot always be estimated accurately. In these cases such experiments may not be conclusive but could be used to define the guidelines for further zero-g testing.

Recognizing the ambitious nature of the new NASA Zero-g Facility, ground simulation of zero and low-g environments may be considered to have great potential for experimental research. As your keynoter, let me leave you with these thoughts - Search for new and novel approaches to extending the duration of ground simulation of the weightless space environment. Don't overlook limited one-g studies where they may assist in developing guidelines for further zero-g testing. Consider the more expensive and less available zero-g vehicles such as aircraft and satellites only after you have fully explored all feasible ground techniques.

PAPER 1

**SATURN V LOW GRAVITY FLUID MECHANICS PROBLEMS
AND THEIR INVESTIGATION BY FULL-SCALE ORBITAL EXPERIMENT**

By Frank E. Swalley, Gordon K. Platt, and Leon J. Hastings
NATIONAL AERONAUTICS AND SPACE ADMINISTRATION
GEORGE C. MARSHALL SPACE FLIGHT CENTER

ABSTRACT

This paper describes the low-gravity fluid mechanics problems of the Saturn V/S-IVB stage, which must coast for an extended period in earth orbit and then restart to place the Apollo into translunar coast. Also described is the Saturn IB liquid hydrogen orbital experiment planned to verify the Saturn V/S-IVB propellant ullaging and orbital venting system.

The anticipated low-gravity fluid mechanics problems of the S-IVB arise primarily from the need to vent the liquid hydrogen tank due to boiloff. It was felt that it is better to maintain constant control of the propellant than to resettle it each time venting is required. Therefore, a system was designed such that the S-IVB vehicle is always accelerated positively. In orbit, the vented hydrogen gas is utilized to provide a minimum acceleration of 2×10^{-5} g. With the continuous venting system a problem of propellant settling

for restart is not anticipated, because the propellants should be bottomed throughout the coast phase.

At injection into orbit, severe dynamic effects are expected due to fluid motions established during ascent flight - e.g., sloshing and formation of thermal convective boundary layers. It is believed that unless baffles or other control devices are installed in the tanks, these disturbances will result in fluid covering the vent exits for an extended period. Confirmation of these suspicions was obtained recently on the Centaur flight, AC-4, where liquid dynamic effects dominated the behavior of the propellants and caused most of the liquid hydrogen to be vented overboard. The disturbances during orbital coast, which are slight as compared with those at injection, are caused by the operation of the attitude control system and the dynamic effects associated with venting.

Since data on fluid behavior in a low-gravity environment are meager and previous vehicle experience is limited, a full-scale orbital experiment is mandatory to insure successful operation of the Saturn V/S-IVB. Such an experiment, using the Saturn IB launch vehicle, has been approved. To monitor the behavior of the propellants, a TV system and additional instrumentation have been added.

SATURN V LOW-GRAVITY FLUID MECHANICS PROBLEMS AND THEIR INVESTIGATION BY FULL-SCALE ORBITAL EXPERIMENT

1 INTRODUCTION

The S-IVB stage of the Saturn V launch vehicle must coast for a maximum of 4-1/2 hr in a 100-nm earth orbit, then restart to place the Apollo into translunar coast. During this orbital coast period, the liquid hydrogen (LH_2) propellant will absorb sufficient thermal energy to evaporate a maximum of 3,000 lb of hydrogen. To keep the hydrogen tank structural weight within reasonable limits, the tank pressure must be relieved. This requirement is the major source of the S-IVB low-gravity fluid mechanics problems. The possibility of liquid oxygen (LOX) tank pressure relief also exists, but is not thought to be as critical. Therefore, the emphasis in this paper will be placed on the hydrogen tank.

Since data on fluid behavior in a low-gravity environment were meager and previous vehicle experience was limited, it was desirable to find a pressure relief system which would be independent of the fluid motions inside the tank (Refs. 1 and 2). No system of this type appears feasible at present. The problem, then, becomes one of designing a vent system which will remove only vapor from the tank. For such a system to operate efficiently, the ullage gases must be located over the entrance to the vent line and the propellant must be kept quiescent to insure that no liquid will be vented.

It appears more logical to maintain constant control of the propellant than to resettle it each time venting is required. Therefore, a system was designed such that the S-IVB vehicle is accelerated positively from first ignition through orbital coast, hopefully keeping the liquid in the bottom of the tank and the vapor in the top. Prior to first ignition of the S-IVB stage, the acceleration is provided by solid-propellant ullage rockets whose firing time overlaps thrust tailoff on the previous stage and thrust buildup on the

S-IVB stage Considering performance, cost, schedule, and reliability, the best system to supply continuous acceleration in orbit is one in which the thrust from the vented hydrogen gas is utilized. Naturally, the highest possible acceleration is desirable, but only enough gas is available to provide an acceleration of 2×10^{-5} g. This acceleration gives a Bond number (ratio of acceleration to surface-tension forces) of approximately 70 in the hydrogen tank and 200 in the LOX tank, which according to equilibrium theory should be adequate. With such Bond number values, the interest is in low-gravity fluid mechanics rather than zero-gravity fluid mechanics.

Obviously, if no other disturbances were present, the propellants would be settled and venting could be accomplished without loss of liquid. Unfortunately, many disturbances or dynamic effects will exist which, it was suspected, would cause venting of substantial amounts of liquid. Confirmation of these suspicions was obtained recently on the Centaur flight, AC-4, where liquid dynamic effects dominated the behavior of the propellants in the tank and caused most of the propellants to be vented overboard. On the S-IVB the dynamic effects would be caused primarily by fluid motions established during ascent flight - e.g., sloshing and formation of thermal convective boundary layers. Such motions will be in a controlled state during boost, but when the acceleration is suddenly reduced at injection into orbit the kinetic energy of these motions will be great enough to create severe propellant agitation. At injection, as a safety factor, an additional acceleration of 5×10^{-4} g for 100 sec will be provided, by auxiliary propulsion, to help gain initial propellant control. After injection into orbit the restoring forces will be very weak and will consist of the 5×10^{-4} g acceleration, and the propellant viscosity and/or eddy viscosity. With only these restraining forces the fluid motions would continue for an extended period of time (on the order of 1,000 sec). However, once these disturbances have been damped no other major problems are anticipated. The disturbances during orbital coast are slight compared with those at injection and are caused by the operation of the attitude control system and the dynamic effects associated with venting. To minimize venting problems, rapid depressurizations of a saturated liquid have been avoided by utilizing a system designed to maintain an almost constant tank pressure.

At some time during the 4-1/2 hr, the engine will be restarted to accelerate the Apollo to earth-escape velocity. With the continuous venting system a problem of propellant settling for restart is not anticipated because the propellant should be bottomed throughout the coast phase and thus in its desired location for engine restart.

Existing knowledge does not permit analyses and/or analytical scaling of small-model tests to be used as a means of verifying the adequacy of the Saturn V/S-IVB orbital propellant settling and venting system. Small-scale tests can be used to study the initial behavior of individual transient phenomena, but it is not possible to duplicate simultaneously all the parameters necessary to study the interactions of the various phenomena, nor is the available testing time sufficient to observe the full duration of the motions. Available theory and experimental results in zero-g and low-g fluid mechanics are concerned primarily with static-equilibrium liquid-vapor interface configurations in small containers of simple shape (Ref. 3). Recently, some information has become available concerning dynamic effects such as draining, propellant settling, and small-amplitude slosh disturbances. However, it is evident that even using these data, a rather severe extrapolation in size is required. While the static-equilibrium data will assist in predicting conditions during orbital coast, they will not aid in the solution of critical dynamics problems at injection into orbit. Obviously, a full-scale low-g orbital experiment is mandatory to insure successful operation of the Saturn V/S-IVB. Such an experiment has been approved using the Saturn IB launch vehicle.

2 GENERAL DESCRIPTION OF SATURN V/S-IVB STAGE AND LH₂ ORBITAL EXPERIMENT VEHICLE

The S-IVB is a multipurpose stage which will be used both on the Saturn IB and Saturn V launch vehicles. It is propelled by one J-2 engine of 200,000 lb thrust, employing LH₂ and LOX. Figure 1 shows the overall configuration and pertinent dimensions of the S-IVB. The LH₂ tank is insulated internally with a reinforced, sealed, polyurethane foam, while the LOX tank is not insulated. The LH₂ and LOX tanks are separated by an insulating common bulkhead. Attitude control is effected by six 150-lb-thrust, storable propellant motors arranged three to a module. Solid-propellant ullage motors are

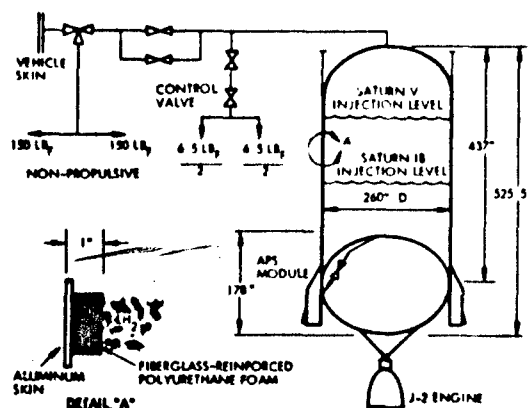


Fig. 1 S-IVB Stage Configuration

provided for propellant settling prior to first burn of the J-2. The LOX and LH₂ engine feed lines and propellant pumps are chilled prior to start by propellant recirculation systems; the propellant, after chilling the hardware, is returned to the main propellant tanks.

As applied to the Saturn IB, the stage does not restart, and the propellant tanks will be essentially depleted at injection into orbit. A nominally nonpropulsive vent system is provided for the

hydrogen tank, and the oxygen tank is vented through a line directed through the center of mass of the stage. Residual propellants and pressurants are blown down through these vent systems to prevent venting during docking maneuvers.

In the Saturn V, the S-IVB will burn into orbit, with approximately 66 percent of its propellant remaining aboard for the second burn. It must be capable of coasting for up to 4-1/2 hr in orbit between burns. To provide for hydrogen venting during coast, a longitudinally directed, continuous venting system has been added. Also, one 70-lb-thrust auxiliary propulsion system (APS) motor has been added to each APS module to settle propellants during damping of propellant motion at injection into orbit, and during engine chill preceding the second burn of the J-2 engine. The S-IVB/V blowdown vents are identical to those on the S-IVB/IB and serve the same purpose.

The S-IVB for the LH₂ orbital experiment is essentially an S-IVB/IB modified to simulate the S-IVB/V during orbital coast. Since the 70-lb, longitudinal-firing ullage engines are not available in the S-IVB/IB, the LOX tank will be vented through longitudinally directed lines to simulate this thrust. To obtain the maximum amount of LH₂ in orbit, the LOX tank will be offloaded and the payload will be replaced by a lightweight shroud.

The continuous-vent system will be added to the S-IVB, modified to give the same longitudinal acceleration as it does to the S-IVB/V. The LH₂ tank will be instrumented with two television cameras. Numerous temperature and liquid-vapor sensors will be added to the LH₂ tank and the propellant feed and vent systems. Vent gas quality also will be measured by a specially developed quality meter.

3 PROPELLANT DYNAMICS AT INJECTION INTO ORBIT

Fluid motions established during ascent are expected to produce severe dynamic effects at injection into orbit. It is believed that these disturbances will result in fluid covering the vent exits for an extended period unless baffles or other control devices are installed in the tanks. In the hydrogen tank, the fluid impingement on previously dry surfaces would result in a high rate of tank pressure rise, since the internal insulation surface will have been heated by pressurization gas during the first firing of the main engine. "Worst case" calculations predict that the LH₂ tank pressure would rise to the nonpropulsive vent band limits in a minimum of 100 sec (Ref. 4). Therefore, it appears that LH₂ tank venting will occur long before the motions have damped out naturally, and a means must be found to gain control earlier.

To help suppress the fluid motions and gain initial control, two 70-lb ullage engines will be fired during J-2 engine thrust decay, and this firing will continue approximately 100 sec. However, the total thrust of 140 lb produces an acceleration of only 5×10^{-4} g. This thrust was added early in the design as a safety factor; now it is believed that the thrust levels required to control the propellant motions by means of acceleration alone would be excessive and that the associated weight penalties would be prohibitive. Therefore, other means must be found for propellant control.

The individual phenomena causing the propellant motions at injection into orbit and the control of these motions will now be discussed.

4 BOOST SLOSH

One of the major sources of energy in the liquid hydrogen propellant at injection into orbit is sloshing incurred during the ascent flight. An idea of the sloshing to be expected in the LH_2 tank of the Saturn V/S-IVB may be gained by examining the S-IV flight data (Ref. 5). From data on flight SA-5 there is evidence of LH_2 sloshing at both the first- and second-mode natural frequencies of approximately 0.4 cps and 0.7 cps. The maximum LH_2 slosh amplitude of about 0.6 ft occurred about 50 sec after S-IV ignition and decayed to about 0.13 ft in approximately 300 sec. Similar results were obtained on the Saturn I flights. Since these values agree well with analytical predictions, confidence in the ability to predict the sloshing on S-IVB was obtained.

An analysis was performed (Ref. 6) to predict the sloshing in the S-IVB LH_2 tank just prior to injection into orbit. An amplitude of 0.42 ft was predicted with a maximum wall velocity of 1.83 ft/sec. Assuming that the kinetic energy associated with the wall

velocity is converted to potential energy, it is found that the liquid can jump 100 ft in the g field of $5 \times 10^{-4} g$ (Fig. 2). Since this jump height is much greater than the distance from the liquid surface to the top of the tank, it is concluded that the vent exit will be covered. If the jump height tolerated were set arbitrarily at one-quarter of a tank diameter, an acceleration of 0.01 g , or 3,000 lb thrust, would be required on the Saturn V. Obviously, the propulsion system required to produce such an acceleration until the motions damp out would impose an unacceptable payload penalty. The simplest solution would be to baffle the hydrogen tank to prevent these large slosh velocities. It was calculated (Ref. 6) that three ring baffles 10 in. wide and spaced 12 in. apart, with the middle baffle located at

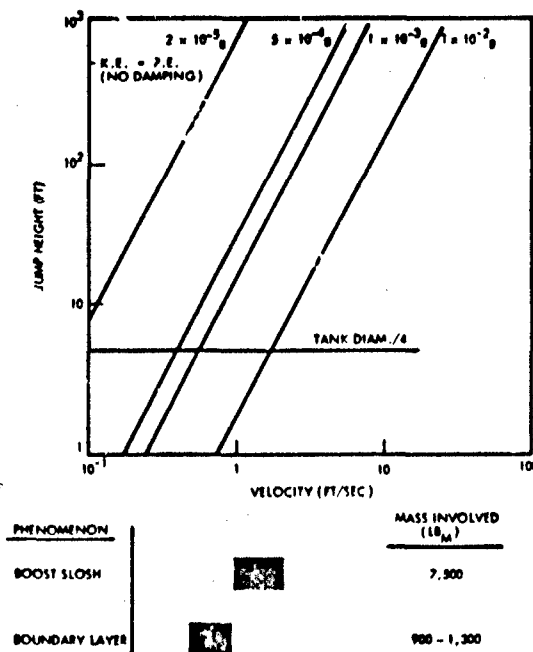


Fig. 2 Potential Liquid Jump Heights at Injection Into Orbit

the liquid level expected at injection, would damp the maximum slosh velocity to 0.15 ft/sec—resulting in jump heights of 0.7 ft at 5×10^{-4} g and 17 ft at 2×10^{-5} g. However, the prediction of a 17-ft jump is not realistic, since the kinetic energy dissipated during the 100 sec of Gemini engine firing and the deflection of the flow by the upper slosh baffle were not considered. Therefore, the three slosh baffles should suppress the boost sloshing adequately. In addition, the three rings allow for some error in predicting the exact liquid level. Efforts now are being made to have the baffles installed on the Saturn IB experiment and all the Saturn V vehicles.

Tests in the Marshall Space Flight Center (MSCF) drop tower also are planned to confirm the existence of the problem and to evaluate the performance of the slosh baffles.

5 THERMAL CONVECTIVE MOTION

During ground hold and ascent, thermal convective patterns will be formed in the liquid propellants due to environmental heating. Velocities and temperatures within the liquid can be estimated by assuming that these convective patterns can be described as boundary layers on the tank walls. Using the analytical procedures of Refs. 7 and 8, and assuming an average acceleration and heat rate during ascent, it is found that the average velocity for the entire boundary layer is 0.5 ft/sec and the average velocity at the liquid interface is 0.7 ft/sec for the Saturn V. On the Saturn IB the average velocities are 0.7 ft/sec for the entire boundary layer and 1 ft/sec at the liquid interface. The mass of fluid in this boundary layer is estimated to be 900 lb on the Saturn IB and 1,300 lb on the Saturn V. During ascent the hot fluid will rise to the top of the tank due to buoyancy forces and, under the influence of the gravitational field, will spread out across the surface. However, when the acceleration is suddenly reduced at injection, the gravitational forces no longer will be strong enough to bend the liquid streamlines over at the surface. Instead, it is believed, the liquid will continue vertically.

An indication of the relative magnitude of the forces governing the fluid behavior at the liquid surface on the Saturn V can be obtained by calculating the Weber number and

the Froude number for the boundary layer. Using the thickness of the boundary layer at the liquid surface as the characteristic length, and the average velocity at the surface, the Weber number is approximately 200. This value indicates that inertia forces predominate over capillary forces. The value of the Froude number for the 5×10^{-4} g field existing after injection into orbit is about 100 - suggesting that inertia forces also are larger than gravitational forces. Therefore, it is concluded that the interface will be broken and the liquid will jump vertically.

If it is assumed that the kinetic energy of the thermal boundary layer is converted into potential energy, it can be seen from Fig. 2 that the jump height for the Saturn V would be 8 ft based on the average velocity of the boundary layer mass and 15 ft based on the average velocity at the surface. For the Saturn IB the distance would be 15 ft and 31 ft - based on the average velocity of the boundary layer mass and at the liquid surface, respectively. Restricting this motion by means of acceleration would be prohibitive, as it was in the case of boost slosh. However, the baffles installed to damp boost sloshing also would deflect the initial upward motion of the convective boundary layer and hopefully would dissipate the kinetic energy. Model tests in a drop tower are planned to confirm these predictions.

6. TERMINATION OF DRAINING

Another source of momentum in the fluid is propellant draining. As propellant is consumed during main-engine firing, the liquid surface in the hydrogen tank is dropping at the rate of 0.05 ft/sec. Even higher local velocities will exist. Near the engine feed line the velocities will be as high as 15 ft/sec. When the engine valve is closed, this momentum will persist. Since the motion cannot continue downward any longer, the liquid will turn, losing some of its energy, and move upward. However, it has been calculated that the velocities are not high enough to be of major concern.

Associated with valve closure is another phenomenon, which is of concern. During static firings on the S-IVB Battleship, engine feed line pressure surges on the order

of 50 psia have been measured. Such pressure surges could cause severe local disturbances in the liquid. To avoid such a possibility, the entrances to the engine feed lines (both LOX and LH_2) will contain baffles and/or diffusers. The configurations of these devices are being determined.

7 STRUCTURAL RELAXATION

During the boost phase of flight the tank sidewalls and lower bulkheads will be deflected. At injection into orbit the structure will relax, or try to return to its undeflected position. In the process, some of the strain energy stored in the structure will be transmitted to the liquid. To determine what effect the structural relaxation would have on the liquid, a simple spring-mass analysis of the Saturn IB vehicle at injection into orbit has been completed (Ref. 9) and a similar analysis will be conducted for the Saturn V. In the analysis it was assumed that the propellants act as point masses attached by springs to the tank. The vehicle structure also was divided into components and connected by springs. The exciting force for the spring mass system, of course, is main engine thrust.

Because of the nature of the assumptions, the analyses predict an oscillatory motion of the liquid masses at thrust termination. Obviously, the liquid will not behave as rigid masses. However, the results can be used to predict the initial average velocity; the results indicate an initial, average, upward velocity of 0.005 ft/sec in the LH_2 tank at injection into orbit. This velocity should not produce significant problems, as can be seen from Fig. 2. A prediction for the Saturn IB LOX tank cannot be made because the LOX residual is small in comparison with the mass of the structure. The spring-mass analysis leaves much to be desired, and work is being initiated to predict theoretically, and confirm by model tests, the interaction of a flexible tank and a fluid.

8 LIQUID COMPRESSION

Even though liquids are not very compressible, the amount of energy stored in the hydrogen because of the hydrostatic head may have a significant effect on the propellant behavior at injection into orbit. The energy stored in the liquid can be calculated by

the methods of Ref. 10. Assuming an LH_2 compressibility factor of $6.25 \times 10^{-6} \text{ ft}^2/\text{lb}_f$, the liquid energy will be 148 ft-lb_f and 13 ft-lb_f for the Saturn IB and V, respectively. If this stored energy is converted into kinetic energy, the average liquid velocity will be 0.2 ft/sec for the Saturn V and 0.6 ft/sec for the Saturn IB. Figure 2 shows that the liquid can jump a maximum of 11 ft in the Saturn IB and 1.4 ft in the Saturn V, at injection into orbit. Further investigation is required to determine the amount of the compression energy that is converted into kinetic energy.

9 INSTRUMENTATION TO OBSERVE INJECTION DYNAMICS

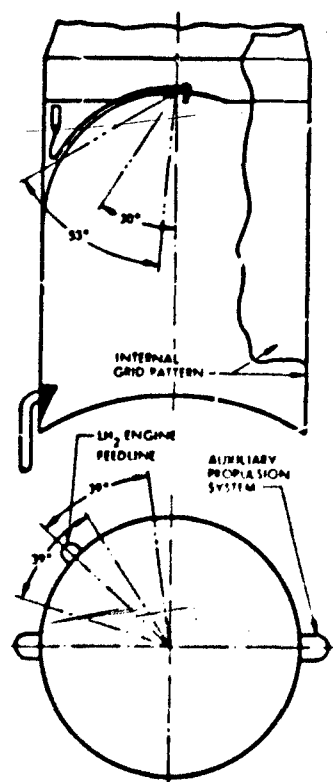


Fig. 3 Television Camera Viewing Angles

In the Saturn IB orbital liquid-hydrogen experiment vehicle and the early Saturn V R&D vehicles, additional instrumentation has been added to the S-IVB stage to monitor LH_2 behavior. To observe the propellant motions, two high-speed (30 pictures/sec) TV cameras have been installed in the manhole cover of the LH_2 tank; the viewing angles are shown in Fig. 3. A grid has been painted on the internal insulation to aid in depth perception. Ground tests have shown that any disturbances on the liquid surface make the interface in that area visible and that the junction of the liquid and the wall is discernible. However, if the liquid is subcooled and quiescent then it is almost like looking into an empty tank. Since liquid agitation and motion are expected, the transparency of the hydrogen should not present any problem.

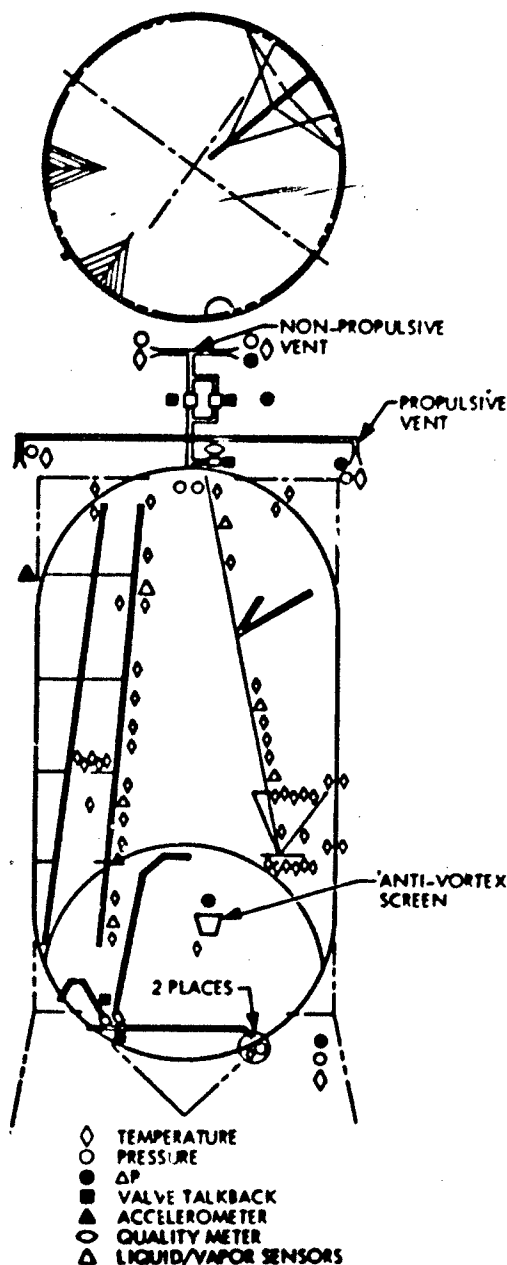


Fig. 4 S-IVB Hydrogen Tank Instrumentation (Applicable to Early Saturn V/S-IVB and to Saturn IB Orbital Hydrogen Experiment Vehicle)

Additional instrumentation such as liquid-level sensors and temperature probes have been added to the tank (Fig. 4). The measurements which will be of particular value in studying liquid dynamics at injection into orbit are those made with the accelerometers, thermal boundary layer survey rakes, the quality meter, and the liquid-vapor sensors. To determine the performance of the Saturn V and IB vent system and the Saturn IB LOX thrust system, pressure and temperature measurements have been located appropriately in the lines. For system operation analysis, valve position indicators have been included. No problems due to capillary effects in the narrow openings of the instruments are expected following injection into orbit since fluid dynamics effects will predominate. Instrument response times are considered adequate (Ref. 11).

Information from all of the instrumentation will be received throughout boost and immediately after injection into orbit. The ground receiving stations and times of coverage are shown in Fig. 5 along with the sequence of events. It can be seen that the fluid motions after injection into orbit can be monitored for approximately 5 min by the tracking station at Bermuda. If additional time is required, a ship may be placed off Bermuda.

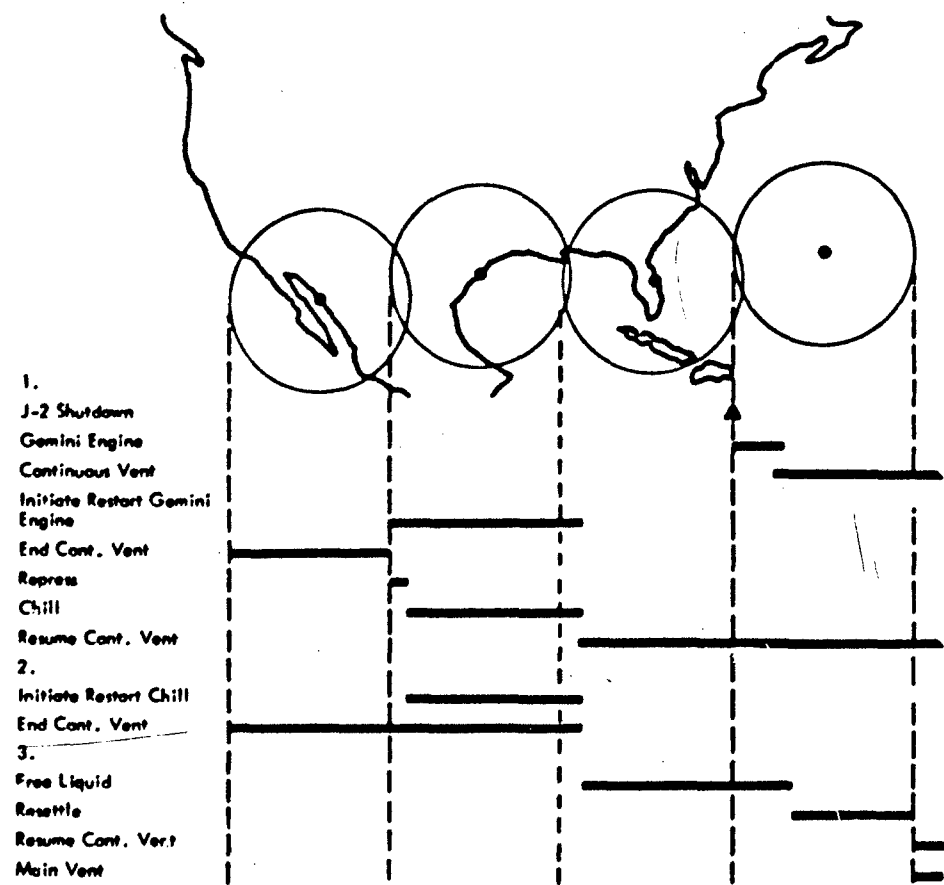


Fig. 5 Orbital Sequence of Events and Ground Tracking Coverage

10 ORBITAL COAST

During the orbital coast phase of the mission the vehicle will be floating freely (almost undisturbed) with no significant maneuvers planned, except in roll to permit astronaut navigational sightings. Therefore, the propellants should be bottomed due to the acceleration produced by the continuous vent system and in a quasi-equilibrium state.

In such a state the equilibrium predictions should apply and indicate what to expect. The shape of the equilibrium liquid-vapor interface in the LH_2 tank has been calculated using the methods of Ref. 12, and is shown in Fig. 6. It can be seen that the interface is flat over most of the tank, rising at the tank walls to satisfy the 0-deg contact angle boundary conditions. According to drop tower experiments on liquid-vapor interface stability, the critical Bond number is 0.84 - which for the S-IVB would mean that any acceleration greater than 10^{-7} g would be significant. Since such low accelerations are of importance, even small forces such as aerodynamic orbital drag (which would normally be neglected) have to be considered. An analysis was conducted to determine the magnitude of all such forces; results are shown in Table 1. Since the continuous vent thrust is an order of magnitude larger, no problem is expected. The only disturbances expected would be those associated with the continuous venting and resulting from the action of the attitude control system. Each of these disturbances will now be discussed.

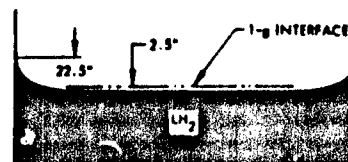


Fig. 6 Equilibrium Liquid-Vapor Interface Shape in the LH_2 Tank During Orbit

Table 1
SUMMARY OF IMPORTANT ACCELERATIONS

<u>Source</u>	<u>Magnitude (g)</u>
Aerodynamic Orbital Drag	10^{-6} (Ref. 13)
Gravity Gradient	10^{-6} (Ref. 14)
Solar Pressure	10^{-9}
Centripetal Force	
Rotation about Vehicle CG	10^{-7}
Attitude Control System	10^{-6}
Crew Movements	?

11 SLOSH INDUCED BY ATTITUDE CONTROL

The attitude control system on the S-IVB stage has a deadband of ± 1 deg and an attitude rate of ± 0.2 deg/sec. When the vehicle exceeds these limits, the proper motor will fire and correct. Each motor has a thrust of 150 lb and produces a step impulse of 7.5 lb-sec. The stage will then "free float" until the limit is again exceeded.

Until recently, no information was available on low-gravity sloshing. Satterlee studied the natural frequency of oscillating liquid columns and their liquid-vapor interface shape in a low-gravity environment (Ref. 14). Unfortunately, the lowest contact angle studied was 15 deg and the amplitudes of the standing slosh waves at the tank wall were not estimated. However, Satterlee's work can be used to estimate the natural frequencies of the LH_2 tank and obtain an idea of what frequencies to avoid in the operation of the attitude control system. Figure 7 is a plot of dimensionless frequency parameter versus Bond number. Since the lines are equally spaced and parallel, it is possible to draw in the line for a fluid of near 0-deg contact angle. For the S-IVB stage at a Bond number of 70 the natural frequency is 1.6×10^{-3} cycles/sec. Also, if the values of natural frequency as predicted by the faired line of Fig. 7 are compared with the conventional high-g theory of Ref. 15, good agreement is found. Such agreement suggests that conventional slosh theory can be used to predict the natural frequency of cylindrical hydrogen tanks at Bond numbers of ≈ 100 or larger.

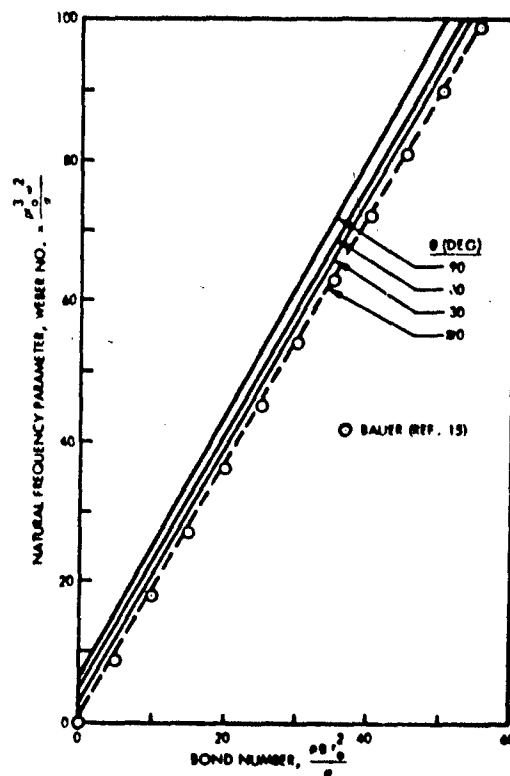


Fig. 7 Non-Dimensionalized Natural Frequency of a Vibrating Liquid Column in a Cylinder as a Function of Bond Number for Various Contact Angles

The natural frequency of the LOX tank was not estimated in similar fashion because the shape of the tank is different, which will have a strong influence on the value. However, the Bond number in the LOX tank, even at the low continuous vent acceleration levels, is high - about 200 if the characteristic length used is the maximum radius. At such Bond number levels, Ref. 14 states, conventional high-g theory should be applicable since the interface is flat. Therefore, modified high-g spherical tank theory (Ref. 16) was used to predict the values of the natural frequencies in the LOX tank. It is found that the natural frequency of the LOX during orbital coast will be approximately 1.6×10^{-2} cps.

Tests are planned in the drop tower at Marshall Space Flight Center (MSFC) to study impulsive low-gravity sloshing and establish the usefulness of 1-g testing in predicting low gravity sloshing. The effect of multiple impulses also will be investigated to determine whether the interface will be broken. Still, neither the tests nor the theory accounts for the effects of multiple-plane impulses which might change the interface shapes. At the present time, low-gravity sloshing is not considered to be a problem on the S-IVB stage. However, analyses are continuing.

12 LH₂ TANK BOILOVER

The continuous vent line contains a modulating valve which will regulate the flowrate in response to the tank pressure. When the valve is opened after the fluid motions at injection into orbit have been damped, it will vent the hydrogen tank slowly to approximately 20 psia and maintain this value thereafter to within ± 0.5 psia. Initially, the liquid will be subcooled and no problems are expected. Toward the end of the venting, some of the liquid will become saturated and bulk boiling will occur, but no significant problems are anticipated at this time. However, once the liquid in the tank has saturated at the 20-psia level, nucleate boiling should occur over the tank walls. This boiling will continue for at least the first orbit until the heat stored in the internal insulation during ascent is dissipated. Then the heat transfer rates should be so low that only natural convection will exist (Ref. 17).

There was some concern about the effect of the loss of buoyancy forces on the bubble growth and detachment. Originally, it was thought that the buoyancy forces were responsible for breaking the bubble away from the wall. Therefore, in a low-gravity field the bubbles would remain attached to the wall and grow until the tank walls were vapor-dominated. Clodfelter (Ref. 18) suggests that the dynamics of the growing bubble, and not buoyancy, cause bubble detachment. For this and other reasons, the authors do not feel that the wall will become vapor-dominated. Nonetheless, this fact is yet to be proven conclusively.

The reduction in the buoyancy forces presents another problem. Once the bubbles have detached from the wall, they will rise very slowly. Since a given mass of hydrogen will occupy about 50 times as much space as a vapor than as a liquid, the vapor interface will rise as the bubbles are formed in the liquid. If the ullage gas is vented too rapidly, the bubbles will not have time to rise and join the ullage before the ullage has been vented away, and the tank will boil over. To determine the interface rise rate for a given acceleration and vent flowrate the bubble sizes and distribution must be known. Unfortunately, there are no theoretical means for predicting the needed information. Some feel for the problem can be obtained by postulating a simplified model. Assume that vapor is generated at a rate equal to the vent flowrate and is uniformly distributed over the tank walls, and that each bubble rises at its terminal velocity without interference from neighboring bubbles. The

bubble sizes are assumed to fit a Maxwellian distribution curve with the average bubble size as a parameter.

Figure 8 shows the predicted interface rise rates for the S-IVB assuming average bubble diameters of 1/2, 1, and 2 in. It can be seen that intolerable interface rise heights are predicted for the small-diameter bubbles. However, low-gravity experiments have shown that hydrogen bubbles tend to coalesce, forming larger bubbles. Therefore, it

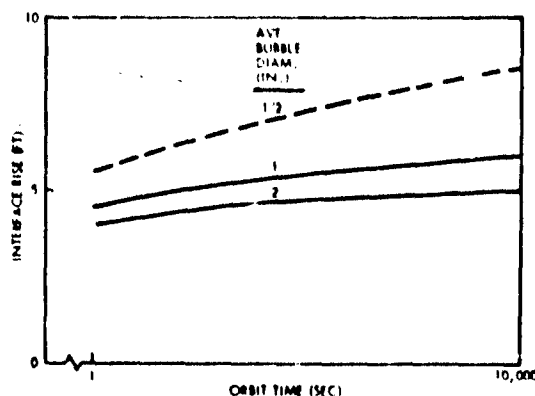


Fig. 8 Liquid-Vapor Interface Rise Due to Bubble Formation on the Tank Sidewall

is believed that large-diameter bubbles will be present in the S-IVB tank. Also, the analysis is conservative in that the maximum rate of vapor formation was used.

Another possibility which may cause the liquid-vapor interface to rise is vapor trapped by the slosh baffles. If it is assumed that each of the two submerged baffles traps a vapor pocket having a volume one-fourth that of a torus of radius equal to the width of the slosh baffle, then the interface would rise 0.2 ft.

Considering all these factors, the liquid-vapor interface in the S-IVB hydrogen tank should not rise more than about 2 ft during continuous venting, and tank boilover is not considered to be a problem.

13 ORBITAL COAST INSTRUMENTATION

The TV system and instrumentation used to observe fluid dynamics at injection into orbit also will provide data on the behavior of the propellants during orbital coast. Standard telemetry information will be available shortly after injection into orbit and at several times during orbit. However, the first visual information on the coast-phase propellant behavior will not be available until Carnarvon, Australia, is reached about 46 min after injection. After Carnarvon, a large gap in the coast data will occur as the vehicle crosses the Pacific on the first pass (Fig. 5). During the coast phase, the data are expected to show a quasi-steady-state behavior and some problems are expected with the performance of the instrumentation due to capillary effects predominating in the narrow openings.

14 MAIN ENGINE RESTART

Before the J-2 engine can be restarted, the pumps and engine feed lines must be conditioned thermostatically. To accomplish this chill, a closed-loop recirculation system is employed for both propellants, with the hot liquids and/or gases being returned to their respective tanks. On the liquid hydrogen experiment, only an LH_2 chilldown will be attempted because sufficient LOX will not be available. The fluids are circulated by

electric-motor-driven pumps. Due to NPSH starting requirements of the LH_2 recirculation pump, the tank must be pressurized by about 2 psi. This increase in pressure is provided by helium gas stored in ambient bottles on the main thrust structure. To repressurize the LH_2 tank, the continuous venting must be terminated. Since the philosophy has been that an acceleration will be applied to the vehicle at all times, the Gemini engines (the LOX thrusting system in the case of the Saturn IB experiment) are started at the termination of continuous venting and continue to supply thrust until after J-2 ignition. The low-g fluid mechanics problems expected during this phase of the mission are concerned with the removal of trapped vapor pockets in the lines and the effect of the returning fluid in the tank.

15 CHILLDOWN

A drawing of the liquid hydrogen recirculation system is shown in Fig. 9. The screen over the entrance to the engine feed line serves as a filter and anti-vortex device. It also helps damp out pressure surges associated with valve closure. However, once

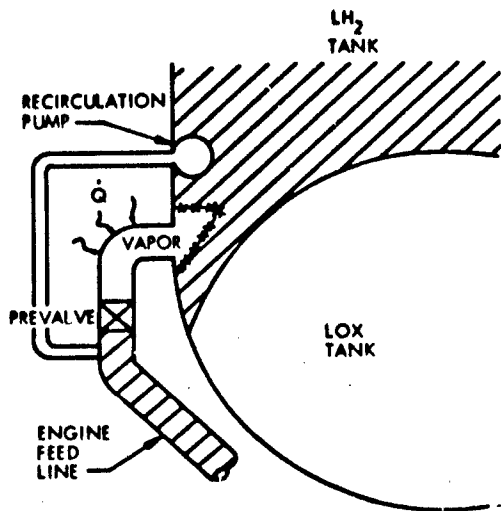


Fig. 9 Liquid Hydrogen Chilldown System

the prevalve is closed the screen and the prevalve act as a vapor trap. Heat transfer calculations show that there is sufficient thermal energy to vaporize the liquid contained between the prevalve and the screen. This vapor will rise to the screen due to the buoyancy forces created by continuous venting, but will not be able to escape. Eventually, the entire pocket will be filled with vapor. During recirculation the prevalve still will be closed and the pocket of vapor will remain. At the end of the recirculation period the prevalve will be opened in an effort to clear the area by fluid flow; the adequacy of this method will be determined by 1-g model tests in the near future.

Another problem associated with the chilldown system is the effect of the momentum of the fluid returning into the tank. Gas velocities as high as 150 ft/sec are predicted and liquid return velocities may be as high as 20 ft/sec. If this energy causes the liquid to mix with the ullage then a pressure decay will occur, resulting in loss of main engine NPSH. Therefore, the recirculation return line inlets in both the LOX and LH₂ tanks will be diffused and/or baffled.

16 INSTRUMENTATION

The TV system and tank instrumentation again will be used to observe any significant disturbances. To monitor the performance of the LH₂ recirculation system, additional pressure and temperature measurements were added. On the experiment, the chill-down sequence will be initiated on the first pass over the U.S. (Fig. 5). The overlap of the receiving stations will permit complete coverage of the chilldown.

17 SECONDARY OBJECTIVES OF SATURN IB EXPERIMENT

After completing the primary mission of verifying the adequacy of the Saturn V/S-IVB venting and settling systems, the Saturn IB experimental vehicle will be used to obtain data on two other low-g fluid mechanics phenomena. First, all axial thrusting will be terminated and the liquid will be permitted to drift forward under the influence of orbital aerodynamic drag. Then the liquid will be resettled at 10^{-4} g. Finally, data will be obtained on high-speed venting of a saturated tank by blowing the hydrogen tank down through the nonpropulsive vent system.

18 CONCLUSIONS

In conclusion, the interest is in low-gravity fluid mechanics, not zero-gravity fluid mechanics. The problems on the Saturn V/S-IVB stage are caused primarily by the requirement of venting, and not propellant settling for engine restart. These problems are dynamic in nature and are most severe at injection into orbit. It is believed that if

the fluid motions at injection can be controlled, particularly as related to boost slosh and thermal boundary layer, the major problem will have been overcome. To suppress these motions to an acceptable level, slosh baffles will be added to the LH_2 tank, and diffusers and/or baffles to all propellant line inlets. During orbital coast a quasi-equilibrium condition is expected, where small forces are important and must be considered. The equilibrium liquid-vapor interfaces are essentially flat. Small disturbances are expected due to the attitude control system and venting, but these are not believed to be serious. Prior to engine restart some problems are anticipated in the removal of trapped vapor pockets from the engine feed lines, but these problems appear to be solvable.

It is not possible to verify completely the design of the ullaging and venting system by analyses or model testing. Therefore, a full-scale orbital experiment will be flown using a Saturn IB vehicle.

It is hoped that this paper supplies information helpful in planning further low-g fluid mechanics research programs. Eventually, it must become possible to design systems for orbital venting and propellant settling which do not require confirmation by full-scale orbital experiments.

19 REFERENCES

1. National Aeronautics and Space Administration, Orbital Storage of Liquid Hydrogen, by J. R. Oliver and W. E. Dempster, NASA TN D-559, 1961
2. Clifford N. Hall, "Subcritical Controlled-Ullage Cryogenic Tankage Concept," J. Spacecraft, Vol. 1, No. 4, Aug 1964
3. National Aeronautics and Space Administration, Static and Dynamic Behavior of the Liquid Vapor Interface During Weightlessness, by E. W. Otto, NASA TM X-52-16, Apr 1964
4. -----, Ullage Pressure in the S-IVB/Saturn V Following First Burn Shutdown, by W. S. Jensen and F. E. Swalley, Marshall Space Flight Center Memorandum R-P&VE-PTF-64-112, 7 Jul 1964

5. National Aeronautics and Space Administration, Results of the Fifth Saturn I Launch Vehicle Test Flight, Marshall Space Flight Center Report MTR-SAT-FE-64-15, Apr 1964 (C), (Note: Referenced data are unclassified.)
6. -----, Baffle Requirements for S-IVB Hydrogen Tank to Eliminate Sloshing When Entering Orbit, by Robert S. Ryan, Marshall Space Flight Center Memorandum R-AERO-DD-31-65, 9 Mar 1965
7. -----, Analysis of Turbulent Free-Convection Boundary Layer of Flat Plate, by E. R. G. Eckert and T. W. Jackson, NACA TR 1015, 1951
8. Lockheed Missiles & Space Company, RIFT Thermodynamics Scaling Law Studies, NSP-63-117, Sunnyvale, Calif., 15 Nov 1963
9. National Aeronautics and Space Administration, Preliminary Investigation of Propellant Separation After Orbital Cutoff of the Saturn IB 203, S-IVB Stage, by J. Harbison, Marshall Space Flight Center Memorandum R-P&VE-SLR-65-26, 17 Mar 1965
10. J. L. McGrew, personal communication with authors, Dec 1964
11. G. K. Platt and F. E. Swalley, "Adequacy of Saturn IB Orbital Experiment Instrumentation," Marshall Space Flight Center Presentation, Dec 1964
12. Lockheed Missiles & Space Company, Analytical and Experimental Study of Liquid Orientation and Stratification in Standard and Reduced Gravity Fields, Report 2-05-64-1, Sunnyvale, Calif., Jul 1964
13. National Aeronautics and Space Administration, Drag Force, Orbital Lifetime and Ground Communication Visibility for Saturn IB Liquid Hydrogen Orbital Experiment, by Ann R. McNair, Marshall Space Flight Center Memorandum dated 19 Oct 1964
14. Stanford University, The Dynamics of the Free Liquid Surface in Cylindrical Containers under Strong Capillary and and Weak Gravity Conditions, by H. M. Satterlee and W. C. Reynolds, Stanford Technical Report LG-2, Stanford, Calif., May 1964

15. National Aeronautics and Space Administration, Theory of Fluid Oscillations in a Circular Cylindrical Ring Tank Partially Filled with Liquid, by H. F. Bauer, NASA Technical Note TND-557, Dec 1960
16. -----, Dynamic Analyses Branch, Saturn V Sloshing Data, Marshall Space Flight Center Memorandum R-AERO-DD-53-64, 24 Jul 1964
17. General Dynamics/Astronautics, The Final Report for the General Dynamics/Astronautics Zero-g Program Covering the Period from May 1960 Through March 1962, Report AY62-0031, 15 Aug 1962
18. Air Force Systems Command, Low-Gravity Pool-Boiling Heat Transfer, by R. G. Clodfelter, Technical Report APL-TDR-64-19, Mar 1964

ACKNOWLEDGEMENT

Material for this paper was contributed by various organizations of the Marshall Space Flight Center. In particular, the contributions of the personnel of the Aero-Astrodynamic Laboratory and the Propulsion and Vehicle Engineering Laboratory are gratefully acknowledged.

DISCUSSION

Lt. P. Bovenkerk, AFRPL, Edwards Air Force Base

When do you plan to conduct the experiment on the Saturn IB launch vehicle?

Swalley

It will be in the 3rd quarter of calendar year 1966.

Marvin Adelberg, Consultant

Why does your liquid vapor interface rise height vary with orbit time in Figure 8?

Swalley

The interface rises with time because the vapor generation exceeds the amount of vapor breaking the liquid surface. This difference decreases with time and the curve levels off.

Lidia Manson, Rocketdyne

Where did you get the 200 Btu/hr/ft^2 for nucleate boiling? All the liquids which I have found start boiling at 250 Btu/hr/ft^2 .

Swalley

The only reference on the initiation of nucleate boiling is the General Dynamics work which showed 250 Btu/hr/ft^2 , but this was a drop tower test. To be conservative we assumed that boiling would begin at our heat flux level of 200 Btu/hr/ft^2 .

Gene Zara, Wright Patterson Air Force Base

Do you assume that all heat transfer to the wall is utilized for vapor generation?

Swalley

Yes. This was another conservative assumption as far as liquid vapor interface rise was concerned.

BLANK PAGE

PAPER 2

**AN EXPERIMENTAL INVESTIGATION OF THE DYNAMIC
BEHAVIOR OF THE LIQUID-VAPOR INTERFACE UNDER
ADVERSE LOW-GRAVITATIONAL CONDITIONS**

By William J. Masica and Jack A. Salzman
NATIONAL AERONAUTICS AND SPACE ADMINISTRATION
LEWIS RESEARCH CENTER

ABSTRACT

The NASA Lewis Research Center has conducted an experimental investigation of the dynamic behavior of the liquid-vapor interface in response to an adverse constant translational acceleration, positively directed from the vapor to liquid phase. The results of the investigation are divided into three phases: The stability characteristics of the interface, the quantitative description of the motion of the interface, and the mechanism of reorientation or collection of liquids.

The discussion of the stability characteristics of the interface is limited to a brief summary of the methods used to acquire the data and the results indicating the validity of the Bond number criterion as the scaling parameter in an induced low gravity environment. In particular the critical Bond number delineating the stable and un-

stable regions of the interface has been verified to be 0.84 for solid-liquid-vapor systems possessing zero-degree contact angles, and is independent of the applied acceleration field.

The motion of the liquid-vapor interface in cylindrical containers is correlated with the applied acceleration and certain system parameters. The profile of the interface following its disruption by an adverse axial acceleration larger than critical, has been noted to assume the form predicted by the inviscid potential theory of G.I. Taylor. The rate at which the vapor phase penetrates the liquid phase can be obtained from the following derived empirical relation:

$$V_o = 0.48 (aR)^{1/2} \left(1 - \left[\frac{0.84}{Bo} \right]^{Bo/4.7} \right), \quad Bo > 1$$

where V_o is the vapor penetration rate,
 a the imposed acceleration,
 R the cylinder's radius,
 and Bo the Bond number.

The leading edge of the interface was found to accelerate over distances comparable to fineness ratios of two, the magnitude of which can be estimated by

$$a_L = \frac{3.8 V_o^2}{R}$$

where a_L is the acceleration of the leading edge, and
 V_o is the calculated vapor penetration rate.

The mechanism of the reorientation or collection mode in Centaur/Saturn geometrical models has been investigated in low acceleration environments. The worst condition of propellant location is assumed in the experiments, i.e., the liquid located at the vent portion of the tank model. Following a period of weightlessness to allow the interface to approach its zero-gravity configuration, an acceleration is imposed on

the system to relocate the liquid at the desired pump inlet portion of the models. While information to date on the mode of collection has been largely qualitative, significant results have been obtained. Despite the existence of a prominent "geyser" when the leading edge impinges on the bottom of the tankage, it has been noted that a large portion of the liquid is being collected. Methods for alleviating the recirculation problem in collection have been investigated and the results are presented in the paper.

NOMENCLATURE

a	system acceleration, cm/sec^2
a_L	interface leading edge acceleration, cm/sec^2
Bo	Bond number
R	cylinder radius, cm
V_L	instantaneous velocity of leading edge, cm/sec
V_O	rate of vapor penetration, cm/sec
ρ	liquid density, gm/cm^3
σ	surface <u>tension</u> , dynes/cm

AN EXPERIMENTAL INVESTIGATION OF THE DYNAMIC BEHAVIOR OF THE LIQUID-VAPOR INTERFACE UNDER ADVERSE LOW-GRAVITATIONAL CONDITIONS

1 INTRODUCTION

The demand for optimum solutions to the problems associated with space-vehicle propellant systems has generated considerable interest in the field of liquid-vapor interface dynamics. However, while the attention given to the subject of propellant behavior during the powered phase of the flight has reached voluminous proportions, only recently has serious discussion considered the gross motion of the propellant under conditions of low gravity-induced environments. The control and stability of the flight of the vehicle are indeed dependent on a knowledge of the former aspects of propellant behavior, but the further requirements of reliable restart capabilities and adequate venting characteristics, following durations of weightlessness encountered in coasting flight, have made the latter aspect of low gravity-induced hydrodynamics equal in significance.

The NASA Lewis Research Center is currently conducting experimental investigations of the behavior of the liquid-vapor interface under the influence of low acceleration environments. The purpose of this paper is to present the results of several phases of these investigations. Particularly discussed are the stability characteristics of the interface, the quantitative description of the motion of the interface, and the mechanism of reorientation or collection in response to adverse constant translational accelerations.

2 FACILITY

To provide the proper environment for the creation of the low-gravity fields with the liquid-vapor interface approaching its quiescent zero-gravity configuration, the

Investigations were conducted in a 2.3-second drop-tower facility. The low accelerations were imposed on the experiment by means of a fast-response gaseous thrust system calibrated on the ground by a combined load-cell, air-bearing stand. The center of mass of the experiment package was located along the thrust axis, and the experiments were carefully aligned so that the adverse low acceleration was parallel to the longitudinal axis of the container and was directed normally from the vapor to the liquid phase. Air drag on the experiment package is kept below 10^{-5} g by allowing the package to fall inside a protective drag shield, designed with a high weight-to-frontal-area ratio and low drag coefficient, and modified by the use of interchangeable spacers to accommodate the added relative displacement of the accelerated package. Figure 1 shows a schematic of the drag shield and experiment package assembly and the sequence of the test drop.

The magnitudes of the low accelerations in these programs ranged from approximately 0.1 to 0.01 g and could be determined by the ground calibration technique to within 4 percent; This value could be substantiated during the test by observing the net accelerated time in the known available distance in the drag shield. Limits to the attainable acceleration levels were imposed by practical drag-shield spacer additions and reasonable acceleration time in which to observe data. Further limitations on the maximum radial dimension of the experiment geometry, due not to absolute size but to zero-gravity formation periods (an effect discussed later), restricted attainable Bond numbers to less than 100.

The liquids employed in the investigation were analytic reagent grade and were restricted to zero-degree contact angles on the containment surfaces. To ensure perfect wetting, elaborate cleaning procedures were adopted, and contamination of the liquids and solid surfaces was carefully avoided. A more detailed discussion of operating procedure is given in Ref. 1.

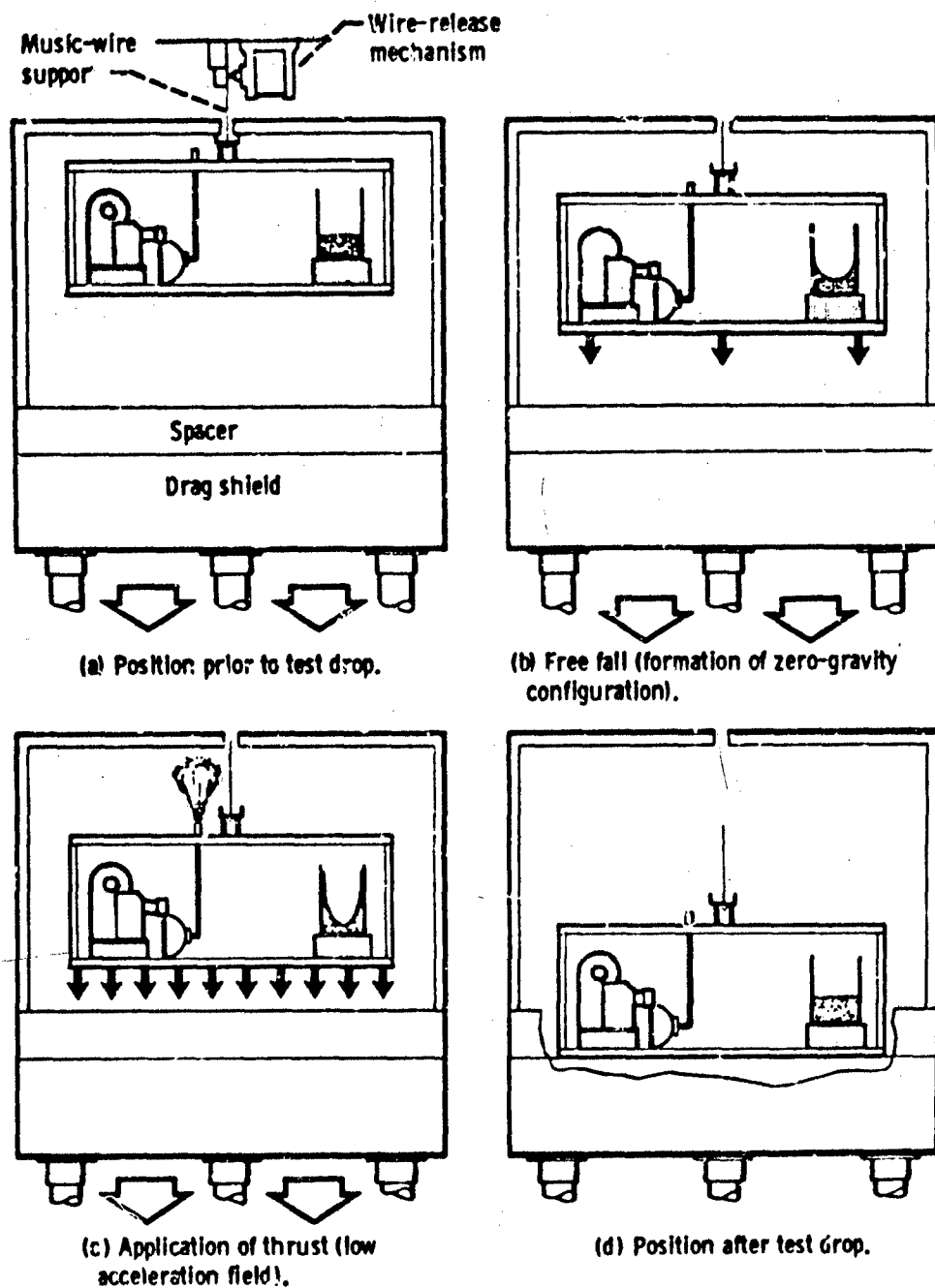


Fig. 1 Sequential Positions of Experiment Package and Drag Shield Before, During, and After Test Drop

3 CRITICAL BOND NUMBER AND STABILITY OF INTERFACE

Formulation of the dimensionless Bond number grouping, consisting essentially of the ratio of acceleration to capillary forces, has led to the successful correlation of the magnitude of acceleration required to disrupt the established liquid-vapor interface configuration (Refs. 1 to 3). The retentive property of the capillary forces provides a region of stability in which the liquid-vapor interface, though deformed, remains static under the influence of adverse gravitational or acceleration-induced forces. The subject has attracted the academic interest of many investigators, but despite its apparent popularity, detailed studies of the phenomenon have been lacking. With perhaps two exceptions (Refs. 4 and 5), only recently have the additional variables of edge effects, contact angles and hysteresis, geometries other than cylindrical, and conclusive experimental verification of the fundamental concepts been considered.

The critical Bond number delineating the stable and unstable regions of the interface in cylinders was shown to be independent of the applied acceleration field and was verified to be 0.94 for solid-liquid-vapor systems possessing zero-degree contact angles exhibiting no hysteresis (Ref. 1):

$$Bo_{crit} = 0.94 = \frac{\rho a R^2}{\sigma} \quad (1)$$

where the density of the vapor phase has been neglected.

Experimental evidence supporting the validity of these conclusions is shown in Fig. 2, where correlation of data obtained both in normal gravity and low acceleration-induced environments has been made with the graph of Eq. (1). The procedure used in obtaining the data resulted in a range of cylinder radii in which stability (no motion of the interface) or instability was observed for each combination of liquid and acceleration field. As such, the critical radius was bracketed, with the net deviation being as small as the physical observation of the disruption or stability of the interface would permit.

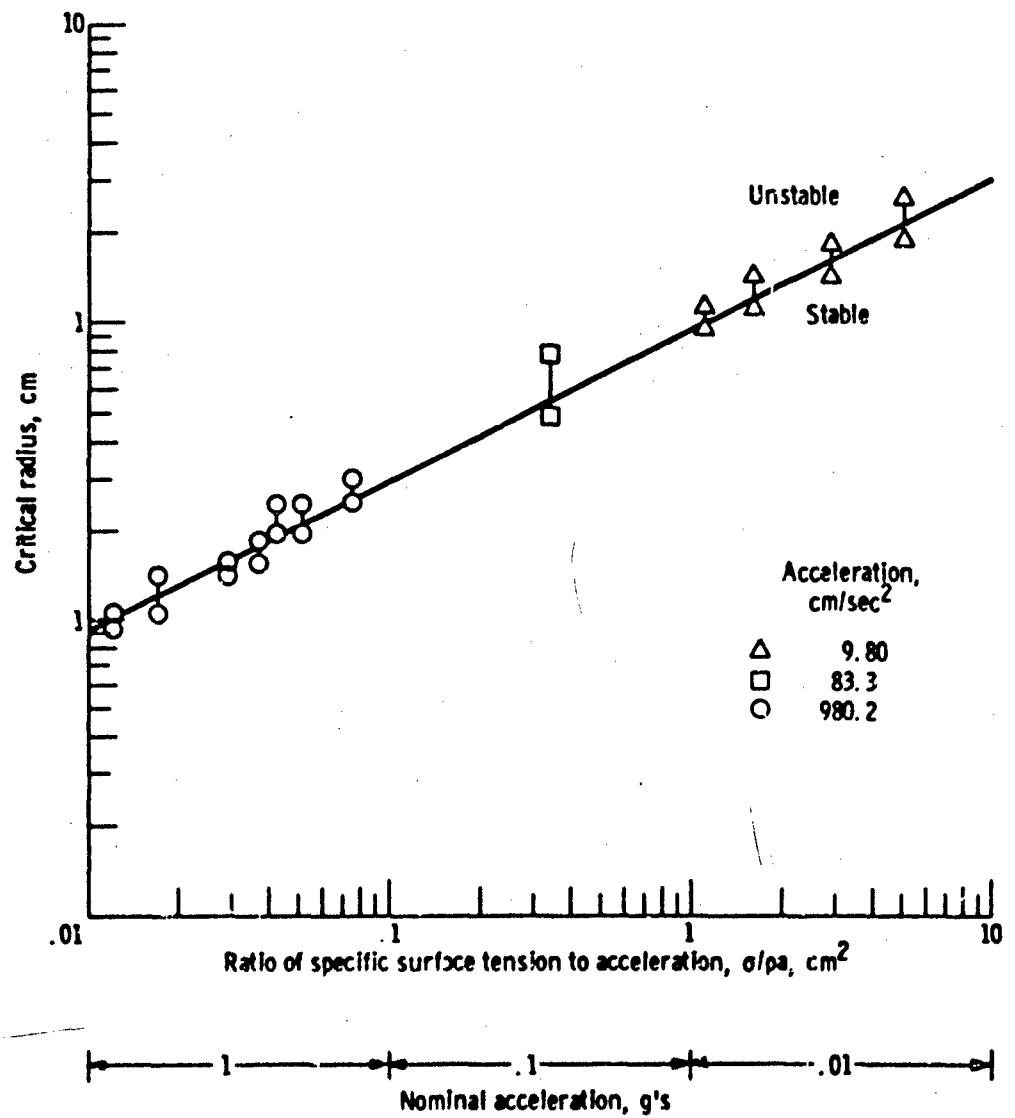


Fig. 2 Interface Stability Delineated by Bond Number Criterion

The fact that the critical Bond number of 0.84 is independent of the acceleration field (the other parameters must of course change to keep the relation constant) is not really astonishing in view of the nature of the surface-tension stabilizing parameter. However, such statements are (for rather obvious reasons), made only after verification. The fact is significant from two viewpoints. First, the scaling of Eq. (1) to actual spacecraft tank dimensions can now be made with certitude. Second, the Bond number itself gains stature as the proper descriptive indication of environmental condition. It is in this latter regard that the phrase "low-acceleration" environment must be used with reservation.

4 ADVERSE BOND NUMBERS GREATER THAN CRITICAL: MOTION OF THE INTERFACE

It can be seen from Eq. (1) that the acceleration required to disrupt the interface in realistic spacecraft tanks is quite small; however, spacecraft will be subjected to a number of disturbances of magnitude most likely to exceed the critical level of allowed acceleration. Various schemes, both active and passive, have been proposed to locate the interface in the presence of these perturbations. One popular example of active locating methods is the proposed use of small auxiliary thrusters, to maintain the proper orientation of the propellant by inducing a low body force environment. The efficiency of the auxiliary thrust method is dependent on the ratio of induced Bond number to the Bond number resulting from the extraneous disturbances; an optimum solution would demand that the auxiliary thrusters should never lose control of the interface. But for missions requiring long-term coast durations, the continual use of these thrusters may cause excessive weight penalties, thus their operation may have to be reduced to intermittent durations. Reliable restart can be ensured by a combination of collection-thrust and pump-inlet baffling; efficient venting characteristics, however, appear to be solely dependent on the performance of these ullage control thrusters to reposition or collect the propellant following interface disruption. The dynamic behavior of the interface during this collection mode is of immediate interest.

The mode of liquid flow following the disruption of the interface in a low acceleration field has been noted in the critical Bond number studies and was observed to be similar to the gravitational motion of large (> one diameter) bubbles in closed vertical tubes. An extensive program conducted under normal-gravity conditions extended the existing correlation of bubble rise velocity through a carefully documented region of Bond numbers ranging from 3.49 to 1,870. The rate of penetration of the vapor phase into the liquid phase for low-viscosity fluids was found to be described by the empirically derived equation

$$V_o = 0.48 (aR)^{1/2} \left[1 - \left(\frac{0.84}{Bo} \right)^{Bo/4.7} \right] \quad (2)$$

For Bond numbers greater than 12, Eq. (2) reduces to

$$V_o = (0.48)(aR)^{1/2} \quad (3)$$

or the form predicted by the inviscid potential theory of G. I. Taylor (Ref. 6). The NASA experimental data for large Bond numbers at one g and intermediate Bond numbers at low gravity are presented in Fig. 3 with the curve of Eq. (2). Other published data is also shown, and the agreement with the empirical equation is seen to be excellent, including Bond numbers approaching one.

Extension of the investigation to low gravity-induced environments verified the validity of the above results in terms of a correct scaling relation. The low-acceleration data in Fig. 3 are satisfactorily correlated by Eq. (2). A photograph showing the profile of the interface under an imposed acceleration of 36.3 cm/sec^2 is shown in Fig. 4(a) and is typical of the observed symmetry of the vapor penetration when adequate zero-gravity formation time and proper thrust alignment were provided. The observed symmetry of the profile, especially the progression of the leading edge, was extremely sensitive to small misalignments in acceleration direction.

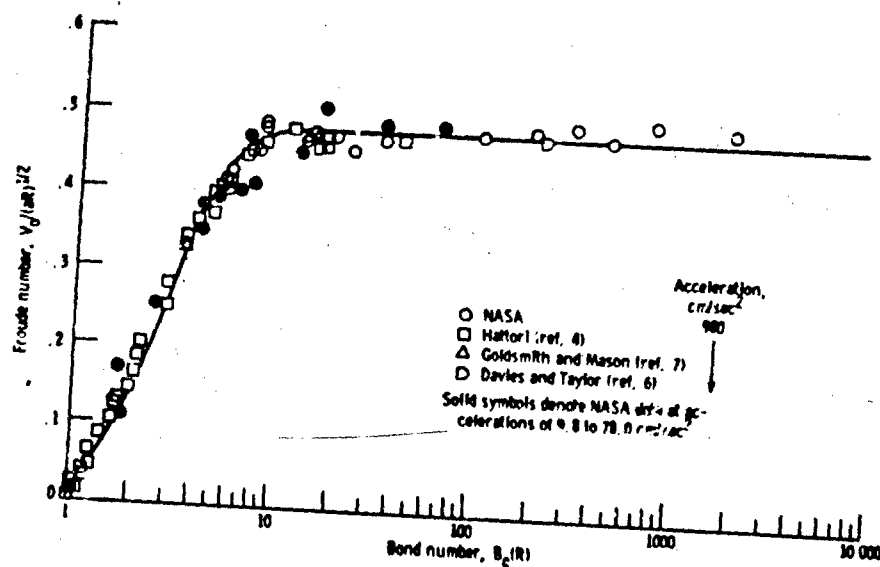


Fig. 3 Experimental Correlation of Vapor Penetration Rate with Bond Number

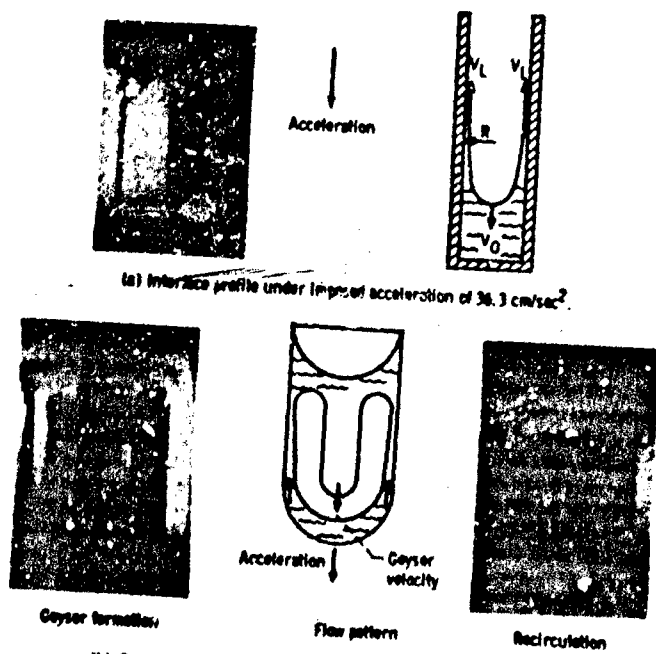


Fig. 4 Interface Profile and Geyser Formation and Recirculation

It is to be noted that the time allowed for the formation of the zero-gravity interface configuration was generally not sufficient to ensure completely quiescent conditions before initiation of the imposed acceleration. This fact is not to be minimized because the formation period represents an initial perturbation to the mode of liquid flow, and a transition region necessarily occurs prior to steady-state regular flow. The mode shape excited by the sudden transition from one-g to zero-g resembles a "hump" centered along the major axis of the cylinder. If sufficient time is not allowed for adequate decay of this formation mode, subsequent vapor penetration rates will be severely affected. In fact, if the formation time is "properly chosen," the imposed acceleration will cause the formation mode to grow exponentially in time in the form of the classic Taylor instability. The competition between formation, transition, and regular flow time in the present 2.3-sec drop-tower facility restricted the radii of the cylinders to a maximum of 4.5 cm.

As a result of these investigations, it is now possible to predict the vapor penetration or ullage velocity under an imposed collection acceleration in spacecraft propellant tanks. For tank radii of the order of 150 cm (5 ft), a typically imposed collection acceleration of 10^{-2} g will result in an ullage velocity of slightly greater than 18 cm/sec. However, one should not estimate the total time required to reorient the propellant (e.g., from the vent portion of the tank) solely from the above results because the situation presented is quite ideal. The ullage velocity correlation given by Eq. (2) has been obtained in unbaffled, flat-bottomed, cylindrical geometries. Internal tank hardware could alter the regular symmetric stage of propellant flow, and the effect of tank extremities may reduce the velocity magnitude. The latter aspect is somewhat doubtful because no observable effect on the ullage velocity due to the flat bottom of right circular cylinders has been noted in the low acceleration studies. The net adverse effect of these two aspects would be a reduction in ullage velocity; therefore, Eq. (2) represents a reasonable estimate of the ullage velocity under a given collection acceleration even when the geometry is less than ideal. However, time estimates for complete collection still cannot be inferred because of the motion of the leading edge of the interface.

The interface leading edge velocity, V_L in Fig. 4(a), unlike the ullage velocity, is not constant. The result is consistent with inviscid theory: If the profiles of the interface and ullage velocity in response to both inertial and gravitational body force accelerations are identical, the continuity equations demand that the bounded leading edge accelerate - a necessary converse of Taylor's argument. An analysis of the leading edge displacement characteristics led to the following equation:

$$a_L = \frac{3.8 V_0^2}{R} \quad \text{for } Bo > 1.7 \quad (4)$$

where a_L is the magnitude of the leading edge acceleration and V_0 is the ullage velocity given by Eq. (2). The empirical correlation of the above equation was based on the actual ullage velocity as observed in each test and is accurate to within 10 percent, the accuracy increasing with increasing Bond numbers. For Bond numbers greater than 12

$$a_L = 0.87 a \quad (5)$$

which indicates a slight departure from the ideal free-fall condition at the wall. The leading edge displacement is undoubtedly viscosity-dependent, but for low-viscosity fluids of the order of one centipoise, and available accelerating distances comparable to cylinder fineness ratios of two, the above relations are valid within the stated accuracy.

5 PROPELLANT COLLECTION BY LOW ACCELERATION-INDUCED FORCES

The significance of the leading edge displacement is that the instantaneous leading edge velocity may be quite large when the liquid eventually converges at the tank bottom. The resultant momentum could then cause the propellant to rebound or geyser back to the top of the tank, and the attempt at collection would merely result in circulating the propellant. The presence of a prominent geyser in flat-bottomed, convex-bottomed

(Apollo), and concave-bottom (Centaur and Saturn) geometries, and the subsequent recirculation, were determined quite early in the drop-tower investigations. It is the presence of this geyser that currently makes total-time estimates of collection literally estimates.

The geysering phenomenon in the Bond number region from 10 to 60 was quite ordered and repeatable with surprisingly little turbulence. Although direct measurements of the geyser were impaired both by refraction and capillary waves in the liquid film along the tank wall, some geometric observations were evident. The geyser is basically a continuous liquid column with a width of between $1/4$ and $1/2$ of the tank diameter. Other than at its initial formation, the geyser maintains its size relative to the tank, exhibiting only slight wave motion due undoubtedly to Rayleigh instability. Representative photographs of the geyser in a Centaur geometry model are shown in Fig. 4(b). In all instances, the geyser was observed to move at a constant velocity, the magnitude being approximately twice the instantaneous leading edge velocity calculated at tank bottom impingement. Further data is needed, however, to firmly establish this correlation. Once the geyser reached the top of the model geometry, the liquid was recirculated.

Despite the geysering formation and recirculation, liquid does accumulate at the bottom of the tank. Actual ratios of liquid accumulation to geyser volume per unit time were estimated, for example, in the Centaur models to be as high as 1:3. The relation, however, describing the accumulation rate is not apparent and sufficient test time is not presently available to obtain total accumulation.

Obviously, the requirements of efficient venting are not compatible with severity of the geyser in the basic collection mode. The reliance on viscous damping to end the recirculation mode would make collection time excessively long. Methods for eliminating or at least alleviating the geysering problem consist simply of changing the direction of flow momentum and dissipating the kinetic energy due to the leading edge flow. Although the latter results in considerable turbulence and small bubble formation, it

appears to be the only feasible solution. Deliberate collection acceleration misalignment and suitable tank baffles were investigated as a means of impeding and redirecting the geyser flow. While the former method may not be too practical, it does merit attention because of its simplicity. For example, a 15 deg thrust misalignment with the major axis of the geometry causes a large angle in the progression of the leading edge. When the leading edge converges at the tank bottom, the resultant geyser is directed toward the wall, and the ensuing agitation causes a considerable increase in total liquid accumulation over symmetrical collection for identical time intervals. The geyser, however, was noted to re-form parallel to the collection acceleration prior liquid had been accumulated; the applicability is only for small residual percentages of propellant. Varieties of baffles in the forms of plates, rings, and shells were also tried, to completely eliminate the geysering problem and to obtain total liquid collection. In general it was discovered that the approach was in part feasible, and that any baffling scheme which would impede and redirect the geyser flow direction to the tank walls or back to the tank bottom would cause a substantial increase in collected liquid. Once these baffles were covered with accumulated liquid, however, their effectiveness was completely lost, and the geyser reappeared almost immediately. For example, a ring-type baffle, placed around the inverted hemispherical bottom of a Centaur model, diverted the leading edge and caused a reservoir of liquid to accumulate with no apparent geyser. Shortly after the collected liquid had covered the ring, however, geysering appeared with little, if any, reduction in severity.

Another baffling technique, which has proven thus far to be the most successful, relies on distinct liquid levels and on an estimate of the residual propellant to be collected. The method is shown in Fig. 5.

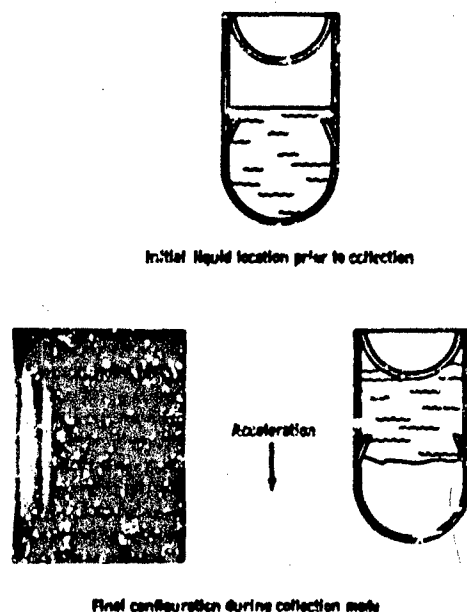


Fig. 5 Collection in Baffled Centaur Tank Geometry

Before collection is attempted, the liquid level is above the angled ring baffle. The collection acceleration causes a typical geysering formation, but once the liquid level drops below the baffle, the leading edge is diverted toward the center of the tank. The geyser flow and the newly directed leading edge flow impinge on each other, which results in considerable turbulence and bubble formation. The turbulence, however, is an effective dissipation factor and the numerous small bubbles settle out quite rapidly. The previously stated relations describing the leading edge and geyser velocities were entirely adequate in determining the point of flow impingement. The photograph in Fig. 5 of a test run using this baffling technique shows successful complete liquid reorientation despite present experimental time limitations.

6 CONCLUSION

In summary, it may be stated that the motion of the liquid-vapor interface in response to low acceleration-induced forces can be predicted; however, accurate time estimates of complete propellant reorientation or collection cannot presently be made because of the geysering phenomena. Baffling techniques designed to obtain collection can be effective, but result in considerable propellant agitation with possible concurrent spacecraft control problems.

7 REFERENCES

1. National Aeronautics and Space Administration, Hydrostatic Stability of the Liquid-Vapor Interface in a Low Acceleration Field, by W. Masica, J. D. Derdul, and D. A. Petrash, NASA TN D-2444, 1964
2. Stanford University, Dynamics of the Free Liquid Surface in Cylindrical Containers Under Strong Capillary and Weak Gravity Conditions, by H. M. Satterlee and W. C. Reynolds, Rept. No. LG-2, 1 May 1964
3. -----, Capillary Hydro-statics and Hydrodynamics at Low G, by W. C. Reynolds, M. A. Saad, and H. M. Satterlee, Rept. No. LG-3, 1 Sep 1964

4. Aeronautical Research Institute, Tokyo Imperial University, On the Motion of a Cylindrical Bubble in a Tube and Its Application to the Measurement of the Surface Tension of a Liquid, by Sin-iti Hattori, Rept. No. 115, Jan 1935
5. F. P. Bretherton, "The Motion of Long Bubbles in Tubes," J. Fluid Mech., Vol. 10, Part 2, pp. 166-187, Mar 1961
6. R. M. Davies and G. I. Taylor, "The Mechanics of Large Bubbles Rising Through Extended Liquids and Through Liquids in Tubes," Proc. Roy. Soc. (London), Sec. A, Vol. 260, No. 1062, pp. 375-390, 7 Feb 1950
7. H. L. Goldsmith and S. G. Mason, "The Movement of Single Large Bubbles in Closed Vertical Tubes," J. Fluid Mech., Vol. 14, Part 1, pp. 42-58, Sep 1962

DISCUSSION

P. B. Abramson, Atomics International

Is the heat input by turbulence sufficient to change the temperature enough to cause cavitation of the pump?

Masica

Our experimental studies in this area were necessarily assumed isothermal and the lack of qualitative information regarding the dissipative process prevents a specific answer to the question. Undoubtedly, the thermodynamics associated with this process could create problems. The increase in temperature due to turbulence will certainly change the net positive suction head and whether cavitation occurs will depend on the original margin provided.

Paul Concus, Lockheed

On your first films in which you showed large to small Bond number transitions, what was the contact angle of the liquid which you used?

Masica

The liquid used in my first films was anhydrous ethanol and the containers were either glass or lucite. Static contact angle measurements of these liquid-solid combinations have shown that the contact angle is very small, approaching zero degrees.

PAPER 3

**INVISCID FLUID FLOW IN AN
ACCELERATING AXISYMMETRIC CONTAINER**

By P. Concus, G. E. Crane, and L. M. Perko
LOCKHEED MISSILES & SPACE COMPANY

ABSTRACT

The problem of fluid motion in an axisymmetric container due to a time-varying axial acceleration arises in connection with the study of the dynamics of liquid propellant in a rocket. A numerical procedure has been developed for computer simulation of an axially symmetric, incompressible, irrotational flow of an inviscid fluid. The method is based on a determination of the velocity potential throughout the fluid satisfying the free-surface boundary condition, to determine the motion of individual particles on the surface via the kinematic equation.

The work to date includes the surface tension as a smoothing term in the computation. Some difficulty was experienced in this approach, and various new methods for treating the surface tension through Bernoulli's equation are being investigated. For example, instead of including the surface tension only as a smoothing term in Bernoulli's equation, the equation itself can be viewed as the differential equation which, with the boundary conditions, defines the surface shape. Such a computation should enable the method to maintain a constant contact angle, and should increase stability of the method.

Stability is also being viewed from a numerical standpoint and it is believed that a modified orthonormalization routine will provide improved stability. An existing numerical program based on a Fourier series representation for the velocity potential will be used in conjunction with a finite difference technique, in the corner formed by the wall-liquid-air interface, to lead insight into the finite difference scheme. It is hoped then to extend the finite difference scheme over the entire interior in order to treat various tank geometries as well as to include the possibility of a draining tank.

The results of this work describe the fluid motion for various initial shapes, accelerations, and surface tensions. The stable problem in which surface oscillations are obtained establishes a contact with previous analytical work, and it is found that the period of oscillation is comparable to that predicted by the linear theory for small oscillations. The present object of concentration is the unstable problem where the liquid runs up the walls of the container, and it is hoped that satisfactory results will also be obtained in this case.

NOMENCLATURE

g_0	Acceleration of gravity at earth's surface
ρ	Density of the fluid
σ	Liquid-vapor surface tension
r_0	Initial radius of the intersection of the free surface with the tank wall
β	$\sigma/\rho r_0^2 g_0$, a dimensionless parameter
$a(t)g_0$	Time-varying axial acceleration
H	Average height of liquid (dimensionless)
ψ	Angle between surface outer normal and vertical
θ_0	Contact angle; angle between the solid surface and the limiting surface tangent at the wall

INVISCID FLUID FLOW IN AN ACCELERATING AXISYMMETRIC CONTAINER

1 INTRODUCTION

The dynamics of liquid propellants in rockets introduced the problem of fluid motion in an axisymmetric container due to a time-varying axial acceleration. The motion is approximated by the axisymmetric, incompressible, irrotational flow of an inviscid fluid in an accelerating symmetrical container. The main points involved in making this approximation are discussed in Ref. 1. The free surface boundary value problem describing such a flow is analytically intractable; however, the following describes a numerical approximation to the solution, which yields promising results. In this approximation the free surface is determined by following the motion of individual particles on the surface, by numerically integrating along the characteristics of the kinematic boundary condition. Simultaneously, the velocity potential in the interior of the fluid, which satisfies Laplace's equation with the boundary condition on the free surface given by Bernoulli's equation, is determined by finite difference methods or by a Fourier series representation, as in Ref. 2, or by a combination of the two methods.

The computing scheme wherein the velocity potential is represented by a Fourier series works well for problems in which the fluid remains essentially at one end of a cylindrical tank, so that the surface undergoes sustained oscillations (Fig. 3), or splashes if the surface tension is too small to support oscillations. However, this representation is restricted in practice to flat-bottomed cylindrical tanks. Moreover, various difficulties occur with problems in which the fluid moves to the opposite end of the tank. The convergence of the series representing the velocity potential has not been investigated in detail; it is suspect at points which lie significantly above the mean height of the fluid. To overcome these difficulties, as well as to allow for a larger class of tank geometries and for the possibility of draining the tank, the velocity potential above a certain height, or throughout the fluid, is represented as a finite difference approximation to a solution of Laplace's equation, subject to the free surface and fixed wall boundary conditions.

In addition, certain "smoothing" devices are incorporated: The numerical integration along the characteristics uses multi-step methods (Adams with variable orders); and Bernoulli's equation may be used for a final revision of the corrected shape. A description of the methods and a discussion of some details of the solution follow.

2 DISCUSSION

Let $\underline{V}(r, z, t)$ be the axially symmetric velocity of a point (r, θ, z) in the fluid at time t . Because the flow is irrotational, $\nabla \times \underline{V} = 0$, and a velocity potential $\varphi(r, z, t)$ exists such that $\underline{V} = \nabla \varphi$. Because the flow is incompressible, the potential satisfies Laplace's equation

$$\nabla^2 \varphi = \varphi_{rr} + \frac{1}{r} \varphi_r + \varphi_{zz} = 0 \quad (1)$$

for $t \geq 0$ in the interior of the fluid (Fig. 1). On the fixed boundaries, i.e., the walls of the tank (and the axis of symmetry), the boundary condition

$$\frac{\partial \varphi}{\partial n} = 0 \quad (2)$$

holds, where n is the outwardly directed normal. The free surface boundary condition, Bernoulli's equation, follows as a first integral of Euler's equation (Ref. 3). For points on the free surface, $z = f(r, t)$, Bernoulli's equation takes the form

$$\varphi_t = \frac{\alpha(t)}{1 + \beta} (f - H) - \frac{1}{2} (\nabla \varphi)^2 + \frac{\beta}{1 + \beta} \frac{1}{r} \frac{\partial}{\partial r} \left[\frac{r f_r}{(1 + r_r^2)^{1/2}} \right] \quad (3)$$

where the coordinates are normalized by dividing distances by the initial radius r_0 of the intersection of the tank and the free surface, by dividing time by

$$\left[\frac{\rho r_0^3}{\sigma \left(1 + \frac{1}{\beta} \right)} \right]^{1/2}$$

and by dividing the velocity potential by

$$\left[\left(1 + \frac{1}{\beta} \right) \frac{\sigma r_0}{\rho} \right]^{1/2}$$

The parameter

$$\beta = \frac{\sigma}{\rho r_0^2 g_0}$$

is dimensionless; it is equal to α/B , where B is the Bond number. The symbols appearing in Eq. (3) and the normalization constants are defined in the list of nomenclature and shown in fig. 1.

Laplace's equation, Eq. (1), and the boundary conditions of Eq. (2) remain invariant under this normalization. For fixed t , Bernoulli's equation, Eq. (3), can also be viewed as a second order differential equation for the shape of the surface f , and (as such) requires two boundary conditions. From symmetry and physical considerations (Ref. 4, Sec. 145, and Ref. 5), the appropriate boundary conditions are that for all t

$$f_r = 0 \text{ at } r = 0, \text{ and } f_r = \cot \theta_0 \text{ at the tank wall,} \quad (3')$$

where θ_0 is the constant contact angle.

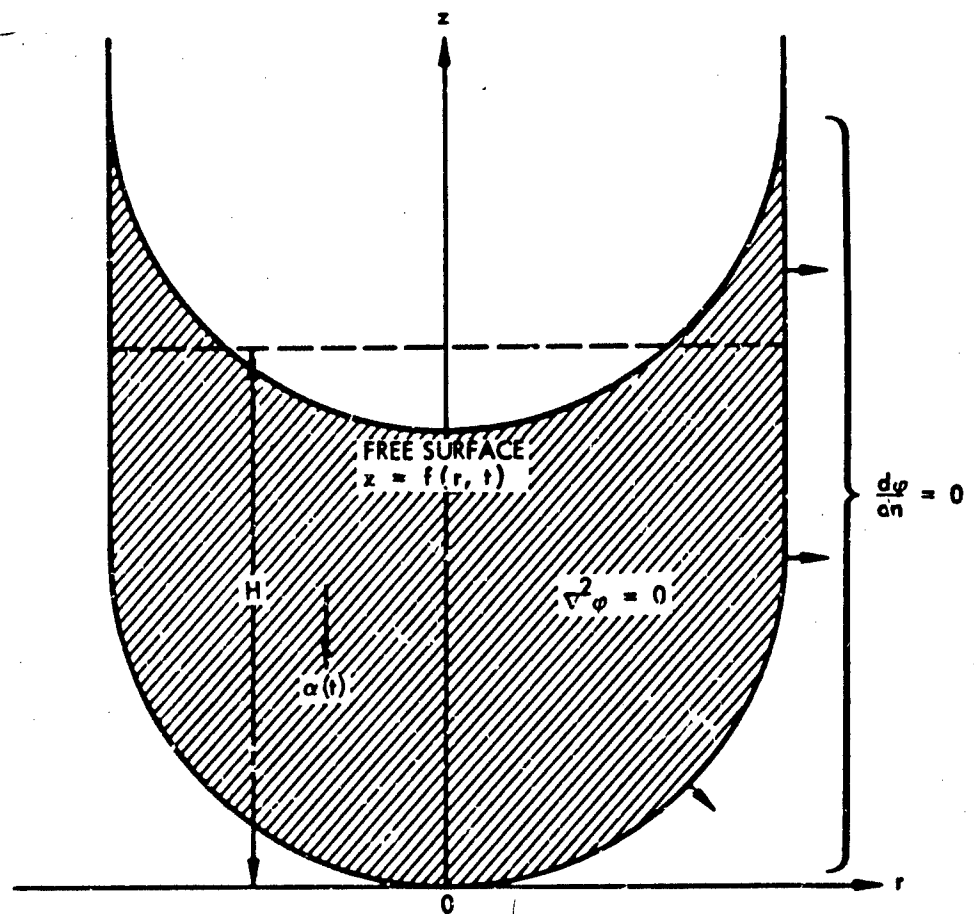


Fig. 1 Tank Geometry and Coordinate System

The remaining equation, which together with Bernoulli's equation defines the motion of the free surface, follows from the definition of the velocity vector \underline{V} of a fluid particle with position vector \underline{s} , namely $\underline{V} = d\underline{s}/dt$. For a particle on the free surface, $z = f(r, t)$, the component form of this vector equation becomes

$$\left. \begin{aligned} dr/dt &= \varphi_r \\ df/dt &= \varphi_z \end{aligned} \right\} \quad (4)$$

when the relation $\underline{V} = \nabla\varphi$ is used.

Because the total derivative $df/dt = f_t + f_r dr/dt$, Eq. (4) is equivalent to the usual kinematic equation

$$f_t = \varphi_z - \varphi_r f_r \quad (4')$$

on $z = f(r, t)$; in fact, the curves $r = r(t)$ and $z = z(t) = f(r(t), t)$ satisfying Eq. (4) are characteristic curves of the first order partial differential equation, Eq. (4'). (See Ref. 6, p. 62).

The initial conditions are

$$\left. \begin{aligned} f(r, 0) &= f_0(r), \quad 0 \leq r \leq 1, \\ \varphi(r, z, 0) &= 0, \quad 0 \leq r \leq 1, \quad 0 \leq z \leq f_0(r), \end{aligned} \right\} \quad (5)$$

and

$$\alpha(0^-) = 0$$

where f_0 is a prescribed function satisfying Eq. (3'). Laplace's equation, Eq. (1), and the boundary conditions of Eqs. (2), (3), (3'), and (4), and the initial conditions of Eq. (5) define the free surface boundary value problem to be solved.

This formulation emphasizes the elliptic aspect of the problem and presents the difficulty of a non-linear boundary condition (of parabolic type) on the free surface. An alternate point of view is to regard Eqs. (3) and (4) as ordinary differential equations for determining r , f , and φ , which are coupled through the velocity potential at

time t . This approach leads to determining the motion of the free surface (the primary practical goal of the problem) by following individual points on the surface. The computational scheme is basically a numerical integration of a first order autonomous system of ordinary differential equations. For an explicit formulation of this system for a cylindrical tank, with a Fourier series representation of the potential, see Ref. 2, Eq. 16.

For more general problems with the potential represented by a finite difference approximation to a solution of Laplace's equation satisfying the free surface boundary conditions, finding the solution reduces to integrating the equation

$$\frac{d\tilde{\varphi}}{dt} = \frac{\alpha(t)}{1+\beta} (f - H) + \frac{1}{2} (\nabla \tilde{\varphi})^2 + \frac{\beta}{1+\beta} \frac{1}{r} \frac{\partial}{\partial r} \left[\frac{r f_r}{(1+f_r^2)^{1/2}} \right] \quad (6)$$

obtained from Bernoulli's equation, Eq. (3), along the characteristics determined by integrating

$$\frac{dr}{dt} = \tilde{\varphi}_r \text{ and } \frac{df}{dt} = \tilde{\varphi}_z .$$

The tilde indicates the value on the free surface, $z = f(r, t)$; $\tilde{\varphi}_r$ and $\tilde{\varphi}_z$ are determined by an approximate solution of Laplace's equation with the boundary conditions of Eq. (2) on the fixed surfaces and the boundary condition on the free surface given by

$$\varphi = \tilde{\varphi}(t) = \varphi(r(t), f(r(t), t)) \quad (7)$$

which follows from Eq. (6); (see also Fig. 2a). Approximation to the solution of Laplace's equation is by a truncated Fourier series or by a finite difference

representation (Ref. 7) or by a combination of the two. The system of Eq. (6) is integrated numerically by an Adams method (Ref. 8) of variable order, using one or two corrector steps as indicated in Fig. 2a. Note that each corrector step involves a solution of Laplace's equation to reevaluate the derivatives ϕ_r and ϕ_z .

Although it would be desirable to have values of ϕ_r and ϕ_z which belong to the r and f used in the predictor step (as indicated by the flow chart above the dashed line in Fig. 2a), the practical expedient is to use the values of ϕ_r and ϕ_z determined in the last correction of the preceding time step; and to use at most two corrector iterations.

Figure 2b indicates an alternate second corrector step in which the effect of the surface tension and of the fixed contact angle of Eq. (3') is more strongly built into the computation by regarding Bernoulli's equation, Eq. (3), as an ordinary non-linear differential equation for $f(r, t)$, t fixed,

$$\frac{1}{r} \frac{\partial}{\partial r} \left[\frac{r f_r}{(1 + f_r^2)^{1/2}} \right] + \frac{\alpha(t)}{\beta} (f - H) = \frac{1 + \beta}{\beta} \left[\frac{d\phi}{dt} - \frac{1}{2} (\nabla \phi)^2 \right] \quad (8)$$

with the Neumann boundary conditions of Eq. (3'). To obtain an improved shape from Eq. (8), new information must be introduced into the right side to make Eq. (8) differ from Eq. (6). As a consequence of Eq. (4'),

$$\frac{\partial \phi}{\partial n} = f_t \cos \psi = \frac{(\phi_z - f_r \phi_r)}{(1 + f_r^2)^{1/2}} \quad (9)$$

holds on the free surface. Thus the velocity potential ϕ , for t fixed, must satisfy Laplace's equation with Neumann's boundary conditions of Eqs. (2) and (9).

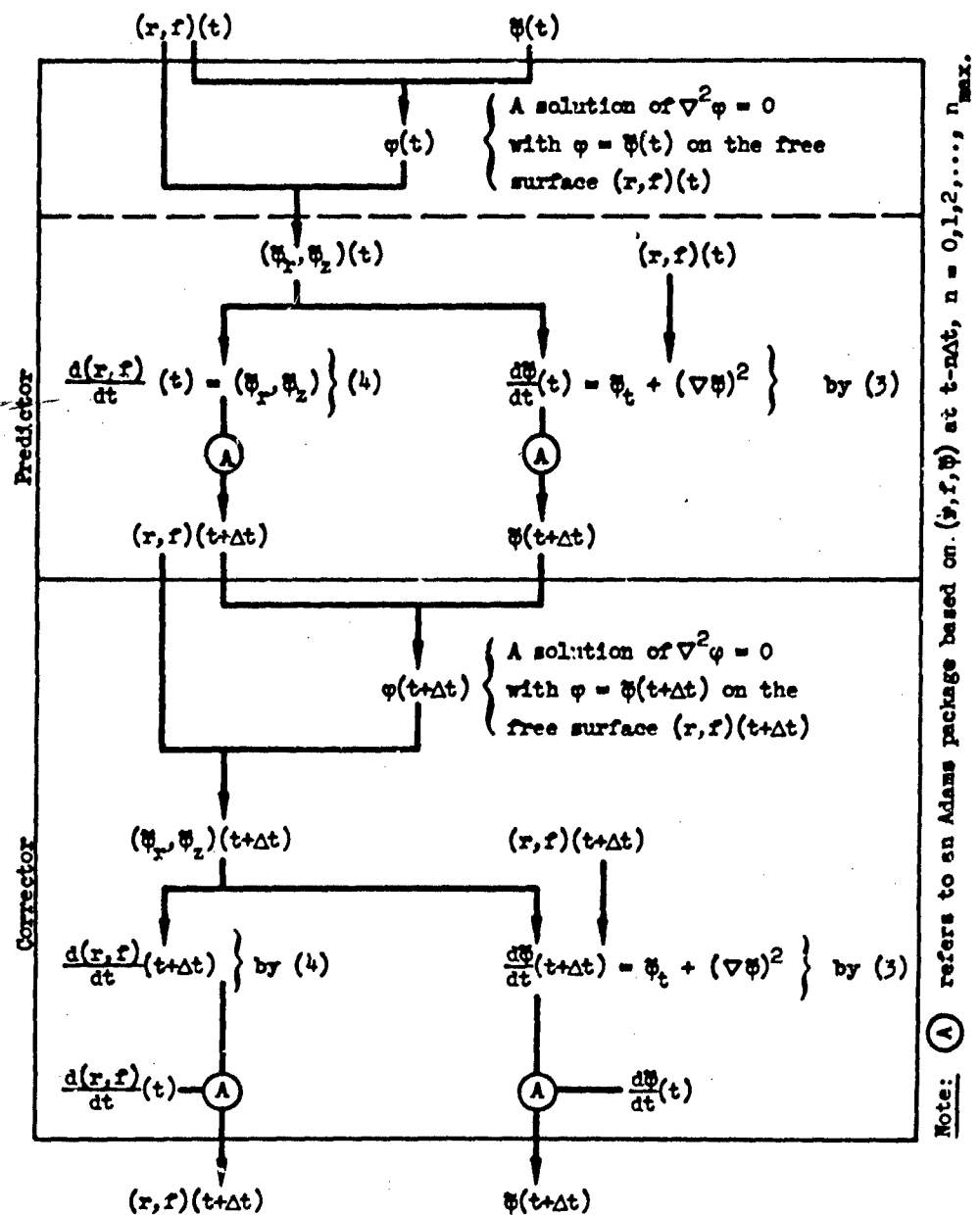


Fig. 2a Diagram of the Computation Scheme

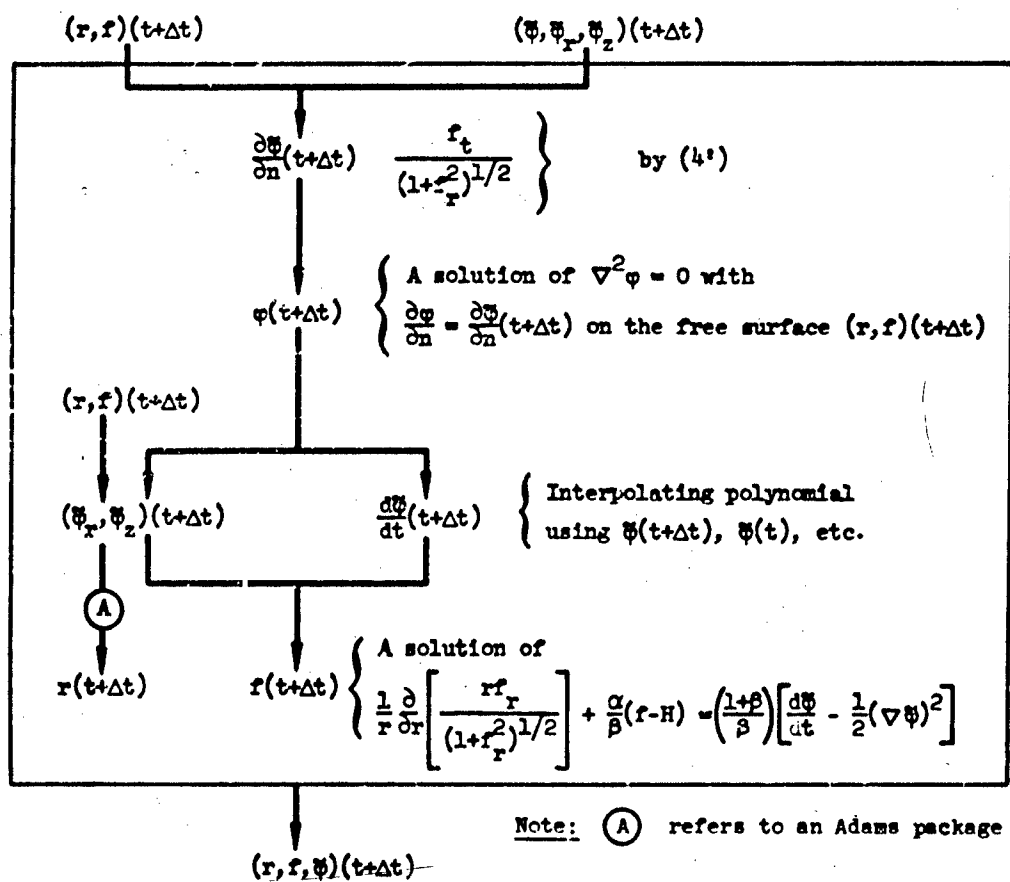


Fig. 2b Alternative to the Final Corrector

An approximate solution to this Neumann problem (determined by expanding around the potential obtained at the last corrector step), with a polynomial interpolation for $d\phi/dt$, gives new values for the right side of Eq. (8). Now the surface shape can be "smoothed" by applying Newton's method to linearize the left side of Eq. (8) with the shape of the last corrector step as initial approximation. In principle, this second

alternative could be used as the corrector step; in practice, however, it is useful only as a final smoothing step, because of the difficulty of solving problems with Neumann boundary conditions.

There is a singular point where the free surface intersects the tank wall; the nature of the singularity is completely determined by the application of the contact angle boundary condition of Eq. (3'). In the Fourier series approach, this boundary condition is handled in an approximate way by including it in the evaluation of the surface tension term in Eq. (6). However, when the Neumann boundary condition of Eq. (9) is used on the free surface to determine ϕ , the subsequent solution of Eq. (8) then allows the contact angle condition to be applied in a more accurate manner as an endpoint condition on f .

3 NUMERICAL RESULTS

At this time the only numerical results available are those obtained by using the Fourier series solution to Laplace's equation as given in Ref. 2. This procedure restricts the tank geometry to that of a flat-bottomed cylindrical container and involves the aforementioned difficulties of computing the fluid motion in the case where the fluid moves to the opposite end of the tank. However, such problems serve to illustrate the numerical results that can be obtained from the computational scheme.

Figures 3 through 6 are piecewise linear plots made by the SC4020 plotter directly from the computer results. Typically, every third shape computed is plotted. Figure 3 shows the effect of an upward acceleration of the tank, $\alpha(t) = -1$, on a fluid initially at rest with a spherical initial free surface shape making a 45 deg contact angle with the wall and a surface tension parameter β equal to that of water in an 0.8-in. diameter cylinder. The surface oscillates (2.5 complete oscillations were computed in 12 min of 7094 computer time) and the average period of oscillation, $T = 0.485 \sqrt{r_0}$ sec (r_0 given in ft), is slightly larger than the period obtained analytically for the linearized problem, $T = 0.434 \sqrt{r_0}$ sec. In Fig. 4, the same case with zero surface tension, $\beta = 0$, a crown-shaped splash develops at the center before any oscillation takes place.

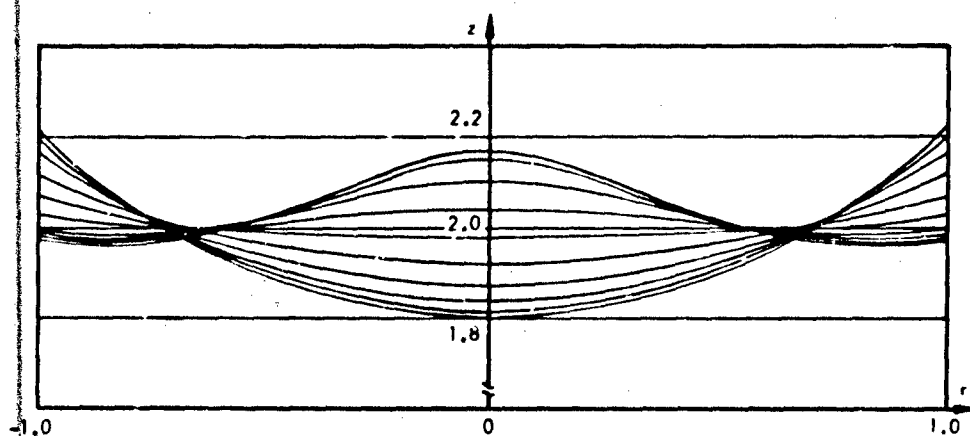


Fig. 3 One Cycle of the Oscillating Surface
 $\alpha(t) = -1.0$, $\beta = 0.05$, $H = 2.0$, $\theta_0 = 45 \text{ deg}$

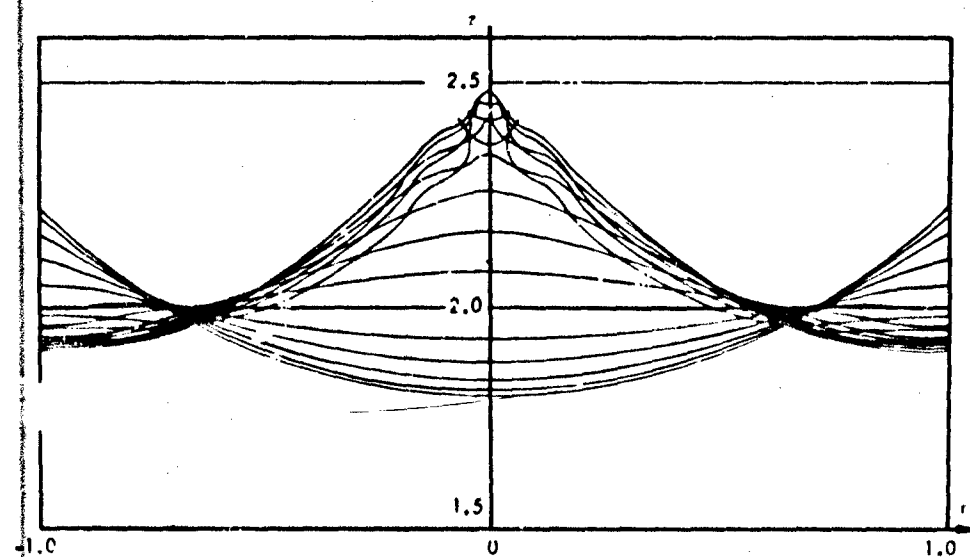


Fig. 4 Development of a Splash on the Surface
 $\alpha(t) = -1.0$, $\beta = 0$, $H = 2.0$, $\theta_0 = 45 \text{ deg}$

Figure 5 shows the effect of a downward acceleration of the tank, $\alpha(t) = +1$, on a fluid with the initial configuration described above and a surface tension parameter β equal to that of water in a 2.5-in. diameter cylinder. As would be expected, the liquid runs up the walls of the cylinder. Computational difficulties were encountered after the last surface shape shown. It is believed that these difficulties can be overcome by

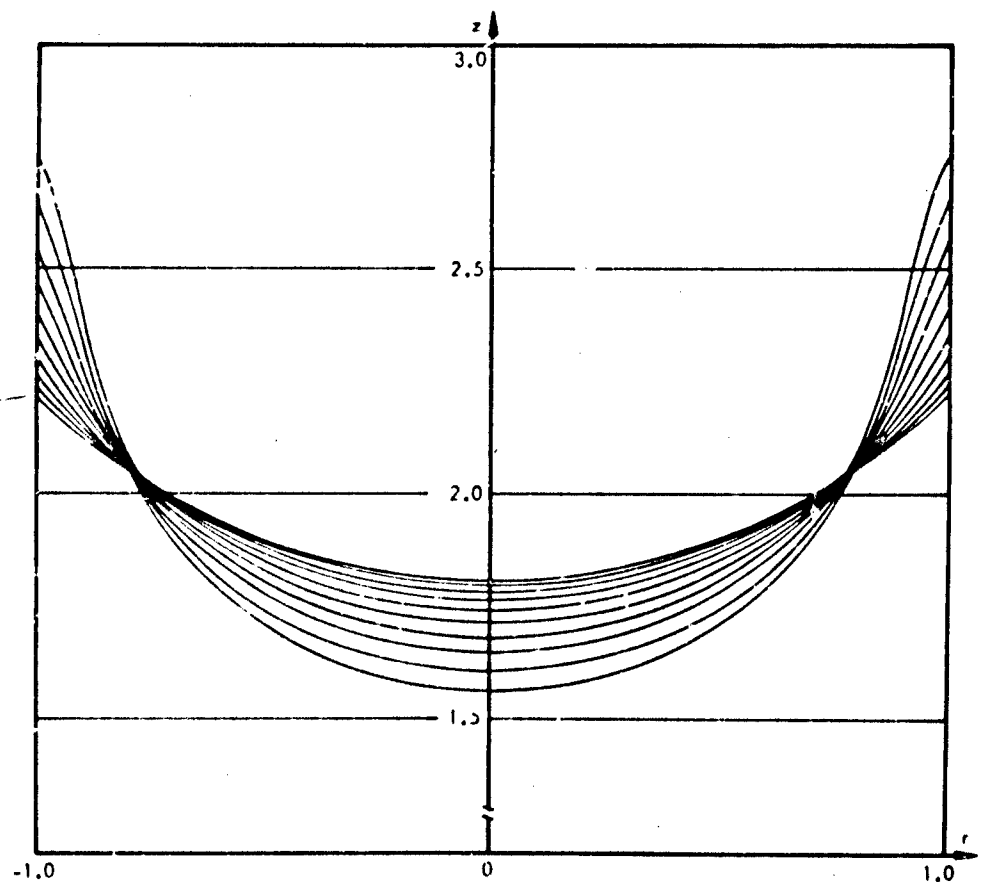


Fig. 5 Fluid Motion With $\alpha(t) = 1.0$, $\beta = 0.005$, $H = 2.0$, and $\theta_0 = 45$ deg

using a multi-step (Adams) method to increase the stability, and by using a finite difference solution to Laplace's equation in the corner, e.g., at all points in the fluid above $z = 2.5$. Figure 6 shows the same case as Fig. 5 with no surface tension, i.e., $\beta = 0$. Breakers similar to those in Ref. 9, p. 367, developed in this case. The development of the breakers is shown in detail in Fig. 7.

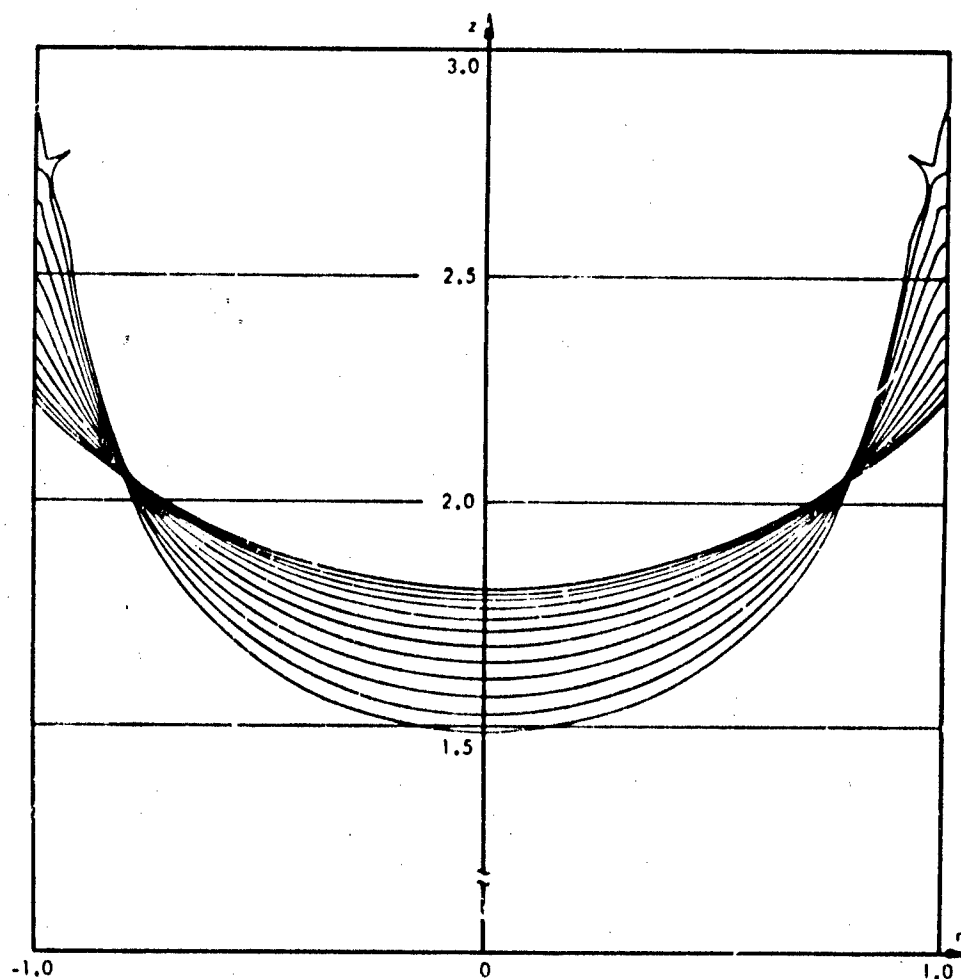


Fig. 6 Fluid Motion With $\alpha(t) = 1.0$, $\beta = 0$, $H = 2.0$, and $\theta_0 = 45 \text{ deg}$

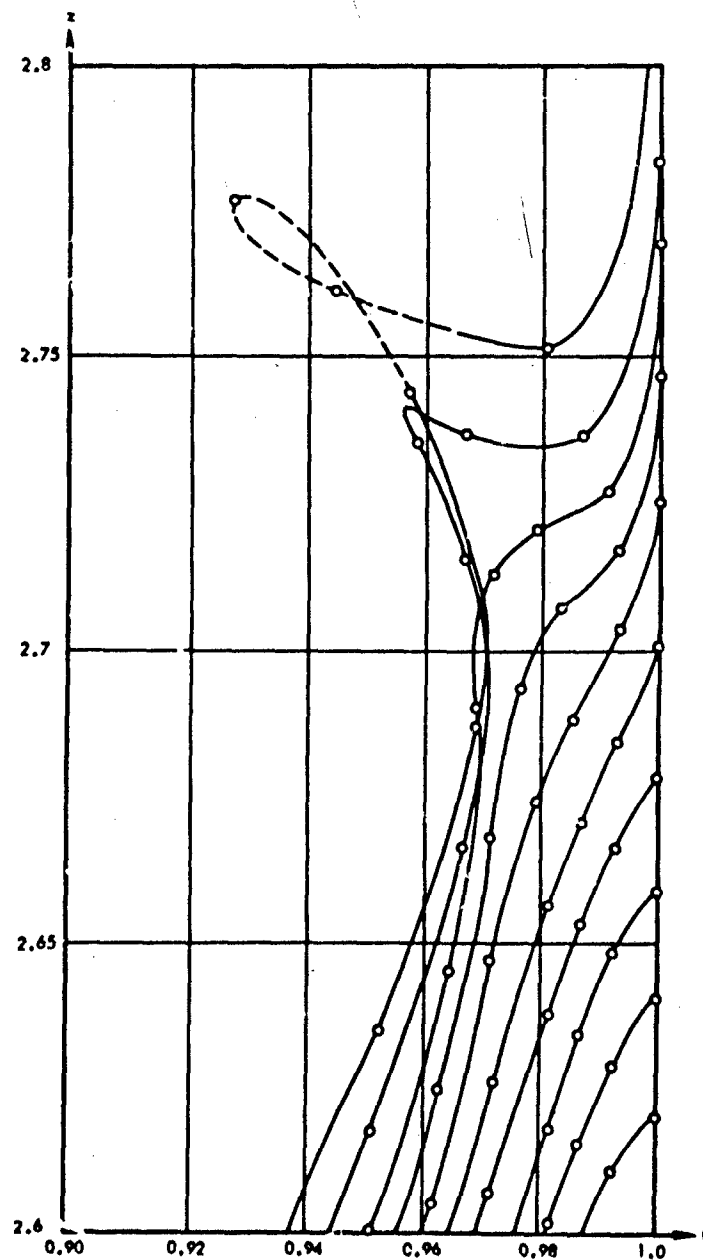


Fig. 7 Development of the Breakers in Fig. 6

4 REFERENCES

1. Stanford University, Department of M. E., Thermo Science Div., by H. M. Satterlee and W. C. Reynolds, The Dynamics of the Free Liquid Surface in Cylindrical Containers Under Strong Capillary and Weak Gravity Conditions, T.R. No. LG-2, 1964
2. L. M. Perko and R. E. Moore, "Inviscid Fluid Flow in an Accelerating Cylindrical Container," to appear in J. Fluid Mech.
3. L. D. Landau and E. M. Lifshitz, Fluid Mechanics, Addison-Wesley Pub. Co., Mass., 1959
4. L. D. Landau and E. M. Lifshitz, Statistical Physics, Addison-Wesley, Permagon Press, 1958
5. P. Concus, "Capillary Stability in an Inverted Rectangular Tank," Advances in Astronautical Sciences, Western Periodicals Co., North Hollywood, Calif., Vol. 14, pp. 21-37, 1963
6. R. Courant and D. Hilbert, Methods of Mathematical Physics, Vol. II, Interscience Pub., New York, 1962
7. R. S. Varga, Matrix Iterative Analysis, Prentice-Hall, Inc., Englewood Cliffs, New Jersey, 1962
8. P. Henrici, Discrete Variable Methods in Ordinary Differential Equations, John Wiley and Sons, Inc., New York 1962
9. J. J. Stoker, Water Waves, Interscience Pub., New York, 1957

DISCUSSION

P. G. Bhuta, TRW Systems Group

I have a comment and a question. The comment concerns the use of Fourier series representation for a nonlinear problem. I don't see any mathematical objection whatsoever in such a representation. Dr. Harkinson's thesis at UCLA under Professor Miles dealt with the problem of nonlinear rotary sloshing. Therein the Fourier series representation was used and the analysis was verified experimentally.

If I understand correctly you showed some trajectories of particles. The formulation that you have is an Eulerian formulation. If you're going to switch over and study motion of individual particles you have to switch to a Lagrangian formulation and I would like to know if you did that and what details you use?

Perko

Well, the motion of individual surface particles is determined by the kinematic characteristic equations. (Eq. 4 and 4' of the symposium paper. This is the same method as that used by Penny and Price in their 1952 Trans. of Royal Society of London paper, pp. 274-276).

Bhuta

Well, there I would like to discuss this point further with you but it seems to me that nonlinear terms are not taken into account when you are switching from the Eulerian formulation to the Lagrangian formulation. You solve the problem by one formulation or another, and every time you make a move from one to another you've got to take that into account.

Paul Concus, LMSC

We have taken all the nonlinear terms into consideration. It is really a mixed Eulerian-Lagrangian formulation in a sense. If one has to move from one system to the other some care must be exercised. We have done this.

Francis C. W. Fung, Cornell Aeronautical Laboratory

There has been some discussion about the series representation. I would like to know if you investigated the convergence of that series. Also in your graphs the contact angle is 45 deg. Does your numerical scheme work for zero contact angle liquids?

Perko

The convergence of the series has been looked into and found to be a very difficult problem. Only token information was obtained and it was found that the convergence was more rapid for points below the average liquid height as you can see from the nature of the series. It contains hyperbolic cosine of λ times Z and so as Z gets large the terms get large and even though the coefficients decrease rapidly, the series converges slowly. This is why for above, say, the average height, we don't know whether the series converges or not. That is one reason why we're resorting to finite differencing even though though it will take longer.

We tried some zero and 15 deg contact angles but it was found that the series representation did not work well in these cases. It did not work at all (in the reorientation problem with hemispherical initial shape) for zero contact angles, worked for a short interval of time for 15 deg angles and worked better for large contact angles - for example the 45 deg case represented here. Again, it is hoped that this is mainly an inherent difficulty in the series representation. We hope that the finite differencing will alleviate this difficulty also. (Actually, some very good results were obtained for 0 deg contact angle with a flat initial shape with a meniscus at the wall, see Fig. 6 of Ref. 2. This again points out the fact that the series representation is inherently better for predicting motion which remains in the region where the series converges most rapidly).

David Lomen, Convair

It is very optimistic on your part to hope to duplicate or predict the films we saw before where definitely rotational motion is involved. I also might say that a more realistic nonlinear approach would be to include rotational effects in the treatment; I would very much like to see something like this done. I would question any prediction based on this model as to the rotational motion we saw in the previous slides.

Perko

Yes, I would not expect this to apply to rotational flow. Again, it is a preliminary study possibly to be expanded this fall if the support is available. However, it is the case for inviscid flow that if the fluid motion is initially irrotational, it will remain so.

PAPER 4

**SOME THERMAL ASPECTS OF A CONTAINED
FLUID IN A REDUCED-GRAVITY ENVIRONMENT**

By S. H. Schwartz and M. Adelberg*

~~DOUGLAS~~ AIRCRAFT COMPANY

ABSTRACT

In this paper a survey of the various factors affecting heat transfer to a liquid in a container is made with primary emphasis placed on their relationship to the problem of the prediction of the pressure buildup in cryogenic propellant tanks. The basic modes of heat transfer are first reviewed and criteria subsequently developed for determining the conditions under which each of these modes will exist. The various heat-transfer modes are also examined in terms of the magnitudes of the acting forces. Critical values of force ratios, above which one force dominates, are developed. The prediction of the conditions under which the inception of boiling will occur is then considered. Estimates are presented based on experimental data. Utilizing laminar and turbulent flow analyses, the location on a vertical wall where the critical temperature is reached is defined as a function of the heat flux and gravity level. A more precise method following the approach of Bergles and Rohsenow

*Consultant.

is also presented. Summary plots indicating the heat-transfer domains are included. Since the transient time period for the sudden heating of a vertical wall is large in the low-heat-flux low-g regime, equations are presented to estimate the transient periods for non-boiling turbulent flow and for boiling flow. Also, other factors involved in the analysis of practical stratification problems are considered, including the critical wall angle where instability effects result and the point where conduction is of the same magnitude as convection. The capabilities and limitations of a few of the existing computer programs for handling stratification are reviewed. Modifications for extending their usefulness are discussed.

NOMENCLATURE

English Symbols

A	Area
c_p	Specific heat
C_1 through C_4	Constants used in boundary layer equations
g	Gravitational constant
g_0	Earth's gravitational constant
Gr	Grashof number
Gr^*	Modified Grashof number
h_{fg}	Latent heat of vaporization
k	Thermal conductivity of fluid
L	Length
M_e	Mass that has flowed into boundary layer in time τ_s
M_o	Mass which has flowed out of boundary layer in time τ_s
M_s	Steady-state mass in boundary layer
\dot{M}	Mass flow rate
\dot{M}_e	Mass flow rate entering system
$\dot{M}_{e,1}$	Mass flow entering at $\tau = 0$

English Symbols

\dot{M}_o	Mass flow rate leaving system
\dot{M}_{stored}	Rate of mass stored
$\dot{M}_{e,s}$	Steady-state mass flow rate entering system
$\dot{M}_{o,s}$	Steady-state mass flow rate leaving system
\dot{M}_s	Steady-state mass flow rate ($\dot{M}_s = \dot{M}_{e,s} = \dot{M}_{o,s}$)
p	Pressure
p_g	Pressure of gas in bubble
p_l	Pressure of liquid
Pr	Prandtl number
q	Heat flux rate
q_{max}	Peak nucleate boiling heat flux
q_w	Heat flux rate at wall
$q_{w,l}$	Laminar wall heat flux rate
$q_{w,t}$	Turbulent wall heat flux rate
r	Notch radius
r_c	Critical notch radius
R_g	Gas constant
Ra	Rayleigh number
Ra^*	Modified Rayleigh number
T_b	Bulk temperature
T_g	Temperature of gas
T_l	Temperature of liquid in boundary layer
T_s	Saturation temperature
T_w	Wall temperature
$T_{w,c}$	Critical wall temperature where boiling begins
ΔT	Temperature difference, $T - T_b$
ΔT_w	Temperature difference $T_w - T_b$
$\Delta T_{w,s}$	Temperature difference $T_w - T_s$
$\Delta T_{w,c}$	Critical temperature difference where boiling begins, $T_{w,c} - T_s$
u^*	Fictitious boundary layer velocity
V	Velocity
V_s	Steady-state velocity in boundary layer

English Symbols

V_{smax}	Maximum velocity in boundary layer
V_{∞}	Free stream velocity
V_1	Velocity outside boundary layer of comparable forced convection flow
\bar{V}	Mean velocity in boundary layer
\bar{V}_s	Steady-state mean velocity in boundary layer
x	Distance along heated wall
x_c	Critical distance along wall where boiling begins
\bar{x}	Mean distance
y	Distance from wall in direction perpendicular to wall

Greek Symbols

α	Thermal diffusivity
β	Coefficient of expansion
δ	Boundary layer thickness
δ_c	Critical boundary layer thickness
$\delta_{s,L}$	Steady-state boundary layer thickness at $x = L$
$\bar{\delta}_s$	Steady-state boundary layer thickness averaged over a length L
δ_s	Steady-state boundary layer thickness at any station
η	Dimensionless gravity constant
μ	Coefficient of viscosity
ν	Kinematic viscosity
$\pi_{F,C}$	Convective Froude number
π_{Gr}	Boiling Grashof number
ρ	Density
ρ_g	Density of gas
ρ_l	Density of liquid
ρ_v	Density of vapor
σ	Surface tension
τ	Time
τ_r	Reference time, system time constant
τ_s	Time to reach steady-state (technically, it is that time which is large compared with τ_r)

SOME THERMAL ASPECTS OF A CONTAINED FLUID IN A REDUCED-GRAVITY ENVIRONMENT

1 INTRODUCTION

Pressure and thermal stratification in a propellant tank as a function of time are of concern for a number of reasons. Excess pressures require venting and bring on the problems associated with it, such as phase separation and non-thrust venting. On the other hand, a nominal thrust level is desirable to assure that the propellant is maintained at one end of the tank, and utilization of propellant boiloff is a logical approach to achieve this desired thrust. Minimum NPSH must also be satisfied for starting rocket motors. The prediction of tank pressure histories and thermal stratification requires knowledge of the heat-transfer process or processes that occur at the tank walls.

In this paper, a survey is made of a number of factors affecting the heat transfer to a liquid in a container. To place these various factors in proper perspective, the basic modes of heat transfer are first briefly reviewed. Then, criteria are developed for determining the conditions under which each of these modes will exist, as well as the time it will take to reach steady state for each mode. An approximate guideline for predicting the mode of heat transfer for a given gravity level-heat-flux domain is presented.

After establishing the regions of domain of the various modes of heat transfer, two particular problem areas are analyzed in some detail - the time required for a boundary layer to reach steady state and the conditions required to initiate boiling. These two problems are given lesser but proper emphasis in a 1-g environment. The problem of the time required to reach steady state is one example of that class of problems whose importance is magnified by a reduced-gravity environment.

2 ESTABLISHMENT OF DOMAINS AND DISCUSSION OF HEAT-TRANSFER MODES

Establishment of the domains of heat transfer requires an understanding of the particular thermal energy mechanism. In this section, the heat transfer modes will be considered

in detail sufficient to estimate the domains where each mode dominates. The discussion emphasizes application to contained cryogenic fluids in a reduced-g environment. One of the related problems is stratification. A number of recent efforts have been reported predicting stratification effects in closed containers (Refs. 1-15) and open containers (Refs. 16-18). Furthermore, in Ref. 19, criteria are presented for the various modes of heat transfer that will occur on the propellant tank wall as a function of both heat flux and gravity. This section will attempt to extend such criteria.

The determination of the mechanism of heat removal will depend on many variables. Some of the more important ones are:

- (1) Gravity vector
- (2) Magnitude and distribution of heat flux
- (3) Geometric parameters, such as baffles, roughness, and distance along the wall
- (4) Fluid properties (thermophysical as well as mechanical. An example of the latter is the fluid velocity imposed by tank draining)
- (5) Transient effects (boundary layer may be thin initially)

In developing the criteria for determining the effect of the above variables on the heat-transfer phenomenon, one must first discuss the possible mechanisms that may occur. Thus, either individually or in some combination, the following mechanisms of energy transport may result:

- (1) Conduction
- (2) Viscous flow throughout container (low-velocity flow)
- (3) Laminar or turbulent boundary layer (thin-boundary layer)
- (4) Stable or unstable (horizontal surface facing upwards) convection (laminar or turbulent)
 - (a) Horizontal surface (gravity vector perpendicular to wall)
 - (b) Inclined surface (include vertical wall)
 - critical angle
 - vertical wall

- (5) Nucleate boiling
 - Horizontal surface
 - Inclined surface
- (6) Film boiling
 - Horizontal surface
 - Inclined surface

First, the domain where the various mechanisms account for the heat transfer will be analyzed to determine their limits. For example, the criterion of incipient boiling will be established. This becomes important when the wall temperature exceeds some critical value and boiling begins. Another critical point is reached when the heat transfer rate is sufficiently great that nucleate boiling or individual bubbles no longer exist and a continuous vapor film or film boiling will occur. This domain and its limits will also be established. At the other extreme, one finds that a third criterion exists for the domain where conduction is an important mechanism of energy transport throughout the propellant tank. This region, as might be expected, will occur for combinations of small values of heat flux and very-low-gravity fields.

The distinction must also be made between steady and non-steady boundary layer flow. Figure 1 is a schematic drawn to orient the reader to the various heat-transfer regimes that may exist. The following discussion will investigate more carefully the boundaries of these domains. Since the time to reach steady flow may be an appreciable fraction of the total time for a space mission, this phase will be discussed first.

2.1 Non-Steady Flow

Analyses of times required to reach steady state have been found in the literature for the laminar case only (Refs. 20, 21, and 22). One such good reference is Siegel

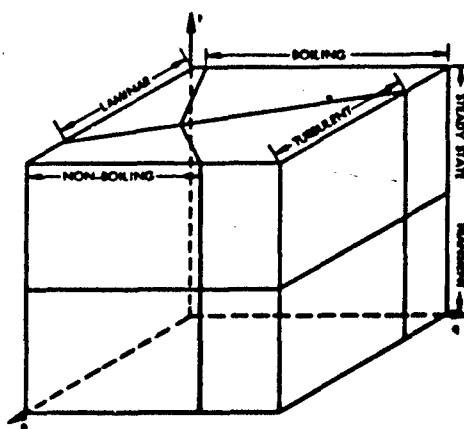


Fig. 1 Diagram of Transient and Steady-State Regions

(Ref. 20). His solution was obtained from the momentum and energy equations which were placed in integral form. Solutions were obtained both for the uniform wall temperature case and the uniform wall heat flux case.

The solution for the uniform temperature problem in terms of the time to reach steady state is

$$\tau_s = 5.24 (0.952 + Pr)^{1/2} (g \beta \Delta T_w)^{-1/2} x^{1/2} \quad (1)$$

which for liquid hydrogen reduces to

$$\tau_s = \frac{1.35 x^{1/2}}{(\eta \Delta T_w)^{1/2}} \text{ sec} \quad (2)$$

For the case of a uniform wall heat flux, the time to reach steady state is expressed as

$$\tau_s = 4.33 (1.68 + Pr)^{2/5} \left(\frac{g \beta q_w}{k \nu^2} \right)^{-2/5} \frac{Pr^{-2/5} x^{2/5}}{\alpha} \quad (3)$$

which for liquid hydrogen reduces to

$$\tau_s = 54 \left(\frac{x}{q_w \eta} \right)^{2/5} \text{ sec} \quad (4)$$

Transient effects are treated in greater detail later.

2.2 Steady-State Flow

The problem of boundary layer flow is somewhat reduced in difficulty when treating steady-state problems. The natural convection boundary layer flow over a vertical wall has been considered for both laminar and turbulent flow. Sparrow and Gregg (Ref. 23) have solved the laminar case for the uniform wall heat flux. The uniform wall temperature case has been covered extensively as, for example, in Ref. 24.

The uniform wall temperature problem in turbulent flow has been treated by Eckert and Jackson (Ref. 25). Vliet (Ref. 19) and others have attacked the turbulent uniform wall heat flux case.

The Rayleigh number is the dimensionless parameter used to predict transition from laminar to turbulent flow in natural convection for the constant wall temperature problem. When the heat flux is uniform, a modified Rayleigh number is used. Both are defined below along with their respective critical values.

- (1) Uniform surface temperature (see Ref. 26)

$$Ra = Gr \cdot Pr = \frac{g \beta \Delta T_w x^3}{\nu^2} \cdot \frac{\mu c_p}{k} \quad (5)$$

$$\left. \begin{array}{l} 10^3 < Ra < 10^9 \text{ (laminar)} \\ 10^9 < Ra \text{ (turbulent)} \end{array} \right\} \quad (6)$$

- (2) Uniform surface heat flux

$$Ra^* = Gr^* \cdot Pr = \frac{g \beta q_w x^4}{k \nu^2} \cdot \frac{\mu c_p}{k} \quad (7)$$

$$\left. \begin{array}{l} 10^5 < Ra^* < 10^{11} \text{ (laminar)} \\ 10^{11} < Ra^* \text{ (turbulent)} \end{array} \right\} \quad (8)$$

The lower limits on the modified Rayleigh number are estimated on the bases of the limits for the unmodified Rayleigh number and the fact that the two have upper limits which differ by two orders of magnitude. The same limit for the modified Rayleigh number laminar flow is suggested in Ref. 19 but the basis for this is not mentioned.

For values of the Rayleigh number below 10^3 (10^5 for the modified Rayleigh number), a gross viscous flow regime exists where the boundary layer equations are no longer valid. For very small values of the Rayleigh number ($Ra \ll 1$), the limit where conduction is the primary mode of heat transfer is approached.

However, in addition to the critical Rayleigh number, there is a critical wall temperature above which non-boiling flow ceases and a boiling type flow begins. This condition is discussed below.

2.3 Inception of Boiling

Inception of boiling will be the term used to describe the condition under which heat-generated vapor bubbles just begin to grow on a heated wall. This condition is met when the fluid near the wall is hot enough to cause evaporation on a liquid-vapor interface which in this case is the surface of the bubble (Ref. 27). For curved interfaces, such as a bubble, this evaporation temperature exceeds the boiling point of the liquid in the container. Hence, bubbles can only grow in a superheated layer of liquid which is most commonly found adjacent to heating surfaces. These surfaces must also be superheated with respect to the boiling point of the liquid. Since the surface conditions must be known in order to predict the wall temperature where boiling first begins (this is discussed below), experimental data are needed. This data combined with the analytical equations for a uniform wall heat flux will predict the wall location where the temperature of the wall is sufficient to produce vapor bubbles.

Experimental data on the incipient boiling point for cryogenics, such as liquid hydrogen, are limited and requires much interpretation and more investigation. Sherley (Ref. 28), Graham et al. (Ref. 29), Class (Ref. 30), Weil and Lacaze (Refs. 31 and 32) found incipient $\Delta T_{w,c}$'s ($T_{w,c} - T_s$) from 1° to 3°F. However, Drayer and Timmerhaus (Ref. 33) apparently found a much lower value for the critical $\Delta T_{w,c}$ of about 0.1°F. Data are presented for a $\Delta T_{w,s}$ ($T_w - T_s$) of range 0.06° to 1.17°F where the boiling was of the nucleate type. Mulford et al. (Ref. 34) also found that nucleate boiling occurred at lower values of ΔT_w than were reported by most other workers.

One fine point regarding the specification of temperature difference is that in some reports it is not made clear whether the bulk temperature or the saturated temperature is to be subtracted from the wall temperature. Of course, in some of these cases the two temperatures are equal. Nevertheless, the comments made above regarding the differences in boiling curves are still valid, since distinguishing between bulk and saturation temperatures cannot account for the very large differences.

Curves of q versus $\Delta T_{w,s}$ are shown in Fig. 2 for the above references along with those shown by Graham et al. Pressure definitely influences the critical value, and the data cited above were selected for the range near 1 atm. Some additional data are also available for higher pressures where the incipient ΔT has a lower value. The data of Graham et al. and Class are presented to illustrate the effects of high pressure. Factors, such as surface orientation and nucleation site characteristics including surface roughness, probably will account for some, if not much, of the data scatter. All of the above described experiments were performed at 1g. Sherley states that a large reduction of g level has no effect upon incipient $\Delta T_{w,c}$. Merte and Clark (Ref. 35)

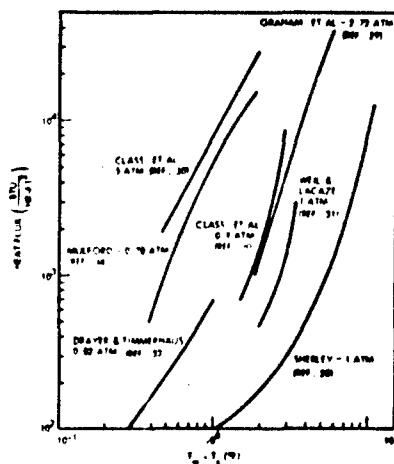


Fig. 2 Boiling Curves for Liquid Hydrogen

found practically no difference in the value of (g/A) incipient for boiling water over a range of accelerations from 1 to 20 g's. Graham et al. imply that their data suggest that an increase in g level will increase the value of the incipient $\Delta T_{w,c}$, but there appears to be insufficient control over the experiments to establish such a trend with confidence. This presumably was not the primary goal of these experiments but was the result of observations made after reducing the data. Although there is much uncertainty regarding the value of the point of incipient boiling, two values (1° and 3° F) are arbitrarily selected in order to illustrate the various domains of heat transfer such as in Fig. 3.

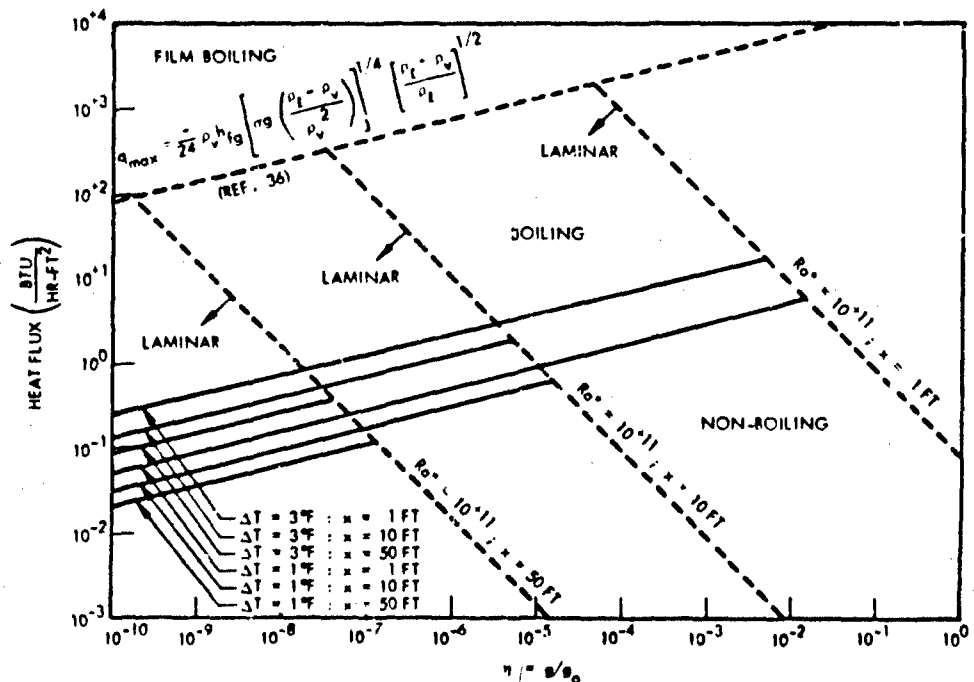


Fig. 3 Heat-Transfer Modes for Natural Convection Laminar Flow Over Uniformly Heated Vertical Wall—Liquid Hydrogen ($T_b = T_s$)

2.4 Laminar Flow - Uniform Wall Heat Flux

In defining the line in Fig. 3 which separates laminar non-boiling flow from boiling flow, Sparrow and Gregg's work will be used. Both 1° and 3°F will be used for the incipient boiling wall temperature difference $(T_{w,c} - T_g)$ for liquid hydrogen at one atmosphere. Thus, the criterion used for initiation of boiling is when the wall temperature at a given location exceeds the saturation temperature by $\Delta T_{w,c}$. To determine the location of the incipient point on the container wall, the following equation developed by Sparrow and Gregg is used

$$\frac{(T_w - T_b)(Gr^*)^{1/5}}{\frac{q_{w,l} x}{k}} = \frac{(360)^{1/5}}{2} \left(\frac{0.8 + Pr}{Pr^2} \right)^{1/5} \quad (9)$$

which holds for $Ra^* < 10^{11}$.

Applying Eq. (9) for the case of incipient boiling, set $(T_w - T_b) = (T_{w,c} - T_g)$ and for $Pr = 1$

$$(Gr^*)^{1/5} = \frac{1.7 q_{w,l} x}{k \Delta T_w} \quad (10)$$

For the case of liquid hydrogen, Eq. (10) can be expressed as

$$q_{w,l} = \frac{18 \Delta T_{w,c}^{5/4} \eta^{1/4}}{x^{1/4}} \quad (11)$$

Here η is the dimensionless gravity constant g/g_0 . The units for q and x are Btu/hr-ft^2 and ft, respectively. Equation (11), when plotted on a graph of q versus η , yields a curve of the critical wall temperature at a fixed location (Fig. 3). Points lying below this line fall in the laminar flow regime and points above this line lie in the

boiling domain. As can be seen, the location of incipient boiling at a fixed gravity level will vary from 1 to 50 ft with less than an order-of-magnitude change in the wall heat flux. It should be noted that the constant modified Rayleigh line of 10^{11} in Fig. 3 may not signify laminar flow in the boiling regime. The flow may become unstable at a lower value of the modified Rayleigh number due to disturbances caused by the bubbles. In any event, there is a need for developing boundary layer equations in the boiling regime.

2.5 Turbulent Flow - Uniform Wall Heat Flux

The area to the right of the critical modified Rayleigh line in Fig. 3 is one of turbulent flow. The case of natural convection turbulent flow along a vertical wall was first solved by Eckert and Jackson (Ref. 25). This was done for the case of a uniform wall temperature where the thermal and velocity boundary layers were assumed to be equal. Vliet (Ref. 19) derived the equations for a uniformly heated axisymmetric vessel. In this analysis for the case of a constant bulk temperature, the relationship between the heat flux and the wall shear was assumed to be

$$q_{w,t} = 0.0225 \rho c_p u^* (T_w - T_b) \left(\frac{\nu}{u^* \delta} \right)^{1/4} \quad (12)$$

Equations for u^* and δ may also be found in Ref. 19, as follows

$$u^* = 13.15 \nu \left(\frac{\beta}{\rho c_p \nu^3} \right)^{5/14} (\eta q_{w,t})^{5/14} x^{3/7} \quad (12a)$$

$$\delta = 0.4084 \left(\frac{\rho c_p \nu^3}{\beta} \right)^{1/14} \left(\frac{1}{\eta q_{w,t}} \right)^{1/14} x^{5/7} \quad (12b)$$

Combining Eqs. (12), (12a), and (12b)

$$\frac{(T_w - T_b)(Gr^*)^{2/7}}{\frac{q_{w,t} x}{k}} = \frac{5.1}{Pr^{5/7}} \quad (13)$$

This equation will be used to predict the point of incipient boiling, although one interesting consequence of this is that it predicts a decrease in the wall temperature along the direction of flow. Since Vliet's analysis used the same heat flux-shear relationship as Eckert and Jackson, this consequence of Eq. (13) does not appear to be inconsistent with the results of Eckert and Jackson who predict an increase in the value of the film coefficient with an increase in x . Equation (13) will be used, even though there may be some question concerning the validity of the result that the wall temperature decreases with distance along the wall.

Equations (12), (12a), and (12b) may be combined to yield, for the case of incipient boiling and saturated hydrogen at 14.7 psia

$$q_{w,t} = 181 \Delta T_{w,c}^{7/5} \eta^{2/5} x^{1/5} \quad (14)$$

The units of $q_{w,t}$ and x are Btu/hr-ft² and ft, respectively. Plotting Eq. (14) in a manner similar to that of Fig. 3 illustrates the values of q and η where boiling occurs in turbulent flow (see Fig. 4). Since these results assume complete turbulent flow, their accuracy will only be acceptable when the laminar portion has a small contribution. Figure 5 is a composite joining both the laminar and turbulent domains. However, the curves are representative of a single location on the wall, 10 ft from the leading edge. An attempt to illustrate these domains as a function of wall length is made in Fig. 6.

2.6 Film Boiling

In Figs. 3, 4, and 5, a curve locating the peak nucleate heat flux is also presented. The theoretical equation supporting this curve is presented in Ref. 36. For heat fluxes exceeding these values, film boiling is to be expected. Film boiling may also take place at lower heat fluxes providing the required larger temperature difference is attained. This critical line presumably applies for all values of x , and this x independence is justified by the fact that most theoretical analyses do not have a length term in their final result. Furthermore, size effects appear to be of second order in reported experiments. On the other hand, no experiments have been reported for large vertical walls. All experiments have been for short vertical walls or other geometries, such as wires or spheres. Thus, it may be that the boiling curve is a function of some significant length as well as the driving temperature.

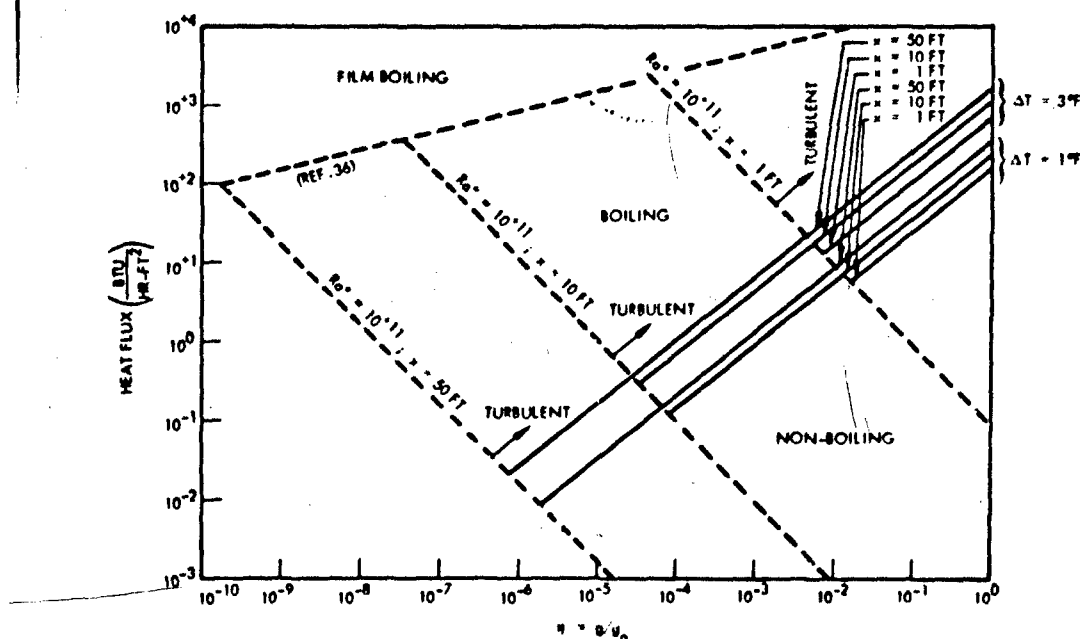


Fig. 4 Heat-Transfer Modes for Natural Convection Turbulent Flow Over Uniformly Heated Vertical Wall—Liquid Hydrogen ($T_b = T_s$)

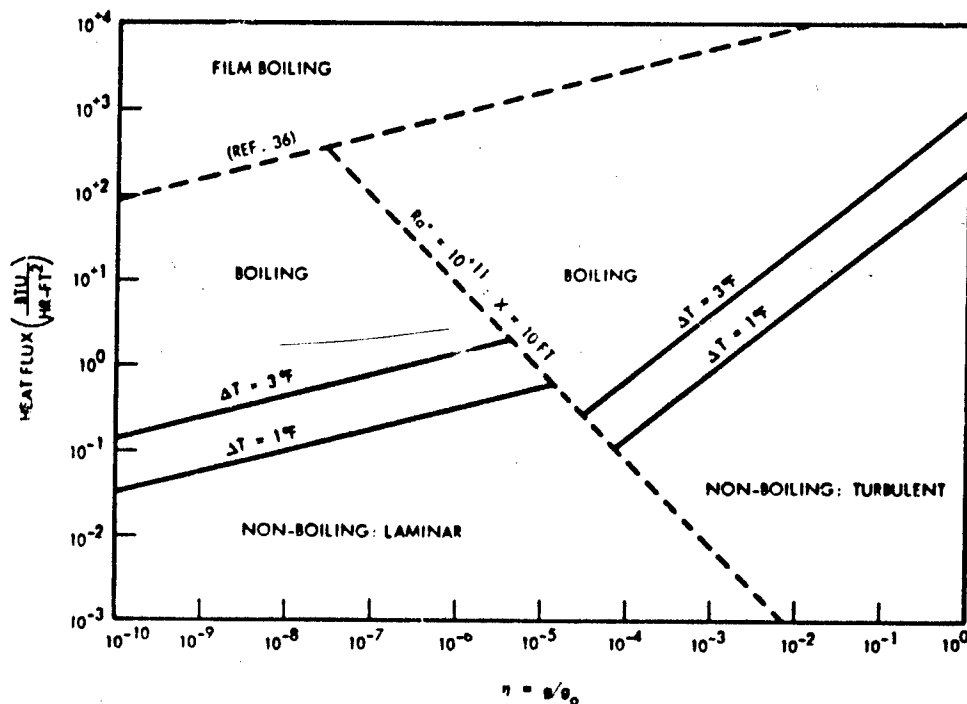


Fig. 5 Laminar and Turbulent Flow Over Uniformly Heated Vertical Wall at $x = 10$ ft—Liquid Hydrogen ($T_b = T_s$)

Pursuing this point further, it may be that the experiments performed to date explored so limited a size range that this effect is yet to be detected. Hence, the critical curve in Figs. 3, 4, and 5 may be different for sizes exceeding the maximum size of the heater currently investigated, which is on the order of 10 in. The film boiling curve is based on a paper by Zuber (Ref. 36) whose equation is in good agreement with many experimental data, including liquid hydrogen.

3 TIME TO REACH STEADY STATE

The time required for a fluid to reach steady state when heat is being transferred by natural convection must be known before the results of the previous steady-state analyses may be applied to a practical spacecraft propellant storage problem. Prior

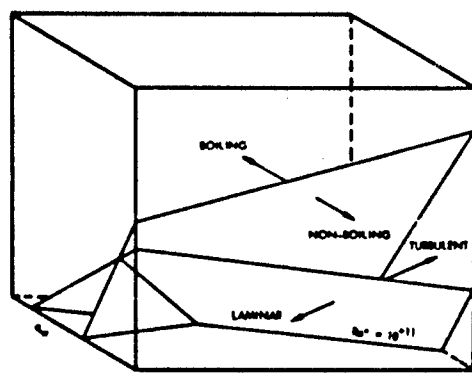


Fig. 6 Three-Dimensional View of Heat Transfer Modes—Steady State

discussion has shown that a number of analyses (Refs. 20, 21, and 22) are available for laminar boundary-layer flow. Although good, these analyses are somewhat complex. Solutions to the turbulent flow case have not been found in the literature.

In order to develop a feel for the time required for turbulent boundary layer flow to reach steady state, an approximate analysis is first developed for the laminar case and compared with the more rigorous solutions. The results are found to be good, so the same approximate approach is then applied to the turbulent case.

The system is defined in Fig. 7. Considering the conservation of mass, in the unsteady condition

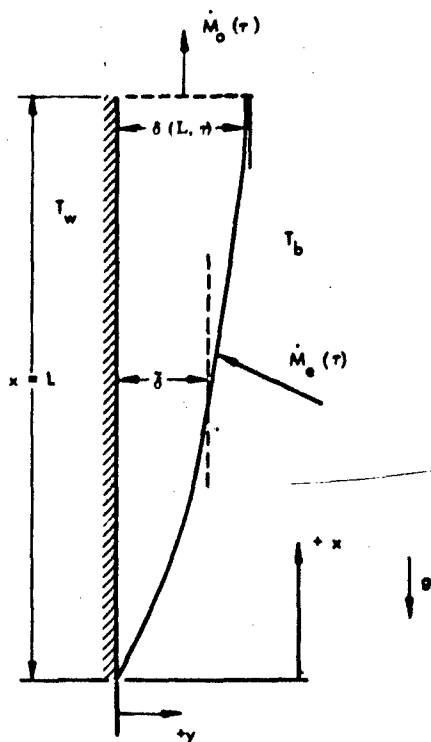
$$\dot{M}_e - \dot{M}_o = \dot{M}_{\text{stored}} \quad (15)$$

The technique to be used will predict the time it takes for the boundary layer of unit width to reach a steady-state configuration where the mass M is

$$M_s = \rho \bar{\delta}_s L \quad (16)$$

where $\bar{\delta}_s$ is the mean boundary layer thickness over a distance L at steady state. Any instant of time during the transient period, the total mass that has flowed into the boundary layer until time τ_s will be

$$M_o = \int_0^{\tau_s} \dot{M}_o d\tau \quad (17)$$



That which has left at some location x will be

$$\dot{M}_o = \int_0^{\tau_s} \dot{M}_o d\tau \quad (18)$$

And steady state is defined as the condition when \dot{M}_{stored} is much less than either \dot{M}_e or \dot{M}_o and, therefore, for practical purposes, is zero.

Hence, at steady state, the differences between the total mass which has entered the system over the transient period and that which has passed out will equal the total mass in the boundary layer or

$$\int_0^{\tau_s} (\dot{M}_e - \dot{M}_o) d\tau = \rho \delta_s L \quad (19)$$

Fig. 7 Boundary Layer in Transient Analysis

At this point, both \dot{M}_e and \dot{M}_o must be defined. Since

$$\dot{M} = \rho VA \quad (20)$$

\dot{M}_o can be expressed as

$$\dot{M}_o = \rho \bar{V}(x, \tau) \delta(x, \tau) \cdot 1 \quad (21)$$

where \bar{V} is the mean velocity in the boundary layer at a distance x from the leading edge at a time τ , and δ is the boundary layer thickness at the same position and the same time. Thus, as expected, M_0 is both time and spatially dependent. The purpose of this approach was to circumvent the more difficult problem of directly solving for $\bar{V}(x, \tau)$ and $\delta(x, \tau)$, in addition to solving for the time necessary to reach steady state. As a result, some reasonable assumptions must be made about the time dependence of δ and \bar{V} . A review of the literature failed to yield experimental data for the transient behavior of a boundary layer thickness. Although it was felt such information should be available in the literature, time did not permit an additional search. The boundary layer thickness growth during the transient period will be expressed by a Taylor series retaining only the terms to second order. Three reasonable conditions which this function should satisfy are shown in Eqs. (22), (23), and (24):

$$\lim_{\tau \rightarrow \tau_s} \delta = \delta_s \quad (22)$$

$$\dot{\delta}_s = 0 \quad (23)$$

$$\delta = 0, \quad \text{when} \quad \tau = 0 \quad (24)$$

thus

$$\frac{\delta}{\tau_s} = a + b \left(\frac{\tau}{\tau_s} \right) + c \left(\frac{\tau}{\tau_s} \right)^2 \quad (25)$$

from Eq. (24), $a = 0$:

Eq. (23), $b = 2c$:

Eq. (22), $c = -1$

so that, Eq. (25) reduces to

$$\frac{\delta}{\delta_s} = 2 \left(\frac{\tau}{\tau_s} \right) - \left(\frac{\tau}{\tau_s} \right)^2 \quad (0 \leq \tau \leq \tau_s) \quad (26)$$

3.1 Laminar Flow Analysis

The relationship for \bar{V} will be obtained from the steady-state solution for \bar{V}_s . Reference 24 shows that for laminar flow

$$\delta_s = C_1 x^{1/4} = 3.93 \left(\frac{\nu^2}{g\beta\Delta T_w} \right)^{1/4} \left(\frac{\alpha}{\nu} \right)^{1/2} \left(0.952 + \frac{\nu}{\alpha} \right)^{1/4} x^{1/4} \quad (27)$$

$$V_{s_{\max}} = C_2 x^{1/2} = \left(\frac{4}{27} \right) \frac{80\alpha}{(3.93)^2} \left(\frac{\nu^2}{g\beta\Delta T_w} \right)^{-1/2} \left(\frac{\alpha}{\nu} \right)^{-1} \left(0.952 + \frac{\nu}{\alpha} \right)^{-1/2} x^{1/2} \quad (28)$$

using Eqs. (27) and (28)

$$V_{s_{\max}} = \frac{C_1}{C_2} \delta_s^2 \quad (29)$$

Now, assume a similar relation exists at any time

$$\bar{V}(x, \tau) = \frac{C_1}{C_2} \delta^2(x, \tau) \quad (30)$$

Therefore, using Eq. (26)

$$\bar{V}(x, \tau) = \bar{V}_s \left[2 \left(\frac{\tau}{\tau_s} \right) - \left(\frac{\tau}{\tau_s} \right)^2 \right]^2 \quad (31)$$

Combining Eqs. (21), (26), and (31) and integrating

$$\int_0^{\tau_s} \dot{M}_O d\tau = \rho \bar{V}_s \delta_s \int_0^{\tau_s} \left[2 \left(\frac{\tau}{\tau_s} \right) - \left(\frac{\tau}{\tau_s} \right)^2 \right]^3 d\tau = 0.46 \dot{M}_s \tau_s \quad (32)$$

The function for \dot{M}_e must satisfy three conditions

(1) $\lim_{\tau \rightarrow \tau_s} \dot{M}_e = \dot{M}_{O,s}$

(2) \dot{M}_e must approach \dot{M}_O monotonically

(3) $\dot{M}_{e,i}$ must be consistent with the relation for δ

Conditions (1) and (3) are obvious, condition (2) is assumed for simplicity. Furthermore, there is no good reason why \dot{M}_e should be first greater than \dot{M}_s and, subsequently, less than \dot{M}_s or vice versa.

An exponential function satisfying the above three conditions is

$$\dot{M}_e = \dot{M}_s + (\dot{M}_{e,i} - \dot{M}_s) e^{-\tau/\tau_r} \quad (33)$$

where τ_r is a reference parameter which may be referred to as the system time constant. No additional physical significance could be found for this parameter. Integrating Eq. (33)

$$\begin{aligned} \int_0^{\tau_s} \dot{M}_e d\tau &= \int_0^{\tau_s} \left[\dot{M}_s + (\dot{M}_{e,i} - \dot{M}_s) e^{-\tau/\tau_r} \right] d\tau \\ &= \dot{M}_s \tau_s + (\dot{M}_{e,i} - \dot{M}_s) \tau_r \left(1 - e^{-\tau_s/\tau_r} \right) \end{aligned} \quad (34)$$

The value of the integral depends upon the value chosen for τ_r , or more precisely (τ_s/τ_r) . Now τ_r is always less than τ_s . Furthermore, steady state is technically reached only for infinite times. Practically speaking, however, τ_s is any value larger than some significant reference time. A reasonable reference time is the system time constant τ_r . Thus, solutions of interest are those for which $(\tau_s/\tau_r) \gg 1$. By starting with values of (τ_s/τ_r) of, say, 10 and then considering increasingly larger values, an asymptote for Eq. (34) may be obtained. This will be done after Eqs. (32) and (34) are substituted into the left-hand side of Eq. (19). Making this substitution

$$\int_0^{\tau_s} (\dot{M}_e - \dot{M}_o) d\tau = \dot{M}_s \tau_s + (\dot{M}_{e,i} - \dot{M}_s) \tau_r \left[1 - \exp\left(-\frac{\tau_s}{\tau_r}\right) \right] - 0.46 \dot{M}_s \tau_s \quad (35)$$

as τ_s/τ_r approaches infinity, Eq. (35) reduces to

$$\lim_{\tau_s/\tau_r \rightarrow \infty} \int_0^{\tau_s} (\dot{M}_e - \dot{M}_o) d\tau = 0.54 \dot{M}_s \tau_s \quad (36)$$

The mean value of δ is required to evaluate the right-hand side of Eq. (19). Using Eq. (27)

$$\bar{\delta}_s = \frac{1}{L} \int_0^L \delta_s dx = \frac{1}{L} \int_0^L C_1 x^{1/4} dx = 0.8 \delta_{s,L} \quad (37)$$

Combining Eqs. (19), (36), and (37) and solving for τ_s

$$\tau_s = 1.48 \frac{L}{\bar{V}_s} \quad (38)$$

The velocity distribution in the boundary layer for laminar flow is (Ref. 25)

$$\frac{v_s}{\frac{27}{4} v_{s_{\max}}} = \frac{y}{\delta} \left(1 - \frac{y}{\delta}\right)^2 \quad (39)$$

hence from Eq. (39)

$$\bar{v}_s = 0.562 v_{s_{\max}} \quad (40)$$

Finally, upon using Eq. (28)

$$\bar{v}_s = 0.415 (g\beta\Delta T_w)^{1/2} (0.952 + Pr)^{-1/2} x^{1/2} \quad (41)$$

Using Eqs. (41) and (38)

$$\tau_s = \frac{3.56 (0.952 + Pr)^{1/2} L^{1/2}}{(g\beta\Delta T_w)^{1/2}} \quad (42)$$

which agrees reasonably well with Siegel's solution considering the approximations that were made. Siegel's solution is

$$\tau_s = \frac{5.24 (0.952 + Pr)^{1/2} L^{1/2}}{(g\beta\Delta T_w)^{1/2}} \quad (43)$$

Thus, one goal is attained; that of demonstrating that an approximate analysis is reasonably consistent with a more rigorous result [compare Eq. (42) with Eq. (43)]. The same approach will now be taken for the turbulent boundary layer case. Although the absolute value of the turbulent steady-state time will be calculated, the ratio of this time to that calculated for laminar flow is the main goal. Hence, although the crude analysis may lead to error in the calculated times, it is hoped that by taking the ratio of turbulent to laminar times, a good estimate will be obtained.

3.2 Turbulent Flow Analysis

In a paper by Eckert and Jackson, the turbulent boundary layer velocity distribution used is

$$\frac{V_s}{V_1} = \left(\frac{y}{\delta}\right)^{1/7} \left(1 - \frac{y}{\delta}\right)^4 \quad (44)$$

where

$$V_1 = 1.185 \frac{\nu}{x} Gr^{1/2} (1 + 0.494 Pr^{2/3})^{-1/2} \quad (45)$$

Solving for \bar{V}_s

$$\bar{V}_s = 0.147 V_1 \quad (46)$$

As in the laminar case it is necessary to obtain relationships for $\delta(x, \tau)$ and $\bar{V}(x, \tau)$. For the turbulent steady-state case, Ref. 25 obtains

$$\bar{V}_s = C_3 x^{1/2} = 0.173 (g\beta\Delta T_w)^{1/2} (1 + 0.494 Pr^{2/3})^{-1/2} x^{1/2} \quad (47)$$

$$\delta_s = C_4 x^{7/10} = 0.565 \left(\frac{g\beta\Delta T_w}{\nu^2}\right)^{-1/10} (1 + 0.494 Pr^{2/3})^{1/10} x^{7/10} \quad (48)$$

From Eqs. (46) and (47)

$$\bar{V}_s = 0.142 (g\beta\Delta T_w)^{1/2} x^{1/2} \quad (49)$$

for $Pr = 1$.

Following the same process as used for obtaining Eq. (31), where as before it is assumed that Eq. (26) holds for turbulent flow as well, there results

$$\bar{V} = \bar{V}_s \left[2 \left(\frac{\tau}{\tau_s} \right) - \left(\frac{\tau}{\tau_s} \right)^2 \right]^{1/1.4} \quad (50)$$

Thus, when integrating Eq. (18) using Eqs. (31) and (50)

$$\int_0^{\tau_s} \dot{M}_o d\tau = \int_0^{\tau_s} \rho \bar{V} \delta d\tau = \rho \bar{V}_s \delta_s \int_0^{\tau_s} \left[2 \left(\frac{\tau}{\tau_s} \right) - \left(\frac{\tau}{\tau_s} \right)^2 \right]^{2.4/1.4} d\tau \quad (51)$$

which when integrated numerically results in the following form

$$\int_0^{\tau_s} \dot{M}_o d\tau = 0.563 \dot{M}_s \tau_s \quad (52)$$

The left-hand side of Eq. (19), using Eq. (52) and the limiting value for Eq. (34) becomes

$$\int_0^{\tau_s} (\dot{M}_e - \dot{M}_o) d\tau = 0.437 \dot{M}_s \tau_s \quad (53)$$

Evaluating $\bar{\delta}_s$ as before

$$\bar{\delta}_s = \frac{1}{L} \int_0^L \delta_s dx = \frac{1}{L} \int_0^L C_3 x^{0.7} dx = \frac{\delta_{s1} L}{1.7} \quad (54)$$

Combining Eqs. (53), (54), and (19)

$$0.437 \dot{M}_s \tau_s = \frac{\rho \delta_{s,L} L}{1.7} \quad (55)$$

Solving for τ_s

$$\tau_s = \frac{0.955 L}{\bar{V}_s} \quad (56)$$

and using Eq. (47) for \bar{V}_s

$$\tau_s = \frac{5.52 \left(1 + 0.494 Fr^{2/3}\right)^{1/2} L^{1/2}}{(g\beta\Delta T_w)^{1/2}} \quad (57)$$

A comparison of Eqs. (57) and (42) reveals that the time for a turbulent boundary layer to reach steady state is about 50 percent greater than for the laminar case, and $Pr \sim 1$. (In a subsequent analysis (Ref. 37), using a different approach, it was found that the transient time for turbulent flows was much shorter than for the laminar case. Probably, experiments are required to resolve this issue.) To show how sensitive the result is to the temporal relation assumed for δ and \dot{M}_e , a simple straight-line relation was also considered

$$\frac{\delta}{\delta_s} = \frac{\dot{M}_e}{\dot{M}_{e,s}} = \frac{\tau}{\tau_s} \quad (58)$$

This results in a coefficient of 10.4 instead of 4.81 in laminar flow [see Eq. (42)] and for turbulent flow, a coefficient of 47.0 instead of 7.35 [see Eq. (57)]. Thus, with the linear distribution, the turbulent time is more than 4 times as long as with laminar flow.

Figure 8 illustrates the relations, assumed in the analysis for the mass flow rate entering the system and the boundary layer thickness.

Figure 9 is based on Eqs. (43) and (57) for liquid hydrogen and helps illustrate cases, such as space vehicle missions, where transient effects for turbulent boundary layers are important. For example, when the gravity level is 10^{-9} g's and the wall temperature, is suddenly raised 1°F above the liquid temperature, the time to reach steady state at a distance of 10 ft from the bottom of the tank will be 360 hr.

The above results can be further justified by an alternate approach to the problem. In this case, Newton's

Second Law of Motion is applied to the system shown in Fig. 7. The shear and buoyancy forces are assumed to be time dependent with the same form as was assumed for δ in the previous second. Upon integration of the Second Law over the time range to steady state, the steady-state times are found to be

$$\tau_s = \frac{0.615(0.952 + \text{Pr})^{1/2} L^{1/2}}{(g\beta\Delta T_w)^{1/2}} \text{ (laminar)} \quad (59)$$

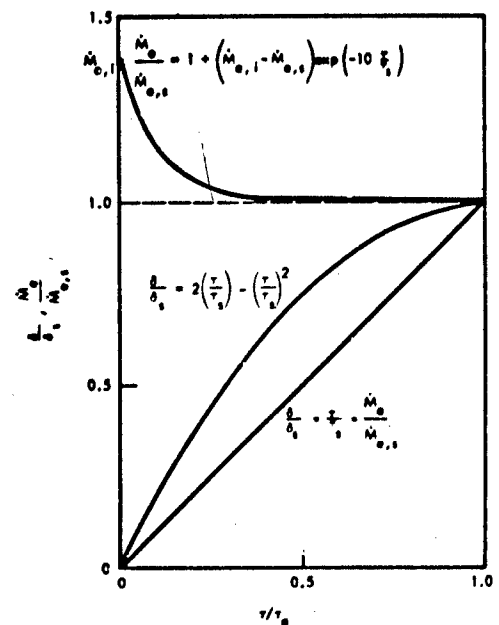


Fig. 8 Time Dependence of Mass Flow Rate and Boundary Layer Thickness

and

$$\tau_B = \frac{1.47 \left(1 + 0.494 \text{Pr}^{2/3}\right)^{1/2} L^{1/2}}{(g\beta\Delta T_w)^{1/2}} \quad (\text{turbulent}) \quad (60)$$

Although the magnitudes are in error, the ratios of times obtained from this very approximate analysis are consistent with the other results in the sense that the turbulent time is found to be approximately twice that of the laminar time.

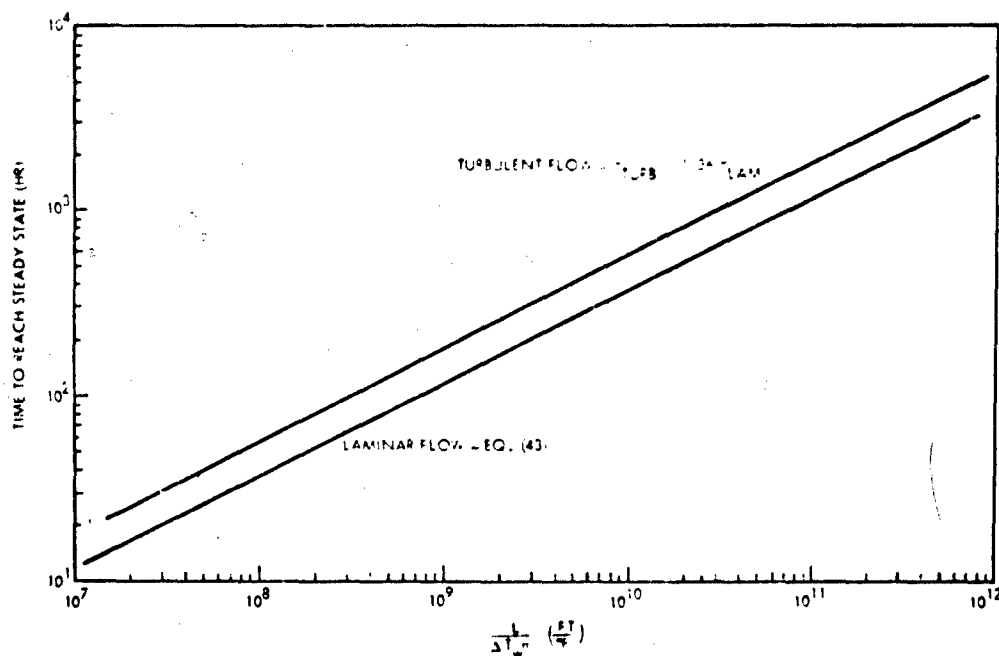


Fig. 9 Time for Natural Convection Boundary Layer Over Vertical Wall to Reach Steady State—Liquid Hydrogen

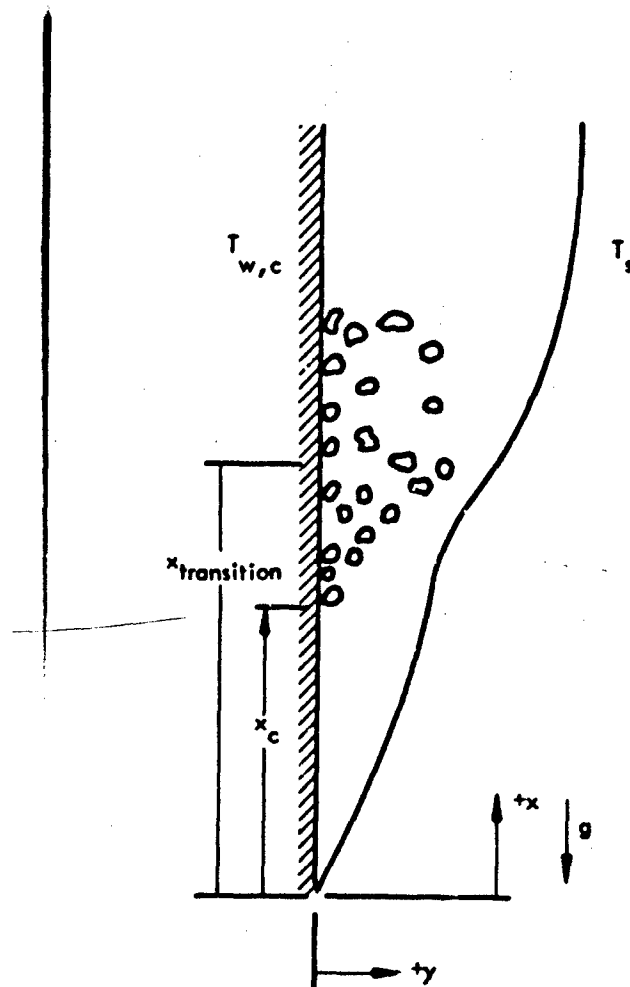


Fig. 10 Boundary Layer in Incipient-Boiling Analysis—Laminar

4 THEORETICAL DETERMINATION OF THE POINT OF INCIPIENT BOILING

A heated vertical flat plate immersed in a liquid will induce convection currents. At the leading edge, the heat transfer coefficient is infinite. Further up the plate, the heat transfer coefficient decreases, and at a critical length measured from the leading edge, the heat transfer coefficient will be so low that the heating rate (assumed to be uniform) will cause local nucleate boiling. The following analysis attempts to determine the effect of the boundary layer flow on the location of the point of incipient boiling. Figure 10 illustrates the system analyzed below.

4.1 Laminar Flow—Natural Convection

The method of Rohsenow and Bergles (Ref. 27) is used to find the incipient boiling point for laminar flow over a vertical wall. [Note that an approach similar to Sato and Matsumura (Ref. 38) may also be applicable.] The primary assumption is that the liquid surrounding a bubble must be hot enough to transfer heat to the bubble. In other words,

the liquid temperature at a distance $y = r$ from the wall must be greater than or equal to the vapor temperature of the bubble. This vapor temperature can be expressed as a

function of the fluid properties and the radius of the bubble. A spherical bubble is in mechanical equilibrium when

$$p_g - p_l = \frac{2\sigma}{r} \quad (61)$$

Then, with the Clapeyron equation and the perfect gas equation

$$\frac{dp_g}{dT_g} \approx \frac{h_{fg} \rho_g}{T_g} = \frac{h_{fg} p_g}{R_g T_g^2} \quad (62)$$

Integrating Eq. (62) and combining with Eq. (61)

$$T_g - T_s = \frac{T_g T_s R_g}{h_{fg}} \ln \left(1 + \frac{2\sigma}{r p_l} \right) \quad (63)$$

and when $2\sigma/rp_l$ is small, Eq. (63) can be simplified to

$$T_g - T_s \approx \frac{2T_s^2 \sigma R_g}{r h_{fg} p_l} \quad (64)$$

In order to determine the critical conditions, two equations must be satisfied

$$T_l = T_g \text{ at } y = r \quad (65)$$

$$\frac{dT_l}{dy} = \frac{dT_g}{dr} \text{ at } y = r \quad (66)$$

The physical meaning for Eq. (65) was described above. Equation (66) insures the minimum wall temperature necessary to achieve the condition described by Eq. (65).

The above equations are presented in Ref. 27.

At this point Eqs. (65) and (66) must be described in more detail where T_l will depend on the temperature profile in the boundary layer. The first such relationship considered will be that used to describe steady-state laminar free convection over a vertical wall; here the liquid temperature, T_l , is given as

$$\frac{T_l - T_s}{T_w - T_s} = 1 - 2 \left(\frac{y}{\delta} \right) + \left(\frac{y}{\delta} \right)^2 \quad (67)$$

Combining Eqs. (67) and (64) and substituting into Eq. (65), yields

$$\frac{2T_s^2 \sigma R_g}{(T_w - T_s) h_{fg} p_f} = r - \frac{2r^2}{\delta} + \frac{r^3}{\delta^2} \quad (68)$$

Now, by taking the derivatives of T_g and T_l in Eqs. (63) and (67) and combining with Eq. (66)

$$-\frac{2T_s^2 \sigma R_g}{(T_w - T_s) h_{fg} p_f} = -\frac{2r^2}{\delta} + \frac{2r^3}{\delta^2} \quad (69)$$

Solving Eqs. (68) and (69) simultaneously yields

$$\frac{r^2}{\delta^2} - \frac{4}{3} \left(\frac{r}{\delta} \right) + \frac{1}{3} = 0 \quad (70)$$

Here the two solutions of r_c are $r_c = 1/3 \delta_c$ and $r_c = \delta_c$. Using

$$r_c = \delta_c/3 \quad (71)$$

(since $r_c = \delta_c$ leads to a trivial solution), in Eq. (68) we find that

$$\delta_c \Delta T_{w,c} = \frac{13.5 T_s^2 R_g \sigma}{h_{fg} P_l} \quad (72)$$

Physically, this implies that for every critical wall temperature, there exists a critical boundary layer thickness such that vapor bubbles can begin to form. However, if Eq. (71) is put into Eq. (72), then

$$r_c \Delta T_{w,c} = \frac{4.5 T_s^2 R_g \sigma}{h_{fg} P_l} \quad (73)$$

This means that the minimum notch size that can initiate bubble formation is

$$r_c = \frac{4.5 T_s^2 R_g \sigma}{h_{fg} P_l \Delta T_{w,c}} \quad (74)$$

and, by inserting the properties of boiling water,

$$r_c \approx \frac{10^{-3}}{\Delta T_{w,c}} \text{ ft} \quad (75)$$

which is of a reasonable order of magnitude. [Note: Eq. (74) is not inconsistent with Eq. (64).] It should be noted that the minimum value of $\Delta T_{w,c}$ or the maximum value of r_c will depend on surface conditions. Hence, it is still necessary to experimentally determine $\Delta T_{w,c}$. However, δ_c is also approximately of the same magnitude as r_c . Hence, one would expect that the distance from the leading edge, where this critical boundary layer thickness is reached, is very small. Using the boundary layer thickness relationship [Eq. (27)], for non-boiling laminar flow over a vertical wall,

$$\delta_c = 3.93 \left(\frac{l^2}{g\beta\Delta T_{w,c}} \right)^{1/4} \left(\frac{\alpha}{\nu} \right)^{1/2} \left(0.952 + \frac{\nu}{\alpha} \right)^{1/4} x^{1/4} \quad (76)$$

Using Eq. (72) an expression for x is obtained

$$x_c = \frac{140 g\beta}{\alpha^2 \Delta T_{w,c}^3} \left(0.952 + \frac{\nu}{\alpha} \right)^{-1} \left(\frac{T_s^2 P_g \sigma}{h_{fg} P_l} \right)^4 \quad (77)$$

Using the values for boiling water at 212°F for a 1-g condition

$$x_c \approx \frac{10^{-4}}{\Delta T_{w,c}^3} \text{ ft} \quad (78)$$

This means that the critical distance where boiling begins is very close to the leading edge. For example, $\Delta T_{w,c}$ is usually on the order of 10°F, so x_c is approximately 10^{-7} ft. As can be seen from Eq. (77), the value of x increases directly with an increase in the gravity level. Thus, there is a tendency for this critical distance to shrink as the gravity level is reduced. From Eq. (73), it may be concluded that the critical notch size is fixed, once the fluid and wall temperatures are fixed, and the critical notch size is independent of g level. Hence, two of the necessary but not sufficient conditions for nucleate boiling are established: bubbles will grow provided that the notch size exceeds the critical value, $r > r_c$, [see Eq. (73)] and provided that these notches are located at positions exceeding the critical distance from the plate leading edge, $x > x_c$ [see Eq. (77)].

Of course, a third condition necessary for boiling is that the conduction limit for q be exceeded. At low heating rates, the heat being presented to a liquid may be accommodated by conduction, even in the extreme of a quiescent liquid.

4.2 Turbulent Flow-Natural Convection

Using the results of Eckert and Jackson (Ref. 25), an identical analysis to that above for turbulent flow may be performed. Here the temperature profile is assumed to be

$$\Delta T = \Delta T_w \left[1 - \left(\frac{y}{\delta} \right)^{1/7} \right] \quad (79)$$

Equation (64) is also used here. The critical conditions, Eqs. (65) and (66) also must be met in this case. First, Eq. (79) is combined with Eqs. (64) and (65) to obtain

$$\frac{2T_s^2 R_g \sigma}{h_{fg} p_f \Delta T_w} r \left[1 - \left(\frac{r}{\delta} \right)^{1/7} \right] \quad (80)$$

Now, by using Eqs. (64), (66), and (79), there results

$$\left. \frac{dT_g}{dr} \right|_{y=r} = - \frac{2T_s^2 R_g \sigma}{h_{fg} p_f r^2} \quad \left. \frac{dT_f}{dy} \right|_{y=r} = - \frac{\Delta T_w}{7\delta} \left(\frac{y}{\delta} \right)^{-6/7}$$

which simplifies to

$$\frac{2T_s^2 R_g \sigma}{h_{fg} p_f \Delta T_w} = \frac{r^2}{7\delta} \left(\frac{y}{\delta} \right)^{-6/7} \quad (81)$$

Finally, solving Eqs. (80) and (81) simultaneously, one finds that

$$r_c = 0.3 \delta_c \quad (82)$$

a result very similar to the laminar case [see Eq. (71)]. And using Eqs. (82) and (80)

$$\delta_c \approx \frac{40 T_s^2 R_g \sigma}{h_{fg} \Delta T_{w,c} p_l} \quad (83)$$

In order to find the critical length x_c , an expression for δ must be used. From (see Ref. 25)

$$\delta = \frac{0.56 x^{0.7}}{\left(\frac{g \beta \Delta T_w}{\nu^2}\right)^{0.1}} (Pr)^{-8/15} \left(1 + 0.494 Pr^{2/3}\right)^{1/10} \quad (84)$$

and putting Eq. (83) into Eq. (84)

$$x_c = \left(\frac{g \beta \Delta T_w}{\nu^2}\right)^{1/7} \left(1 + 0.494 Pr^{2/3}\right)^{10/7} \left(\frac{40 T_s^2 R_g \sigma}{h_{fg} p_l \Delta T_{w,c}}\right)^{10/7} Pr^{16/21} \quad (85)$$

and, by using the values of boiling water at 1g

$$x_c \approx \frac{0.027}{\Delta T_{w,c}^{9/7}} \text{ ft} \quad (86)$$

which, although much larger than that for laminar flow, is also a very small length. Therefore, one may conclude that the point of incipient boiling, under normal or reduced-g conditions, will be very close to the leading edge for fluids having properties similar to water.

4.3 Inception of Boiling - Forced Convection

Forced convection effects which may manifest themselves when the tank is being drained or filled, for example, may be so great as to dominate the free convection phenomena.

When the forced convection effects become large, the forced convection boundary layer may be thinner than the one for free convection.

An approximate analysis (Ref. 39) for the important parameter, which may be used to distinguish forced convection from free convection heat transfer, is a reciprocal Froude convective number, and its critical value is about 1 for low Grashof numbers and 10 for high Grashof numbers.

$$(\pi_{F,C})^{-1} = \left(\frac{Lg\beta\Delta T}{v^2} \right)_{\text{critical}} = \begin{cases} 1 & 10^4 < \pi_{Gr} < 10^7 \\ 10 & 10^7 < \pi_{Gr} < 10^{11} \end{cases} \quad (87)$$

Forced convection will now be examined to determine its effect on the location of the incipient boiling point. The laminar temperature profile assumed is

$$\frac{T_f - T_w}{T_s - T_w} = \frac{3}{2} \left(\frac{y}{\delta} \right) - \frac{1}{2} \left(\frac{y}{\delta} \right)^3 \quad (88)$$

Using Eqs. (64), (65), and (88)

$$\frac{2T_s^2 R_g \sigma}{h_{fg} p_f r} = (T_w - T_s) \left[1 + \frac{1}{2} \left(\frac{r}{\delta} \right) - \frac{3}{2} \left(\frac{r}{\delta} \right)^3 \right] \quad (89)$$

Now combining Eq. (66) and the derivatives of Eqs. (64) and (88) one obtains

$$\frac{2T_s^2 R_g \sigma}{h_{fg} p_f r^2} = (T_w - T_s) \left[\frac{3}{2\delta} - \frac{3}{2\delta} \left(\frac{r}{\delta} \right)^2 \right] \quad (90)$$

PAPER 5

**DISTRIBUTION OF NONCONDENSABLE GASES
IN LIQUIDS UNDER LOW-g CONDITIONS**

By M. E. Welch and E. Funk

NATIONAL AERONAUTICS AND SPACE ADMINISTRATION

GEORGE C. MARSHALL SPACE FLIGHT CENTER

ABSTRACT

Vapor and/or noncondensable gas are distributed in propellant lines and tanks of any space vehicle utilizing liquid propellants. Operational difficulties arise as a result of this condition. The distribution of vapor and/or noncondensable gas produced from orbital entry transients and attitude control transients decays into broad distribution bands under low-g conditions. There is a finite probability that, under low-g conditions, a sufficiently large vapor space will be found near the propellant suction lines at any specified time to produce "vapor lock" and thereby prevent engine restart. Vapor distributions that occur under normal operational conditions produce random pressure fluctuations as a result of condensation in the propellant lines. This condition is possibly one of the several causes of the "Pogo Effect."

Vapor and/or noncondensable gas distributions are, of course, also of primary concern in the study of the degree of cavitation produced in flight. It is with the first of these three problems that the authors are predominantly involved.

This paper discusses the first of three phases of an overall investigation of liquid-vapor and noncondensable liquid gas distributions produced under highly turbulent flow conditions and under different degrees of mechanical agitation. Specifically, the phase discussed herein is the determination of the initial distribution produced from an arbitrary energy input under variable g fields. The results obtained merely provide the initial condition for the time-dependent distribution function. The time-dependent function provides the means for calculating the probability that a sufficiently large vapor space will be found near the suction lines at the time of restart to produce "vapor lock." Since the space is limited, the more involved time-dependent functions and derivations are deleted. Furthermore, since the time-dependent functions describe the probability of failure of a specific space vehicle under specified restart conditions, the authors feel that this information should be more closely scrutinized before it is published in the open literature.

The data utilized herein were obtained under 1- g conditions. The distribution function was formulated by superimposing a theoretical distribution function derived for zero- g conditions or a semiempirical distribution function dependent on the acceleration field. The theory was verified within the experimental error. The predicted low- g distribution will be verified when the appropriate data can be obtained.

NOMENCLATURE

a	Acceleration
A	Constant
E	Surface energy
E_j	Surface energy of j^{th} group of bubbles
g	Acceleration due to gravity

g'	Ratio of a/g
k	Constant
l	Diameter of bubble
L	Characteristic length of container
N	Total number of bubbles in region considered
N_j	Number of bubbles in region considered with surface energy E_j
α	Constant
β	Constant
λ	Constant
ρ	Specific gravity referred to water at 4°C
σ	Interfacial tension
ω	Number of independent ways to distribute N bubbles so they are associated with surface energy E_j
$\rho a L^2 / \sigma$	Bond number

DISTRIBUTION OF NONCONDENSABLE GASES IN LIQUIDS UNDER LOW-g CONDITIONS

1 INTRODUCTION

During space-vehicle thrust decay and entry into zero-g conditions, liquid propellants are pitched against the tank bulkheads dispersing the liquid and gas phases. The bubbles formed are not all the same size but cover a large range of sizes. These bubbles create cavitation and engine restart problems. To establish safe limits of restart times, the rate of liquid settling must be known. To determine the rate of liquid settling, it is necessary to know the size distribution of the bubbles.

Bubbles in emulsions have been investigated more thoroughly than dispersed bubbles. Jellinek* analyzed emulsions with a purely statistical approach by utilizing the arithmetic mean of the bubble diameters. Rossi† assumed that emulsion phases are broken down at random giving the most probable distribution according to Boltzmann. To determine the most probable distribution Rossi assumed that the total volume and number of bubbles was constant. Favstova and Vlodavets‡ also used a probability approach to describe the distributions. Others have approached the problem in a statistical or empirical manner but, as yet, no derivation has fit all distributions of dispersed phases.

Siemes and Borchers† investigated the sizes of air bubbles in water columns and analyzed them according to the mean diameter and standard deviation. They produced

*H. H. G. Jellinek, J. Soc. Chem. Ind. (London), Vol. 69, 1950, p. 225

†C. Rossi, Gazz. chim. ital., Vol. 63, 1933, p. 190

‡V. N. Favstova and I. N. Vlodavets, Kolloid, Zhur., Vol. 17, 1955, p. 456

†W. Siemes and E. Borchers, Chem. Eng. Sci., Vol. 12, No. 2, 1960, p. 77

bubbles by injecting air through a porous plate. This process is not representative of the random formation that occurs in propellant tanks; therefore, the analysis would not be expected to fit the true distribution.

A parameter that has been neglected in past analyses is the surface tension of the fluid. Since bubble sizes are a function of the surface tension, a distribution derivation based on surface tension is considered in this report. The analysis utilizes the probability statistics of Boltzmann.

2 APPARATUS AND PROCEDURES

The testing systems used are presented in Fig. 1. The apparatus were 12 by 6 by 1 in. and 24 by 6 by 6 in. plexiglas tanks mounted in a stand that allowed them to spin. The contained liquid was agitated severely by spinning the tank, and thereby dispersing the gas within the liquid. The spinning was stopped and the bubbles formed were photographed instantly with a high-speed camera. The phases used were water-air, menthanol-air, and ether-air. Test pressure conditions were atmospheric.

3 JUSTIFICATION OF THE MATHEMATICAL DESCRIPTION OF DISTRIBUTION

If one attempts to describe the position and size of each bubble formed by the agitation of a gas-liquid system confined to a specified region, insurmountable mathematical difficulties arise. The dilemma is equivalent to that encountered in describing dynamical systems containing large numbers of particles. One's natural tendency is to use statistical methods and thereby forego any attempt to describe each bubble and its position.

The distribution-function derivation presented herein is developed with the general arguments utilized to obtain the Boltzmann distribution for the description of an ideal gas confined to a specified volume. An inherent difficulty exists in this application. The size of the samples considered is not comparable to those considered in the

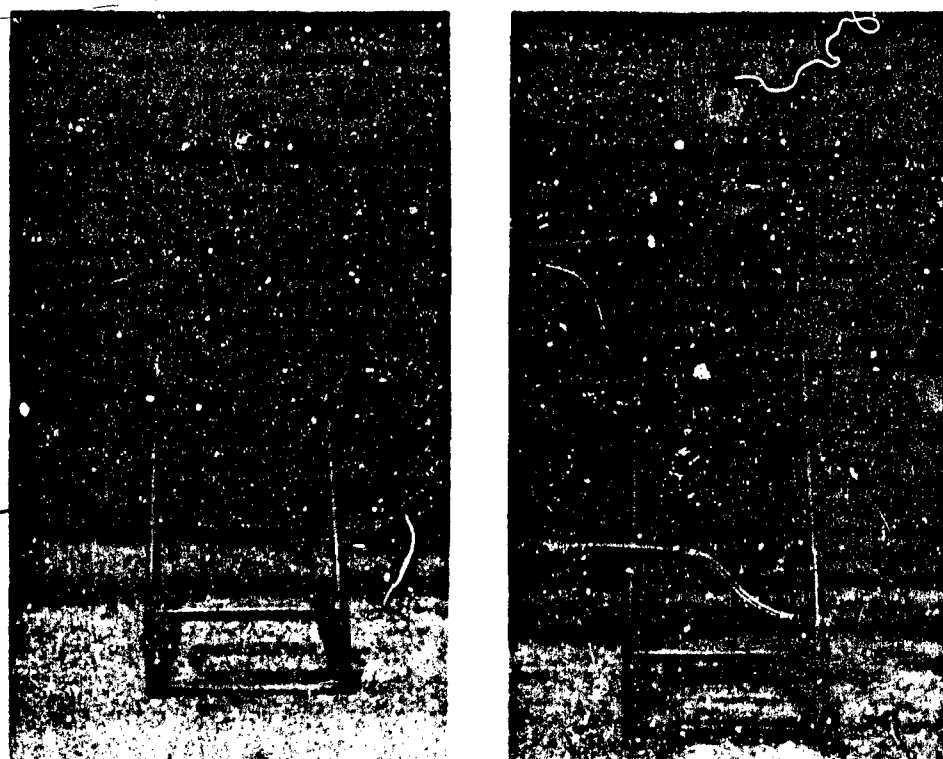


Fig. 1 Test Apparatus

kinetic theory of gases. Since some of the mathematical manipulation depends on approximations that are accurate only for large numbers, the size of the sample is important. One can statistically ascertain the error associated with the sample size. However, since experimental data are to be fit, it is more expedient to derive the equations on a large sample basis and let the accuracy of the results justify the means.

Several basic differences exist in the physical system and the associated derivation presented herein and the comparable case of molecular motion of ideal gases. One

is concerned with the distribution of surface energy whereas, in the kinetic theory of gases, one is concerned with the distribution of position and momentum for identical particles. The problem of bubble distribution is further complicated by several physical conditions. As the diameter increases, the bubbles become unstable, fragment, and produce a distortion of the distribution function. The smaller bubbles combine with the larger ones and migrate in a direction opposite to the direction of the g field. Since only the initial distribution produced from agitation is being considered, the last two conditions are of no concern.

One may follow either of two procedures in the derivation of the distribution function to include the effect of the increase of bubble instability with size. One method requires that the a priori probability for the size be precisely determined and utilized in the derivation of the canonical distribution. The other method, which involves the superposition of two distribution functions, is more convenient from the mathematical viewpoint and is more practical to employ with the stability information presently available. The latter method was employed by the authors.

One distribution function is derived with the assumption that an infinite energy range is possible, that the probability of bubbles of the same size falling in any energy interval is the same for all, and that the bubbles are all spherical. A second function is derived to describe the distribution produced from the spontaneous fragmentation of the larger bubbles. The complete distribution function is a linear combination of these two functions.

The former distribution function is obtained by closely following the reasoning involved in the derivation of the Boltzmann distribution. Utilizing this reasoning, one finds that the number of independent ways to distribute N bubbles so that N_j possess a surface energy E_j is

$$\omega = \frac{N!}{N_1! N_2! \dots N_n!} \quad (1)$$

The total number of bubbles present is

$$N = \sum_{j=1}^n N_j \quad (2)$$

and the total surface energy is

$$E = \sum_{j=1}^n N_j E_j \quad (3)$$

If one is concerned only with the initial distribution, then E represents the energy input utilized for surface formation and N represents the total number of bubbles initially produced. The solution of this system for the most probable distribution is, therefore, the limit of the time dependent distribution as time approaches zero. The most probable distribution is obtained by the same procedure as that utilized in the derivation of the Boltzmann distribution. Equations for the change of ω , E , and N are set equal to zero as follows:

$$\sum_{j=1}^n (\ln N_j) \delta N_j = 0 \quad (4)$$

$$\sum_{j=1}^n E_j \delta N_j = 0 \quad (5)$$

$$\sum_{j=1}^n \delta N_j = 0 \quad (6)$$

Utilizing Lagrange's method for undetermined parameters, one obtains the relationship:

$$\sum_{j=1}^n (\ln N_j + \lambda' E_j + \beta) \delta N_j = 0 \quad (7)$$

therefore

$$\ln N_j + \lambda E_j + \beta = 0$$

and

$$N_j = A \exp(-\lambda E_j) \quad (8)$$

The procedure utilized to obtain Eq. (8) is, of course, equivalent to that for deriving of the Boltzmann distribution. However, E_j represents surface energy rather than kinetic energy:

$$N_j/N = \exp(-\lambda E_j) / \sum_{j=1}^n \exp(-\lambda E_j) \quad (9)$$

Equation (9) can be expressed as an approximation of the original continuous distribution as follows:

$$\Delta N/N = \exp(-\lambda E_j) \Delta E_j / \sum_{j=1}^n \exp(-\lambda E_j) \Delta E_j \quad (10)$$

If E was originally divided into equal increments, Eq. (10) can be rewritten as follows:

$$dN/NdE = \lambda \exp(-\lambda E)$$

Equation (10) can be written in terms of l as follows:

$$dN/Ndl = \lambda \sigma l \exp\left(-\frac{\lambda'}{2} \sigma l^2\right) \quad (11)$$

It is also of interest to express Eq. (11) in terms of the most probable diameter (l_p). The expression for the most probable diameter is, of course, obtained by equating d^2N/dl^2 with zero:

$$l_p = 1/\sqrt{\lambda^2 \sigma} \quad (12)$$

The most probable diameter is, therefore, inversely proportional to the square root of surface tension, and

$$dN/Ndl = \left(l/l_p^2 \right) \exp \left[-\frac{1}{2} (l/l_p)^2 \right] \quad (13)$$

Equations (11) and (13) are valid for infinite containers under zero-g conditions. Under other g conditions, the fluid head gradient that exists along the axis of a bubble in the direction of the acceleration field has a tendency to distort and fragment the bubble. The physical system can be visualized as follows: The bubble distribution is produced in accordance with Eq. (11) and the larger bubbles are distorted and/or fragmented instantaneously as a result of the fluid head gradient that is applied across the bubbles at the time of formation. The Bond number, which is the ratio of the inertial force per unit depth of fluid ($\rho g' A_c$) and the surface tension (σ), therefore, is a measure of the tendency of the fluid head to distort and/or fragment a bubble of a given size. The distribution produced by fragmentation should follow the same functional form as Eq. (11); that is

$$dN'/N'dl = \alpha' l \exp \left(-\frac{\alpha'}{2} l^2 \right) \quad (14)$$

The physical systems represented by Eqs. (13) and (14) are equivalent. However, α' and N' in Eq. (14) are governed by the size of the bubbles from whence this distribution came as well as by the randomness of the process. Since the Bond number $\rho g' A_c / \sigma$ is a measure of the instability of the larger bubbles under a finite acceleration, one would expect α' and N'/N to be expressible in terms of this dimensionless

group. Furthermore, since the corresponding parameter in Eq. (11) is $\frac{\lambda'}{2}\sigma$, one can, by analogy, rationalize that $\alpha' = k' \sigma / \rho g'$. This rationalization is justified by the worth of the equation for the prediction of data:

$$dN'/N'dt = k' A_c \frac{\sigma}{\rho g'} t \exp \left(-\frac{k''}{2} \frac{\sigma}{\rho g'} t^2 \right) \quad (15)$$

If the diameter at which fragmentation becomes appreciable is sufficiently large, the effect of fragmentation on N in Eq. (11) is negligible, and the complete distribution function can be written as follows

$$\begin{aligned} dN/Ndt &= \lambda' \sigma t \exp \left(-\frac{\lambda'}{2} \sigma t^2 \right) + \gamma k' A_c \left(\frac{\sigma}{\rho g'} \right) t \exp \left(-\frac{k''}{2} \frac{\sigma}{\rho g'} t^2 \right) \\ \gamma &= \frac{N'}{N} = k''' \left(\frac{\rho g'}{\sigma} \right) \\ dN/Ndt &= \lambda' \sigma t \exp \left(-\frac{\lambda'}{2} \sigma t^2 \right) + A_c k' k''' \left(\frac{\sigma}{\rho g'} \right)^2 t \exp \left(-\frac{k''}{2} \frac{\sigma}{\rho g'} t^2 \right) \\ dN/Ndt &= \lambda' \sigma t \exp \left(-\frac{\lambda'}{2} \sigma t^2 \right) + \alpha \beta \left(\frac{\sigma}{\rho g'} \right)^2 t \exp \left(-\beta \frac{\sigma}{\rho g'} t^2 \right) \end{aligned} \quad (16)$$

It is convenient, for purposes of data processing, to determine the equation for accumulation. Since the least accurate counts are the smaller diameter counts, Eq. (16) is integrated from t to infinity rather than from zero:

$$(1/N) \int_t^\infty dN = \exp \left(-\frac{\lambda'}{2} \sigma t^2 \right) + \alpha \frac{\sigma}{\rho g'} \exp \left(-\beta \frac{\sigma}{\rho g'} t^2 \right) \quad (17)$$

The values of α , β , and λ' can be obtained easily by use of the asymptotic characteristics of Eq. (17). For small values of t

$$\ln \left(\int_t^\infty dN \right) = \ln (N) - \frac{\lambda'}{2} \sigma t^2 \quad (18)$$

For large values of t

$$\ln \left(\int_t^{\infty} dN \right) = \ln \left(N \alpha \frac{\sigma}{\rho g^*} \right) - \beta \frac{\sigma}{\rho g^*} t^2 \quad (19)$$

4 EXPERIMENTAL DETERMINATION OF THE PARAMETERS IN THE DISTRIBUTION FUNCTION

Twelve experimental distributions were obtained for ether-air, methanol-air, and water-air systems. The total number of bubbles lying between a given diameter and infinity was plotted against the square of the diameter. These plots clearly indicate the straight-line sections predicted by Eqs. (18) and (19). The ether-air runs involved the greatest range for the small diameter asymptote (Fig. 2). This, of course, is due to the small value of interfacial tension between air and ether.

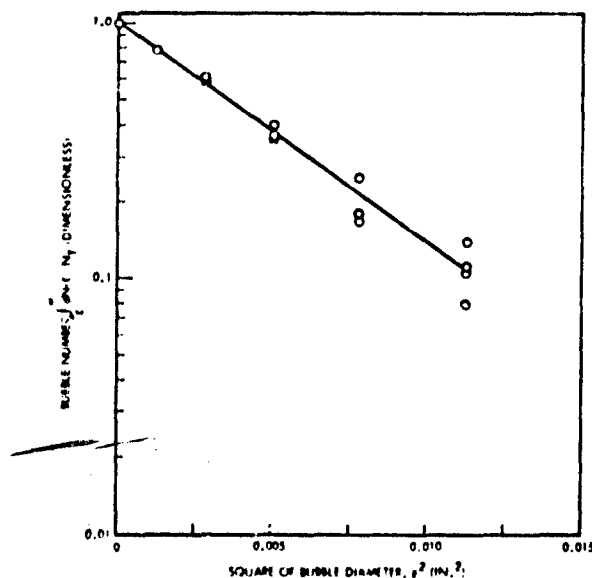


Fig. 2 Accumulative Plot for Ether (Small t Asymptote)

Equation (18) was fit to each of the four experimental runs by the method of least squares. The values were obtained for N and each run was normalized by dividing the accumulated count by N . The normalized runs were then plotted and the best least-squares fit of the normalized form of Eq. (18) was obtained. The standard deviation for the data was 0.027. The results are shown in Fig. 2.

The water-air runs involved the greatest range for the large diameter asymptote. This, of course, was due to the large interfacial tension between air and water. Equation (19) was fit to the large l asymptote for each of the four runs by the method of least squares. In this case the value of $\alpha N\sigma/\rho g'$ was obtained and used to normalize each of the four runs. The method of least squares was utilized again to obtain the best fit of the normalized form of Eq. (19) to all of the data involved. The standard deviation of the normalized data was found to be 0.029. These results are shown in Fig. 3.

With the values obtained for the parameters, Eq. (17) can be written as follows:

$$(1/N) \int_l^\infty dN = \exp(-9.35 \sigma l^2) + 0.105 \frac{\sigma}{\rho g'} \exp\left(-1.2 \frac{\sigma}{\rho g'} l^2\right) \quad (20)^*$$

Equation (20) was then used to calculate the accumulation $\left(\int_l^\infty dN\right)$ for the methanol-air system. The result was compared with the methanol-air data (Fig. 4), and was found to predict the experimental results. The entire range of the ether-air and water-air data also was calculated with Eq. (20) and compared with the experimental data (Figs. 5 and 6). Typical bubble distributions for ether-air and water-air systems are shown in Figs. 7 and 8.

5 CONCLUSIONS

Because Eq. (20) predicted the methanol-air results (Fig. 4) and the range of the ether-air and water-air data that was not used for correlation, it might be concluded that the basis of the derivation is reasonable.

*Mixed units are used for convenience in data evaluations:

g' (dimensionless)

l^2 (in. ²)

ρ (dimensionless)

σ (ergs)

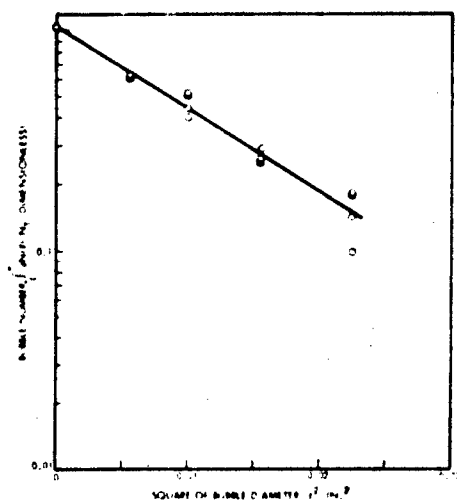


Fig. 3 Accumulative Plot for Water
(Large l Asymptote)

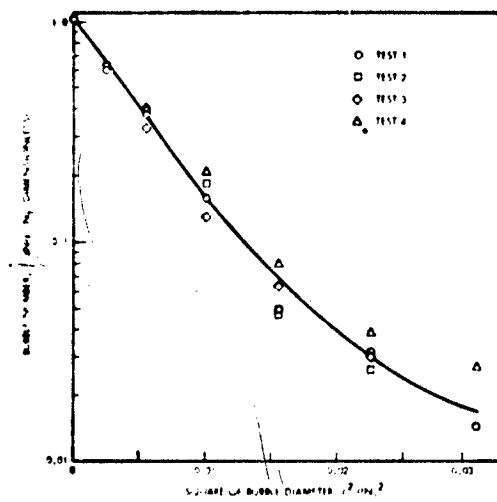


Fig. 4 Accumulative Plot and Theoretical
Function for Methanol

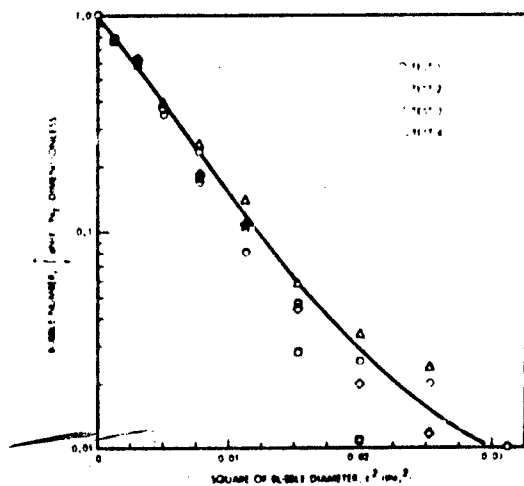


Fig. 5 Accumulative Plot and Theoretical
Function for Ether

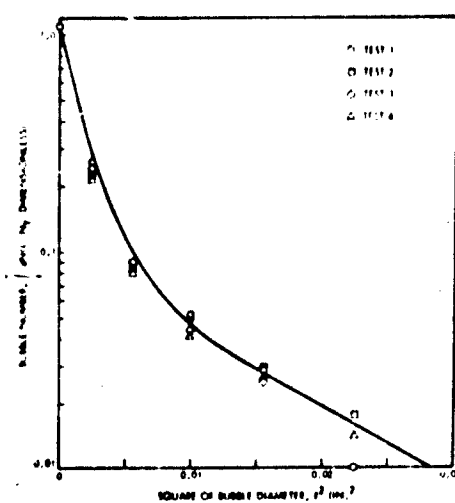


Fig. 6 Accumulative Plot and Theo-
retical Function for Water



Fig. 7 Bubble Distribution in Ether-Air System



Fig. 8 Bubble Distribution in Water-Air System

If the nature of the second term in the right-hand member of Eq. (20) is investigated, it becomes readily apparent through the application of L'Hospital's rule that this term approaches zero as the acceleration field approaches zero. Therefore, under zero-g conditions Eq. (20) reduces to

$$\int_0^{\infty} dN = \exp(-9.35 \sigma t^2) \quad (21)$$

and the distribution function is

$$dN/Ndt = 18.7\sigma t \exp(-9.35 \sigma t^2) \quad (22)$$

It is convenient, for comparison, to consider Eq. (22) in its dimensionless form:

$$dN/Ndz = z \exp\left(-\frac{1}{2}z^2\right) \quad (23)$$

where $z = (\sqrt{18.7\sigma})l$.

The dimensionless distribution functions at both zero-g and 1-g conditions are shown graphically in Fig. 9.

These results are physically reasonable. Under zero-g conditions, no fluid head exists across a bubble to produce fragmentation or distortion and the derivation of the first distribution function becomes applicable without modification.

The most probable diameter produced under zero-g conditions is

$$l_p = 0.231/\sqrt{\sigma} \quad (24)$$

An arbitrary amount of energy was utilized in each of the four runs for each liquid-air system. Since the most probable diameter remained constant within the experimental error, for each liquid-air system, one may conclude that only the total number of bubbles produced is affected by the energy input. However, this conclusion can only be drawn with considerable reservation because no measure of the energy that was utilized for the formation of surface could be made. The possibility of making such measurements is being investigated.

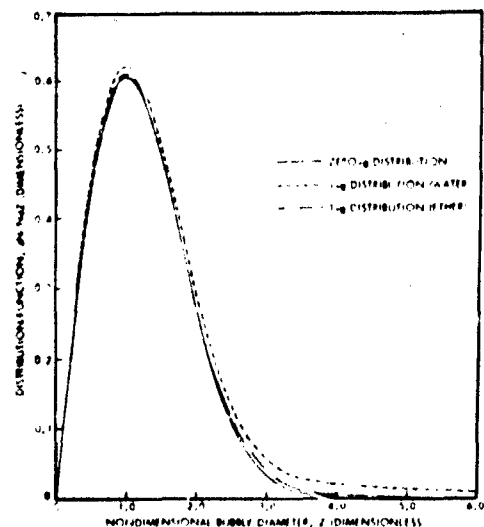


Fig. 9 Dimensionless Distribution Function for Zero- and 1-g Conditions

DISCUSSION

Paul Abramson, Atomics International

I notice in your initial discussion of the derivation that you've assumed conservation of bubbles and conservation of surface energy for bubbles and I wonder if you'd justify that for me?

Welch

I'm not sure I can justify it, but only by imagination, rationalization and the fact that it fits the data. What we imagined was a distribution function which we first broke up into equal increments of energy. This E_j that we see here is the midpoint value in energy between E and $E + \Delta E$, so that our range here in each increment is $E_j - \Delta E/2$ and $E_j + \Delta E/2$. Our number that we used, N_j , is actually the iteration of the function between E and $E + \Delta E$ to give us the total number. We wanted to do this so that we could write this function for the number of independent ways that the distribution could be formed. Actually what we are doing is taking our imaginary continuous distribution function, breaking it up into increments and using this to derive the equation for omega. We had a problem handling this in the same manner that the Boltzman distribution is handled because we have to take N as constant and surface energy as constant whereas actually N and time progress. Both N and the surface energy vary so we imagine a condition where the total number decreased as time progressed and we said we're going to try to step through in order to get a time dependent function that we can handle. We'll try to step through increments in time and we'll try to approximate each increment in time with an equilibrium condition. Assuming we can do this and assuming we can evaluate the constant for these increments of time, for each increment of time we will have a constant N and a constant E . Now, that we see in this paper is actually the very first increment of time and that our E then is actually the first energy or the amount of energy that initially goes into reduction of surface.

Abramson

I just might suggest that conservation of mass might be used instead of conservation of number of bubbles.

Welch

Yes, we tried conservation of volume which is close to conservation of mass in this case. The distribution function that resulted from this didn't fit the data too well. What it actually amounted to was the fact that we had our data there and we just kept deriving functions until we came up with one that fit, then we tried to rationalize a justification for that distribution of function.

Marvin Adelberg, Consultant

Is it your conclusion that the bubble size distribution doesn't change in zero-g?

Welch

No, it actually does change. As we increase the g level the distribution distorts. This is shown on the curves of the distribution function vs. the dimensionless Z. These bubbles were generated by agitating the tank.

Adelberg

That resolves the area of difficulty since heat generated bubbles are more in line with the problems I'm referring to. The two mechanisms are considerably different.

H. Merte, University of Michigan

In regard to the last figure you showed, are those water and ether data the plots of the equation which results from having determined the constants from your data?

Welch

Yes. The first five data points for the water and ether runs were used to evaluate λ prime in the idealized distribution and then provide five data points for the water curve used to evaluate the β in the fragmentation distribution. The intercept of the normalized data points was used to determine gamma. We got our constants using the first portion of the ether/air runs and the last portion of the water/air runs. Then we calculated the remainder of both of these curves and the whole range for the methanol case.

George Huson, Bellcomm

How long do you think this fragmentation period for large bubbles is, and is it always going to be short with respect to settling time?

Welch

I think the fragmentation time is almost instantaneous. This was our assumption anyway.

BLANK PAGE

PAPER 6

**THE FLUID MECHANICS OF CONDENSING MERCURY
IN A LOW-GRAVITY ENVIRONMENT**

By R. T. Lancet,* P. Abramson,* R. P. Forslund †

ABSTRACT

Experimental and analytical results are presented for condensing mercury (Hg), which show that vapor and liquid pressures, drag, and momentum, with proper design, are adequate to maintain stable vapor-liquid interfaces during all phases of ground and orbital operation. Transient temperature and pressure distributions are presented for the startup phase of a multiple-tube horizontal radiator condenser during system operation. The indicated behavior of the liquid-vapor interfaces during startup is shown. Confirmation of such behavior is provided by motion pictures of Hg condensing in a single glass tube.

Various forms of possible instability are analyzed and related to their effect on the performance of the Mercury Rankine Program power system. Interface instability as

*Atomics International Division, North American Aviation, Inc., Canoga Park

†Graduate student, MIT, Cambridge, Mass. - formerly with the Atomics International Division, North American Aviation, Inc.

controlled by surface tension, tube size, and gravitational forces is discussed, along with runback and liquid-leg instability due to negative accelerations (body forces opposed to the direction of vapor flow). Inherent instabilities controlled by the relations between the momentum recovery, friction and drag pressure losses, and condensing length are also discussed. In each of these areas of stability, some definite conclusions are presented which, in the writers' opinion, indicate that condensing in a low- or zero-g environment presents no problems that cannot be easily provided for in design.

A brief description is made herein of the Atomic International facility used for studying the phenomenon of condensing Hg. A film which concisely surveys much of the condensing phenomena to which a Rankine power system will be exposed, is part of an oral presentation. The film, of Hg condensation in single glass tubes, shows:

- The influence of tube diameter
- The mannerisms of noncondensable entrainment
- The effect of positive and negative accelerations applied to the interface in a one-g environment
- Transient accelerations
- Startup, and Hg vapor luminescence

The discussion includes an interpretation of the film and the extrapolation of the data therein to a zero-g environment.

Three analytical models for describing the pressure drop associated with two-phase flow of Hg are developed and discussed, indicating their limitations and the preferred model. Two recent modifications to these models are described. The first, a method of treating momentum loss by basic transport theory, results in momentum loss factors (ratio of momentum loss to mean stream momentum) of 10 percent and eliminates a variable often used to empirically correlate the data. The second describes the mechanism by which condensation influences the velocity profile, and the resultant change in friction factor. The treatment is based upon that used for development of equations of flow in pipes with porous walls.

NOMENCLATURE

A	tube cross sectional flow area
C_f	friction coefficient
D	tube hydraulic diameter
D_c	core diameter
E	total energy
f	friction factor
K	entrance acceleration and loss coefficient
L	condensing length
L_o	reference condensing length
l	$x_2 - x_1$
n	number of g's
P_{LM}	regulated liquid manifold pressure
P	pressure
P_o	inlet total pressure
Q	volume flow rate
r_o	distance from center of rotation to liquid manifold
r_1	distance from center of rotation to interface
r	radial location in tube
R	tube flow area radius
R	pipe radius
Re_o	condensing Reynolds number
Re_o	axial Reynolds number based on diameter
T	temperature
U	average axial velocity
U'	axial velocity of <u>condensing</u> particles hitting the wall
\bar{U}	mean U
\bar{U}'	vector fluctuation
U_o	inlet axial velocity
U'_o	inlet velocity to perturbed tube
U_{max_o}	maximum inlet axial velocity

U_{λ}	axial velocity at $r = \lambda$
U_L	liquid velocity
U_V	vapor velocity
v	radial velocity
v^*	wall shear velocity
W	weight flow of vapor
W_t	total flow through tube (liquid plus vapor)
W_l	weight flow of liquid
x	axial distance
X	the runback distance measured from the inlet
y	momentum loss factor = V'/U
λ	mean free path
η	dimensionless radius squared = $(r/R)^2$
η^*	wall shear Reynolds number
μ	viscosity of host fluid
ν	kinematic viscosity of host fluid
ρ	density
τ	shear stress
ϕ^2	ratio of two phase pressure gradient to single phase vapor pressure gradient
ψ	vapor quality
δ_{cr}	droplet diameter
$\langle v \rangle$	expected velocity (in./sec)
k	Boltzmann's constant = 1.38×10^{-16} erg/°K
m	mass of one molecule of Hg = 3.33×10^{-22} grams

ACRONYMS

MRP	Mercury Rankine Program
RC	Radiation Condenser

THE FLUID MECHANICS OF CONDENSING MERCURY IN A LOW-GRAVITY ENVIRONMENT

1 INTRODUCTION

In any Rankine power system, the vapor must be condensed. The question is whether the condenser can be designed to operate in a stable fashion in a low-or zero-g environment. It is necessary to rely on the liquid and vapor momentum and drag forces to maintain stable operation, because the stabilizing effect of the earth's gravitational field is no longer available. In some applications, accelerations are encountered which result in forces opposing condensation.

The most stable condensing configuration is a single tube; this, however, involves a severe weight penalty for electrical power systems in the kilowatt range, and multiple parallel-tube condensing must be considered. For large radiation condensers, tapered tubes offer significant advantages in terms of reduced Hg startup inventory, and greater stability due to higher average vapor velocities. The present radiation condenser proposed for the Mercury Rankine Program has 40 parallel tapered condensing tubes. Both round and rectangular tubes are being considered; the final selection will be based on fabrication capability.

The investigation of mercury condensing behavior is being carried out in four areas simultaneously: (1) stability, (2) startup phenomenon, (3) gas entrainment, and (4) pressure-drop evaluation. A discussion follows of the work that has been done and is still being done in these areas.

2 DISCUSSION OF STABILITY

Some of the major influences on stable operations of a mercury radiator condenser (RC) are examined in some detail herein. In particular, interface, zero-g liquid leg, force field liquid leg, and runback instabilities are discussed.

2.1 Interface Instability

This particular type of instability is an interface stability phenomenon, and is discussed thoroughly in Ref. 1; application to condensing Hg is discussed in Refs. 2 and 3. Accelerations applied at any particular frequency to the liquid-vapor interface will cause a change of shape in any small irregularities already existing in that interface. In general, the interface is stable if the resultant body forces are applied from the lighter to the denser fluid and unstable if vice versa. Neglecting surface tension effects, Taylor (Ref. 4) found that the initial growth of the amplitude of the disturbance was exponential in time. Surface tension was found by Bellman and Pennington (Ref. 5) to cause a surface wave length dependence, where wave lengths shorter than a critical value were stable and longer wave lengths were unstable. This critical wave length is given by

$$\lambda_{CR} = 2\pi \left[\frac{\sigma}{\frac{g}{g_c} (\rho_L - \rho_V)} \right]^{1/2} \quad (1)$$

Equation 1 is interpreted to mean that the interface is stable if the tube diameter is less than half the critical wave length, and unstable if it is larger than $\lambda_{CR}/2$. In Ref. 6, the Taylor wave criterion was applied to round Hg condenser tubes in a one-g field with Hg as the fluid at 600° F. The experimental range of critical diameters, dependent upon surface finish and adhesion between Hg and the tube, was from 0.125 to 0.168 in. The analytical prediction of the modified equations gives $\lambda_{CR}/2 \approx 0.136$ in., for Hg at room temperature. Reference 6 discusses a modification to the theory (generated above) which is attributed to contact angle, interface curvature, and adhesive properties between the liquid-vapor interface and the tube wall. The modification is manifest in the form of a region of meta-stability which extends up to tube diameters as large as $3.8317 \sqrt{\sigma / [(g/g_c) (\rho_L - \rho_V)]}$ (which one observes to be slightly larger than

the value predicted above) and down to tube diameters as low as $1.835 \sqrt{\sigma / (g/g_c)(\rho_L - \rho_V)}$ (which is significantly lower than the value predicted above). This lower diametral limit is chosen for design purposes because it is the most conservative.

It was found that in applying Taylor's criterion to rectangular tubes (Ref. 7), the critical dimension is along the gravitational force vector. With the tube in a horizontal position, the horizontal dimension could be above critical but the vertical dimension governed the stability of the interface. On the other hand, if the interface is horizontal, both dimensions must be below the critical size to maintain a stable interface.

Reference 7 found the critical dimension to be 0.18 in. for room temperature Hg in the glass ducts.

In all the Mercury Rankine Program (MRP) applications considered to date, the interface in the condensing tubes is stable either because the acceleration level is so low (~ 0.05 g's) that the tube diameter is below the critical diameter, or because the direction of acceleration is from the vapor to the liquid, therefore inherently stable. For example, if the local acceleration is 0.05 g's, the critical diameter would be about 4.5 times the value on earth. From the previous consideration, the critical value would be from 0.56 to 0.75 in. The increase in critical diameter was verified in Ref. 2, where tubes of 0.625 in. diameter and 0.5 in. diameter, filled with water and Hg respectively, were found to have stable interfaces in a near zero-g environment. Since typical 10-ft-long MRP tube sizes run from 0.25 to 0.35 in. at the vapor inlet, to 0.125 to 0.20 in. at the liquid outlet, the tubes are well below the critical diameter.

2.2 Zero-G Liquid-Leg Instability

In a zero-g environment, a perturbation in condensing length of one tube in a multi-tube condenser may result in an instability (liquid leg entering the vapor manifold). This will occur whenever the pressure on the vapor side of the interface decreases, when the condensing length decreases while the pressure in the liquid leg is held constant either by a pressure regulator (as in the MRP), or by the fact that the remainder of the tubes have not significantly changed their operating condition. The conditions under which this kind of instability occurs can best be explained by examining in detail the

factors which influence the shape of the curve of the interface pressure as a function of the condensing length.

To simplify the pressure-drop equation for the purpose of examining the factors influencing condensing stability at zero-g, incompressible flow is assumed. To account for the fact that condensation occurs and the stream velocity varies along the condensing tube, it is assumed that:

- 1) Area = constant, not varying with distance
- 2) $U(x) = U_o^1 (1 - x/L_o)$
- 3) $U_o^1 = U_o(L/L_o)$

This presents a very special case of condensation, one with a linear quality profile. However, experience with radiator designs to date indicates that the quality does not deviate by more than two or three percent from the linear profile. Furthermore, this assumption will not significantly affect the result and does simplify it. While this represents a very special case, the major conclusion can be shown to be essentially independent of these particular assumptions.

Based on these assumptions the resulting pressure drop equation is

$$P = P_o + [2 - y - K] \frac{\rho U_o^2 L^2}{2g_c L_o^2} - \frac{4\rho U_o^2 L^2}{2g_c D L_o^2} \int_0^1 \phi^2 f_L \left(1 - \frac{x}{L}\right)^2 d\left(\frac{x}{L}\right) \quad (2)$$

which gives for the interface pressure, assuming an average $\phi^2(\bar{\phi}^2)$ and an average $f(\bar{f})$,

$$P_i = P_o + \left[(2 - y - K) \frac{L^2}{L_o^2} - \frac{4L^3 \bar{\phi}^2 \bar{f}}{3D L_o^2} \right] \frac{\rho U_o^2}{2g_c} \quad (3)$$

Equation 3 shows that the condenser will be completely stable as long as $(2 - \gamma - K) < 0$, or if the condensing length is greater than the critical condensing length when $(2 - \gamma - K) > 0$. By differentiating Eq. 3 and setting it equal to zero, the critical length is found to be

$$L_{CR} = \frac{(2 - \gamma - K) D}{2\phi^2 \bar{f}} \quad (4)$$

Figure 1 is a plot of Eq. 3, showing the interface pressure on the vapor side vs condensing length for equilibrium conditions at each condensing length.

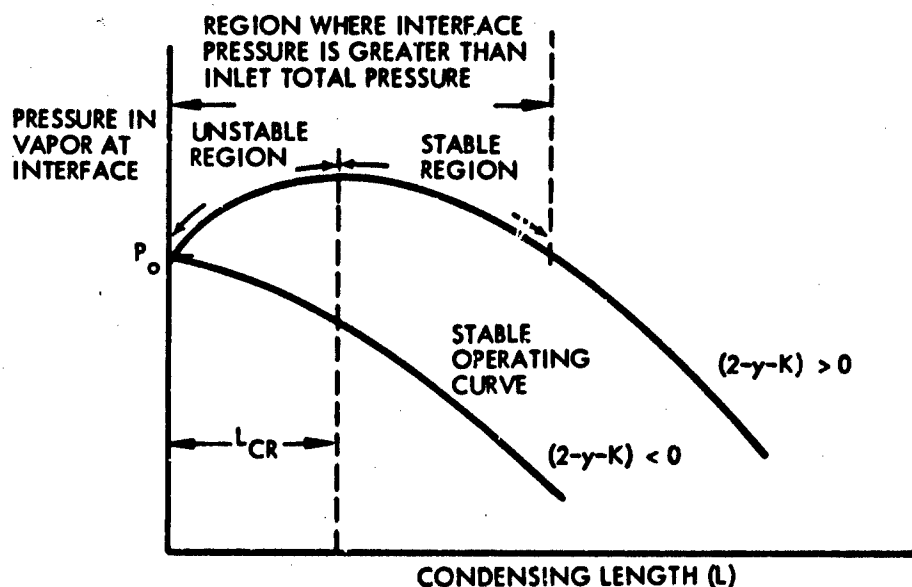


Fig. 1 Typical Zero-g Instability Pressure Variations

From Fig. 1, the criterion for stability in zero-g when one tube out of many is perturbed is

$$\frac{dP_i}{dL} < 0 \quad (5)$$

Figure 1 shows that it is possible, for small momentum losses during condensing, to have an interface static pressure which is greater than the incoming total pressure, hence the interface might move toward the inlet. To match the pressure drop data of Ref. 2, it was empirically determined that the condensate must give up an average of 28.5 percent ($y = 0.57$) of the mean stream momentum flux. For an acceleration and entrance loss factor (K) of 1.5, this would require the static interface pressure to be less than the inlet total pressure by seven percent of the inlet dynamic head. However, more refined analytical models (see para. 4.7) predict that this factor y is much closer to 10 percent, permitting the interface pressure to be greater than the inlet total pressure.

If the latter case turns out to be true, as is expected, it will be necessary to maintain the condensing length greater than that given by Eq. 4. For the MRP reference design, for $y = 0.1$, Eq. 4 gives

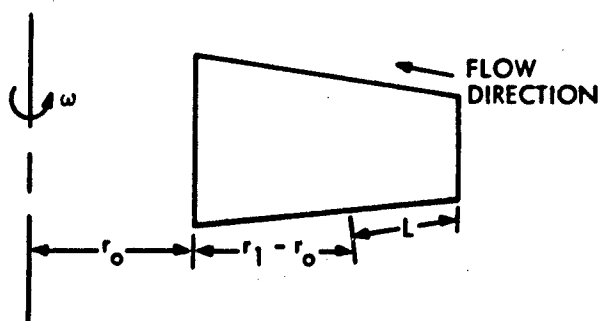
$$L \approx \left(\frac{2 - 0.1 - 1.5}{0.02} \right) D = 20D \quad (6)$$

During steady-state operation the MRP condensing length is about 110 in. During startup, however, the condensing length decreases until the RC is heated and the condensing pressure reaches the steady-state condition. The minimum condensing length during startup of MRP condensers is about 20 in., or an $L/D \approx 65$, and no zero-g condensing instabilities are expected. This has been verified by flat horizontal RC's, and is true even when allowing for the errors resulting from the simplifications introduced during the derivations of Eq. 4.

2.3 Force Field Liquid-Leg Instability

In the presence of negative accelerations opposed to the condensing direction, liquid-leg instability may result if vapor pressure forces are not adequate. These instabilities, if allowed, will result in spilling liquid into the vapor manifold and/or vapor into the liquid manifold for the single perturbed tube. The opposite or the same may occur for the other tubes following the instability in the initially perturbed tube.

Let us consider the case where the RC is rotating about some center, say at a distance r_o from the base of the RC



The pressure on the interface by the liquid is then given by

$$\frac{P}{\rho} = \frac{\omega^2 r_1^2}{2} - \frac{\omega^2 r_o^2}{2} + \frac{P_{LM}}{\rho} \quad (7)$$

where the second term on the right is a constant for a given r_o .

For an investigatory case, $r_o = 41.25$ in. and a tube length of 10 ft, the plots of pressure (P) vs. condensing length (L) were generated for various ω , shown in Fig. 2. These curves show the pressure that would be present in the liquid at the interface as a function of L for a particular ω . To determine the influence of these pressures upon stability, one must examine the perturbation line of a single tube through the operating point (particularly ω and L). The operating point is established considering that the liquid in all tubes rises simultaneously until the vapor pressure equals the liquid pressure. The vapor pressure rises due to the decreased condensing length and the rise in condensing temperature that accompanies the reduction in radiating area. In this case, the flow to each tube is constant and the manifold pressure rises as the condensing length decreases, until the liquid and vapor pressure become equal. Having established the operating point, the single tube perturbation line is calculated, assuming

the manifold pressure is constant and the flow varies with the condensing length in the single perturbed tube.

Examination of Fig. 2 shows that interface perturbations will be stable as long as

$$-\left(\frac{dP}{dL}\right)_{\text{vapor}} > -\left(\frac{dP}{dL}\right)_{\text{liquid}}$$

For a tapered rectangular tube typical of a MRP RC, Ref. 9 shows the curves of vapor side pressure at the interface vs L for two cases. One case considers the rise in vapor side interface pressure due both to the reduction in condensing length and to the rise in condensing temperature. The other case considers only the former and is much more conservative. The true line of operating points probably lies between the two. These curves are superimposed on the liquid-side interface pressure vs condensing length (L) curves in Fig. 2.

The result is that the RC is stable when its operating point occurs at $\omega < 0.917$ rad/sec for the maximum variation in vapor manifold pressure, or at $\omega < 0.4$ rad/sec for no variation in vapor manifold pressure. In both cases the interface remains stable. Larger negative accelerations or vehicle tumbling can be handled without going to excessive RC pressure drops, by performing the final condensing in a single tube which is oriented normal to the acceleration forces as shown in Fig. 3.

In this case it is easy to see that $(dP/dL)_{\text{liquid}} = 0$ and a stable condition exists. It is also apparent that this configuration is stable for acceleration forces parallel to the single tube as long as changes from one direction to the other are not so rapid as to prevent the interface from returning to its stable position shown in Figs. 4 and 5.

While this configuration can be made stable for large negative- g forces, the weight penalty becomes significant due to the increased tube diameter (for the same system pressure drop) and corresponding increase in Hg inventory and meteoroid armor.

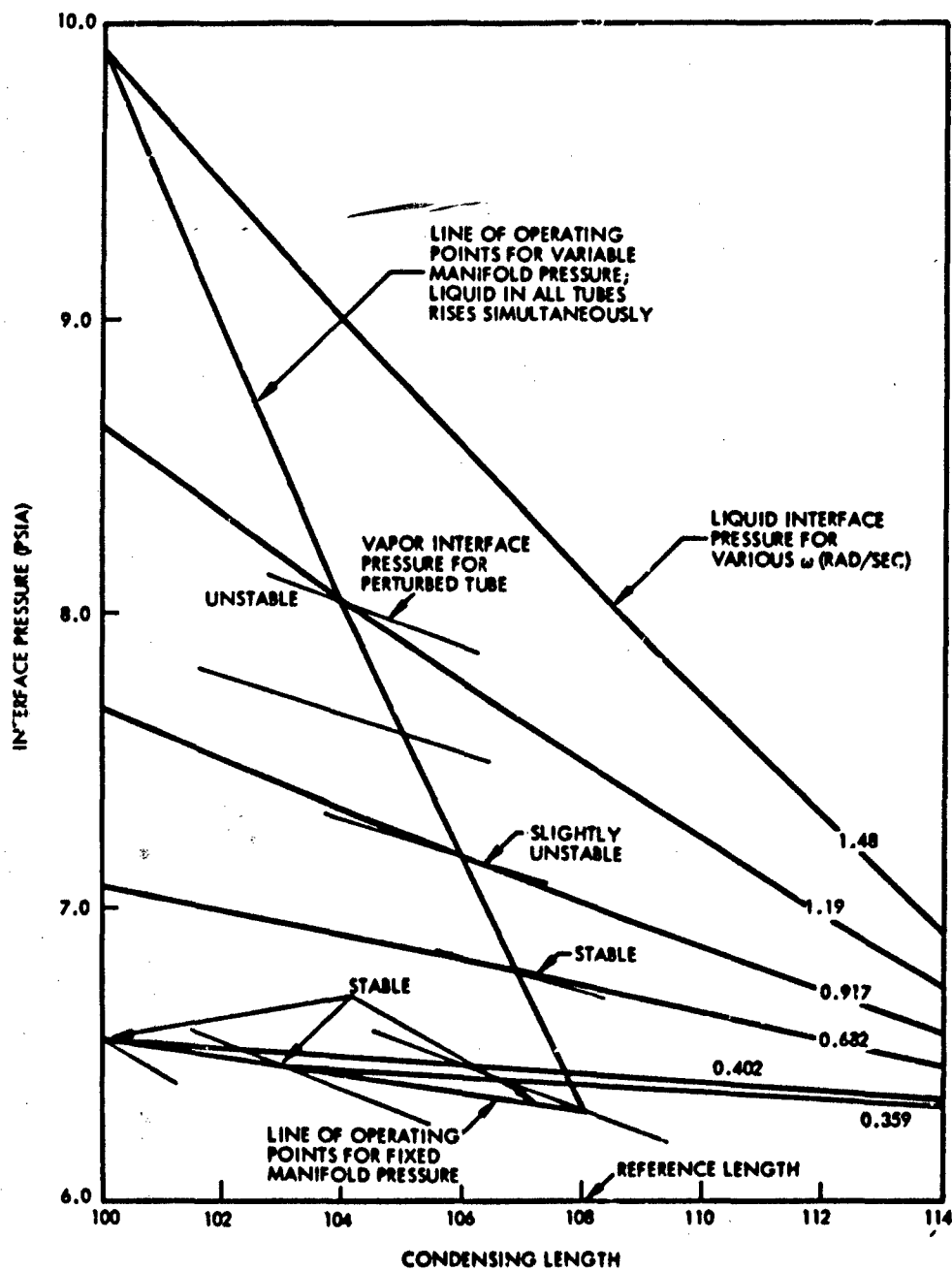


Fig. 2 Negative-g Radiator Condenser Operating Characteristics (from Ref. 9)

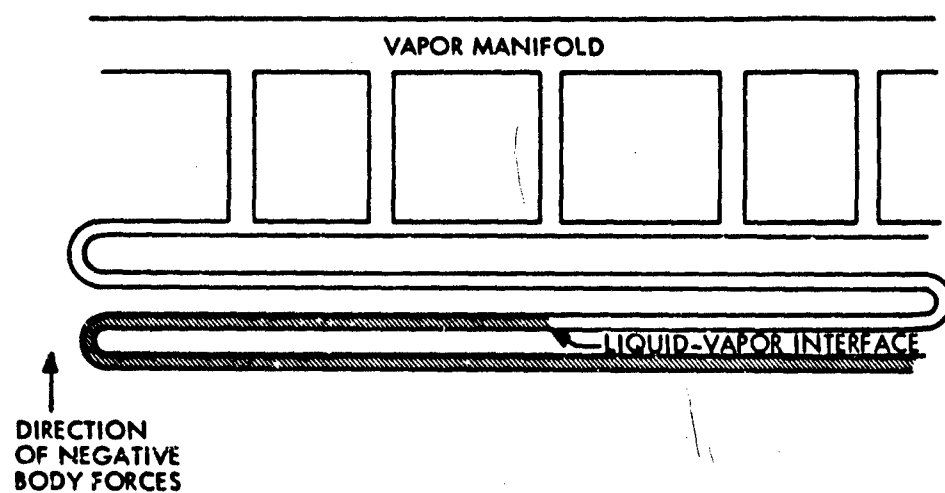


Fig. 3 Single Tube Final Condensation

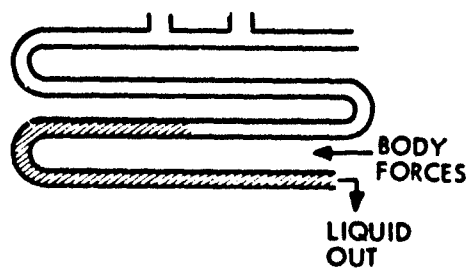


Fig. 4

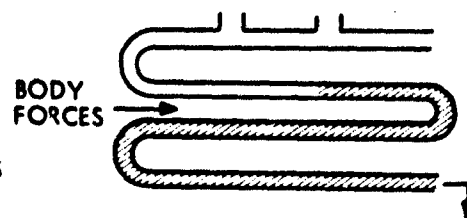


Fig. 5

Another approach to stable condensing in negative-g fields is the use of an indirect condenser which can more readily be favorably oriented and has shorter liquid sub-cooler lengths.

2.4 Runback Instability

The condition termed "runback" occurs when, in a negative-g field, a portion of the condensate in the condensing region flows back against the vapor flow. Severe oscillations occur as the runback liquid blocks the vapor flow path and causes the vapor pressure to rise, thus creating a pressure difference across the runback slug that causes it to be slammed back into the liquid leg. Runback is a phenomenon peculiar to wetting condensation in above- and below-critical-diameter tubes, and to nonwetting condensing flow in above-critical-diameter tubes. As negative accelerations (forces directed from the liquid toward the vapor) are applied to the condenser, the vapor drag forces are not large enough to prevent the interface from deforming and running back into the vapor stream.

Runback under wetting conditions was analyzed by Koestel (Ref. 6). He assumed that runback occurred at the point where the wall shear went to zero. He found that the distance to the point of runback could be represented by the relation

$$\frac{\left(\frac{x}{L}\right)^{1/3}}{1 - \frac{x}{L}} = \frac{204.5 \rho_V \bar{U}_0^2 \left(1 + \frac{2d \text{Re}_0}{64 L}\right)^{2/3}}{\rho_L^{1/3} \mu_V^{2/3} n^{2/3} \text{Re}_0^{4/3}} \quad (8)$$

From the experimental data, Koestel estimated that $L_b \approx 0.8 L_c$ would minimize the effects of runback slugging in tubes of diameters ≤ 0.5 in. This reduces Eq. 8 to

$$U_0 = 308 \left(\rho_L \rho_V\right)^{1/2} \frac{d^2 n}{\mu_V} \quad (9)$$

where U_0 is the required inlet vapor velocity to maintain a stable flow condition.

In the case of the MRP, if wetting of the condenser tubes occurs, the above criterion predicts stable operation (small pressure fluctuations) for negative acceleration up to

0.078 g's. It is apparent that an RC for space applications can be designed to avoid the instabilities considered here, and with a minimum weight penalty.

3 EXPERIMENTAL WORK

Considerable experimental work has been performed at AI with horizontal and vertical RC's and in single-tube condensing. Some of the most pertinent results will be discussed in the following sections.

3.1 Transient Horizontal Hg RC Startup Behavior

To simulate zero-g system operation, a system was assembled using a flat horizontal RC at the same elevation as the centerline of the combined turbine-alternator-pump unit. The radiator, which had 44 tapered tubes, approximately 0.3-in. inlet diameter, and 10 ft long, was capable of rejecting about 50 kw of thermal power, at a 600° F condensing temperature, to the water-cooled vacuum chamber. This system was operated for 1,200 hours, including complete system startups, with no indications of any instabilities. Of particular interest is the startup behavior, which is best explained by reference to Figs. 6 and 7 which show how the condensed Hg collects in a slug and simultaneously grows and moves down the tube. The pressure in the region downstream from the liquid slug should be equal to the vapor pressure, or approximately 10^{-4} psia. When the liquid slug reaches the condensing tube exit, the interface moves upstream as the temperature and pressure (Fig. 9) continue to rise. Finally the pressure rises high enough (actually it slightly overshoots the steady-state value) and draining of the RC commences. Draining continues until the steady-state operating conditions are reached. Figure 7 is based on observations of startup in single pyrex tubes and the experimental temperature and pressure measurements (see Figs. 8 and 9) taken on the 44-parallel-tube horizontal RC. The horizontal RC operated in a stable fashion; the transient startup behavior is adequate and can be predicted.

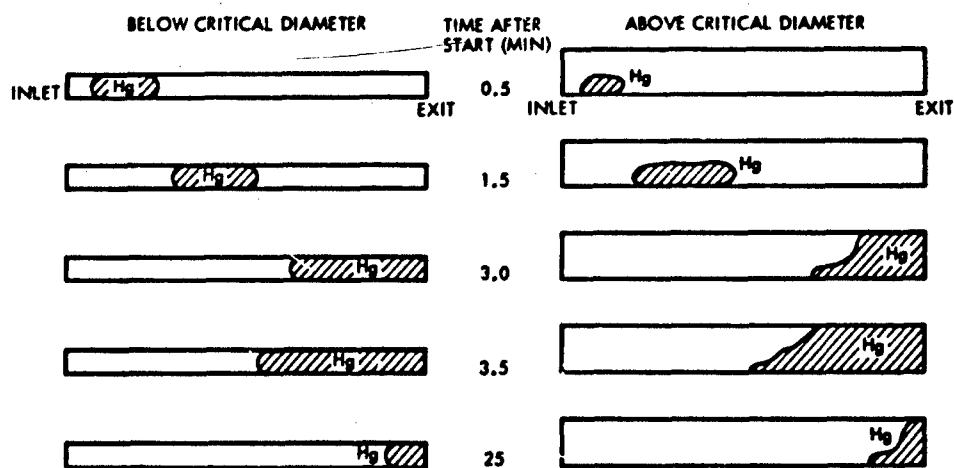


Fig. 6

Fig. 7

Horizontal Mercury Condensing Startup in Below- and Above-Critical-Diameter Tubes

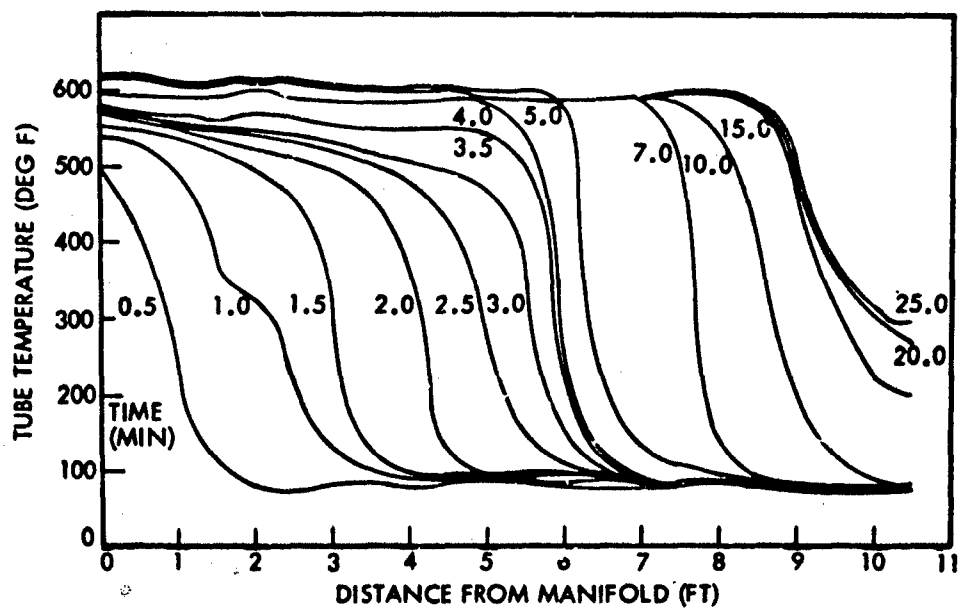


Fig. 8 Startup Transient Temperature Variations for Horizontal Mercury Condensers

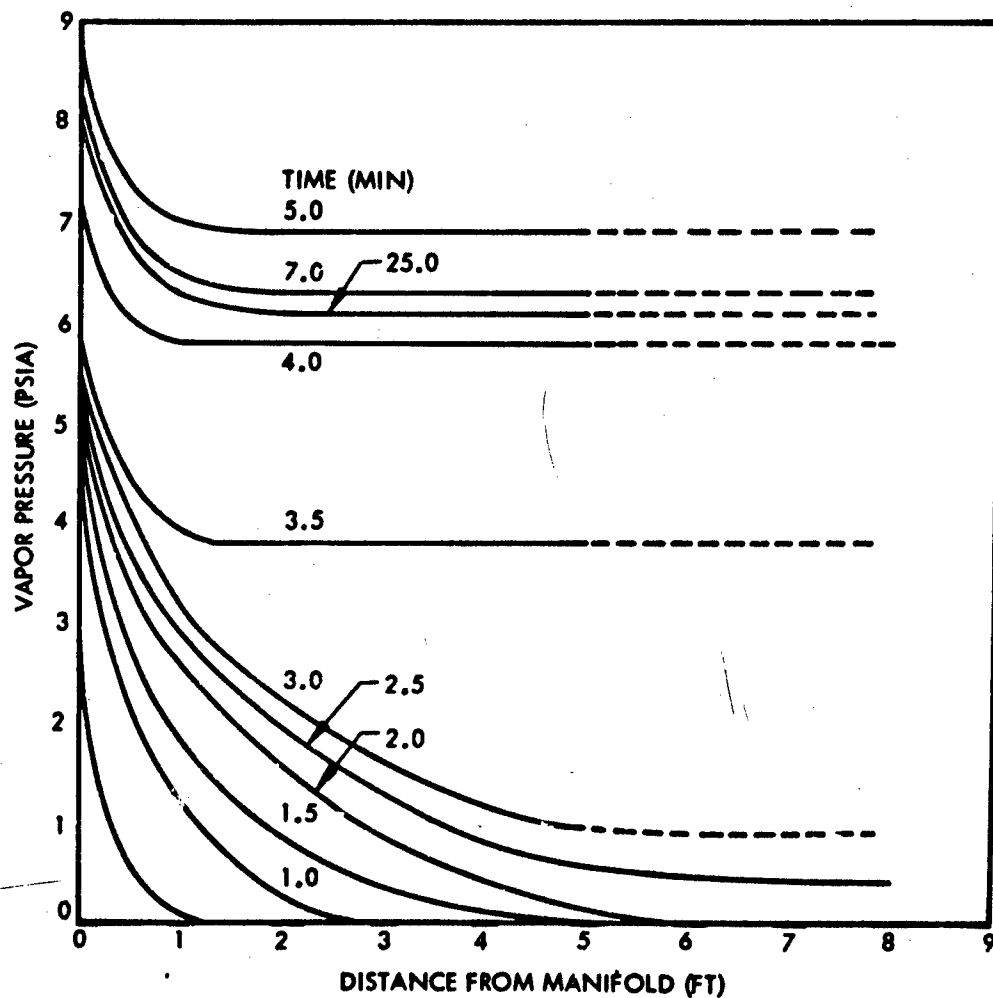


Fig. 9 Startup Transient Pressure Variations for Horizontal Mercury Condensers

3.2 Description of Hg Condensing Photograph Study

This work was carried out in the test installation shown in Fig. 10 and described in Ref. 10. Normal and high speed photographic studies were made to provide qualitative

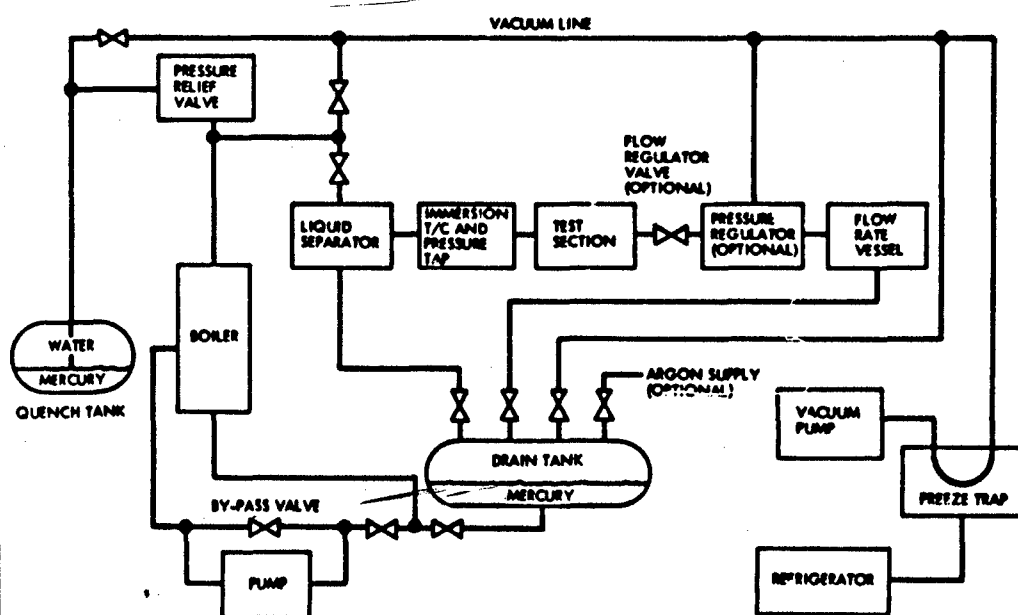


Fig. 10 Schematic of Mercury Loop

data concerning interface and liquid-leg stability, and to determine the influence of noncondensable gases upon the nonwetted condensing process of Hg. These studies surveyed the condensing phenomena in 0.125-in. ID (below-critical diameter) and 0.3-in. ID (above-critical diameter) pyrex condensing tubes. The tubes were operated in angles of inclination of from -5° to $+10^\circ$ from the horizontal. The operating conditions were set for inlet pressures from 8 to 12 psia at roughly 700°F , with flow rates at 0.3 to 0.4 lbm/min in the large tube and 0.1 lbm/min in the small tube. These flows are slightly below the 0.5 lbm/min per tube in the MRP. At constant flow and

condensing length, the inlet pressure was varied with angle of inclination. Several condensing lengths were also examined at each inclination. The loss of hydrogen from the fuel elements to the NaK system results in a net transfer to the Hg system where it collects in the RC. Therefore, noncondensable gases were introduced at a large flow rate (compared to that expected in the MRP) to examine interface effects.

3.2.1 Stability

It was observed that the critical (capillary) diameter as predicted for Hg does indeed have the main stabilizing influence upon surface stability at the liquid-vapor interface. The films indicated that the 0.125-in. diameter tube held a stable interface under all orientations tested; that even when large disturbances were created upon that interface by incoming droplets, the disturbances were rapidly damped.

Studies of the liquid-vapor interface in the above-critical-diameter tube also showed the expected phenomena. In a horizontal or "downhill" condensing position, there were no forces that could cause a droplet (thrown from the interface by the surface waves) to move upstream. The interface therefore held an overall equilibrium position, although the interfacial tension was not sufficient to immediately damp all perturbations. However, in an "uphill" condensing orientation, droplets which separated from the interface were moved upstream by gravitational forces. Since the droplet was then moving against a flux of condensing vapor, its motion was eventually reversed and it was given a large momentum toward the interface.

Large amounts of liquid were released in the phenomenon being described. There appeared to be no actual separation of the interface into droplets, but the interface became elongated. This could be due to the time limitations, since it is known that the equilibrium configuration is a group of spherical droplets, but it is also known that the time to reach equilibrium is quite large. The upstream end of the interface, which had been exposed to the nonequilibrium conditions for the longest time, did actually form a group of spherical droplets. Some of these droplets moved in an oscillating pattern along the tube axis, moving upstream under gravity until the vapor momentum flux reversed the motion, then moving toward the interface until gravitational

forces reversed that motion. This phenomenon is peculiar to non-wetted runback. Somewhat downstream of these oscillating droplets, a continuous but quite elongated interface exists. This interface distorts as liquid runs into its upstream end. As the upstream end grows in size (and mass) it moves farther upstream and encounters more vapor flux. The shear and momentum forces of the vapor deform this interface until it bridges the tube, at which time it receives a large impulse from the vapor, driving the entire liquid runback downstream into the stationary liquid leg. When the runback is slammed into the liquid leg, a large pressure pulse is transmitted into the liquid. Pulses as great in magnitude as ± 2.5 psia were observed. (The minus readings may be due to instrumentation oscillations rather than actual pressure fluctuations.)

It is pertinent to point out at this point that no runback would be possible in a zero-g environment. This is due to the Taylor wavelength criterion which gives $\lambda_{cr} = \sqrt{\sigma / [(g/g_c)(\rho_L - \rho_V)]}$; i.e., for zero-g the critical wavelength becomes infinite. This also gives a criterion for determining maximum allowable g levels. The phenomena presented in this discussion are visualized in the accompanying motion picture.

3.2.2 Noncondensibles

Part of the photographic study was concentrated on determining the influence of non-condensable gases upon condensation phenomena. In the reactor power system of the MRP, hydrogen is used as the moderator component in the reactor fuel elements. This hydrogen diffuses out into the primary loop fluid (NaK) and is carried along with it, constantly diffusing out of the NaK piping walls. Hydrogen is thereby introduced into the Hg system in the boiler and carried around the Hg loop until it reaches the condenser. The influence of noncondensable gases on the condensing processes was examined in both the above- and below-critical-diameter tubes. It was found that bubbles are entrained in the liquid leg in all cases except downhill condensing in above-critical-diameter tubes.

Above-Critical-Diameter Tubes. In the greater-than-critical-diameter tube, the influence and mechanism of entrainment of noncondensibles was greatly influenced by the orientation of the tube with respect to gravity.

1) Horizontal Condensing: In a horizontal position, noncondensibles build up vertically ~~above~~ the liquid vapor interface and cause the interface to elongate; interfaces were observed as long as 20 in. in a 0.3-in. tube. As the interface elongates, the influence of condensate droplets (which formed upstream and ran into the leading edge of the interface) becomes more marked. These droplets set up traveling waves of relatively constant amplitude in the nearly horizontal interface surface. As the wave travels downstream along the interface, it reaches a position where the amplitude of motion is greater than the gap between the liquid and the top of the tube (which is filled with gas). At any axial location from this position downstream to the end of the noncondensibles, the surface wave has sufficient amplitude to bridge the tube and trap a bubble of noncondensibles. However, the noncondensibles would be held in the liquid leg only by the small adhesion force of Hg to glass. This type of entrainment is therefore unstable. Only when a sufficient amount of liquid builds up in the bridging process, thus providing a new end for the interface, can the bubble be physically entrained. However, if a following surface wave of sufficient energy and proper phase angle arrives at the position of bridging before a great deal of liquid has built up in the bridge, this wave could tear loose the bond and return the interface to its original configuration, with the result that no entrainment takes place. Once a bubble is entrained in this manner it moves haltingly toward the tube exit, sometimes stopping as liquid flows underneath it until shear forces at the Hg-gas-tube interfaces are sufficient to tear the Hg loose and move the bubble.

This describes the mechanism by which small bubbles of noncondensable gases can be entrained into the liquid leg of a condenser. The only other way that noncondensibles will pass the liquid-vapor interface in an above-critical-diameter tube is by very small bubble entrainment when droplets smash into the interface.

2) Downhill Condensing: In a downhill condensing orientation in an above-critical-diameter tube, the liquid-vapor interface assumes a horizontal configuration. Droplets which form upstream are observed to run through the noncondensable layer and into the interface. Little viscous drag occurs on the droplets in the noncondensable layer. The only apparent mechanism of entrainment is the formation of small bubbles when droplets hit the interface.

3) Uphill Condensing: In an uphill condensing orientation in above-critical-diameter tubes, the runback phenomenon generates such violent interface motion that noncondensibles cannot build up to large amounts but become continuously entrained by the interface and rise under buoyant forces toward the tube exit. The entrained bubbles are small and frequent. Due to violent surface motion, there may also be some very small bubbles entrained which are similar to the bubbles entrained by droplets impinging on the interface in other orientations.

Below-Critical-Diameter Tubes. At this stage in the discussion of the influence of noncondensibles upon condensation, it is important to point out that in a zero-g environment, the critical wavelength is infinite. The previous discussion applies only to condensation in an environment containing large mass attraction fields; the following discussion is pertinent to the zero-g environment.

Noncondensable entrainment in a below-critical-diameter tube appeared to be independent of orientation in the gravitational field to the extent of the tests performed, which varied between -6° and $+10^\circ$ from the horizontal position. The liquid-vapor interface is held in a stable position by surface tension effects. Noncondensibles accumulate in the vapor region immediately upstream of the interface, and in this region little or no lig condensation occurs. When the slug of noncondensibles becomes appreciable (the actual amount was not measured in these experiments, but it is estimated to be of the order of 10 tube diameters) the droplets condensing upstream are slowed by viscous damping in the gas. These droplets agglomerate rapidly to form large drops in the noncondensable region. Eventually the formation of these large droplets is so rapid that they bridge the tube before arrival at the interface. A slug of noncondensibles is then entrained ahead of the large drop. At inlet pressures of 10 to 12 psia and liquid flows of 0.1 lbm/min, the typical slug lengths observed were 1 to 2 tube diameters. The noncondensibles accumulate upstream from this new interface and the process is repeated with regularity. Never was the entire noncondensable region entrained at once; approximately the same small quantity was entrained regularly, providing flow conditions were not varied. The influence of the pertinent flow parameters (Hg and noncondensable flow, pressure, and condensing length) are presently being investigated but are not discussed here.

The principal result is that noncondensibles will be entrained into the liquid leg in large bubbles in the condenser in zero- and low-g fields regardless of tube diameter. It is therefore expected that the MRP condenser will behave in this manner.

3.2.3 Hg Vapor Luminescence During Startup

At low pressure (approximately 1 psia) Hg vapor luminescence in the $6^3P - 7^3S$ (4358 Å) blue, and $6^3P_2 - 7^3S$ (5460 Å) green spectra was observed. The literature revealed no information concerning the origin of the stimulating energy but did mention that the presence of nitrogen in electron-excited transitions of Hg in the 6^3P_1 state transfers them to the metastable 6^3P_0 state, and the transition back to ground is made stronger by as much as an order of magnitude for the violet (4047 Å) luminescence. This line was not the strongest observed; however, the possibility of some nitrogen being present is not ruled out.

A strong electrostatic field was observed on the outside of the pyrex condensing tube when the luminescence was present but not when the luminescence was absent. By wrapping a coil of bare silver wire clockwise for about 5 in. of tube and counterclockwise for 5 in. more and letting one end arc to ground, an electrostatic potential of ~22 kv was determined to exist on the tube. By grounding the wire and measuring the current, a constant current of 2 μamps was drawn while the light was centered in the tube. Whether the wire was grounded or not, the light seemed to follow the wire. This is not unexpected if the vapor flow is a plasma and the coil acts as a boundary condition.

To determine if the light was accompanied by or actually created by the charge, the tube was wrapped in aluminum foil and grounded. This left a possible potential on the inside of the tube of only 10 volts, which should be negligible compared to 22 kv. The luminescence persisted. It was also observed, but unfortunately not yet captured on film, that at the downstream end of the luminescent pattern, droplets of Hg liquid appear to spew out of the light.

Several possibilities are proposed as sources for the exciting energy of the observed transitions. The most plausible at present is that instead of condensing, some portion

of the energy required to force the vapor into the liquid state (heat of condensation) is going into exciting electrons in the Hg atoms. When these electrons no longer see the exciting energy and have made their last transition to ground state, then the vapor condenses. This would explain the droplets spewing out of the luminescent pattern on the downstream side. The heat of condensation is ~ 127 Btu/lbm or 9.31×10^{-23} Btu/at m, whereas the energy required to excite (in a single step) the transition is 43.3×10^{-23} Btu. The energies are the right order of magnitude and a cluster of sufficient size could supply the proper excitation.

3.2.4 Summary of Experimental Work for Single-Tube Condensing Tests

- The influence of Taylor's criterion governed interface stability
- Non-wetted runback in above-critical-diameter tubes appeared similar to the wetted runback discussed by previous investigators
- Noncondensable slugs will be picked up by a condenser in a zero-g environment, in a negative-g environment for both above- and below-critical-diameter tubes, and in a low positive-g environment when the diameter is below the critical value
- Hydrodynamic performance during startup is predictable, but the origin of Hg vapor luminescence observed during startup remains undetermined

3.2.5 Summary of Future Experimental Work Planned

- Pressure drop and stability studies with tapered tubes
- Verification of zero-g liquid-leg stability analysis
- Detailed noncondensable entrainment tests
- Wetting vs non-wetting stability and pressure drop study

4 PRESSURE DROP MODELS

Accuracy of the pressure drop prediction influences the RC area and weight, since one of the tolerances which must be allowed for is the uncertainty in the condensing pressure. In addition, the pressure drop analysis is used in all the stability evaluations, and errors in the pressure drop analysis will be reflected in errors in the predicted margin for stable operations. A small but continuing effort has therefore been extended toward improving the pressure drop analysis.

Three condensing pressure drop models are discussed following. The first two use the improved Lockhart-Martinelli correlation of Baroczy (Ref. 11); the third uses the fog-flow correlation of Koestel (Ref. 12). Model No. 1 has been used with moderate success to predict the total pressure drop for design purposes. Experimental data has shown that it does not very well predict the pressure profile along the tube; however, the profile is not as important for design purposes as the total pressure drop. Model No. 2 is a fog-flow model that uses the Baroczy correlation and closely predicts the same pressure drop as Model No. 1, but the pressure profile matches the data much better. The recently introduced Fog-Flow Model of Koestel has not as yet been used by AI to predict pressure drop. This model shows some merit, mainly due to its simplicity, and is being considered in this program. The following discussion is a brief outline of the work presented in Ref. 10.

4.1 Improved Lockhart-Martinelli Correlation of Baroczy and Sanders

To date, the most accepted method for predicting pressure drop in isothermal two-phase flow in horizontal pipes is based on the Martinelli method (Refs. 13 and 14). This method relates the two-phase pressure drop to the pressure drop that would occur if the vapor phase were flowing alone by

$$\Delta P_{T.P.} = \phi^2 \Delta P_{\text{host fluid}} \quad (10)$$

The coefficient ϕ^2 is correlated to the Martinelli parameter X^2 which is the ratio of the pressure drop of the liquid flowing alone to the pressure drop of the vapor flowing alone.

Since the properties of liquid Hg differ significantly from the fluids used in the discussed correlation, tests were conducted with Hg and nitrogen to certify that the same correlating technique was valid (Ref. 3). The correlation technique was verified; however, it was found to be improved with the introduction of another parameter, the vapor Reynolds number (Ref. 11). The smoothed curves of this correlation are shown in Fig. 11.

4.2 Condensing Pressure Drop Model No. 1 (Refs. 11 and 15)

For Model No. 1 the following assumptions are made (see Fig. 12):

- The control volume includes both the liquid and vapor flow; however, the momentum of the liquid is assumed to be negligible, so that only the vapor is considered in the momentum terms
- The liquid volume fraction is very small so that the vapor flow area is taken to be the cross-sectional area of the tube
- No body forces are present since space operation with no acceleration is assumed
- The velocity of the liquid is assumed to be negligible

With these assumptions in mind, the equation for forces on the control volume is:

$$-AdP - \tau_w dA_w = \frac{1}{g_c} W dU + \frac{1}{g_c} U(1-y) dW \quad (11)$$

which reduces to (see Ref. 10)

$$\frac{dP}{dx} \left[\frac{W_t^2 \psi^2}{A^2 \rho^2 g_c} \frac{d\rho}{dP} - 1 \right] = \frac{\phi^2 \tau_w W_t^2 \psi^2}{2g_c D \rho A^2} + \frac{W_t^2 \psi}{g_c \rho A^2} (2-y) \frac{d\psi}{dx} - \frac{W_t^2 \psi^2}{g_c \rho A^3} \frac{dA}{dx} \quad (12)$$

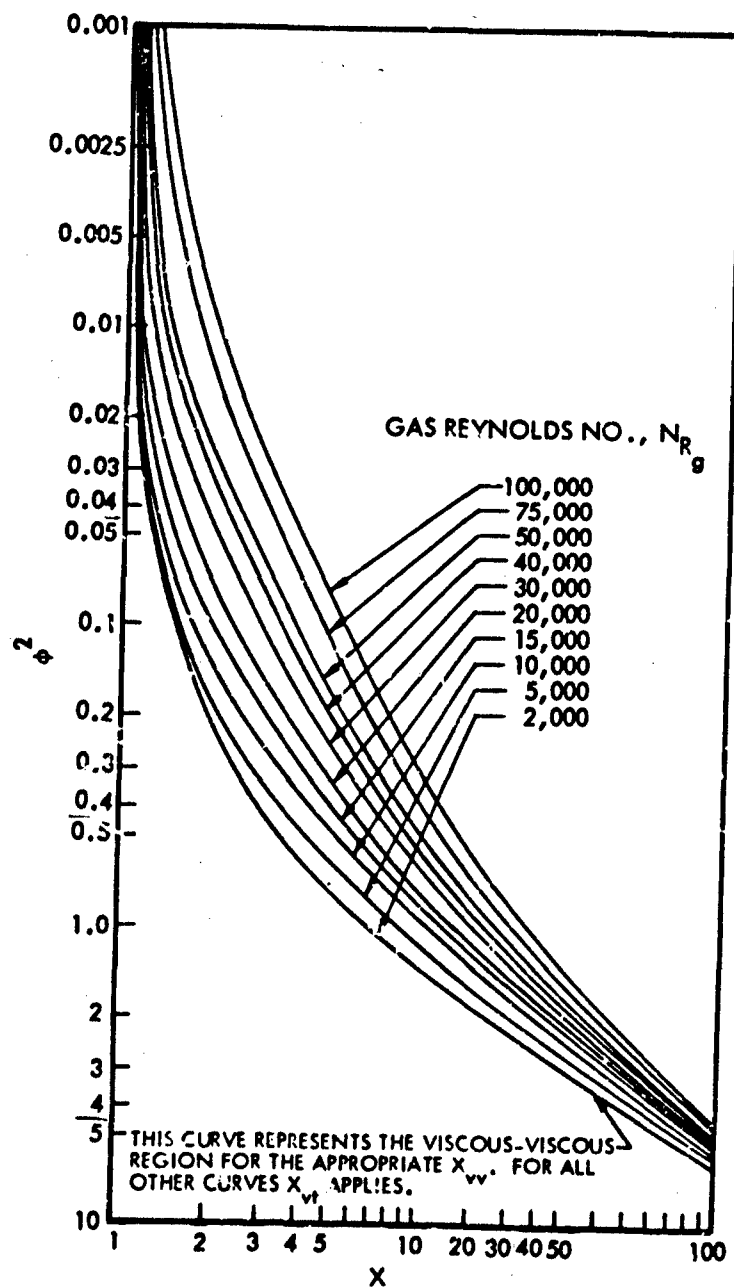


Fig. 11 General Correlation for Two-Phase, Two-Component Pressure Drop

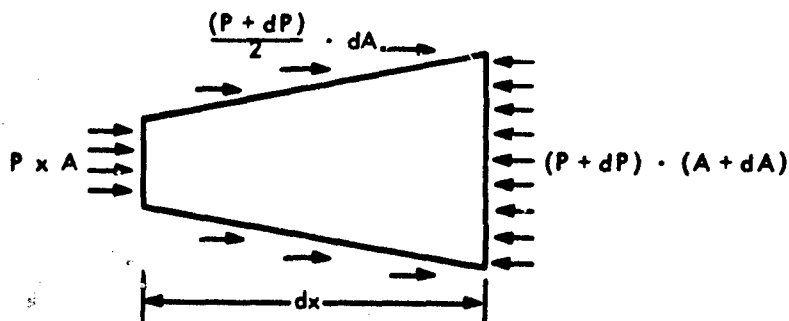


Fig. 12 Assumptions for Model No. 1

With the knowledge of the pressure of the vapor at a particular point, the vapor temperature, density, and variation of density with pressure are known. Also known at the particular point are the quality, quality gradient, area, area gradient, and the equivalent diameter. The fictitious liquid and vapor pressure gradients and the vapor Reynolds number can be calculated for this point so that ϕ^2 can be evaluated. With the foregoing, and an assumed value for y , the pressure gradient can be evaluated. A standard numerical integration of this type permits calculation of the pressure drop in a condenser tube.

In the derivation of the momentum equation for Model No. 1, a momentum term was obtained:

$$-\frac{1}{g_c A} U(1-y) \frac{dW}{dx} \quad (13)$$

This term represents the momentum that can be recovered from the vapor about to be condensed. If the vapor molecule at the main stream velocity (U) leaves the control volume at an axial velocity greater than zero, less momentum becomes available to the remainder of the main stream. Physically, the molecule, with an initial stream velocity (U), loses some of its momentum to the main stream and collides with the condensing surface with a velocity U'_v . If U'_v is equal to U , ($y = 1$), no momentum can be recovered. The momentum recovery which does occur is due to the diffusion of the noncondensing vapor at that point. If U'_v is zero ($y = 0$) all the momentum is recovered. Since a molecule must make its way through the boundary layer to be condensed, it is thought that it has ample opportunity to give up most of its momentum in the boundary layer before colliding with the condensing surface.

Although it is believed that y is close to zero, y until recently was a correction parameter in the pressure drop computer program. The purpose of this y factor was to match the predicted pressure drop with experimental data so that condenser tube design had some experimental basis. A value of y equal to 0.57 was used in the past for design purposes. This value was obtained in the attempt to match some low-pressure (approximately 8 psi inlet) condensing runs of Ref. 8. An average for the four runs was used. The measured and predicted pressure profiles for these runs are shown in Fig. 13. However, it was found that y was not a constant correction factor. Evaluation of y for various other runs at higher pressures indicates a decrease in y with increase in pressure. For further considerations of Model No. 1 see Ref. 10. An analytical derivation leading to $y > 0.1$ is developed in a following section.

4.3 Momentum Equation for Model No. 2

When the momentum of both the liquid and vapor are considered, the pressure drop equation becomes

$$-AdP - \tau_w dA_w = \frac{1}{g_c} \left[W dU_v + W_l dU_l + (U_v + U'_v) dW + (U_l - U'_l) dW_l \right] \quad (14)$$

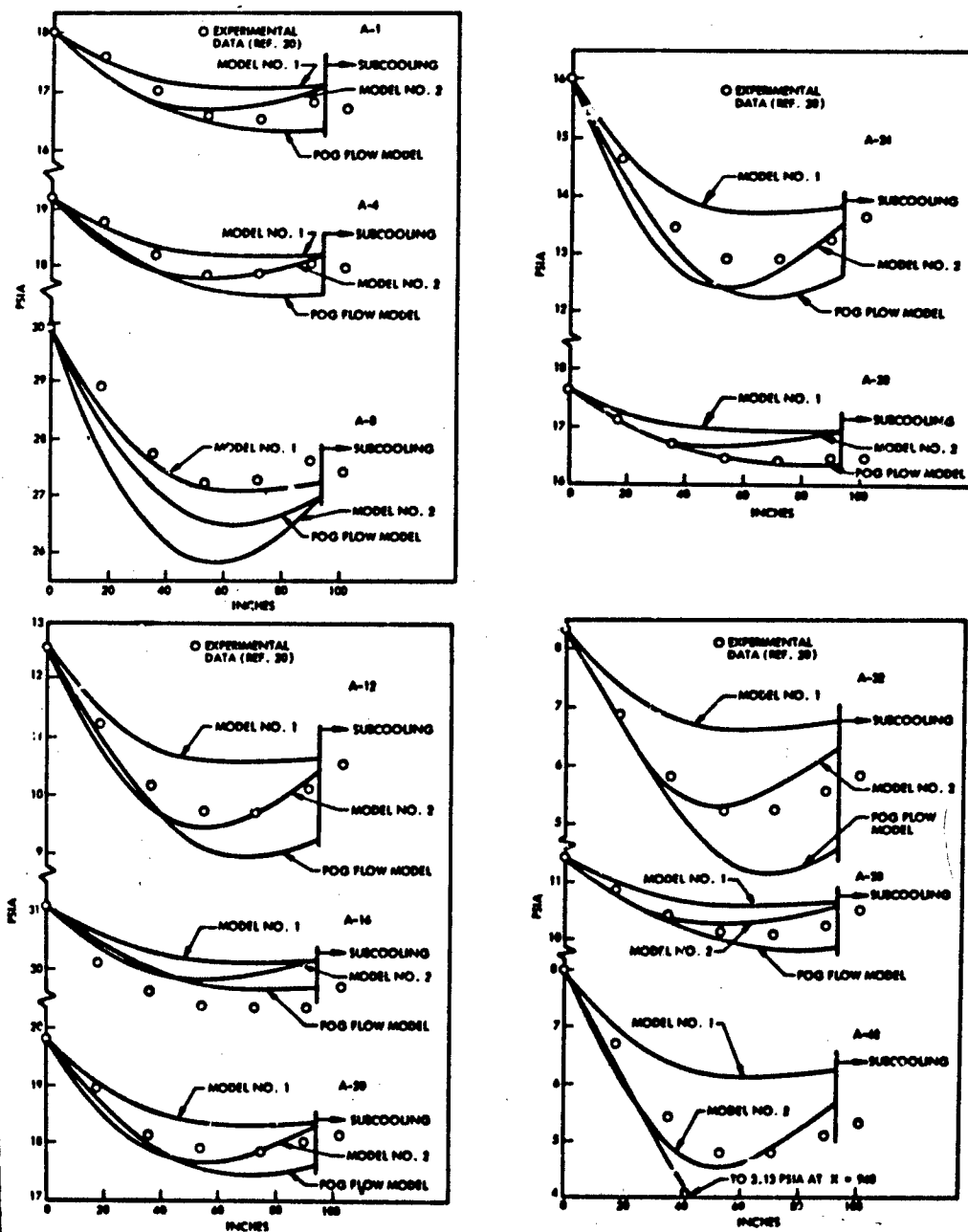


Fig. 13 Comparison of Pressure Profiles Predicted by Models No. 1 and 2 and Fog-Flow Model, with Arbitrarily Selected Series "A" Run of Ref. 8

Assuming fog flow $U_t = U_v$ and zero initial entrainment velocity $U_t' = 0$, Eq. 14 becomes

$$-AdP - \tau_w dA_w = \frac{1}{g_c} [W_t dU - Uy dW] \quad (15)$$

or in terms of gradients (see Ref. 10)

$$\frac{dP}{dx} \left[\frac{W_t^2 \psi}{\rho A^2 g_c} \frac{d\rho}{dP} - 1 \right] = \frac{1}{g_c} \left[\frac{\phi^2}{D} \frac{W_t^2 \psi^2}{2\rho A^2} + \frac{W_t^2}{\rho A^2} \frac{d\psi}{dx} - \frac{W_t^2 \psi}{\rho A^3} \frac{dA}{dx} - y \frac{W_t^2 \psi}{\rho A^2} \frac{d\psi}{dx} \right] \quad (16)$$

Note the difference in the momentum equation in Eqs. 11 and 15. The first right hand term of Eq. 15 includes the total weight flow, whereas in Model No. 1 only the vapor flow is included. Since the vapor flow decreases along the length of the tube, less momentum is recovered in the first term of Model No. 1 for the same velocity gradient. Assuming y equal to zero for both models, the second term in Model No. 2 is zero and in Model No. 1 it is equivalent to the first term. Figure 14 is a normalized plot of

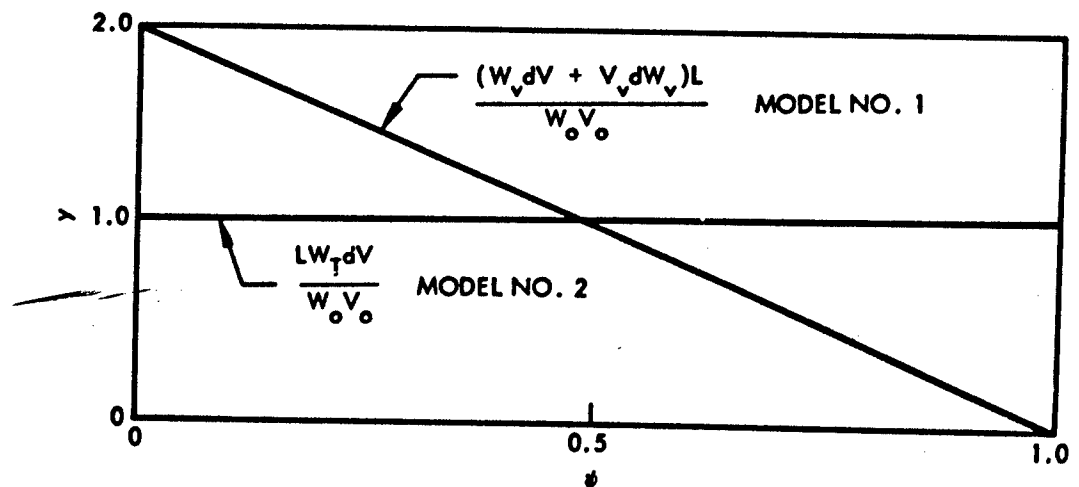


Fig. 14 Momentum Recovery Terms for Incompressible Flow vs. Quality. Comparison of Model No. 1 with Fog-Type Flow

the momentum terms for the two models vs vapor quality. For simplicity, incompressible flow is assumed. Although the total momentum to be recovered is the same for both models (same area under curves), greater momentum recovery occurs at first in Model No. 1, thus reducing the slope of the pressure profile. Little momentum recovery is left toward the end of the condenser. In Model No. 2, the momentum recovery is spread evenly over the length of the tube. The initial pressure gradient is steeper than in Model No. 1, but toward the end it is less steep. In most cases the momentum recovery toward the end is larger than the frictional gradient so that the pressure gradient becomes distinctly positive, with the minimum pressure located at approximately two-thirds of the condensing length.

In incompressible flow, either model would suffice for the total pressure drop since ϕ^2 , U , etc., would vary similarly along the tube and the momentum recovery is the same. But in compressible flow, the density drops more rapidly in Model No. 2 because the pressure gradient is steeper. However, the local vapor flow rates are similar, so that higher velocities occur in Model No. 2, thus an unrecoverable steepening occurs in the pressure gradient. The overall effect is to increase the pressure drop over that predicted by Model No. 1. The increase is more noticeable when the ratio of the pressure drop to the pressure level is large.

4.4 Fog-Flow Condensing Pressure Drop Model

A second means for predicting the frictional pressure gradient in condensing flow was proposed by A. Koestel (Ref. 12). Due to the simplicity of the model an analytic value of the two-phase factor is achieved:

$$\phi^2 = \left(\frac{D}{D_c} \right)^{4.75} \frac{1}{\psi^{0.75}} \quad (17)$$

where

$$\frac{D}{D_c} = f(We_t), \quad \text{the tube Weber number} = \frac{\rho U^2 \delta_{cr}}{2U g_c} \quad (18)$$

The calculation of D/D_c involves a prediction of the drop size variation along the tube and is covered in detail in Ref. 12.

Close to the interface (roughly the final 20 percent of the condensing length), the predicted diameter of the entrained droplet becomes very large, eventually exceeding the diameter of the tube and approaching infinity at the interface where the velocity is zero. This large droplet size is due to the fact that the total lift force of the vapor on the liquid droplet is dependent upon the droplet surface area. Furthermore, the test correlation for the droplet lift-off model was a very large flat plate, where the droplet size did not significantly change the flow pattern as it does in a tube. In this region, ϕ^2 rapidly approaches infinity due to the reduction in the core diameter (D_c), and then becomes incalculable due to the negative value for the core diameter ($D_c = D_t - 2\delta_{cr}$). As a temporary remedy for this problem, limits have been set on the droplet diameter so that this model can be currently used to predict pressure drop. For the predictions presented in this report, ($\delta_{cr} \leq 0.1 D_t$) has been used.

Furthermore, the Reynolds numbers for this region are generally less than 2000, indicating that viscous flow exists. A laminar fog-flow, two-phase factor can also be obtained by the same method. In the development, the quality term vanishes and ϕ^2 becomes a function of (D_t/D_c):

$$\phi^2 = \left(\frac{D}{D_c} \right)^4 \quad (19)$$

Still, one is plagued with the problem of the diameter ratios and the questionable assumption that the mixture viscosity is usually equal to the vapor viscosity. The assumptions for the Fog-Flow-Model are the same as for Model No. 2 and the resulting momentum equation is identical, except that ϕ^2 is calculated using Eq. 18.

4.5 Comparison of Models

A comparison of the three models (with y equal to zero) with experimental pressure drops taken from Ref. 8 is shown in Fig. 13. The effect of the difference in the momentum terms of Models No. 1 and 2 is clearly seen. The pressure gradient for Model No. 1 is not as steep due to the high initial momentum recovery, and the profile is fairly flat toward the end of the tube where the frictional gradient and momentum recovery are small. The opposite is true of Model No. 2; the initial gradient is steep but the recovery toward the end is large.

The Fog-Flow pressure profile shows the same trends as does Model No. 2, since their equations are similar except for the evaluation of the two phase factor ϕ^2 . Note also that the experimental data shows the same trends as Model No. 2 and the Fog-Flow Model; that is, a steep initial profile, a minimum point, and a considerable rise in pressure. The difference between Model No. 2 and the Fog-Flow Model is attributed to the large values of ϕ^2 in the latter. Note that the gradients near the interface are steeper than the experimental data for Model No. 2 and less steep for the Fog-Flow Model. This is attributed to the lower ϕ^2 factor in the improved Lockhart-Martinelli correlation, and the extremely high ϕ^2 factors in the Koestel correlation. The ϕ^2 inferred from the data appears to be somewhere between the two. Some of the discrepancies between the models and the data may be due to flow measurement error.

4.6 Analytical Prediction of Momentum Loss Factor

The following approach was used to determine the expected momentum loss by the flowing vapor:

- 1) Determine the mean free path (λ) of the vapor.
- 2) Assume that, on the average, a molecule colliding with the wall had its last collision at a distance λ from the wall.
- 3) Assume that upon collision with the wall a vapor molecule either:
 - a) Sticks to the wall and condenses, giving up all its momentum, or
 - b) Bounces off the wall, retaining all its axial momentum.

- 4) Determine the mean velocity in the flow layer at distance λ from the wall and estimate the fluctuations in that velocity due to turbulence.
- 5) If the velocity fluctuations are significant, evaluate condensation percentage for the molecules striking the wall.
- 6) If this percentage is large, modify the mean velocity at the distance λ by assuming that the Gaussian velocity distribution obtained in noncondensing flow now has part of its distribution removed (from the side with velocities lower than the mean). This gives a new mean velocity to the layer at λ .
- 7) If the percentage condensing is less than 50 percent, assign the noncondensing mean velocity to the layer at distance λ .

4.6.1 Calculation of Mean Free Path

It has been shown that vapor density, viscosity expectation value velocity, (kinetic), and mean free path are related by

$$\mu = 0.310\rho \langle v \rangle \lambda \quad (20)$$

and using

$$\langle v \rangle = \sqrt{3kT/m}$$

we get

$$\langle v \rangle = 10.43 \sqrt{T(^{\circ}\text{F}) + 460} \text{ in./}(\text{sec} \cdot \text{R})^{1/2} \quad (21)$$

so

$$\lambda = \mu / (0.310\rho \times 10.43 \sqrt{T + 460}) \quad (22)$$

Figure 15 shows λ vs temperature. (The saturation temperature and pressure were used to evaluate μ and ρ .)

4.6.2 Calculation of Velocity Fluctuation

Figure 16 shows Laufer's Data (Ref. 16) on axial velocity fluctuation in turbulent compressible pipe flow. Also shown is the approximate mean free path of the vapor in the condenser.

Since the average distance that a molecule must travel to reach the wall with no intermediate collisions is the mean free path, one can say that the molecules hitting the wall had their last collision a distance equal to the mean free path from the wall. Since there are no intermediate collisions, molecules that hit the wall and condense must give up momentum which they had in the layer a distance of the mean free path (λ) from the wall. However, one must observe that Laufer measured $(U')^2$ (the square of the fluctuation) and not U' .

In a layer in midstream, it is assumed that the velocity distribution is a Gaussian distribution about the mean velocity for that layer. This symmetry is caused by continuity, since

as many molecules must enter the layer from above as from below. In the case of condensing flow, particularly at high condensing rates, an asymmetric distribution would be expected since some of the molecules that would have transferred to that layer from one closer to the wall do not transfer, but are condensed. Laufer's data did not have this asymmetry because he did not have condensation. To apply Laufer's

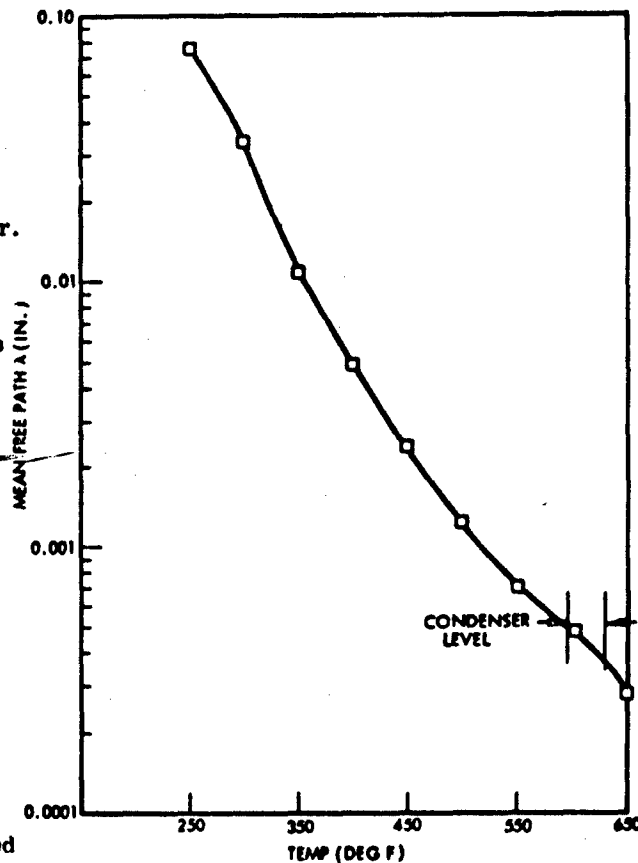


Fig. 15 Mean Free Path λ (Inches) vs. Temperature (Deg F) for Saturated Mercury Vapor

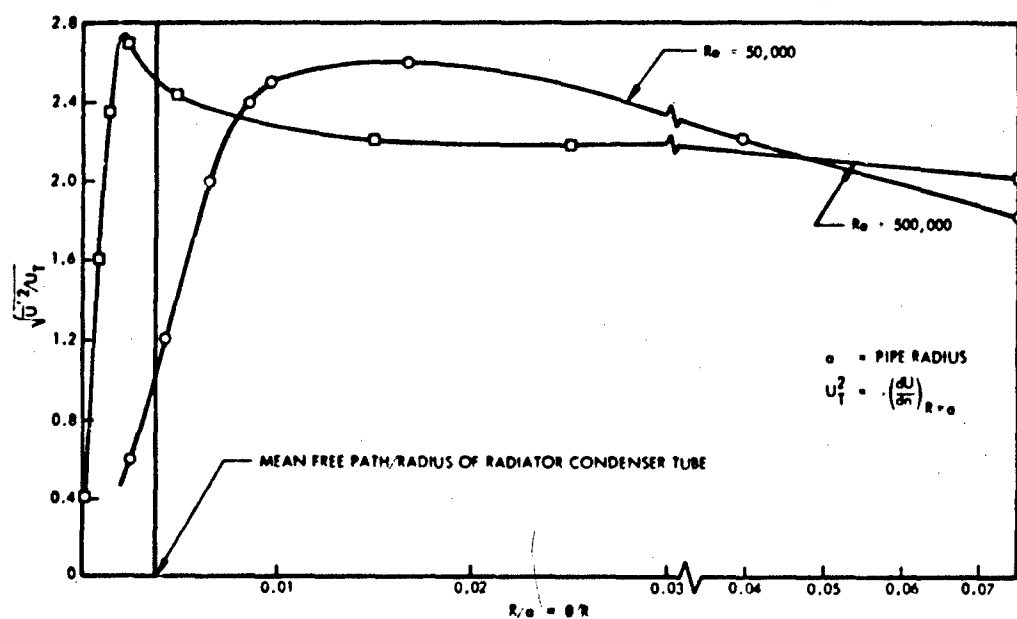


Fig. 16 Axial Velocity Fluctuation vs. Distance from Pipe Wall (Compressible Flow); Data of Laufer (Ref. 16)

data to the case of extremely high condensing rate flow, the author assumed that in the layer a distance λ from the wall, the mean velocity of Laufer's data is actually the lowest velocity of that layer for condensing flow. This will be true only in cases where approximately 50 percent or more of the molecules striking the wall condense. (In our case less than one percent of the impinging molecules condense, so Laufer's data may be employed as is. This particular discussion of an asymmetric distribution is not important unless the condensing length becomes very short.) The worst case would cause the distribution of velocities in the layer λ to appear as shown in Fig. 17.

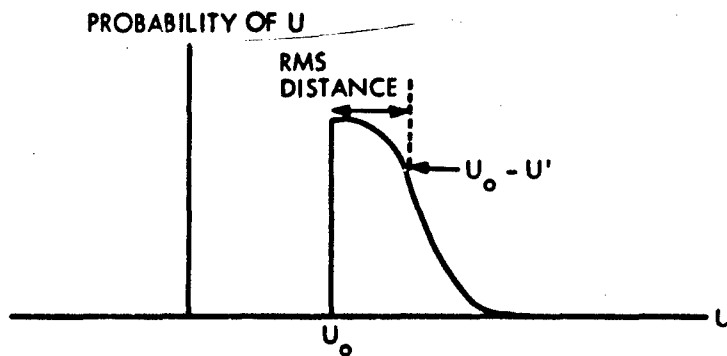


Fig. 17

Upon examining Fig. 16, it was found that the fluctuation velocity U' was approximately equal in velocity to $U_t = V^* = \text{shear velocity}$, for Reynolds number of 50,000. This means the velocity distribution at λ in condensing flow might have a new mean velocity larger than that of noncondensing flow, but only if the condensing rate is very high. This was validated by calculations.

Turbulent Flow. To estimate y , using the universal velocity profile, we find that the shear velocity $V^* = \sqrt{\tau/\rho}$ is defined by

$$V^{*2} = 0.03325 (\bar{U})^{7/4} \nu^{1/4} R^{-1/4} \quad (23)$$

Representative values for operating conditions are

$$\begin{aligned} \bar{U} &= 169 \text{ ft/sec} \\ R &= 0.135 \text{ in.} \\ \nu &= 4.43 \times 10^{-2} \text{ in.}^2/\text{sec}^2 \end{aligned}$$

and we get

$$V^* = 124.3 \text{ in./sec.}$$

The wall shear Reynolds number is given by

$$\eta^* = \frac{yV^*}{\nu} \quad (24)$$

using $y = \lambda = 0.0005 \text{ in.}$, we get $\eta = 1.41$.

Using Fig. 20.4 on page 405 of Ref. 17, we see $\log \eta = 0.15$ falls in the laminar sublayer, i.e., the distance λ is within the sublayer. In that layer, the universal velocity profile gives

$$\frac{U_\lambda}{V^*} = \frac{\lambda V^*}{\nu} \quad (25)$$

which gives

$$U_\lambda = 175 \text{ in./sec.},$$

but the average velocity is

$$\bar{U} = 2030 \text{ in./sec.},$$

so

$$y = U_\lambda / \bar{U} = 0.0863;$$

In other words, a condensing molecule arriving at the wall from a distance λ away gives up 8.63 percent of the mean vapor velocity when condensing.

Laminar Flow. In laminar flow, we have the velocity profile

$$U = \frac{dp}{dx} \left[\frac{1}{4\mu} (R^2 - r^2) \right] \quad (26)$$

and

$$\bar{U} = \frac{dp}{dx} \left(\frac{1}{8\mu R^2} \right)$$

which gives for U_λ

$$\frac{U_\lambda}{\bar{U}} = \frac{4\lambda}{R} \quad (27)$$

This equation was used for laminar flow.

These equations were programmed into the numerical solution of the pressure drop equation (Model No. 2) discussed earlier in this report. The same data (Ref. 8) was compared to this modified analysis, and results for a typical case are shown in Fig. 18. There is better prediction of the pressure drop using this model, but further deviation from the measured pressure profile.

Since the evaluation of y by the foregoing method is a credible one in contrast to the use of y as a curve fitting parameter, it is felt that y should be calculated in this manner. Another correlating parameter can be used to make the data fit the analysis. The parameter may depend on other phenomena of flow, such as the slip ratio (or holdup) which should affect the frictional portion of the pressure gradient. Investigations are under way in this area.

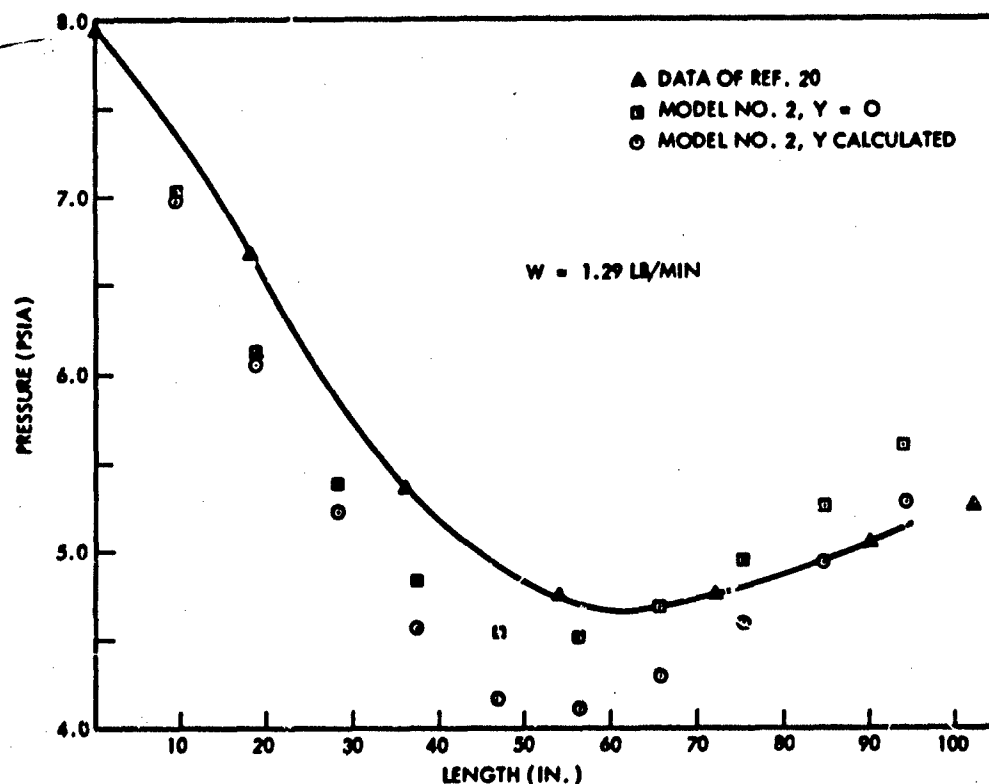


Fig. 18 Pressure Profile During Condensation

4.7 Condensation Effect on Friction Factor

The second modification of the flow theory is the influence of condensation upon the velocity profile and its resultant effect upon friction factor. It is known that suction or injection through the boundaries of a pipe in which a fluid is flowing changes the flow pattern in that pipe. The analysis presented here assumes that the velocity profiles of condensing flow are identical to flow with boundary layer suction. For the laminar regime, a potential flow model was developed (Yuan and Finkelstein, Ref. 18) which gives a perturbation solution to the flow equations, resulting in an approximate equation (within ± 10 percent) for the velocity profile. For the turbulent regime, experimental data of Ref. 19 are analyzed and fitted to a curve to give friction factor as a function of

axial flow Reynolds number, and the ratio of condensing Reynolds number to the axial flow Reynolds number. It is observed that for typical Hg condensers of the MRP, the effect on friction factor results in rather poor correlation to test data (Ref. 8), relative to previous prediction methods.

4.7.1 The Influence of Condensation in Laminar Flow of the Host Fluid

The following equation for the velocity profile in a recent study with boundary layer suction is derived in Ref. 18:

$$U = U_o \left[\frac{1}{1 - Re_c/8 + \frac{83}{5400} Re_c^2} + \frac{4Re_c x}{ReR} \right] \left\{ 1 - \eta + \frac{Re_c}{36} (-2 + 9\eta - 9\eta^2 + 2\eta^3) + \frac{Re_c^2}{10800} (166 - 760\eta + 825\eta^2 - 300\eta^3 + 75\eta^4 - 6\eta^5) \right\} \quad (28)$$

recalling

$$\tau_w = \mu \left. \frac{dU}{dr} \right|_{r=R}$$

we get

$$\tau = \mu U_o \frac{2}{R} \left[\frac{1}{1 - \frac{Re_c}{18} + \frac{83Re_c^2}{5400}} + \frac{4Re_c x}{ReR} \right] \left[1 + \frac{Re_c}{12} - \frac{13}{540} Re_c^2 \right] \quad (29)$$

from the continuity equation we get

$$\bar{U}_x = \bar{U}_o + 2V_o \frac{x}{R} \quad (30)$$

or, remembering that in laminar flow $U_o = U_{max}/2.0$, we get

$$\frac{\bar{U}_x}{U_o} = 1 + \frac{4V_o x}{U_{max_o} R} = 1 + \frac{4Re_c x}{ReR} \quad (31)$$

where

$$Re = \frac{U_{max} R}{\nu}$$

Now returning to Eq. 29, and observing that for $\lambda < 1$ the first term in brackets differs from 1.00 by less than 5 percent, which might well be due to inaccuracy in the perturbation solution, we see that within the accuracy of the solution Eq. 29 could be written

$$\tau = \frac{4\mu\bar{U}_x}{R} \left[1 + \frac{Re_c}{12} - \frac{13Re_c^2}{540} \right] \quad (32)$$

or, since we often write τ in the form $\tau = f\rho V_2^2$ we can rewrite Eq. 29 as

$$\tau = \left[\frac{16}{Re_{local}} \right] \frac{\rho\bar{U}^2}{2} \left[1 + \frac{Re_c}{12} - \frac{13Re_c^2}{540} \right] \quad (33)$$

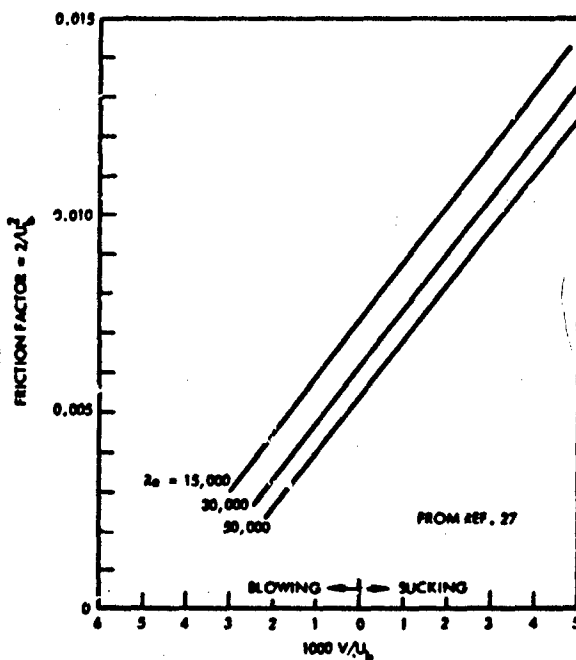
(based on D)

which returns to the well known Darcy-Weisback equation for $Re_c = 0$.

One might say that the second term in brackets also differs from 1.0 by less than the error introduced by the perturbation solution, and this is indeed a valid point. However, as justification for the approximation Eq. 33, consider that that equation shows only a factor which modifies the normal friction factor (f) for noncondensing flow, while Eq. 29 shows modification to the mean velocity itself. It is assumed that a

porous boundary only introduces a radial component of velocity and should not affect the mean axial velocity as calculated for the particular axial flow rate at that position.

Since we expect small Re_c , only the solution for small Re_c was used, and we have held f constant at $f(Re_c = 1.75)$, for values of $Re_c > 1.75$. The 1.75 was determined to be the point at which the next term in the solution was greater than half the last term given, an arbitrary cutoff point.



4.7.2 The Influence of Condensing in Turbulent Flow of the Host Fluid

Fig. 19 Prediction of Friction Factor

In Ref. 19 the coefficient of friction in turbulent flow was experimentally determined for small suction and injection rates. Figure 19 presents their data. In Fig. 19

U_b = bulk velocity = \bar{U} = volume flow/area

$$U_b^* = \frac{U_b}{\sqrt{\tau}}$$

where

τ = wall shear

We recall that

$$\tau = C_f \frac{\rho \bar{U}^2}{2} \quad \text{or} \quad C_f = \frac{2\tau}{\rho \bar{U}^2}$$

So define $\sqrt{\tau/\rho} = V^*$ = effective shearing velocity or we could write

$$C_f = \frac{2V^{*2}}{\bar{U}^2}$$

or defining

$$\frac{\bar{U}}{V^*} = \bar{U}^*$$

$$C_f = \frac{2}{(\bar{U}^*)^2} \quad (34)$$

which is plotted in Fig. 20. These curves in Fig. 20 all obey the equation

$$C_f = 0.0793 \text{Re}^{-0.25} + \frac{1.4 V}{U_b} \quad (35)$$

which is valid for $2 \times 10^{-3} < \text{Re} < 10^5$.

4.7.3 Application to Friction Factor

Equations 33 and 35 are applied respectively to the laminar and turbulent flow regimes of the host fluid during condensing flow. These new friction factors are then multiplied by the ϕ^2 obtained from investigations of non-condensing two-phase flow. This completes the application of the influence of boundary suction on the friction factor.

4.7.4 Application to Momentum Loss

We now turn attention toward the influence of boundary suction on the velocity profile, and therefore upon the momentum loss (which is dependent upon velocity profile). In the previous section, momentum loss by a condensing fluid is shown to be determined from the mean free gas path and the velocity profile.

Laminar Flow. Using the previous assumption that the discrepancy in the first term in brackets of Eq. 29 is in error due to the nature of the solution, we apply Eq. 33 to the velocity profile in the laminar regime, with the result that in laminar flow

$$U = 2\bar{U}_x \left[1 - \eta + \frac{Re_c}{36} (-2 + 9\eta - 9\eta^2 + 2\eta^3) + \dots \right] \quad (36)$$

and for a distance the mean free path λ from the wall,

$$U_\lambda = 2\bar{U}_\lambda \left[1 - \frac{(R - \lambda)^2}{R} + \frac{Re_c}{36} \left[-2 + 9 \frac{(R - \lambda)^2}{R} \right] + \dots \right] \quad (37)$$

Ignoring second order effects, this may be rewritten as

$$\frac{U_\lambda}{\bar{U}} \approx 2 \left[\frac{7 Re_c}{36} - \frac{Re_c^2}{18} + \frac{\lambda}{R} \left(2 - \frac{Re_c}{2} + \frac{Re_c^2}{9.08} \right) \right] \quad (38)$$

This is denoted the momentum loss factor y

$$y_{\text{laminar}} = 2 \left[0.194 Re_c - 0.0555 Re_c^2 + \frac{\lambda}{R} \left(2 - 0.5 Re_c + 0.11 Re_c^2 \right) \right] \quad (39)$$

Turbulent Flow. Recall that Blasius gave, for $2000 < Re < 10^5$

$$\begin{aligned}\tau_o &= \frac{1}{8} \left(0.3164 Re_D^{-0.25} \right) \rho \bar{U}^2 = \frac{\rho \bar{U}^2}{2} \left(0.0793 Re_D^{-0.25} \right) \\ &= 0.03325 \rho \bar{U}^{7/4} \nu^{1/4} R^{-1/4}\end{aligned}\quad (40)$$

Also recall that the friction velocity, V^* is defined by

$$V^* = \sqrt{\tau_o / \rho}$$

i.e., from

$$\tau_o = \rho V^{*2}$$

We see therefore that V^* , which determines the shape of the velocity profile, varies with the square root of τ_o and therefore with the square root of the friction coefficient. We showed earlier that with suction velocity V ,

$$\tau_o = \frac{\rho \bar{U}^2}{2} \left(0.0793 Re^{-0.25} + 1.4 \frac{V}{\bar{U}} \right)$$

So we see that V^* becomes

$$V^* = \sqrt{\tau_o / \rho} = \frac{\bar{U}}{\sqrt{2}} \left[0.0793 Re^{-0.25} + 1.4 \frac{V}{\bar{U}} \right]^{1/2} \quad (41)$$

Using this calculation for V^* , and the method of Ref. 18 for momentum loss, the previous momentum loss calculations are modified to include the influence of suction on velocity profile.

4.7.5 Results and Conclusions

MCPD-1, a digital computer program employing the Fog-Flow Model using the Baroczy-Sanders two-phase factors, was modified to incorporate the influence of radial velocity on friction factor. Predictions for TRW run Number A-12, was made and is shown in Fig. 20. We see that the agreement between test data and analysis is not as good as that obtained in previous sections. For this reason, until better test data is available for comparison, this method is not recommended. It is apparent that the influence of condensation on the velocity profile will yield a different friction factor for condensing two-phase flow than for noncondensing two-phase flow.

The question is: To which factor do we attribute the change? Since we assume that the friction factor of the host fluid is a host fluid velocity profile property, it remains unchanged for noncondensing flow, and any change is attributed to a fluid property change (such as density or molecule distribution or mean free path). However, we know that condensation gives the fluid a radial velocity (in pipe condensers) which it does not have in noncondensing flow; furthermore, it is reasonable to believe that this radial velocity changes the flow pattern in a manner identical to that of boundary layer suction. The conclusion one draws is that one must consider the host fluid noncondensing friction factor to be a function of the wall shear stress (velocity profile) and must

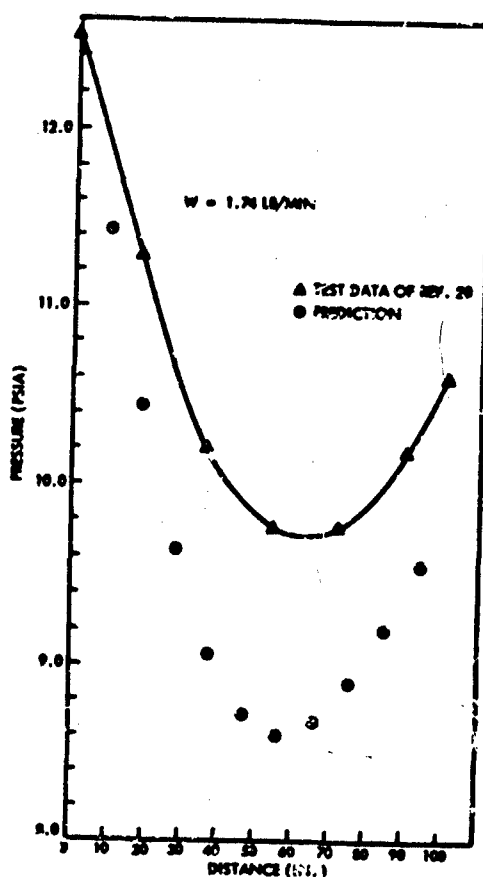


Fig. 20 Condensing Pressure Profile

modify the wall shear stress appropriately when condensation introduces a radial flow component to be superimposed on the normal noncondensing velocity profile.

5 REFERENCES

1. N. Zuker and M. Tribus, "Further Remarks on the Stability of Boiling Heat Transfer," AECU-3631, January 1958
2. "SNAP II Power Conversion Topical Report No. 13 Offbase Testing," TRW ER 4670
3. R. Kiraly and A. Koestel, "Condenser Development and Design Study," The SNAP 2 Power Conversion System Topical Report No. 8, TRW Report No. ER-4104, June 1960
4. G. I. Taylor, "The Instability of Liquid Surfaces When Accelerated in a Direction Perpendicular to This Plane," Proc. Royal Society, London, A-201, 1950, p. 192
5. R. Bellman and R. H. Pennington, "Effects of Surface Tension and Viscosity on Taylor Instability," Quar. Appl. Math 12, 1954, p. 181
6. A. Koestel, et al., "Space Radiator Study," ASD-TDR-61-697
7. R. Forslund, "Interface Stability in Rectangular Tubes Within Gravity Field," NAA-SR-TDR-8960*
8. R. G. Gido and A. Koestel, "Mercury Wetting and Nonwetting Condensing Research," Progress Report No. 3, TRW Report No. ER-5214, January 1963
9. R. Forslund, "Stability Analysis of the SNAP 2 Radiator Condenser With Vehicle Tumbling During Steady State," NAA-SR-TDR-8843*
10. R. P. Forslund, "SNAP Mercury Rankine Program Mercury Condensing Experiments," NAA-SR-9801*
11. C. J. Baroczy and V. D. Sanders, "Pressure Drop for Flowing Vapors Condensing in a Straight Horizontal Tube," NAA-SR-MEMO-6333*

*Internal document, Atomic International Division, North American Aviation, Inc.

12. A. Koestel, et al., "Fog-Flow Mercury Condensing Pressure Drop Correlation," Third Annual High Temp Liquid Metal Heat Transfer, ORNL, September 1963
13. Martinelli, Boelter, Taylor, Thomsen, and Morsing, "Isothermal Pressure Drop for Two Phase, Two Component Flow in Horizontal Pipes," TRANS ASME, Vol. 66, 1944, p. 139
14. Lockhart and Martinelli, "Proposed Correlation of Data for Isothermal Two Phase, Two Component Flow in Pipes," Chemical Engineer Progress, Vol. 45, 1949, p. 39
15. R. P. Forslund, "Pressure Drop Program for Condensing Mercury in the SNAP 2 Condenser," NAA-SR-9064, September 17, 1963*
16. John Laufer, "The Structure of Turbulence in Fully Developed Pipe Flow," NACA-TR-1174
17. Schlichting, Boundary Layer Theory, McGraw Hill
18. Yuan and Finkelstein, "Laminar Pipe Flow With Injection and Suction Through a Porous Wall," ASME Transaction, May 1956
19. University of Michigan, "Heat and Momentum Transfer From the Wall of a Porous Tube," by Churchill and Stubbs, ERI-2323-9-f, March 1957

*Internal document, Atomics International Division, North American Aviation, Inc.

DISCUSSION

Marvin Adelberg, Consultant

An analysis of mine concerning the formation of droplets or slugs in a condensation heat transfer process indicates that the performance of a condenser can be g sensitive. Did you make heat transfer measurements? If not, this might be brought out by tests in which the setup is first tilted one way and later the other, the results of the two being compared afterwards. I would recommend that you do this, if you haven't already.

Abramson

We have not tried to determine condensing heat transfer coefficients. We looked at some techniques which would allow us to estimate them, considering only small system modifications, and concluded that we could only obtain order of magnitude estimates at best. Because the radiation resistance from the tube is large compared to the condensing resistance, we probably could not identify the change in condensing coefficient resulting from tilting downward to tilting upward. In any case, all our tests have some g effect normal to the tube axis which might be significant.

We understand that J. A. Albers* at the NASA Lewis Research Center has made pressure drop tests under 1-g and zero-g conditions and that his measurements indicate an insensitivity to gravity level. The distribution of droplets is, of course, different.

*J. A. Albers and R. P. Macosko, "Experimental Pressure-Drop Investigation of Nonwetting, Condensing Flow of Mercury Vapor in a Constant-Diameter Tube in 1-G and Zero-Gravity Environment", NASA-TN D-2838, June, 1965.

PAPER 7

**DYNAMIC RESPONSE OF LIQUIDS IN PARTIALLY FILLED
CONTAINERS SUDDENLY EXPERIENCING WEIGHTLESSNESS**

By Francis C. W. Fung
CORNELL AERONAUTICAL LABORATORY, INC.

ABSTRACT

The problem of dynamic response of liquid in partially filled containers after sudden removal of body forces is solved as an initial boundary-value problem for both two-dimensional and cylindrical containers. The initial free surface is assumed to be symmetrical with respect to the vertical axis of the container, thus restricting the analyses to unidirectional body forces acting along the vertical axis. Additional assumptions are that the flow is inviscid and that the slope of the free surface is everywhere small, so that the problem can be linearized. It is found a posteriori that the linearizing assumptions are justified as long as $\cot \theta$ is small compared to unity, where θ is the contact angle.

Under the linearizing assumptions, the free-surface response can be represented by an infinite series of surface waves, symmetrical with respect to the vertical axis of the container. It is found that the amplitudes of the higher modes diminish as $1/n^4$ for

the two-dimensional case, and as $1/Z_n^4$ for the cylindrical case (where $n = 1, 2, 3, \dots$, and Z_n are zeros of Bessel function of first kind and first order). The dynamic free surface shapes with $\cot \theta < 1$ are derived for both wetting or nonwetting liquids.

When available experimental data are interpreted in the light of this analysis, reasonably good agreement is found, despite the fact that most experiments have been conducted for liquids with $\cot \theta$ not necessarily small compared to unity. Specifically, this linearized analysis yields a time law for the free-surface vertex motion that compares favorably with experimental observations. Also the free-surface shape, as predicted by this analysis, agrees well with the observed general shape. Finally, the frequency and shape of the higher modes explain an observed "unexpected" vertex rising at early times of drop-tower experiments conducted for wetting liquids.

DYNAMIC RESPONSE OF LIQUIDS IN PARTIALLY-FILLED CONTAINERS SUDDENLY EXPERIENCING WEIGHTLESSNESS

1 INTRODUCTION

A great deal of interest has recently been shown in the phenomenon of weightlessness as introduced by the advent of space flight. For space ships carrying liquid fuels and liquids required to sustain the passengers, it is necessary that the behavior of the liquid-vapor interface in containers in the absence of body force be understood (Ref. 1).

In the absence of body forces, the surface forces of cohesion (surface tension) and adhesion (wettability), remain as the dominant forces affecting behavior of the liquid. As a first step toward attaining an understanding of the behavior of the liquid-vapor interface when surface forces dominate, some researchers have revived the calculation of the static free surface shapes produced under various gravity conditions (corresponding to change of Bond number). Among this group of researchers are notably Benedikt (Ref. 2), Reynolds (Ref. 3), and Li (Ref. 4), who have established beyond any doubt that in the absence of body force the static free surface attains a constant curvature shape governed by the contact angle and container geometry.

With respect to the dynamic behavior of the liquid-vapor interface during weightlessness, the literature indicates that analytical efforts, as a whole, have been directed toward establishing stability criteria by solving the corresponding free oscillation (eigenvalue) problem. In this regard, Concus (Ref. 7) concerned himself with the stability of liquid-vapor interface in an inverted rectangular channel. Anliker and Pi (Ref. 6) extended the analysis to containers with various bottom shapes; however, contact forces were neglected. One important finding of Ref. 6 is that stability is affected by bottom shape if the equilibrium surface intersects the bottom of the container. Satterlee and Reynolds (Ref. 8) extended their analysis to include possible variation of the contact angle, and treated the particular case of a cylindrical container. These analyses showed that motions of the free surface are stable under zero body force conditions.

We also find that numerous drop-tower experiments have been conducted by NASA (Refs. 9, 10) and Shuleikin in the U. S. S. R. (Refs. 11, 12) to study the response of liquid-vapor interface of contained liquid after step removal of body force. Subsequent to the earlier experiments, NASA has performed an extensive series of measurements (Refs. 13, 14, 15) designed to shed light on the time required for the liquid-vapor interface to reach the constant curvature equilibrium shape in partially filled containers. At this point, the time required to reach final equilibrium remains unsettled, and questions still remain as to the detailed time history of the interface motion. Despite the obvious need for analytical results, efforts in this direction have been relatively sparse and unproductive. For example, an attempt was made (Ref. 16) to study the interface motion of liquid in a partially filled cylinder after step removal of the unidirectional body force acting along the axisymmetric axis. No meaningful results were obtained because the formulation effectively neglected the all-important surface forces. Paynter (Ref. 5) developed a simple energy analysis to predict the motion of the liquid-vapor interface in a spherical container after step removal of body force. As a result of his assumption that the interface always maintains a constant-curvature configuration during the motion, his analysis is in effect a quasi-static analysis. Furthermore, this assumption is known to violate experimental observations (Ref. 14).

The objective of the study reported herein has been the treatment of the dynamic response of the liquid-vapor interface, after step removal of body force, as an initial boundary value problem. Because of correspondence with experimental results, the initial body force has been assumed to act along an axisymmetrical axis of the container, such that only symmetrical motion need be considered. Both two-dimensional and cylindrical containers have been treated in the following analysis.

2 FORMULATION OF THE BASIC EQUATIONS

Consider a liquid with density ρ , surface tension σ , and kinematic viscosity ν enclosed in a container with the characteristic dimension L . In the absence of body force it has been shown (Refs. 8, 17) that the surface forces dominate viscous forces for most liquids when placed in containers having characteristic dimension of practical

interest, say one cm or larger. Thus, in the following analysis, we assume the liquid to be inviscid and the motion to be irrotational. For irrotational flow a scalar potential ϕ exists such that

$$\vec{V} = -\nabla\phi \text{ where } \vec{V} \text{ is the velocity vector} \quad (1)$$

Together with the assumption of incompressibility we can express the continuity equation as

$$\nabla^2 \phi = 0 \quad (2)$$

The equation of motion for the liquid-vapor interface can be expressed in the following familiar form, derivable from Bernoulli's equation (Refs. 6, 8):

$$\frac{p_g}{\rho} - \frac{\sigma}{\rho} J + \Omega + \frac{v^2}{2} - \phi_t = C(t) \quad (3)$$

where p_g is the vapor pressure, J is the total curvature of the liquid-vapor interface, v is the magnitude of the velocity, Ω is the body force potential, and $C(t)$ is Bernoulli's constant. As shown in Figs. 1 and 2, we let f denote the initial liquid-vapor interface and S the time-varying liquid-vapor interface following the removal of body force. On expressing Bernoulli's equation in terms of f and S , we obtain, respectively, the static equation governing the initial free surface shape:

$$\frac{p_g}{\rho} - \frac{\sigma}{\rho} J_f + N g f = C \text{ at } f \text{ for } t < 0 \quad (3a)$$

and the equation governing the time-varying interface after the body force is annulled:

$$\frac{p_g}{\rho} - \frac{\sigma}{\rho} J_S + \frac{v^2}{2} - \phi_t = C \text{ at } S \text{ for } t > 0 \quad (3b)$$

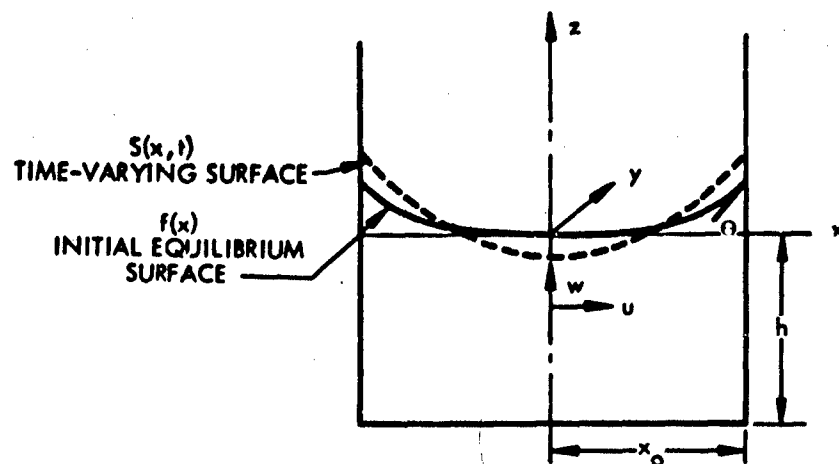


Fig. 1 Coordinate System for Liquid in Two-Dimensional Channel

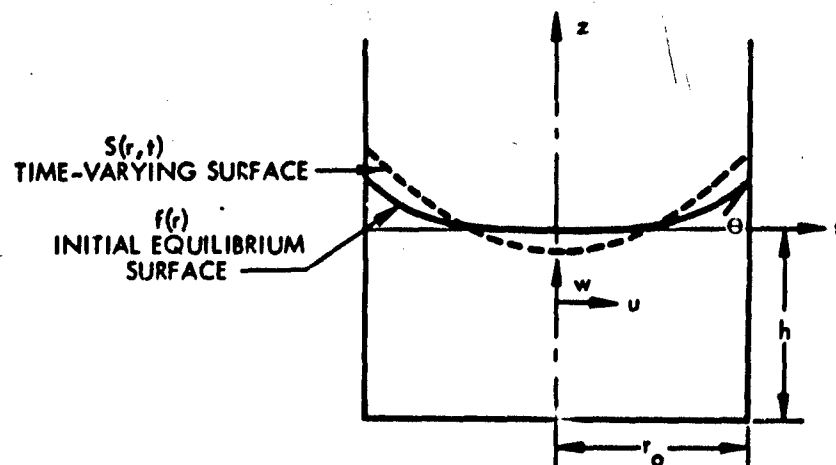


Fig. 2 Coordinate System for Liquid in Cylindrical Container

where J_f and J_S are the total curvatures for the free surfaces f and S respectively. Note in Eq. (3a) we have restricted ourselves to a unidirectional body force acting in the negative z direction, where for convenience the body force has been expressed as a constant multiple N of the usual gravitational force due to the gravitational acceleration g .

With the coordinates chosen as shown in Figs. 1 and 2 (such that $f(0) = 0$), the Bernoulli's constant is evaluated from Eq. (3a) to be

$$C = \frac{P_R}{\rho} - \frac{\sigma}{\rho} J_f(0)$$

On substituting into Eq. (3a), the static equation for the initial free surface shape becomes:

$$J_f - \beta^2 f = J_f(0) \text{ at } t < 0 \quad (4)$$

where $\beta^2 = N\rho g/\sigma$

In like manner, the dynamic condition for the time-varying liquid-vapor interface becomes

$$\alpha^2 J_S + \phi_t - \frac{v^2}{2} = \alpha^2 J_f(0) \text{ at } S \text{ for } t > 0 \quad (5)$$

where $\alpha^2 = \sigma/\rho$.

Since we require that the free surface remain a free surface, we have the following kinematic condition for the time-varying interface S :

$$\frac{dF}{dt} = 0 \text{ at } S \quad (6)$$

where $F = z - S$ is the equation of the time-varying interface S .

In the following sections of the report, linearized versions of Eqs. (5) and (6), together with Eq. (2), are solved to obtain the transient response of the free surface, where the initial free surface is given by Eq. (4), and with ϕ satisfying the condition of no normal flow across solid boundaries,

$$\frac{\partial \phi}{\partial n} = 0 \quad (7)$$

at the walls of the container.

3 THE SYMMETRIC MOTION RESPONSE IN TWO-DIMENSIONAL CONTAINERS

Consider liquid in an infinitely long rectangular channel oriented with respect to a set of cartesian coordinate axes as shown in Fig. 1. It has been shown from consideration of differential geometry (Ref. 8) that the curvature is related to surface shape (for the two-dimensional case) as follows:

$$J_f = \frac{f_{xx}}{[1 + f_x^2]^{3/2}} \quad \text{and} \quad J_s = \frac{s_{xx}}{[1 + s_x^2]^{3/2}}$$

where the subscripts denote differentiation.

In the following, we assume that the slope of the free surface is at all times small compared to unity. This assumption permits us to linearize the above curvature expressions by dropping the product terms. It should be noted that this assumption is always satisfied during the steady state as long as we require $\cot \theta$ to be small compared to unity, where θ is the static contact angle. It is possible to show, a posteriori, that the slopes of the time-varying free surface s are small whenever the static contact angle θ is in the neighborhood of $\pi/2$. We note that the linearized curvature expressions can also be found by an alternative method as suggested by Landau and Lifshitz (Ref. 18).

On substituting the linearized curvature expressions in Eq. (4), we obtain the equation for the initial free surface f in the following form:

$$f_{xx} - \beta^2 f = f_{xx}|_{x=0} \quad \text{for } t < 0 \quad (8)$$

Similarly, the dynamic condition of Eq. (5) can be written as:

$$\alpha^2 S_{xx} + \phi_t - \frac{1}{2} v^2 = \alpha^2 f_{xx}|_{x=0} \quad \text{at } S \text{ for } t > 0$$

From the kinematic boundary condition of Eq. (6) we obtain, for the two-dimensional container, that

$$\frac{dz}{dt} - S_t - S_x \frac{dx}{dt} = 0 \quad \text{at } S$$

where $dz/dt = w$, $dx/dt = u$ are the vertical and horizontal velocities respectively. Together with Eq. (1), the above kinematic condition can be expressed as

$$S_t = -\phi_z + S_x \phi_x \quad \text{at } S \quad (9)$$

At this point, we linearize the dynamic condition by assuming the $1/2 v^2$ term to be of smaller order than ϕ_t , and we also linearize the kinematic condition by dropping the $S_x \phi_x$ term in comparison with ϕ_z . It will be shown, a posteriori, that both of the above approximations hold as long as $\cot \theta$ has been assumed small compared to unity. Accordingly, we obtain the following set of linearized boundary conditions:

$$S_t + \phi_z = 0 \quad \text{at } S \quad (10)$$

and

$$\alpha^2 S_{xx} + \phi_t = \alpha^2 f_{xx}|_{x=0} \quad \text{at } S \quad (11)$$

Equations (10) and (11), together with the equation of continuity of Eq. (2) and boundary condition of Eq. (7) (i.e., no normal flow across solid walls) are the governing equations that we choose to solve. We combine Eqs. (10) and (11), by eliminating S . Together with Eq. (2) we obtain

$$\phi_{tt} + \alpha^2 \phi_{zzz} = 0 \text{ at } S \quad (12)$$

Let

$$\phi(x, z, t) = \varphi(t) \bar{\varphi}(x, z) \quad (13)$$

and substituting in Eq. (2) we have

$$\bar{\varphi}_{xx} + \bar{\varphi}_{zz} = 0 \quad (14)$$

A solution of Laplace's equation [i.e., Eq. (14)] with the following boundary conditions $\partial\phi/\partial x = 0$ at $x = \pm x_0$, and $\partial\phi/\partial z = 0$ at $z = -h$ yields (Ref. 18):

$$\bar{\varphi}(x, z) = \sum_{n=0}^{\infty} A_n \cosh[k_n(h+z)] \cos(k_n x)$$

where $k_n = n\pi/x_0$

On substituting Eq. (13), together with the above expression for $\bar{\varphi}(x, z)$ in Eq. (12), we obtain

$$\varphi_{tt} \sum_{n=0}^{\infty} A_n \cosh[k_n(h+S)] \cos(k_n x) + \alpha^2 \varphi \sum_{n=0}^{\infty} A_n k_n^3 \sinh[k_n(h+S)] \cos(k_n x) = 0 \quad (15)$$

On restricting ourselves to the case that h/x_0 is of order unity or larger, we will neglect S/x_0 henceforth in comparison with h/x_0 . This is consistent with our linearization scheme and will also be justified a posteriori. After simplification and letting $\varphi(t) = \sum_{n=0}^{\infty} \varphi_n(t)$ we obtain from Eq. (15) an infinite set of equations governing φ_n

$$(\varphi_n)_{tt} + \omega_n^2 \varphi_n = 0$$

where $\omega_n^2 = \alpha^2 k_n^3 \tanh(k_n h)$ and $n = 1, 2, 3, \dots$

If we require in addition that $\varphi(0) = 0$, the above set of equations yields

$$\varphi = B_0 t + \sum_{n=1}^{\infty} B_n \sin(\omega_n t)$$

Hence, substituting φ and $\bar{\varphi}$ in Eq. (13), we obtain finally

$$\phi = C_0 t + \sum_{n=1}^{\infty} C_n \cosh[k_n(h+z)] \cos(k_n x) \sin(\omega_n t) \quad (16)$$

From the linearized kinematic condition of Eq. (10) we have

$$S_t = -\phi_z = - \sum_{n=1}^{\infty} C_n k_n \sinh(k_n h) \cos(k_n x) \sin \omega_n t$$

Therefore

$$S = \sum_{n=1}^{\infty} \frac{C_n k_n}{\omega_n} \sinh(k_n h) \cos k_n x \cos \omega_n t + g(x)$$

The function $g(x)$ can be determined from the initial condition $S(x, 0) = f(x)$, hence

$$S(x, t) = \sum_{n=1}^{\infty} \frac{C_n k_n}{\omega_n} \sinh(k_n h) \cos(k_n x) (\cos \omega_n t - 1) + f(x)$$

On defining $d(x, t) = S(x, t) - f(x)$ as the displacement from the initial free surface, we have

$$d(x, t) = \sum_{n=1}^{\infty} \frac{C_n k_n}{\omega_n} \sinh(k_n h) \cos(k_n x) (\cos \omega_n t - 1) \quad (17)$$

The constants C_n can be determined from the linearized dynamic condition of Eq. (11), which at $t = 0^+$ reduces to

$$\phi_t|_{t=0} = \alpha^2 \left(f_{xx}|_{x=0} - f_{xx} \right) \quad (18)$$

On applying the initial free surface Eq. (8) to the right side we have $\phi_t|_{t=0} = -Ng f$.

On substituting ϕ_t as obtained from Eq. (16) and f (as derived in Appendix A) into the above, we obtain

$$C_0 + \sum_{n=1}^{\infty} C_n \omega_n \cosh(k_n h) \cos k_n x = \frac{Ng \cot \theta}{\beta \sinh(\beta x_0)} [1 - \cosh(\beta x)] \quad (19)$$

In Appendix B, the constants C_n are evaluated by performing Fourier analysis on Eq. (19). With C_n thus determined, Eq. (17) becomes

$$d(x, t) = \frac{2 \cot \theta}{x_0} \sum_{n=1}^{\infty} (-1)^n \frac{\beta^2 \cos(k_n x)}{k_n^2 (k_n^2 + \beta^2)} (1 - \cos \omega_n t)$$

Let us introduce a characteristic time τ defined by $\tau = 1/\omega_1$ and a characteristic dimension x_0 . We thus obtain the dynamic displacement in the following nondimensional form.

$$\bar{d}(\bar{x}, \bar{t}) = 2 \cot \theta \sum_{n=1}^{\infty} (-1)^n \frac{\bar{\beta}^2 \cos(n \pi \bar{x})}{(n\pi)^2 (\bar{\beta}^2 + n^2 \pi^2)} (1 - \cos \bar{\omega}_n \bar{t}) \quad (20)$$

where all barred quantities are nondimensional, viz., $\bar{\beta}^2 = (N\rho g/\sigma) x_0^2$ is the initial Bond number, $\bar{\omega}_n = \omega_n/\omega_1$, and $\bar{t} = t/\tau = \omega_1 t$.

4 THE SYMMETRIC MOTION RESPONSE IN CYLINDRICAL CONTAINERS

For liquid in a cylindrical container, we adopt the set of polar coordinate axes shown in Fig. 2. Since the initial free surface is symmetric with respect to the vertical axis, the motion response after step removal of body force must be axisymmetric. Following the procedures used for the two-dimensional container, we can immediately write the governing equations for the axisymmetric case in their linearized form:

Continuity equation:

$$\frac{\partial^2 \phi}{\partial r^2} + \frac{1}{r} \frac{\partial \phi}{\partial r} + \frac{\partial^2 \phi}{\partial z^2} = 0 \quad (21)$$

Kinematic free-surface condition:

$$S_t + \phi_z = 0 \text{ at } S \quad (22)$$

Dynamic free surface condition:

$$\alpha^2 J_S(r, t) + \phi_t = \alpha^2 J_f \Big|_{r=0} \quad t > 0 \text{ at } S \quad (23)$$

where $\alpha^2 = g/\rho$.

Initial static equilibrium equation:

$$J_f(r) - \beta^2 f(r) = J_f(r) \Big|_{r=0} \text{ at } t = 0^- \quad (24)$$

where $\beta^2 = N\rho g/\sigma$

Wall condition:

$$\frac{\partial \phi}{\partial n} = 0 \text{ at } r = r_0 \text{ and } z = -h \quad (25)$$

Consistent with the assumption that $\cot \theta < 1$, the expression for total curvature can be linearized to yield (Ref. 8):

$$J_f = \frac{1}{r} \frac{d}{dr} \left(r \frac{df}{dr} \right) \text{ and } J_g = \frac{1}{r} \frac{\partial}{\partial r} \left(r \frac{\partial S}{\partial r} \right) \quad (26)$$

(For an alternative development, see Ref. 18)

On combining Eqs. (21), (22), (23), and (26) we obtain

$$\phi_{tt} + \alpha^2 \phi_{zzz} = 0 \text{ at } S \quad (27)$$

which equation is identical to the combined dynamic and kinematic boundary condition obtained for the two-dimensional container. As before, we let

$$\phi(r, z, t) = \phi(t) \bar{\phi}(r, z) \quad (28)$$

and from Eq. (21), we obtain

$$\frac{1}{r} \frac{\partial}{\partial r} (r \bar{\phi}_r) + \bar{\phi}_{zz} = 0 \quad (29)$$

The solution to Eq. (29), subject to the wall conditions of Eq. (25), and the condition that $\bar{\phi}$ be finite at $r = 0$ are known (Refs. 19, 20), viz.

$$\bar{\phi}(r, z) = \sum_{n=0}^{\infty} A_n \cosh [k_n (h + z)] J_0(k_n r)$$

where k_n must be chosen such that $J_1(k_n r_0) = 0$, i.e., $k_n r_0 = Z_n$ are the zeros of the Bessel function of the first kind and first order. On substituting Eq. (28) together with solution for $\bar{\phi}$ into Eq. (27) we obtain:

$$\phi = C_0 t + \sum_{n=1}^{\infty} C_n \cosh [k_n (h + z)] J_0(k_n r) \sin \omega_n t \quad (30)$$

where $\omega_n = \alpha k_n^{3/2} [\tanh(k_n h)]^{1/2}$

From the linearized kinematic condition of Eq. (22), we have that

$$S_t = -\phi_z = - \sum_{n=1}^{\infty} C_n k_n \sinh [k_n (h)] J_0(k_n r) \sin \omega_n t$$

Therefore

$$S(r, t) = \sum_{n=1}^{\infty} \frac{C_n k_n}{\omega_n} \sinh(k_n h) J_0(k_n r) \cos \omega_n t + g(r)$$

where we have taken h/r_0 to be large compared to unity and have neglected S/r_0 in comparison to h/r_0 as in the two-dimensional case.

Since at $t = 0^-$, $S(r, 0) = f(r)$ we have

$$d(r, t) = \sum_{n=1}^{\infty} \frac{C_n k_n}{\omega_n} \sinh(k_n h) J_0(k_n r) (\cos \omega_n t - 1) \quad (31)$$

where again we have defined $d(r, t) = S(r, t) - f(r)$ as the displacement from the initial equilibrium surface. The constants C_n can be determined from the linearized dynamic condition of Eq. (23), which at $t = 0^+$ reduces to

$$\phi_t|_{t=0} = \alpha^2 \left[\frac{1}{r} \frac{1}{dr} (rf_r) \Big|_{r=0} - \frac{1}{r} \frac{d}{dr} (rf_r) \right]$$

On substituting for ϕ_t , as obtained from Eq. (30), and on applying the initial equilibrium equation to the right-hand side, we obtain

$$C_0 + \sum_{n=1}^{\infty} C_n \omega_n \cosh(k_n h) J_0(k_n r) = -Ngf \quad (32)$$

which upon substitution for f , as given in Appendix A, yields

$$C_0 + \sum_{n=1}^{\infty} C_n \omega_n \cosh(k_n h) J_0(k_n r) = \frac{Ng \cot \theta}{\beta L_1(\beta r_0)} [1 - I_0(\beta r)] \quad (33)$$

where I_0 and L_1 are modified Bessel functions of the zeroth and first order respectively.

In Appendix B, the constants C_n are evaluated by performing Fourier-Bessel analysis on Eq. (33). With C_n thus determined, Eq. (31) becomes

$$d(r, t) = \frac{2 \cot \theta}{r_0} \sum_{n=1}^{\infty} \frac{\beta^2 J_0(k_n r)}{k_n^2 (k_n^2 + \beta^2) J_0(k_n r_0)} (1 - \cos \omega_n t)$$

We now introduce a characteristic time τ (defined by $\tau = 1/\omega_1$) and the characteristic dimension r_0 , and obtain the dynamic displacement in the following nondimensional form:

$$\bar{d}(\bar{r}, \bar{t}) = 2 \cot \theta \sum_{n=1}^{\infty} \frac{\bar{\beta}^2 J_0(Z_n \bar{r})}{Z_n^2 (Z_n^2 + \bar{\beta}^2) J_0(Z_n)} (1 - \cos \bar{\omega}_n \bar{t}) \quad (34)$$

Where all barred quantities are nondimensional, viz., $\bar{\beta}^2 = N \rho g / \sigma r_0^2$ is the initial Bond number, $\bar{\omega}_n = \omega_n / \omega_1$, and $\bar{t} = t / \tau = \omega_1 t$.

On comparing $\bar{d}(\bar{r}, \bar{t})$ to the expression obtained for $\bar{d}(\bar{x}, \bar{t})$ (i.e., for the two-dimensional container) one finds that they are similar in form. Note that in the present case $J_0(Z_n \bar{r})$ plays the role of $\cos(n\pi \bar{x})$, Z_n plays the role of the zeros of the sine function which is $n\pi$, and $J_0(Z_n)$ plays the role of $\cos(n\pi)$ which is $(-1)^n$.

5 DISCUSSION OF RESULTS

For the linearized system, we see that the response of the free surface to a step removal of body force (originally aligned with the longitudinal or axisymmetric axis of the container) can be represented by an infinite series of symmetric surface waves. Furthermore, the amplitudes of the higher modes diminish as $1/n^4$ for the two-dimensional channel, and as $1/Z_n^4$ for the cylindrical container. The frequencies of these response modes are given by $\omega_n = (\sigma/\rho)^{1/2} (n\pi/x_0)^{3/2} [\tanh(n\pi h/x_0)]^{1/2}$ for the two-dimensional channel and by $\omega_n = (\sigma/\rho)^{1/2} (Z_n/r_0)^{3/2} [\tanh(Z_n h/r_0)]^{1/2}$ for the

cylindrical container. It should be recognized that these modal frequencies are necessarily the same as the results yielded by the corresponding eigenvalue problem (Refs. 6, 8, 18).

The dynamic free surface shapes (as given by the first three modes) have been computed for various container dimensions with the results plotted in Figs. 3 and 4. A value of the specific surface tension σ/ρ corresponding to the properties of water has been used in the computations, and the contact angle has been assumed to be 75 degrees, consistent with our linearizing restriction on θ . The initial load factor N has been chosen to be unity, the situation that prevails in drop-tower experiments. Figure 3 (computed for a rectangular channel with $x_0 = 10$ cm) and Fig. 4 (computed for a cylindrical container with $r_0 = 10$ cm) are composite plots showing the main

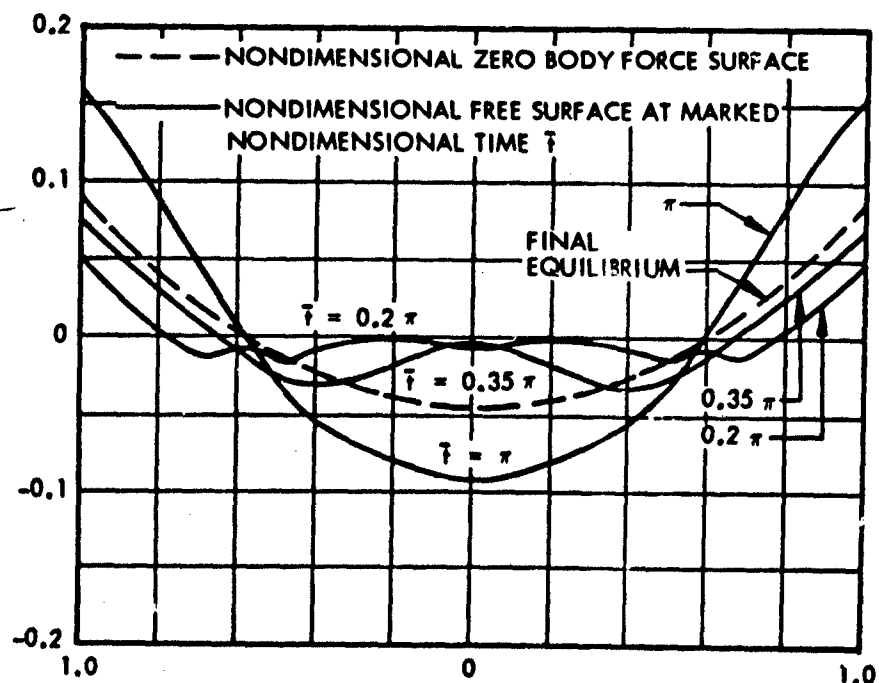


Fig. 3 Time History of Free Surface in a Rectangular Channel

features of the time history of the free surface. The particular characteristic dimension of 10 cm was selected because the NASA experiments were conducted for containers of roughly the same dimension. All plots are for h/x_0 or h/r_0 of order unity or larger.

It is not surprising that the predicted oscillating behavior of the free surface has not been fully confirmed by experimental observations. An examination of the characteristic frequencies associated with the dimensions of test containers indicates that the dominant observable oscillation has a long period in comparison with the time available for observation in drop-tower experiments. For a typical test container of 10 cm radius, the period of oscillation (as calculated from $2\pi/\omega_1$, the period of dominant

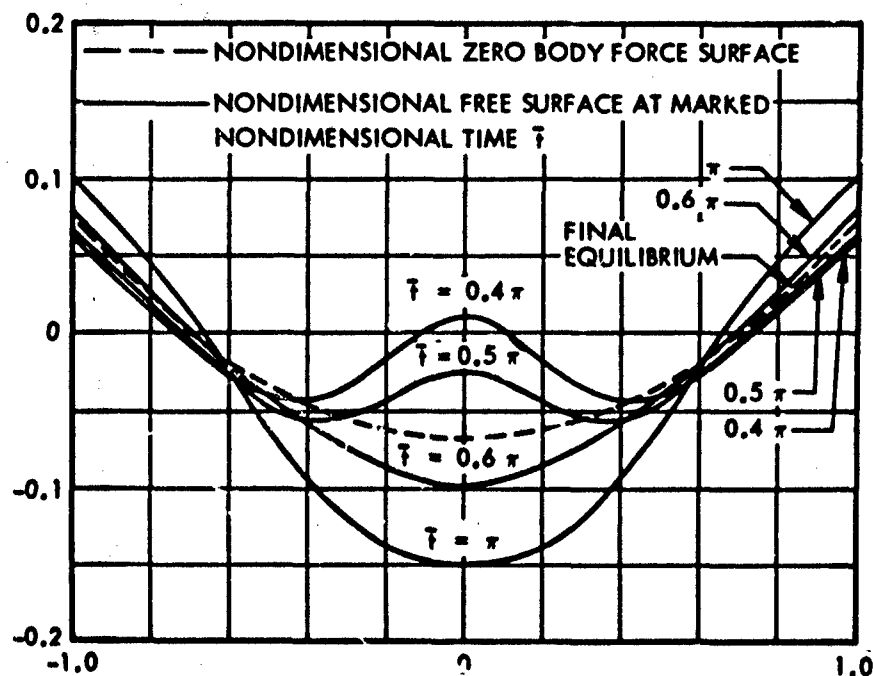


Fig. 4 Time History of Free Surface in a Cylindrical Container

mode) is of the order of 10 seconds for most test liquids. However, the time available in drop-tower experiments has been limited to approximately two seconds. It should be noted that a container of one cm characteristic dimensions has a period of 0.2 second for the first mode. Thus Shuleikin in Refs. 11 and 12, when testing small puddles of nonwetting liquids of 0.5 cm characteristic radius, was able to observe the oscillating response.

A physical explanation of the observed and predicted oscillation behavior can be stated in the following manner. The body forces in the initial steady state may be considered as the mechanism whereby the free surface is displaced from its zero body-force configuration (Refs. 2, 3, 4). It is easy to visualize that on sudden removal of body forces the free surface will move towards its preferred zero body-force configuration. The inertia of the liquid will carry it past that state as shown in Figs. 3 and 4; however, the excess curvature and surface tension will then act as a restoring force, inducing the resulting oscillations. On drawing an analogy with a simple harmonic oscillator, it can be shown that the free surface will oscillate around its zero body-force configuration.

Let us now consider the validity of the assumptions that the free-surface slope is at all times small and that v^2 is small with respect to ϕ_t provided only that $\theta \approx \pi/2$. An examination of the solution for the free surface shape in the form $\bar{S} = \bar{f} + \bar{d}$ for either the two-dimensional or cylindrical container shows that when either \bar{f} or \bar{d} dominates corresponding to small or large Bond number, respectively, in the initial steady state, the maximum value of \bar{S} is of the order $\cot \theta$. Similarly one can show that the maximum slope of the free surface \bar{S} is also of the order of $\cot \theta$. In order to check the validity of the linearizing assumption that $1/2 v^2$ is small compared to ϕ_t , we evaluate both terms as given by the present solution. It is found that for the case of large Bond number in the initial steady state corresponding to maximum response motion, the ratio of $1/2 v^2$ to ϕ_t goes as $\cot \theta$. Hence, restricting $\cot \theta$ to a small value as compared to unity is equivalent to stating that $1/2 v^2$ is small compared to ϕ_t . From physical considerations we can see that the restriction that $\cot \theta$ be small limits the response to "small-amplitude motions". In the limit, i.e., $\theta \rightarrow \pi/2$, there is no response after the removal of body force, since the initial free surface shape is already in final equilibrium.

6 COMPARISON OF RESULTS WITH EXPERIMENTS

Mingert, et al, (Ref. 14) made drop-tower measurements of the time required for the vertex of the one-g free surface to traverse the straight-line distance to a point corresponding to the constant curvature static equilibrium position. These measurements led to the postulation of the following time behavior law for cylindrical containers, viz.

$$T = 0.146 \left(\frac{\rho}{\sigma} \right)^{1/2} (D)^{3/2}$$

where T is the elapsed time defined above and D is the diameter of the cylinder.

On examining Fig. 4 we find that the free surface vertex passes the predetermined point somewhere between $\bar{t} = \pi/2$ and $\bar{t} = 3\pi/2$. Interpolating between the two values, we obtain a value of T corresponding to $\bar{t} = 0.56\pi$. Therefore:

$$T = \frac{0.56\pi}{\omega_1} = \frac{0.56\pi(2)^{-3/2}}{(Z_1)^{3/2} [\tanh(Z_1 \bar{h})]^{1/2}} \left(\frac{\rho}{\sigma} \right)^{1/2} (D)^{3/2}$$

On substituting $Z_1 = 3.83$ and assuming \bar{h} to be of order unity, we have

$$T = 0.085 \left(\frac{\rho}{\sigma} \right)^{1/2} (D)^{3/2}$$

Since the drop-tower experiments (Ref. 14) were conducted with liquids with zero contact angles, the noted difference in the scaling constants for the time T is in large part due to the extent to which the experiment violates our linearizing assumptions.

An additional experimental finding in support of the present analysis is provided by the observation of a rise near the center of the free surface at very early times following release of the drop-tower package. (Private communication with Mr. Donald Petrash of NASA.) This rise of the free surface near the vertex is fully reconciled

by the results of this analysis. At times that are small compared to the period of first mode, the higher modes (which possess higher natural frequencies) manifest full wave amplitudes before the first mode has had time to produce a large drop in the vertex. A comparison of the period of oscillations of the first and second modes shows that:

$$\frac{\omega_2}{\omega_1} = \left(\frac{2\pi}{\kappa}\right)^{3/2} \approx 2.82 \text{ for the two-dimensional case}$$

$$\frac{\omega_2}{\omega_1} = \left(\frac{Z_2}{Z_1}\right)^{3/2} \approx 2.48 \text{ for the cylindrical case}$$

While the ratio of the period of the free oscillations is of course independent of the initial conditions, the solution indicates that the relative importance of the higher modes is increased as Bond number is increased in the initial steady state. For large Bond numbers the ratio of the displacements of second to first mode approaches:

$$\left|\frac{\bar{d}_2}{\bar{d}_1}\right| = \frac{\pi^2}{(2\pi)^2} \approx \frac{1}{4} \quad \text{for the two-dimensional container}$$

$$\left|\frac{\bar{d}_2}{\bar{d}_1}\right| = \frac{Z_1^2 J_0(Z_1)}{Z_2^2 J_0(Z_2)} \approx \frac{1}{4} \quad \text{for the cylindrical container}$$

Accordingly, it should be possible to observe an appreciable bulge of the free surface at the vertex when the displacement of the first mode is still small. In Figs. 3 and 4 the free surface shape is plotted at $\bar{t} = 0.375\pi$ and $\bar{t} = 0.4\pi$ for the two-dimensional and cylindrical containers, respectively, in order to show this phenomenon at its maximum. For the cylindrical container, the vertex bulge actually rises appreciably above the initial free surface.

Our previous result expressed as a dynamic displacement from the initial free surface can also be interpreted as an equivalent wave motion, $\bar{\eta}$, about a final equilibrium free surface, \bar{g} . Equating $\bar{S} = \bar{\eta} + \bar{g}$ to our previous result $\bar{S} = \bar{f} + \bar{d}$, we obtain for the two-dimensional case

$$\bar{\eta}(\bar{x}, \bar{t}) = -2 \cot \theta \sum_{n=1}^{\infty} (-1)^n \frac{\bar{\beta}^2 \cos(n\pi\bar{x})}{(n\pi)^2 (\bar{\beta}^2 + n^2 \pi^2)} \cos(\bar{\omega}_n \bar{t})$$

and

$$\bar{g}(\bar{x}) = \bar{f}(\bar{x}) + 2 \cot \theta \sum_{n=1}^{\infty} (-1)^n \frac{\bar{\beta}^2 \cos(n\pi\bar{x})}{(n\pi)^2 (\bar{\beta}^2 + n^2 \pi^2)}$$

where $\bar{f}(\bar{x}) = \frac{\cot \theta}{\bar{\beta} \sinh(\bar{\beta})} [\cosh(\bar{\beta}\bar{x}) - 1]$ is the initial equilibrium free surface.

Consider now the case when the Bond number, $\bar{\beta}^2$, is large in the initial steady state, corresponding either to large container dimension or load factor, N . We see that $\bar{f}(\bar{x}) \rightarrow 0$ and

$$\bar{g}(\bar{x}) \approx 2 \cot \theta \sum_{n=1}^{\infty} (-1)^n \frac{\cos(n\pi\bar{x})}{(n\pi)^2}$$

By simple Fourier analysis one can show that

$$\sum_{n=1}^{\infty} (-1)^n \frac{\cos(n\pi\bar{x})}{n^2} = \frac{\pi^2}{4} \left(\bar{x}^2 - \frac{1}{3} \right)$$

Therefore,

$$\bar{g}(\bar{x}) \approx \frac{1}{2} \cot \theta \left(\bar{x}^2 - \frac{1}{3} \right)$$

which is a solution to the linearized static equation for the free surface when body forces vanish. Furthermore, this solution satisfies the constancy of total liquid volume condition of

$$\int_0^1 \bar{g}(\bar{x}) d\bar{x} = \int_0^1 \bar{f}(\bar{x}) d\bar{x} \approx 0$$

Similarly one can easily show that the free surface shape in the cylindrical container, for the case when the Bond number is large in the initial steady state, can be expressed as

$$\bar{S}(\bar{r}, \bar{t}) = \bar{g}(\bar{r}) - 2 \cot \theta \sum_{n=1}^{\infty} \frac{\bar{\beta}^2 J_0(Z_n \bar{r})}{Z_n^2 (\bar{\beta}^2 + Z_n^2) J_0(Z_n)} \cos(\bar{\omega}_n \bar{t})$$

where $\bar{g}(\bar{r}) \approx \frac{\cot \theta}{2} \left(\bar{r}^2 - \frac{1}{2} \right)$ is a solution to the linearized static equation for the free surface when body forces vanish.

In the other limit, i. e., when the Bond number approaches zero in the initial steady state, we see that \bar{g} then approaches \bar{f} for either the two-dimensional or the cylindrical container, and that \bar{f} in this case is the zero body force equilibrium configuration. It naturally follows that $\bar{\eta}$ vanishes in this case since the free surface is already in final equilibrium.

With our free surface motion expressed as a wave motion about the final equilibrium configuration, one can clearly see that the contact angle remains constant during motion and is equal to the initial contact angle. This is a direct consequence of our linearized kinematic free surface shapes in Figs. 3 and 4 are plotted with this alternative interpretation of \bar{S} by taking into consideration the first three fundamental modes of $\bar{\eta}$.

7 REFERENCES

1. Unterberg, W., Congelliere, J., "Zero Gravity Problems in Space Power Plants: A Status Survey," ARS Journal, June 1962
2. Benedikt, E. T., "Ephydrostatics of a Liquid in a Rectangular Tank with Vertical Walls," Report ASL-TM-60-38, Northrop Corporation, November 1960
3. Reynolds, W. C., "Hydrodynamic Considerations for the Design of Systems for Very Low Gravity Environments," Report LG-1, Stanford University, September 1961
4. Li, Ta, "Hydrostatics in Various Gravitational Fields," Journal of Chem. Phys., Vol. 36, No. 9, May 1962
5. Paynter, H. L., "Time for a Totally Wetting Liquid to Reform from a Gravity-Dominated to a Nulled-Gravity Equilibrium State," AIAA Journal, Vol. 2, No. 9, September 1964
6. Anliker, M., Pi, W. S., "Effects of Geometry and Unidirectional Body Forces on the Stability of Liquid Layers," SUDAER No. 150, March 1963
7. Concus, P., "Capillary Stability in an Inverted Rectangular Channel," Second Symposium on Physical and Biological Phenomena Under Zero G Conditions, Los Angeles, California, January 1963
8. Satterlee, H. M. and Reynolds, W. C., "The Dynamics of The Free Liquid Surface in Cylindrical Containers Under Strong Capillary and Weak Gravity Conditions," Report LG-2, Stanford University, May 1964
9. Petrash, D. A., Nelson, T. M. and Otto, E. W., "Effect of Surface Energy on the Liquid-Vapor Interface Configuration During Weightlessness," NASA Technical Note D-1582, January 1963
10. Siegel, R., "Transient Capillary Rise in Reduced and Zero-Gravity Fields," Journal of Applied Mechanics, Vol. 28, No. 2, June 1961
11. Shufelkin, V. V., "Ground-Level Experiments With Weightless Fluids," Soviet Physics-Doklady, Vol. 6, p. 985, 1964

12. Shuleikin, V. V., "Secoud Series of Ground-Level Experiments With Weightless Fluids," Soviet Physics-Doklady, Vol. 8, No. 12, p. 1221, June 1964
13. Petrash, D. A., Zappa, R. F. and Otto, E. W., "Experimental Study of the Effects of Weightlessness on the Configuration of Mercury and Alcohol in Spherical Tanks," NASA Technical Note D-1197, April 1962
14. Siegert, C. E., Petrash, D. A. and Otto, E. W., "Time Response of Liquid-Vapor Interface After Entering Weightlessness," NASA Technical Note D-2458, August 1964
15. Siegert, C. E., Petrash, D. A. and Otto, E. W., "Behavior of Liquid-Vapor Interface of Cryogenic Liquids During Weightlessness," NASA Technical Note D-2658, February 1965
16. Randolph, B. W., "Linear Approaches to the Dynamics of Fluids Subjected to Time Varying Body Forces," Report 63-21, Northrop Space Laboratories, April 1963
17. Benedikt, E. T., "Scale of Separation Phenomena in Liquids Under Conditions of Nearly Free Fall," ARS Journal, February 1959
18. Landau, L. D. and Lifshitz, E. M., "Fluid Mechanics," Course on Theoretical Physics, Vol. 6, Pergamon Press, London, 1959
19. Courant, R. and Hilbert, D., Methods of Mathematical Physics, Interscience Publishers, New York, 1953
20. Gray, A., Mathews, G. B. and MacRobert, T. M., A Treatise on Bessel Functions and Their Applications to Physics, MacMillan and Company, Ltd., London 1931

ACKNOWLEDGEMENT

The author wishes to express his appreciation to Dr. Irving C. Statler and Mr. Leonard Segel for useful discussions and constructive criticisms during the course of this research effort and the preparation of this paper.

Appendix A

SOLUTIONS TO THE LINEARIZED EQUATIONS GOVERNING THE EQUILIBRIUM SURFACES IN THE PRESENCE OF BODY FORCES

A. The linearized governing Eq. (8) for the initial equilibrium surface is

$$f_{xx}(x) - \beta^2 f(x) = f_{xx}(x)|_{x=0}$$

for the two-dimensional container.

The solution consists of a homogeneous part f_H and a particular solution f_p . We obtain

$$f_x = f_H(x) + f_p(x) = Ae^{\beta x} + Be^{-\beta x} - \frac{f''(0)}{\beta^2}$$

On evaluating A, B, and $f''(0)$ using the boundary conditions:

at

$$x = 0; \quad f(x) = 0, \quad f'(x) = 0$$

at

$$x = \pm x_0; \quad |f'(x)| = \cot \theta$$

yields

$$f(x) = \frac{\cot \theta}{\beta \sinh(\beta x_0)} \left[\cosh(\beta x) - 1 \right]$$

B. The linearized governing Eq. (24) for the initial equilibrium surface is:

$$\frac{1}{r} \frac{d}{dr} (r f_r) - \beta^2 f(r) = \frac{1}{r} \frac{d}{dr} (r f_r) \Big|_{r=0}$$

for a cylindrical container.

The solution to the homogeneous equation is the modified Bessel's function (Ref. 20) and the particular solution is a constant, viz:

$$f(r) = A I_0(\beta r) - \frac{B}{\beta^2}$$

where

$$B = \frac{1}{r} \frac{d}{dr} (r f_r) \Big|_{r=0}$$

On evaluating A and B using the boundary conditions:

at

$$r = 0; \quad f(0) = 0$$

at

$$r = r_0; \quad f_r(r_0) = \cot \theta$$

yields

$$f(r) = \frac{\cot \theta}{\beta I_1(\beta r_0)} [I_0(\beta r) - 1]$$

Appendix B

CALCULATION OF THE CONSTANTS C_n IN EQUATIONS (19) AND (33)

A. Equation (19) for the two-dimensional container can be rewritten in the following form:

$$\frac{C_0 \sinh(\beta x_0)}{\alpha^2 \beta \cot \theta} - \sum_{n=1}^{\infty} a_n \cos k_n x = 1 - \cosh(\beta x) \quad (19a)$$

where

$$a_n = - \frac{C_n \omega_n \cosh(k_n h) \sinh(\beta x_0)}{\alpha^2 \beta \cot \theta}$$

Performing Fourier analysis on Eq. (19a) we obtain

$$a_0 = \frac{C_0 \sinh(\beta x_0)}{\alpha^2 \beta \cot \theta} = 1$$

and

$$a_n = \frac{2}{x_0} \int_0^{x_0} \cosh(\beta x) \cos \frac{n\pi x}{x_0} dx$$

Substitute

$$\cosh(\beta x) = \frac{1}{2} (e^{\beta x} + e^{-\beta x})$$

we obtain

$$a_n = (-1)^n \frac{2\beta}{x_0} \frac{\sinh(\beta x_0)}{\beta_0 + (n\pi/x_0)^2}$$

hence,

$$C_n = \frac{2 \cot \theta}{x_0} (-1)^{n+1} \frac{\alpha^2 \beta^2}{\omega_n \cosh(k_n h) [\beta^2 + k_n^2]} \quad \text{for } n = 1, 2, \dots, \infty$$

B. Equation (33) for the cylindrical container can be rewritten in the following form:

$$\frac{C_0 I_1(\beta r_0)}{\alpha^2 \beta \cot \theta} - \sum_{n=1}^{\infty} a_n J_0(k_n r) = 1 - I_0(\beta r) \quad (33a)$$

where

$$a_n = - \frac{C_n \omega_n \cosh(k_n h) I_1(\beta r_0)}{\alpha^2 \beta \cot \theta}$$

Performing Fourier-Bessel series analysis (Ref. 20) on Eq. (33a) we obtain

$$a_0 = \frac{C_0 I_1(\beta r_0)}{\alpha^2 \beta \cot \theta} = 1$$

and

$$a_n = \frac{2}{r_0^2 [J_0(k_n r_0)]^2} \int_0^{r_0} J_0(k_n r) J_0(\beta r) r dr$$

To evaluate a_n we let $u = J_0(k_n r)$, which satisfies the Bessel's equation

$$r^2 \frac{d^2 u}{dr^2} + r \frac{du}{dr} + k_n^2 r^2 u = 0 \quad (a)$$

and $v = I_0(\beta r)$ which satisfies the modified Bessel's equation

$$r^2 \frac{d^2 v}{dr^2} + r \frac{dv}{dr} - \beta^2 r^2 v = 0 \quad (b)$$

Combining (a) and (b), we obtain

$$(k_n^2 + \beta^2) r u v = \frac{d}{dr} \left(u r \frac{dv}{dr} - v r \frac{du}{dr} \right)$$

Integrating once, we have

$$(k_n^2 + \beta^2) \int_0^{r_0} u v r dr = r \left(u \frac{dv}{dr} - v \frac{du}{dr} \right) \Big|_0^{r_0}$$

Substituting for u and v , the above yields

$$\begin{aligned} (k_n^2 + \beta^2) \int_0^{r_0} J_0(k_n r) I_0(\beta r) r dr &= r_0 \left[\beta J_0(k_n r_0) I_1(\beta r_0) + k_n I_0(\beta r_0) J_1(k_n r_0) \right] \\ &= r_0 \left[\beta J_0(k_n r_0) I_1(\beta r_0) \right] \end{aligned}$$

since $J_1(k_n r_0) = 0$ (wall condition).

On substituting the above result in a_n we obtain

$$a_n = \frac{2\beta}{r_0} \frac{I_1(\beta r_0)}{(\beta^2 + k_n^2) J_0(k_n r_0)}$$

and

$$C_n = -\frac{2 \cot \theta}{r_0 J_0(k_n r_0)} \frac{\alpha^2 \beta^2}{\omega_n \cosh(k_n h) (\beta^2 + k_n^2)} \quad \text{for } n = 1, 2, \dots, \infty$$

PAPER 8

LOW-GRAVITY LIQUID REORIENTATION

By M. P. Hollister and W. M. Satterlee
LOCKHEED MISSILES & SPACE COMPANY

ABSTRACT

This paper describes an experimental study of the reorientation of liquids in cylindrical containers under the action of low and high acceleration (or gravity). Using a 25-ft drop facility, a series of experiments was performed with carbon tetrachloride as the liquid in a lucite cylinder of 3.16-cm radius. By accelerating the test specimen parallel to the cylinder axis during free fall, reorientation Bond numbers of 8.7 and 185 were produced. The resulting free-surface reorientation flow was observed photographically. In this manner, the reorientation behavior of liquids under low- and high-gravity conditions was investigated. Flat, convex, and concave tank bottom shapes as well as varying liquid depths were used.

In a related investigation conducted by another group, a numerical program was developed to calculate the time-dependent motion of the free surface of an inviscid, incompressible fluid subject to a constant or time-varying acceleration field acting along the cylinder axis.

Limitations in both the analytical and experimental portions of the program resulted in obtaining only qualitative correlation between the numerical program and experiments. Conclusions reached on the basis of this work and the experience of other investigators are:

- (1) For a given initial flatness of the free liquid surface, there is a value of reorientation Bond number below which a single large bubble forms and rises in a direction opposite to that of reorientation body forces. Above this value, the free surface breaks in a more complicated way, and liquid falls in the center of the cylinder following the body force direction.
- (2) When the initial free-surface shape is a segment of a sphere, only the single large bubble is formed.
- (3) The wavefront trajectory at the wall travels at less than the free-fall rate. For low B_R the wavefront response initially is more rapid due to the initial accelerating effect of surface tension.
- (4) The rise rate of the large central bubble formed as described above is reduced as the bubble approaches a hemispherical tank end.

NOMENCLATURE

English Symbols

a	Acceleration (cm/sec^2)
B	Bond number based on radius
d	Displacement; liquid wavefront displacement at cylinder wall (cm)
D	Diameter (cm)
F	Camera frame rate (frames/sec)
g_0	Unit gravitational acceleration = $980 \text{ cm}/\text{sec}^2$
h	Distance through liquid from liquid surface to end of tank, measured along cylinder axis (cm)
H	Original liquid depth (cm)
n	Frame number

English Symbols

r	Radial distance from cylinder axis (cm)
R	Test tank radius (cm)
t	Time (sec)

Greek Symbols

β	Kinematic surface tension, σ/ρ (cm^3/sec^2)
ρ	Liquid density (gm/cm^3)
σ	Liquid-gas surface tension (dynes/cm)
τ	Characteristic response time

Subscripts

c	Critical wavelength or cylinder radius
g	Normalized on "free fall" response time
R	Reorientation
s	Normalized on surface tension response time
t	Differentiation with respect to time

Superscript

$*$	Nondimensional quantity
-----	-------------------------

LOW-GRAVITY LIQUID REORIENTATION

1 INTRODUCTION AND SUMMARY

Low-gravity liquid reorientation is part of a class of liquid-gas, free-surface flow problems of interest in the study of liquid propellant behavior in rocket tanks under low-gravity orbit conditions. Low-gravity, free-surface flow includes such problems as propellant slosh, tank draining, and liquid-gas phase separation. Information generated in these and similar investigations is useful in those areas of optimization of vehicle design which call for such improvements in propellant management as passive propellant orientation or ullage rocket impulse conservation. Life-support equipment using a liquid as a working fluid and as part of a process in small containers also would benefit. Such aspects as the time required for the liquid to reorient to the tank bottom, and estimates of the rate and manner that the liquid drains from one end of a container to the other, are also of interest.

In the investigation reported here, liquid reorientation refers specifically to the flow of liquid from one end of a closed cylindrical container to the other under the action of a local acceleration parallel to the cylinder axis and directed toward the liquid from the gas. During this reorientation the liquid flows in an annular sheet along the tank walls, with the gas "rising" centrally into the liquid and ultimately assuming the well known Taylor bubble shape. However, with the flat initial surface shape characteristic of the high-gravity condition followed by a high reorientation Bond number, a central flow of liquid is generated in addition to the wall flow pattern; this central flow is delayed relative to the trajectory of the liquid wavefront at the wall. It is estimated that when the reorientation Bond number is less than 10, this central liquid flow will not occur and the gas will tend to form the Taylor bubble shape.

The objective of this program was to develop, through analytical and experimental correlation, approximate techniques to describe and predict the reorientation of liquids in low-gravity and high-gravity fields. Also, the experimental program was designed to provide more specific insight into the flow process than was obtainable in a series of

earlier investigations.* Finally, the additional experience gained in the technique of drop testing with controlled test accelerations will be applied in the design of the LMSC drop-test facility now planned.

This report describes the results of an analytical and experimental investigation of liquid free-surface behavior during axial flow from one end of a partially filled, enclosed, cylindrical container to the other. The flow is induced by virtual gravity acceleration acting normal to the initial liquid-gas interface and directed from the liquid to the gas. A numerical program was developed to calculate the time dependence of the free surface of an inviscid, incompressible fluid subject to a constant or time-varying acceleration field. Using the 25-ft drop facility at Stanford University, a series of experiments was performed with carbon tetrachloride in a lucite cylinder of 3.16-cm radius. By acceleration of the test specimen during free fall, reorientation Bond numbers of 8.7 and 185 were produced, inducing free-surface reorientation flow which was recorded photographically. In this manner, the reorientation behavior of liquid under low- and high-adverse gravity conditions was investigated, as was the terminal draining behavior of the liquid as the rising Taylor bubble approached the end of the tank.

Although certain restrictions encountered in the numerical solution, together with limitations in the experimental apparatus, prevented a quantitative correlation between the analytical and experimental results, qualitative agreement was noted. In addition, a number of specific noteworthy features of the liquid reorientation flow process were exhibited during the experimental program.

2 ANALYTIC PROGRAM

In a parallel effort within the overall propellant reorientation program at LMSC, an analytic description of the free-surface behavior during reorientation flow was developed by L. M. Perko and R. E. Moore.** The details of this work will be reported elsewhere. The results of the analysis are of interest to the extent of any correlation with the results the experimental program.

*Lockheed Missiles & Space Company. Test Report, Low-Gravity Liquid Reorientation Study, by M. P. Hollister and H. M. Satterlee, LMSC-A664570, Sunnyvale, Calif., 1 May 1964.

**L. M. Perko and R. E. Moore, "Inviscid Fluid Flow in an Accelerating Cylindrical Container," to be published in J. Fluid Mech.

The operation of the numerical program is not as yet entirely satisfactory, particularly when an essentially flat interface is imposed as the initial condition. The sensitivity of the solution to such factors as the smoothness of the initial surface and the size of the time steps for iteration, have not been fully determined. In addition, the numerical calculations are sensitive to the manner in which the effect of surface tension is included in the computation.

Work is in progress to improve the analytical description of the flow for incorporation into the numerical program.

3 EXPERIMENTAL PROGRAM

3.1 Description of the Test

The testing was performed with the 25-ft free-fall facility in the Thermosciences Laboratory at Stanford University. This facility provides approximately 1 sec of free-fall test time. Figure 1 shows schematically the configuration of the test equipment. The Stanford facility consists of a drag shield, hoist and release mechanism, pneumatic

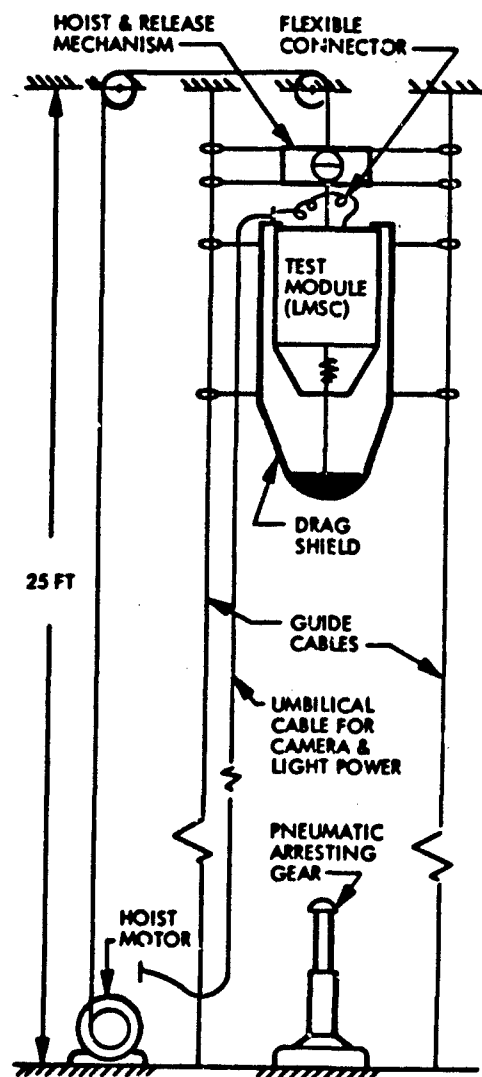


Fig. 1 Twenty-five-ft Drop Facility Layout

arresting gear, guide cables, and necessary electrical power and compressed air. The test module, test specimens, and instrumentation were provided by LMSC. Figure 2 shows the test module emplaced in the drag shield, with the shield side panels open.

The drag shield, which weighs 71 lb, encloses the test module and provides an essentially drag-free environment in a cylindrical cavity about 18 in. in diameter by 3-1/2 ft long. Prior to release into free fall, the drag shield is suspended on the test module at the upper ring flange. The test module in turn is connected to the hoist through a solenoid-activated mechanical release coupling. The hoist and release mechanism is shown in Fig. 3.

The test module provided by LMSC is shown in three photographic views of Figs. 4, 5, and 6, and schematically in Fig. 7. It consists of an aluminum structure on which is mounted the test tank, optical instrumentation, spring motors and acceleration tubes. The module weighed 36.9 lb with all equipment installed.

The test tank was a lucite block, 3.25 by 3.25 by 4.5 in., into which a cylindrical hole 3.16 cm in radius had been drilled to a depth of 10 cm. The open end of the hole was covered tightly during testing. A convex hemispherical bottom shape was obtained by attaching a lucite hemisphere at the tank bottom. To obtain the concave hemispherical tank bottom shape, a glass tube with one end formed into a hemisphere was inserted in the test tank; in this case the inner diameter was 5.64 cm.

The test liquid employed was carbon tetrachloride, which has a low ratio of surface tension to density, σ/ρ , of $16.8 \text{ cm}^3/\text{sec}^2$. This choice was made to provide as high a Bond number, B_R , as possible during reorientation.

The behavior of the liquid specimen in the test tanks during reorientation was recorded with high-speed motion picture photography, using a Milliken DBM4 camera with a 140-deg shutter operated at a nominal rate of 400 frames/sec. A 17-mm lens, shimmed out from the camera to provide focusing, was employed. The lucite test tank was

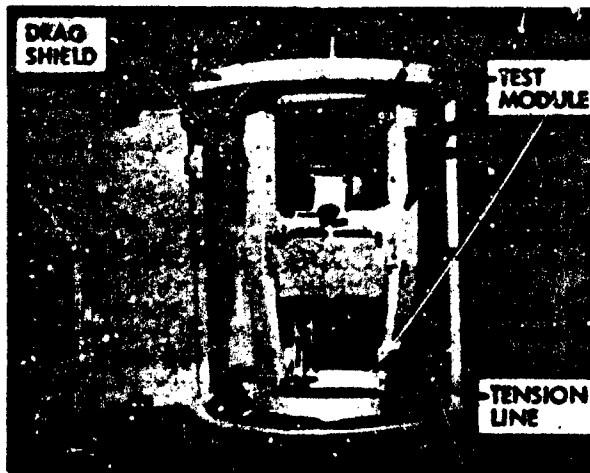


Fig. 2 Test Module in Drag Shield

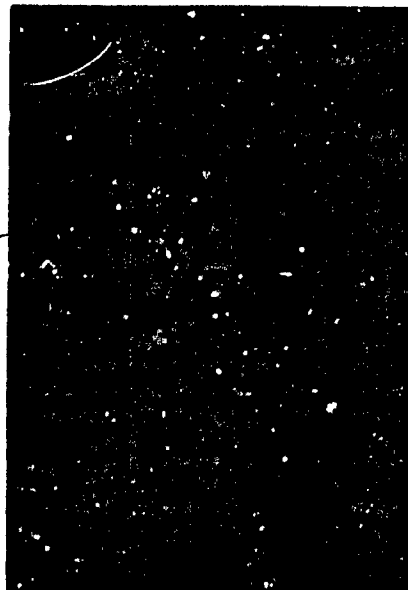


Fig. 3 Hoist and Release Mechanism

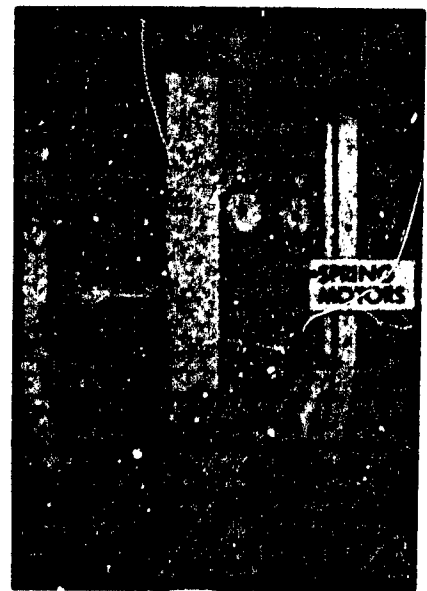


Fig. 4 Spring Motor Location

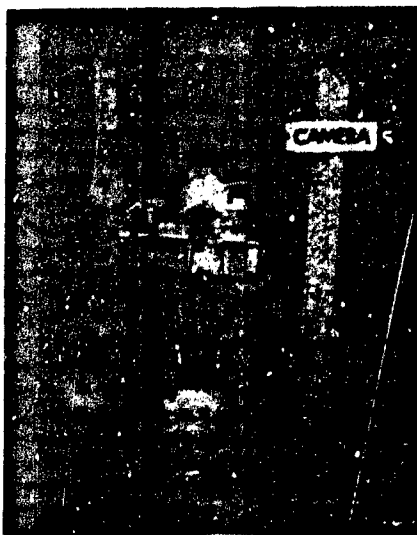


Fig. 5 Camera Location

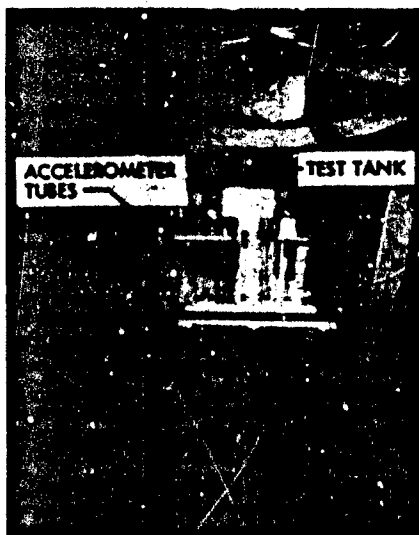


Fig. 6 Accelerometer and Tank Location

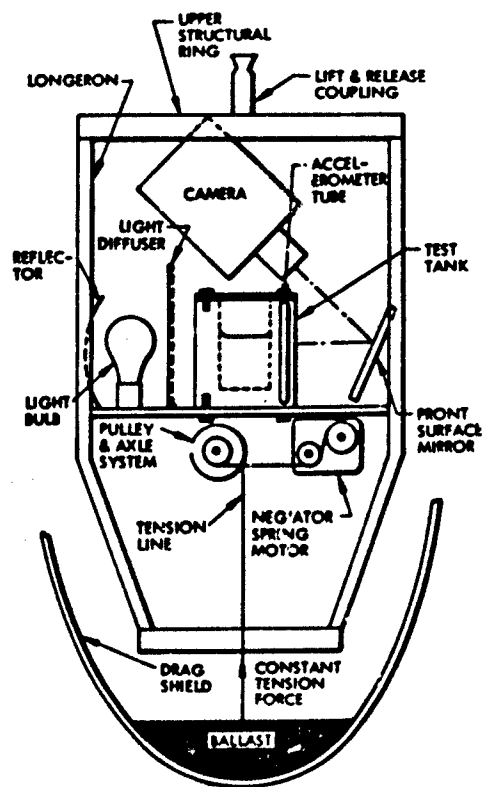


Fig. 7 Schematic Diagram of Test Module Inserted in Drag Shield

back-lighted with a 75-w opal photo-enlarger bulb behind a frosted-plastic diffuser screen. In combination with the test fluid employed, the arrangement provided excellent liquid-gas interface discrimination and minimum refractive distortion. Figure 8 is an example of the pictorial record obtained.

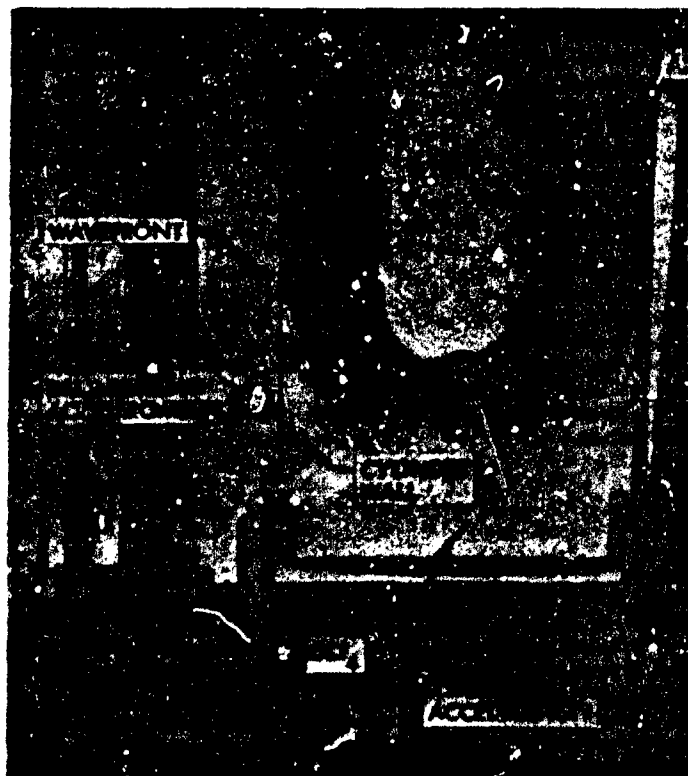


Fig. 8 Liquid Reorientation ($B_R = 8.7$)

The camera's field of view also included an accelerometer, adjacent to the test tank with axes parallel to the tank's cylindrical axis, consisting of an evacuated glass tube containing a steel ball bearing. The camera record of the motion of the bearing with respect to the test module provided a rectilinear trajectory with which the capsule acceleration relative to a "freely falling" reference frame was determined.

To fix the instant of capsule release into free fall, a microswitch mounted on the release mechanism was opened by motion of one of the capsule release fingers - shutting off a light-trace signal and thus providing a time zero reference on the film. Timing light pips placed on the film at 0.01-sec intervals provided elapsed-time information. Displacements were measured from the film as a function of frame number with a precision film reader.

A 28-vdc supply provided electrical power to the camera and to the 100-cycle timing light generator, while the first-motion light required a 150-vdc power supply.

Accelerations relative to a zero-g, or free-falling, reference frame were imposed on the test module by applying a constant force during the drop period, as diagrammed in Fig. 7. A Neg'ator spring motor has the property of a constant spring force over the length of its extension. Thus, the tension force in the line is constant as the motor reels in the line, pulling the drag shield and test module together following release into free fall. Since the mass of the test module is essentially constant (the only deviation is that produced by the movement of the relatively small amount of test liquid) this constant force yields a constant acceleration. By varying combinations of pulley sizes with a 1-lb or 5-lb force motor, a range of test accelerations is available. Figure 4 shows the Neg'ator motors mounted on the test module.

Primary test conditions were as follows; two runs were made at each setting:

- (1) Acceleration (nominal): 13.3 cm/sec^2 , 319 cm/sec^2
- (2) Initial liquid level, H/D: 0.7, 0.5, 0.3
- (3) Tank bottom shape: flat, concave hemispherical, convex hemispherical

For the convex hemispherical tank bottom shape no runs were made at $H/D = 0.3$. Tests were run at all other combinations of the listed conditions.

3.2 Acceleration Measurement

The acceleration experienced by the test capsule was computed from the photographic record of capsule motion with respect to a freely falling body - the ball bearing in the accelerometer tube. The displacements of the ball bearing from a reference point on the test module were measured from the film with a Gerber film reader. These displacements, along with the elapsed time corresponding to the respective film frames, provided a rectilinear trajectory from which the capsule acceleration was computed. The computation was complicated somewhat due to a constant drift rate superimposed on the acceleration trajectory by the relaxation of structural strain energy stored under $1 g_0$ conditions and released upon initiation of the drop; the net effect is a "springing away" of the ball bearing. The drift rate was noted also during the zero-g drop-test runs.

Since the acceleration values obtained are fundamental to the quantitative conclusions drawn in the investigation, and since some dispersion of acceleration values was obtained from the data reduction, the possible sources of error and uncertainty should be examined. Strictly speaking, we are concerned here with uncertainties in the following:

- (1) The repeatability and constancy in the Neg'ator force-versus-displacement rate characteristic during operation
- (2) Transcribing the data on ball-bearing displacement as a function of time, and the propagation of this uncertainty in the curve-fitting data reduction technique

In the experimental program sufficient time and funds were not available to investigate the dynamic characteristics of the spring motors. Thus a quantitative statement cannot be made concerning the first-listed uncertainty. The approach taken here was to determine the magnitude of the second source of uncertainty and from this and the gross features of the data, to infer the magnitude of the first source of uncertainty.

Table 1 lists data for the test runs for which time-versus-distance data were reduced. Approximately 50 to 100 readings were recorded for each of the high and low runs. Each set of readings was used as input to a least-squares polynomial fit routine written

Table 1
SELECTED TEST RUN DATA

Run No.	Acceleration (cm/sec ²)			Standard Deviation of Computed from Mean Acceleration (percent)
	Computed	Mean	Design	
91701C 91702B 92202B 92304B 92306B	317.1 316.9 298.6 309.4 313.6	311.1	319	±2.9 (4.6 cm/sec ²)
92203B 92204B 92205B 92206B 92301B	14.44 16.10 15.36 14.52 12.61	14.61	13.3	±10.2 (1.49 cm/sec ²)

for the IBM 7094 digital computer. In this routine, time was the independent variable and distance the dependent variable. Polynomials of second through fifth order were fitted to the input data. Although second-order polynomials fit the data reasonably well, the square of the deviation between input values and the calculated curve decreased as the order of the polynomial was increased. However, the deviation never became random; i.e., the input values systematically fluctuated about the calculated curve, indicating nonconstant behavior in the spring motor system.

A single-sample error analysis using the method presented by Kline and McClintock* was conducted to ascertain if measurement errors could account for the dispersion of the computer accelerations from run to run. A $\pm 2\sigma$ deviation corresponds approximately to the 20-to-1 odds used as a basis for measurement uncertainty in the error analysis. Table 1 indicates that a 2σ interval is ± 2.9 percent for the high-acceleration

*S. J. Kline and F. A. McClintock, "Describing Uncertainties in Single Sample Experiments," Mech. Eng., Jan 1953.

measurements and ± 10.2 percent for the low-acceleration measurements. The uncertainty interval or error contribution due to measurement data-reduction error as calculated is ± 4.4 and ± 1.5 percent for the high- and low-acceleration levels, respectively. Based on only three points, this error contribution is conservatively large. Nevertheless, these values indicate the degree of accuracy that can be expected from the acceleration-sensing technique. The relatively small deviation of the high-acceleration data indicates that any force-system nonrepeatability or nonlinearity of the 5-lb motor is not discernable within the basic accuracy of the data-reduction technique. However, for the low-acceleration cases it must be concluded that the dispersion of the acceleration values is due at least partly to nonrepeatability and nonlinearity, which are proportionately greater for the 1-lb motor.

3.3 Test Results

Data regarding the behavior of the liquid were taken from the motion picture film records by projecting selected frames onto graph paper and tracing wave profiles for specific times. In this manner, the wave profiles and trajectories of surface wave displacement versus time were obtained.

To present the data in an organized manner and interpret any trend in behavior, the time and distance measurements were nondimensionalized. Since the reorientation tests were essentially gravity dominated it seemed logical to base the nondimensionalization on free-fall behavior; also, such treatment was consistent with that used in the theoretical program. Displacement was nondimensionalized on tank radius, R . For all except the zero-gravity runs, time was nondimensionalized on "free fall" through a distance d as the characteristic response time. The zero-g data were compared with the response time for surface-tension-dominated phenomena. Thus we have:

$$r^* = r/R$$

$$d^* = d/R$$

$$h^* = h/R$$

$$t_g^* = t/\tau_g, \text{ with } \tau_g = \sqrt{\frac{2R}{a}}$$

where a is the test acceleration, and

$$t_g^* = t/\tau_g \text{ with } \tau_g = \sqrt{\frac{\sigma R^3}{\rho}}$$

where σ is the liquid surface tension and ρ the density.

Time, t , is related to the film frame number by the relation

$$\Delta t = \frac{\Delta n}{F}$$

where Δn is the number of frames elapsed during the time interval Δt and F is the camera frame rate (which was constant over each test run within ± 1 percent).

For the test conditions imposed, the pertinent parameters were the following:

R	= 3.16 cm for flat bottom, 2.8 cm for concave
σ/ρ	= 16.8 cm ³ /sec ² for CCl ₄
a_{low}	= 14.61 cm/sec ² (B_R = 8.7 for flat bottom, 6.8 for concave)
a_{high}	= 311 cm/sec ² (B_R = 185 for flat bottom, 145 for concave)
$\tau_g(\text{high } B_R)$	= 0.143 sec
$\tau_g(\text{low } B_R)$	= 0.658 sec
τ_g	= 1.372 sec

3.3.1 Wave Profiles. Figures 9 through 11 display normalized wave shapes in cross section, traced directly from the film records at selected nondimensionalized times.

To compare the behavior of the low and high B_R flow patterns at each H/D level, the low and high B_R profiles are displayed together. The left half of the cylinder contains the wave profiles for the low-reorientation-Bond-Lumber cases, while those

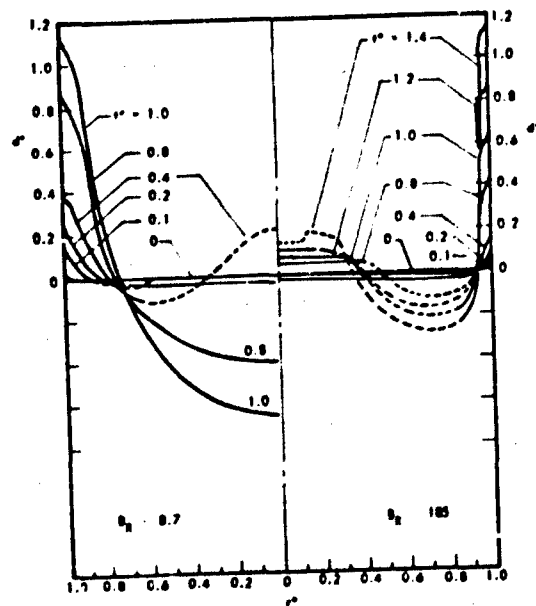
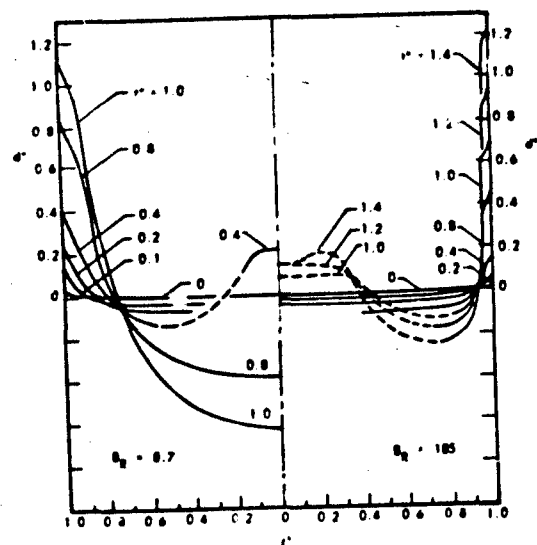


Fig. 9 Wave Profiles - $H/D = 0.5$ (top) and $H/D = 0.7$

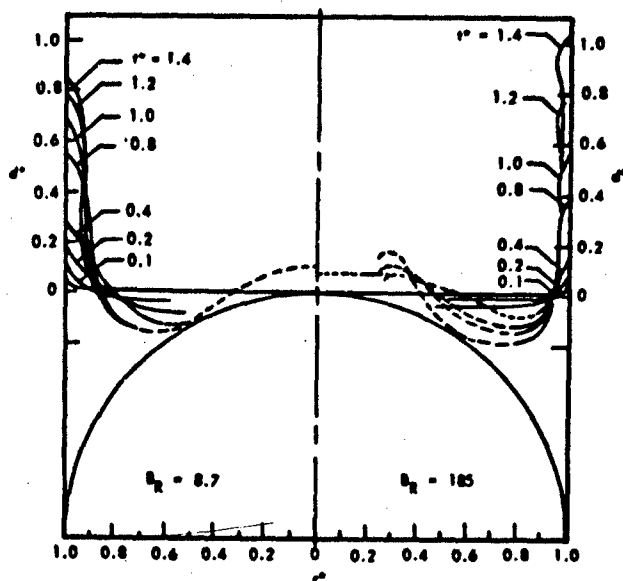
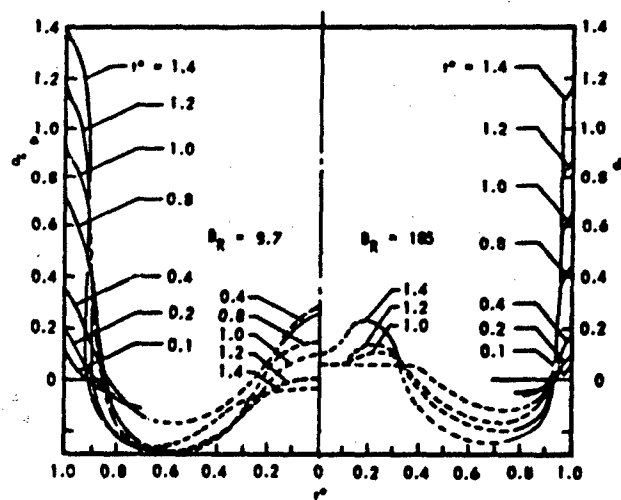


Fig. 10 Wave Profiles - $H/D = 0.25$ (top),
and $H/D = 0.5$ With Convex Tank Bottom

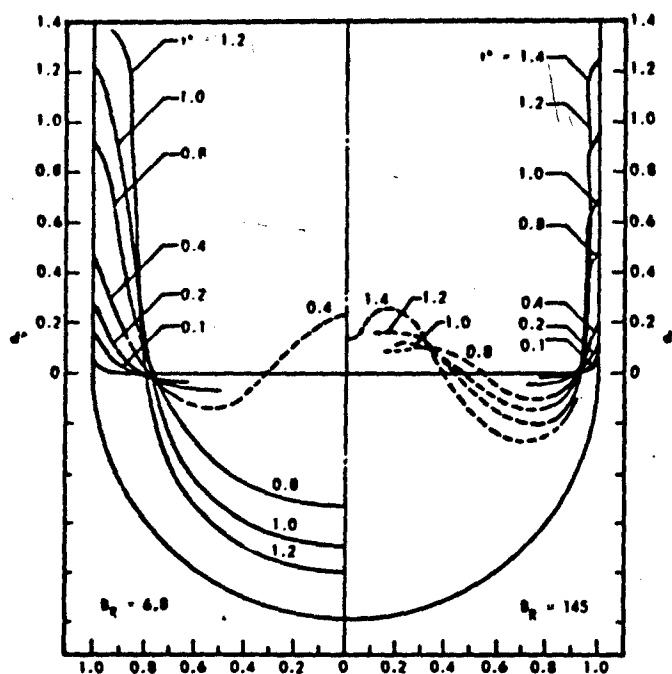


Fig. 11 Wave Profiles - $H/D = 0.5$ With Concave Tank Bottom

wave profiles to the right of the centerline occurred during the high-reorientation-Bond-number runs.

A number of features of these wave profiles will be discussed. At the outset it must be emphasized that the shape of the wavefront immediately adjacent to the wall (i.e., the leading edge of the wave) for $r^* \geq 0.96$ was not defined clearly on the film, due to the optical refraction. Accordingly some extrapolation was necessary to fix the position of this leading edge. Dashed-line portions of the wave shape traces (Figs. 9 through 11) also indicate regions where the exact position of the liquid surface either could not be seen or was distorted by refraction. In these cases also, interpolation between known points was employed to "fair in" the surface shape.

For all H/D values and bottom shapes shown in the figures and within the t^* value range obtained, the response of the low B_R waves in terms of progression along the wall is more rapid than in the high B_R cases. (This feature will be discussed further below.) The forms of the low B_R surface shapes differ markedly from those in the high B_R cases. The high B_R wall sheets are thinner, with correspondingly greater local surface curvature at the leading edge of the wave.

Perhaps the most striking feature is the appearance of a "hump" or wave located in the center of the cylinder. This initial wave occurs in all cases including the surface reorientation during the zero-g run. For the high B_R reorientation cases, this central wave grows in amplitude continuously and develops a secondary wave or central depression. However, in the case of the low B_R runs, the initial growth of the central wave under the influence of the local gravity is arrested and reversed, causing the decay and eventual disappearance of this central axial flow.

The different behavior of this central wave is due to the stabilizing effect of the liquid surface tension in the case of the low B_R flow. Based on the flat interface theory (90-deg contact angle) as presented in another report,* the criterion for stability of a surface wave in a cylindrical container is that the Bond number based on tank radius not exceed 3.59. Since the low reorientation Bond number cases were run at $B_R = 8.7$, we can scale the critical dimension for wave stability, r_c^* :

$$\frac{B_{crit.}}{B_R} = \left(\frac{r_c^*}{r_R} \right)^2 = \frac{(r_c^*)^2}{1}$$

*Stanford University Department of Mechanical Engineering, The Dynamics of the Free Liquid Surface in a Cylindrical Container Under Strong Capillary and Weak Gravity Conditions, by H. M. Satterlee and W. C. Reynolds, Test Report LG-2, Stanford, Calif., 1 May 1964.

$$r_c^* = \sqrt{\frac{B_{crit.}}{B_R}} = \sqrt{\frac{3.39}{8.7}}$$

$$r_c^* = 0.625$$

Examination of the wave profiles for $B_R = 8.7$ shows that the central half wavelength measured from the tank centerline is less than this value. Thus the wave perturbation generated in this case is stable and does not grow without limit. In the high-acceleration case where $B_R = 185$, the stable half wavelength is scaled at $r_c^* = 0.135$. The central wave occurring in these cases has a larger characteristic dimension and hence is unstable.

It is felt that the singular features of these free-surface flows during reorientation that have been noted above can be explained, at least qualitatively, in terms of the surface shape just prior to the test period. Since the test cylinder radius was 3.16 cm, the initial Bond number under $1 g_0$ was 580 with the correspondingly flat initial surface shape. The meniscus at the wall provides the initial surface perturbation for the unstable wall wave growth during reorientation. This vertical flow along the wall is fed with liquid from the annular region at the surface adjacent to the wall. The potential for flow into this region from the liquid in the center is low due to the flat configuration and the resulting absence of a pressure gradient. Thus, an annular depression is developed adjacent to the wall leaving a standing wave in the center of the tank. Whether this center wave grows in amplitude or is stabilized such that the central liquid is forced to flow outward and down the wall is dependent on the ratio of the surface tension to hydrostatic pressure gradients as expressed by the reorientation Bond number.

3.3.2 Wavefront Trajectories. The trajectories of the liquid wavefront at the cylinder wall were recorded and are shown in Fig. 12. The displacement of the liquid at the wall, d^* , is measured from original liquid level at the wall. All times are normalized on free-fall behavior except the zero-gravity tests. Included on this plot for reference is the free-fall trajectory curve, $d^* = (t^*)^2$ for a particle initially at rest.

The most obvious feature displayed in Fig. 12 is the more rapid response of the low B_R reorientation wavefront compared with those of the runs for $B_R = 185$. After this initial lead is obtained, the low B_R trajectories appear to parallel those for the high B_R .

The equilibrium location of the liquid front at the wall under a zero-g condition with a hemispherical shape (zero contact angle) has been indicated at $d^* = 0.57$. Beyond this point, the initial accelerating effect of surface tension in relaxing from the high Bond number initial condition is no longer present, and the wavefront trajectory appears to parallel that for the high B_R cases.

Except for the case where $H/D = 0.3$ and $B_R = 8.7$, no initial liquid level or tank bottom effect is discernible as far as wave growth at the wall is concerned.

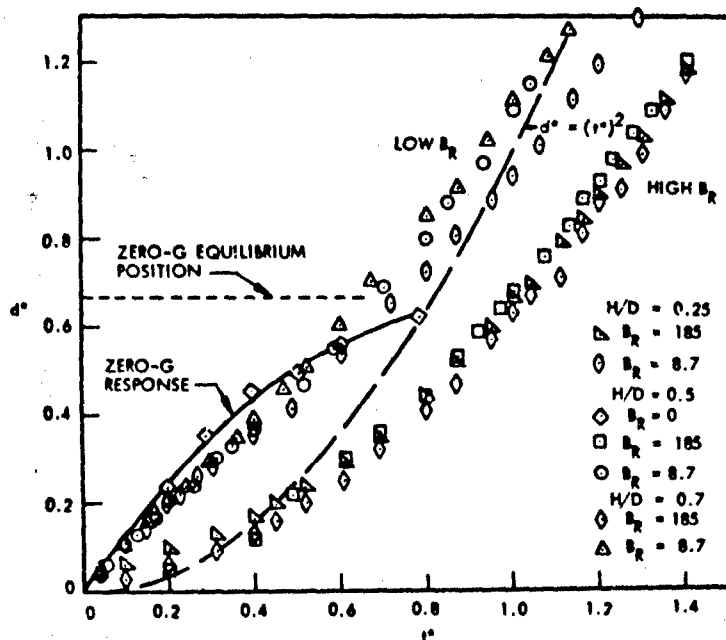


Fig. 12 Wall Wavefront Trajectories

The difference in response of the high B_R and low B_R wavefronts at the wall is an effect of the gravity-dominated initial condition. Figure 12 shows that the character of the response of the low B_R flow is initially similar to that for the zero-g reorientation (Fig. 13), which was surface-tension dominated. The initial surface shape is stressed relative to the zero-g configuration. Since the reorientation flow passes through this condition when the gravity vector is reversed, the initial effect of surface tension is to aid the reorientation. In the case of the low B_R flow, this additional force is noticeable, whereas for the high B_R , gravity-dominated flow, it is not.

Another feature, displayed in Fig. 12, is the departure of the wavefront trajectories from free-fall behavior. The behavior was noted also by Emmons, Chang, and Watson

in a series of experiments on the instability of finite surface waves.* They report a wavefront acceleration at a wall of 0.6 to 0.7 of the virtual gravity. The curve $d^* = 0.65 (t^*)^2$ fits the high B_R data very well. This slow response probably is due to a combination of viscous drag at the wall, thinning out of the sheet in accordance with

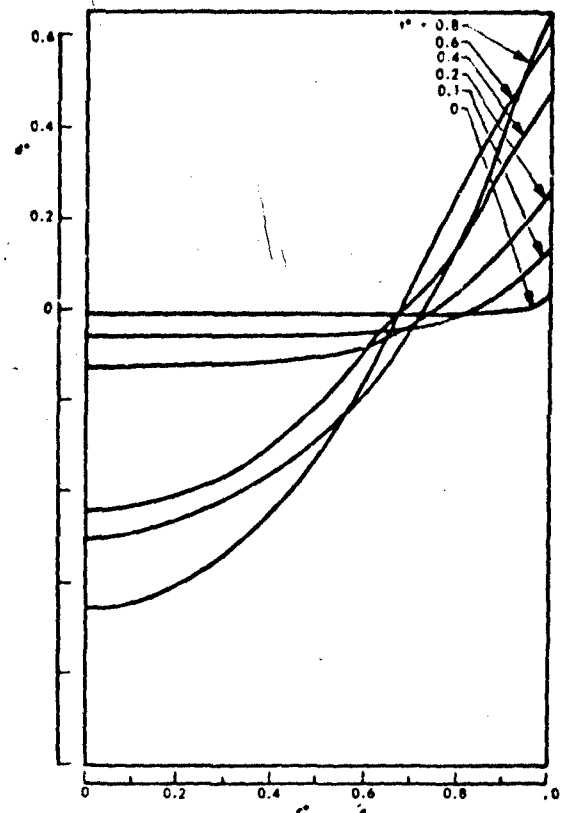


Fig. 13 Zero-g Wave Profiles

*H. W. Emmons, C. T. Chang, and B. C. Watson, "Taylor Instability of Finite Surface Waves," *J. Fluid Mech.*, Vol. 7, Part 2, 1960.

continuity, and the resulting locally high surface curvature at the wavefront. This curvature creates relatively high pressures at the wavefront that retard flow into this region to replenish the liquid being removed in the boundary layer.

For the low B_R wavefront trajectories the relation

$$d^* = 0.65(t^* + 0.35)^2$$

fits the data for the region $t^* > 0.3$. The initial effect of surface tension during these low B_R tests can be approximated by the relation

$$d^* = t^*$$

$$0 \leq t^* \leq 0.3$$

As shown in Fig. 10 the primary effect of the proximity of the tank end is that it produces a thinner wall sheet than would otherwise occur during a low B_R flow. The results, as shown in Fig. 12, are a slower wavefront response than in the other low B_R runs, and a behavior more similar to that for a

high B_R . This effect is indicated more clearly in Fig. 14, which shows data for the hemispherical tank bottom shapes.

For the concave tank end, no bottom effect is apparent at $H/D = 0.5$. For the convex tank end, however, the effect of the protrusion of the tank end into the central liquid region again produces a slower wave response at the wall at $B_R = 8.7$, even in this case slower than that for the high B_R data.

3.3.3 Terminal Flow Effect. It was decided during the latter phase of the

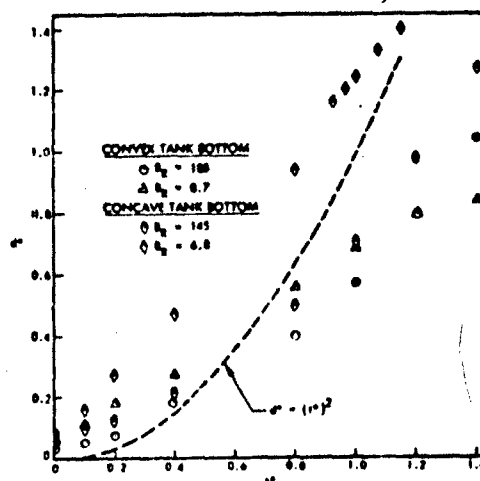


Fig. 14 Wall Wavefront Trajectories (Hemispherical Tank Bottom, $H/D = 0.5$)

program to extend the scope slightly to include an investigation of the terminal behavior of the centrally rising liquid-gas interface as it approaches the end of a hemispherical tank (concave toward the tank). This investigation required additional data reduction near the end of the concave tank bottom runs. These data were then compared with the simple theory developed in Appendix A. Figure 15 shows a typical test frame.

From the film record the displacement of the central liquid surface relative to the hemispherical tank end was measured, along with the elapsed time. Only the runs at $B_R = 6.8$ could be used since for the runs at $B_R = 145$ the standing central liquid wave previously discussed prevented the formation of the single-Taylor-bubble flow configuration. One test run did not provide sufficient time to set up a steady-state draining situation at some large initial liquid depth in order to observe the entire draining of the hemispherical tank end. Accordingly, data from runs at liquid depths of $H/D = 0.7$, 0.5 , and 0.3 were taken with the objective of observing the entire draining process in three segments. The data from each run were related to data from the former at the same h^* value. The data obtained in this manner have been plotted in Fig. 16. Equations (A.8) and (A.10) of Appendix A are also shown. Since the value of $t^* = 0$ for the Taylor bubble, Eq. (A.10) — and hence the position of the data on the t^* scale — is arbitrary, the curve for Eq. (A.10) was placed so as to match the slope of the data for the run at $H/D = 0.7$. Smoothed curves were drawn through these displacement points, and slopes were determined. The results are plotted in Fig. 17 along with the curves for Eqs. (A.6) and (A.9), Appendix A.

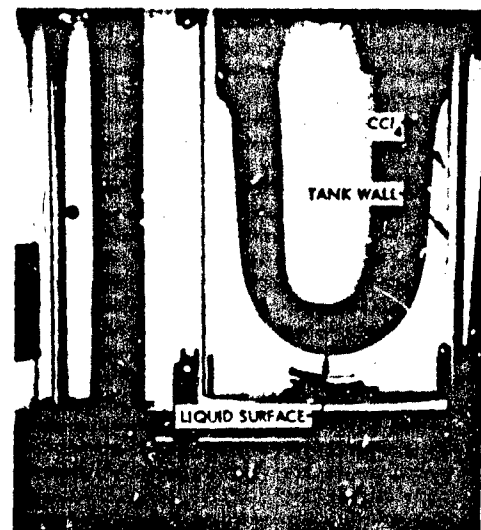


Fig. 15 Liquid Reorientation in Tank With Hemispherical End

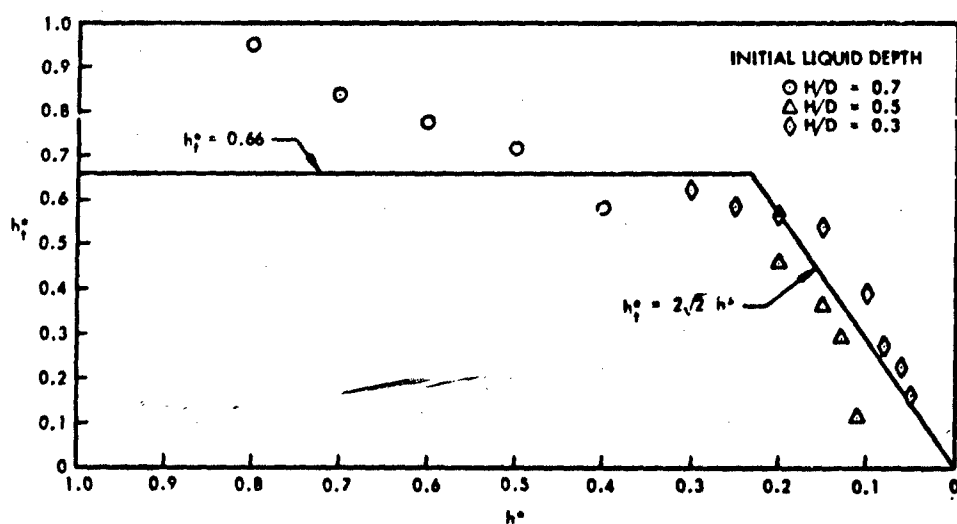


Fig. 16 Taylor Bubble Velocity Approaching Hemispherical Tank End

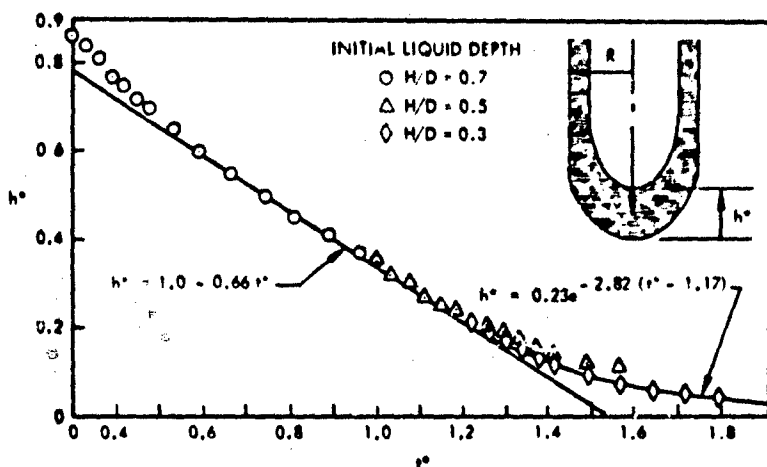


Fig. 17 Taylor Bubble Trajectory Approaching Hemispherical Tank End

Transient surface velocities are present during the transition from the flat initial surface shape to the steady-state draining flow pattern. To avoid these wave oscillations, readings were taken as late as possible during the test run. The higher-than-expected velocities for $1.0 < h^* < 0.7$ are residuals from this transition.

Notwithstanding these problems, examination of Figs. 16 and 17 indicates that a terminal effect is present as the Taylor bubble approaches the tank end. Although the h_t^* values for $H/D = 0.5$ do not agree with that for $H/D = 0.3$, at the same h^* the terminal draining effect, as represented by Eq. (A.8), provides a good approximation to the data.

3.4 Correlation Between Experimental and Analytic Results

During the final phase of the program an attempt was made to correlate the liquid behavior in the experimental runs with that predicted by the numerical program. The results were largely unsatisfactory. Starting from the flat initial condition, the numerical program developed unstable oscillations in the surface shape after a short period of time. Also, the manner in which the surface tension term is incorporated in the calculations seems to influence the progression of the calculation and to prevent the growth of surface shapes that can be correlated with experimental observation. Improvements in the numerical procedure are being investigated at this time, with the expectation that more satisfactory performance can be obtained.

Nonetheless, a certain degree of qualitative similarity in the two areas of investigation was noted. Figure 16 is a computer plot of liquid reorientation from a high Bond number (i.e., flat) initial surface shape with no surface tension during the reorientation. This corresponds to an infinite reorientation Bond number ($\beta = 1/B_R = 0$). The development of an annular trough next to the wall and the resulting central standing wave can be seen. This configuration was seen in the later stages of development in the experimental runs.

The computer plot shows the bottom of the trough at an r^* value of approximately 0.75. The wave profiles for the high B_R experimental runs also indicate the initial position for the bottom of the annular trough at $r^* \approx 0.75$.

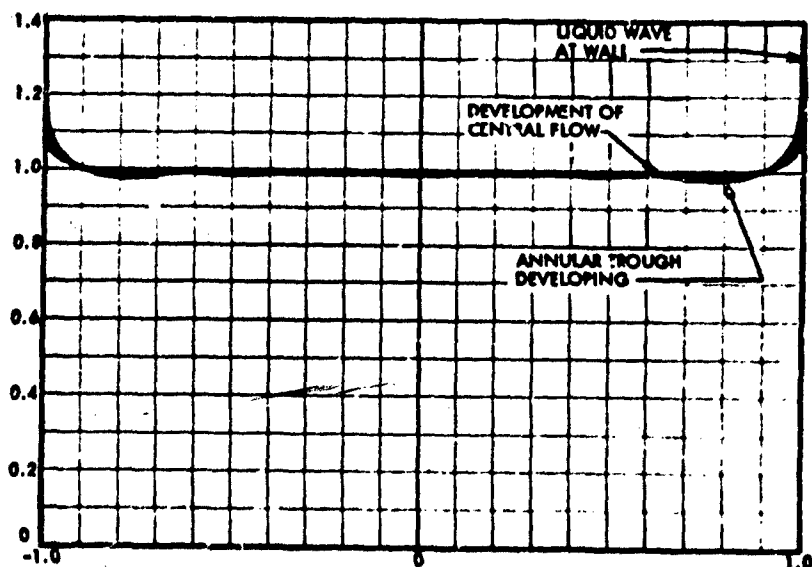


Fig. 18 Computer Plot of Liquid Reorientation From a Flat Interface
(Initial Bond No. = 220; Reorientation Bond No. $\rightarrow \infty$)

The numerical program behaved more satisfactorily when a highly curved (i. e., low- or zero-gravity) initial surface shape was used. Unfortunately, this initial condition could not be duplicated experimentally. Prior to initiation of the reorientation acceleration, a period of low or zero gravity is necessary to allow the formation of the highly curved surface shape. This feature for delayed reorientation during the drop was not designed into the Stanford drop-test facility.

4 CONCLUSIONS

A number of general features associated with the reorientation of liquids in closed, partially filled cylindrical containers were observed during this investigation. The

basic configuration of the flow is determined by the shape of the liquid surface at the onset of the adverse acceleration producing the reorientation flow. For a quiescent initial condition, as in this investigation, the meniscus at the wall is the dominant surface perturbation governing the subsequent liquid flow. The initial flow then becomes a cylindrical sheet of liquid flowing "down" the tank wall with the gas penetrating the central portion of the liquid.

For large reorientation Bond numbers ($B_R = 180$ or greater) the wall wavefront does not follow the normal free-fall trajectory. In these cases the wavefront trajectory can be approximated by the relation

$$d^* = 0.65 (t^*)^2$$

For reorientation under low-level body forces where $B_R \approx 10$, wavefront response is quicker in nondimensional form than that for the high B_R response. In these cases the wavefront trajectory has the form

$$d^* = 0.95 t^* \text{ for } 0 < d^* < 0.4$$

$$d^* = 0.65 (t^* + 0.35)^2 \text{ for } 0.4 < d^* < 1.2$$

The reorientation flow is further characterized by the combination of initial surface shape and the magnitude of B_R . For a high-gravity, flat initial surface shape the flow for a large B_R during reorientation generates centrally located standing waves that are themselves unstable and grow to produce liquid flow "down" the center of the tank. For $B_R < 10$, this central flow pattern is stabilized by surface tension so that the integral Taylor bubble shape results in the entire liquid mass traveling along the wall.

Investigations of terminal draining behavior as the liquid-gas interface approaches the top of a hemispherical tank end indicate that a decrease in the interface velocity occurs.

The departure of the interface velocity from the value given by Taylor* begins at an h/r of about 0.23. A good approximation for the time-displacement of the interface measured from the tank end is

$$h^* = 0.23 e^{2.82(1.17 - t^*)} \text{ for } t^* > 1.17$$

When the initial interface shape approximates the zero- g , spherical segment interface shape, the central bubble and wall sheet configuration always appears, even for high values of B_R .

Appendix A TERMINAL FLOW THEORY

As the liquid reorients toward the drain end of the tank, it flows in a relatively thin sheet which covers the cylindrical walls and the hemispherical forward end. If it is assumed that the liquid is incompressible and inviscid, and that its motion is irrotational, a simple theory can be developed to account for the effect of the hemispherical end. Referring to Fig. A-1, the continuity equation for the thin sheet of liquid in the hemispherical tank end, using subscripts to denote partial differentiation, is

$$h_t + h u_s + u h_s + \frac{1}{R} u h \cot \frac{\theta}{R} = 0 \quad (A.1)$$

where s is a curvilinear coordinate following a meridian of the tank walls. The Euler momentum equation in this direction can be written; if it is further assumed that at any point along the meridian in the thin sheet of liquid the velocity is a function of its

*R. M. Davies and G. E. Taylor, "The Mechanics of Large Bubbles Rising Through Extended Liquids and Through Liquids in Tubes," Proc. Roy. Soc. (London), Series A, Vol. 200.

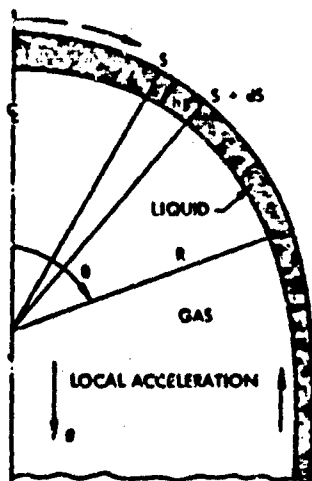


Fig. A-1 Coordinate System for Sheet Flow Analysis

location and not of time, then this equation can be integrated to give the Bernoulli equation along a streamline in the s direction:

$$\frac{p}{\rho} + \frac{u^2}{2} - gR \left(1 - \cos \frac{s}{R} \right) = \text{constant} \quad (\text{A.2})$$

The gas pressure in the tank is constant. It can be deduced that the liquid pressure also is constant. The Bernoulli equation; then, can be written

$$\frac{u^2}{2} = gR \left(1 - \cos \frac{s}{R} \right) \quad (\text{A.3})$$

If Eq. (A.1) is evaluated at $s = 0$, the result is

$$h_t + 2u_s = 0, \quad s = 0 \quad (\text{A.4})$$

Substitution of the velocity from the Bernoulli equation into Eq. (A.4) at $s = 0$ gives the following result, which is a velocity of the bubble near the hemispherical end:

$$-h_t = 2 \frac{h}{R} \sqrt{gR} \quad (\text{A.5})$$

This relation can be written in nondimensional form as

$$-\frac{dh^*}{dt^*} = 2\sqrt{2} h^* \quad (\text{A.6})$$

where

$$h^* = h/R$$

$$t^* = v \sqrt{\frac{2R}{g}}$$

Equation (A. 5) can be integrated to determine the time for the bubble to move through a given distance along the axis of the cylinder near the hemispherical end. The result is

$$\ln \frac{h_1}{h} = 2 \sqrt{\frac{R}{g}} (t - t_1) \quad (A. 7)$$

Rewriting Eq. (A. 7) in nondimensional form, we have

$$\ln \frac{h_1^*}{h^*} = 2 \sqrt{2} (t^* - t_1^*)$$

or

$$\frac{h_1^*}{h^*} = e^{2\sqrt{2}(t^* - t_1^*)} \quad (A. 8)$$

Taylor's theory* for the steady-state rise rate of a large gas bubble in a liquid-filled cylinder yields the relation:

$$v = K \sqrt{gR}$$

where R is the cylinder radius and g is the local gravitational acceleration. The value of K obtained by Taylor from potential flow theory is 0.464. Harmathy**

*R. M. Davies and G. E. Taylor, "The Mechanics of Large Bubbles Rising Through Extended Liquids and Through Liquids in Tubes," Proc. Roy. Soc., Vol. 200.

**T. Z. Harmathy, "Velocity of Large Drops and Bubbles in Media of Infinite or Restricted Extent," Am. Inst. Chem. Engr. J., Vol. 6, No. 2, Jun 1960.

reports an effect of surface tension on the gas rise rate. Based on the experimental data of Hutton, Dumitrescu, Davies, Taylor, et al., Harmathy specifies a value for K of 0.46 for the reorientation Bond number of 8.7 obtained during this low- g reorientation test. This value for K will be used to check the correlation of the end-effect theory.

If h is the distance from the tank end to the rising bubble interface along the cylinder axis, we can write

$$\frac{dh}{dt} = -v = -0.46\sqrt{gR}$$

which upon normalization becomes

$$\frac{dh^*}{dt^*} = -0.66 \quad (\text{A.9})$$

Integrating between h_0 at t_0 and h at t , we have

$$h^* - h_0^* = -0.66(t^* - t_0^*)$$

Setting $h_0^* = 1$ and $t_0^* = 0$ yields

$$h^* = 1 - 0.66 t^* \quad (\text{A.10})$$

To connect the steady-state relation with the end-effect theory and obtain values for h_1^* and t_1^* we equate the bubble velocities as represented by Eqs. (A.6) and (A.9), yielding $h_1^* = 0.23$. For this value of h_1^* we obtain $t_1^* = 1.17$ from Eq. A-8.

PAPER 6

INTERFACIAL STABILITY OF LIQUID LAYERS ON ELASTIC SURFACES

By R. D. Smith

LOCKHEED MISSILES & SPACE COMPANY

The material in this paper will constitute part of a dissertation to be submitted for the Ph.D. Degree at Stanford University, Department of Aeronautics and Astronautics.

ABSTRACT

The criteria associated with the dynamic stability of a liquid layer supported by an elastic surface are investigated theoretically by means of a linear vibration analysis. The investigation takes into consideration certain aspects concerning the orientation and stability of liquids stored in elastic containers of space vehicles operating under low-gravity conditions. It was assumed that a layer of incompressible, inviscid fluid having a flat liquid-gas interface is stored in a two-dimensional rectangular channel having either flexible walls or a flexible floor. These flexible surfaces are elastic plates supported at their edges in such a manner that the middle surfaces undergo only bending deflections. Moreover, the boundary conditions are assumed to be of the simple homogeneous variety representing either clamped or hinged edges.

To assess low-gravity conditions realistically, the effect of surface tension at the free surface of the fluid layer is taken into account. Particular emphasis is given to the

study of the individual effects of the flexibility of the channel walls and floor on the stability criteria. The influence on stability of fluid depth, plate bending stiffness, and edge conditions is also examined. A simplified analysis is used to evaluate in a qualitative manner the nonlinear effects due to in-plane deflections of the middle surface of the flexible floor.

The dynamic stability criteria are given in the form of a set of inequalities involving the net unidirectional body force intensity g , both for channels with rigid walls and flexible floors, and for channels with rigid floors and flexible walls. In addition, verification of these criteria for antisymmetric oscillations of the fluid in the channel having rigid walls and a flexible floor is presented in terms of a plot of the squares of the first eight eigenfrequencies of the system versus the body force intensity g . A result of particular interest with regard to the design of elastic fluid containers for space vehicles is that, for a channel having a flexible floor, there is a finite upper bound for the range of values of g required for the dynamic stability of the system. This upper bound increases monotonically with the bending stiffness of the channel floor.

NOMENCLATURE

English Symbols

a	Half the undeformed length of the flexible floor
c, f	Arbitrary functions of time
E	Young's Modulus
g	Net unidirectional body force intensity
G	A modified Green's function
h	Height of the fluid layer above the origin of coordinates at static equilibrium
L	Height of the undeformed flexible walls
m	Mass per unit area of the flexible floor and walls
p	Pressure field in the fluid
p_0, p_1	Constant external gas pressures

q_1, q_2, q_3	Arbitrary functions of time
T	Time
u, w	Surface tension
$\bar{V} = (V_x, V_z)$	Total displacements of a point at the middle surface of the flexible floor in the +x and -z directions
\bar{w}	Two-dimensional vector velocity field of the fluid
\tilde{w}	Static component of w
w_1, w_2	Dynamic component of w
\bar{w}_1, \bar{w}_2	Total displacements of the middle surface of the flexible walls at $x = -a$ and $x = a$ respectively
\tilde{w}_1, \tilde{w}_2	Static components of w_1 and w_2
(x, y, z)	Dynamic components of w_1 and w_2
	Cartesian coordinates

Greek Symbols

α	Separation constant
$\bar{\nabla} = \left(\frac{\partial}{\partial x}, \frac{\partial}{\partial z} \right)$	Two-dimensional gradient operator
δ	Thickness of the flexible walls and floor
n	Free surface displacement from static equilibrium in the +z direction
ν	Poisson's ratio
ρ	Density of the fluid
σ_n	Eigenfrequencies associated with free vibration of the flexible floor
$\tilde{\phi}, \phi$	Velocity potential functions
$\psi_n(x), \psi_n(z)$	Sets of orthonormal eigenfunctions for the respective problems of the free vibration of the flexible floor and walls
ω	System eigenfrequency

INTERFACIAL STABILITY OF LIQUID LAYERS ON ELASTIC SURFACES

1 INTRODUCTION

An important consideration in the design and operation of space vehicles is the ability to predict the location of various stored liquids in their respective containers in a low-gravity environment. Prediction is necessary so that the engine and the life-support equipment may be activated at the proper time. An important step in predicting the location and orientation of stored masses of liquid is to determine any dynamic instabilities that may arise for motions of the liquid about given states of static equilibrium. Many of the studies performed in this area are concerned with evaluating the effects of surface tension at the liquid-gas interface, and of the body force distribution on the dynamic stability of static-equilibrium liquid configurations in containers having various geometries. References 1 through 3 are representative of such analyses.

R. M. Beam (Ref. 1) has obtained dynamic stability criteria for layers of liquid of uniform depth spread over rigid cylindrical and spherical surfaces. Wen Yi Pi (Ref. 2) considered various two- and three-dimensional containers whose surfaces (obtained by an inverse method) were not representable in a simple manner in a coordinate system where the "separation of variables" technique may be applied to Laplace's equation. A flat-bottomed cylindrical container was examined by H. M. Satterlee (Ref. 3) who also investigated the effects on the stability criteria of the equilibrium contact angle and the dynamic variation in the contact angle at the liquid-gas interface. In all cases the analyses were concerned with rigid containers. The liquid storing containers used in the space vehicles do, however, exhibit elastic properties. This is particularly true of the fuel tanks that are thin-walled structures with dimensions about the same as the overall dimensions of the vehicle.

This paper presents the results of a study of the effects that container flexibility has on the stability criteria associated with the stored liquid at a given state of static equilibrium.

The analysis will concern itself with a two-dimensional channel-like container, in which is stored a layer of incompressible inviscid fluid having a flat static equilibrium-free surface. The floor is assumed to be a two-dimensional Bernoulli-Euler plate, while the walls are considered rigid. A linear vibration analysis is used to study the stability of small motions of the system about the static equilibrium configuration. Instabilities associated with the flexible floor that are predicted by the linear analysis are more extensively studied by a non-linear representation of the system.

Stability criteria are then determined for a container with flexible walls and a rigid floor. As in the previous case, the flexibility is simulated by simple Bernoulli-Euler plates.

2 ANALYSIS FOR THE CASE OF A FLEXIBLE FLOOR

2.1 Statement of the Problem

Consider a two-dimensional channel of rectangular cross section having rigid walls and a flexible floor, as shown in Fig. 1. In this channel is stored an incompressible,

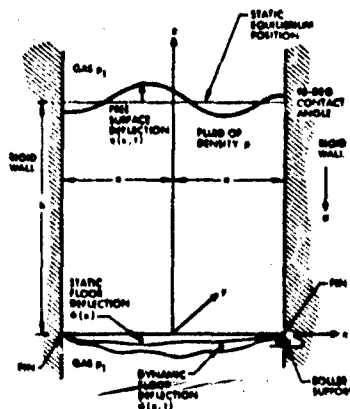


Fig. 1 Two-Dimensional Channel With Flexible Floor

inviscid fluid of density ρ and surface tension T . The surface of the fluid, as well as the region below the floor, is characterized by a constant gas pressure p_1 . It will also be assumed that the density of the gas above and below the fluid is so small that, during vibratory motions of the system, only a negligible amount of energy is lost by way of acoustic radiation into the gas.

Let (x, y, z) denote a cartesian coordinate system fixed in inertial space with origin located as shown in Fig. 1.

2.2 Consideration of the Dynamics of the Interior of the Fluid

Since the fluid has been assumed inviscid, the condition of equilibrium (in the sense of D'Alembert) at a point can be characterized as:

$$-\frac{\bar{\nabla} p}{\rho} - g \bar{\nabla} z = (\bar{\nabla} \cdot \bar{\nabla}) \bar{\nabla} + \frac{\partial \bar{\nabla}}{\partial t} \quad (1)$$

Since

$$(\bar{\nabla} \cdot \bar{\nabla}) \bar{\nabla} = \bar{\nabla} \left(\frac{v^2}{2} \right) - \bar{\nabla} \times \bar{\nabla} \times \bar{\nabla} \quad (2)$$

Equation (1) with the assumption of irrotational flow, i.e., $(\bar{\nabla} \times \bar{\nabla} = 0)$, becomes

$$\bar{\nabla} \left(\frac{v^2}{2} + gz + \frac{p}{\rho} \right) + \frac{\partial \bar{\nabla}}{\partial t} = 0 \quad (3)$$

Another consequence of the irrotationality of the flow is that there is a function $\tilde{\phi}$ such that

$$\bar{\nabla} = -\nabla \tilde{\phi} \quad (4)$$

Equation (3) then becomes

$$\bar{\nabla} \left(\frac{v^2}{2} + gz + \frac{p}{\rho} - \frac{\partial \tilde{\phi}}{\partial t} \right) = 0 \quad (5)$$

or

$$\frac{v^2}{2} + gz + \frac{p}{\rho} - \frac{\partial \tilde{\phi}}{\partial t} = f(t) \quad (6)$$

Where $f(t)$ is an arbitrary function of time. For convenience, $f(t)$ will be taken as

$$f(t) = gh + \frac{p_1}{\rho} + c(t)$$

where $c(t)$ is equally arbitrary and h is the height of the fluid layer above the origin of coordinates at static equilibrium.

We will also define

$$\phi(x, z, t) = \tilde{\phi}(x, z, t) + \int_0^t c(t) dt$$

Equation (6) then becomes

$$\frac{v^2}{2} + g(z - h) + \frac{p - p_1}{\rho} - \frac{\partial \phi}{\partial t} = 0 \quad (7)$$

Since the operator $\bar{\nabla}$ does not contain the variable t , Eq. (4) can be rewritten as

$$\bar{\nabla} = -\bar{\nabla} \phi \quad (8)$$

The analytic characterization of fluid incompressibility is

$$\bar{\nabla} \cdot \bar{V} = 0 \quad (9)$$

which means that

$$\nabla^2 \phi = 0 \quad (10)$$

Since the walls of the channel are rigid,

$$\left. \frac{\partial \phi}{\partial x} \right|_{x=\pm a} = 0 \quad (11)$$

2.3 The Dynamics of the Free Surface of the Fluid

The free surface of the fluid is assumed to have a static equilibrium position denoted by $z = h$ and a dynamic displacement in the $+z$ direction from the static equilibrium position denoted by $\eta(x, t)$ for the range $-a \leq x \leq a$. The microscopic interactions of the molecules of the liquid and the gas above it give rise to a macroscopically definable surface possessing a macroscopically measurable tension of constant magnitude. This surface can be simulated for the purposes of continuum mechanics by a massless prestretched membrane of constant tension T .

Another macroscopic manifestation of intermolecular interactions is the "contact angle" or the angle, measured in the fluid, at which the free surface joins the walls. In the interest of reducing the complexity of the analysis, the contact angle will be assumed to possess a value of 90 deg for any motion of the free surface. This assumption corresponds to the conditions:

$$\left. \frac{\partial \eta(x, t)}{\partial x} \right|_{x=\pm a} = 0 \quad (12)$$

The dynamic equilibrium, in the sense of D'Alembert, of an element of the continuum model of the free surface, can be expressed as:

$$-T \left\{ \frac{\frac{\partial^2 \eta}{\partial x^2}}{\left[1 + \left(\frac{\partial \eta}{\partial x} \right)^2 \right]^{3/2}} \right\} = p(x, h + \eta(x, t), t) - p_1 \quad (13)$$

Using Eq. (7), the pressure at the free surface can be expressed as:

$$p(x, h + \eta(x, t), t) = p_1 + \rho \left[\frac{\partial \Phi}{\partial t}(x, h + \eta, t) - \frac{V^2(x, h + \eta, t)}{2} - g\eta \right] \quad (14)$$

Substitution into Eq. (13) yields:

$$-T \left\{ \frac{\frac{\partial^2 \eta}{\partial x^2}}{\left[1 + \left(\frac{\partial \eta}{\partial x} \right)^2 \right]^{3/2}} \right\} = \rho \left(\frac{\partial \Phi}{\partial t} - \frac{1}{2} |\nabla \Phi|^2 \right) \Big|_{z=h+\eta} - g\eta \quad (15)$$

In addition to Eq. (15), there must be a restriction to the effect that no fluid passes through the idealized free surface membrane. This restriction takes the form of

$$\frac{D}{Dt} [z - \eta(x, t)] = 0 \quad (16)$$

Expanding the substantial derivative and using Eq. (8), Eq. (16) becomes

$$\left. \frac{\partial \eta(x, t)}{\partial t} + \frac{\partial \phi(x, z, t)}{\partial z} - \frac{\partial \phi(x, z, t)}{\partial x} \frac{\partial \eta(x, t)}{\partial x} \right|_{z=h+\eta(x, t)} = 0 \quad (17)$$

2.4 Considerations of the Dynamics of the Flexible Floor

The flexible floor will be characterized as a simply supported plate of infinite extent in the y direction that possesses the following parameters:

- E = Young's modulus
- ν = Poisson's ratio
- m = mass per unit width
- δ = thickness
- $2a$ = undeformed length

The total deflection of the middle surface of the plate from the coordinate plane, $z = 0$, in the $-z$ direction will be denoted by $w(x, t)$. It will be assumed that only simple bending takes place such that plane sections remain plane during deflection of the middle surface. It will also be assumed that the strain in the middle surface is negligible in comparison with the maximum strain due to bending. This assumption limits the validity of the analysis to the range of deflections for which $|w(x, t)| \ll \delta$. Further, this assumption gives rise to the requirement that one edge of the analytical model of the floor be on a roller support, as shown in Fig. 1. Also, the effects of shear deflections and rotary inertia will be neglected.

Under the above restrictions, the condition of the dynamic equilibrium, in the sense of D'Alembert, of an element of the floor can be written as

$$D \frac{\partial^4 w(x, t)}{\partial x^4} + m \frac{\partial^2 w}{\partial t^2} = p[x, -w(x, t), t] - p_1 \quad (18)$$

where

$$D = \frac{E\delta^3}{12(1-\nu^2)}$$

Using Eq. (7), we obtain

$$p(x, -w, t) = p_1 + \rho \left[\frac{\partial \Phi}{\partial t}(x, -w, t) - \frac{1}{2} |\nabla \Phi(x, -w, t)|^2 + g(h + w) \right] \quad (19)$$

Substitution of Eq. (19) into Eq. (18) yields

$$D \frac{\partial^4 w}{\partial x^4} + m \frac{\partial^2 w}{\partial t^2} = \rho \left[\frac{\partial \Phi}{\partial t}(x, -w, t) - \frac{1}{2} |\nabla \Phi(x, -w, t)|^2 + g(w + h) \right] \quad (20)$$

As in the case of the free surface, Eq. (20) must be accompanied by a kinematic condition given by

$$\frac{D}{Dt} [z - (-w(x, t))] = 0 \quad (21)$$

or

$$\frac{\partial \Phi(x, z, t)}{\partial z} + \frac{\partial \Phi(x, z, t)}{\partial x} \frac{\partial \eta(x, t)}{\partial x} - \frac{\partial w(x, t)}{\partial t} \bigg|_{z=-w(x, t)} = 0 \quad (22)$$

Since the plate is assumed simply supported at $x = \pm a$, the conditions

$$w(\pm a, t) = \frac{\partial^2 w(x, t)}{\partial x^2} \bigg|_{x=\pm a} = 0 \quad (23)$$

must be imposed.

2.5 Linearization of the Equations of Motion

The equations of motion given by Eqs. (15), (17), (20), and (22) may be linearized for those motions of the system in which the quantities

$$\begin{aligned} \eta & , \quad \frac{\partial \eta}{\partial x} , \quad \frac{\partial \eta}{\partial t} \\ w & , \quad \frac{\partial w}{\partial x} , \quad \frac{\partial w}{\partial t} \end{aligned}$$

and

$$\frac{\partial \phi}{\partial x} , \quad \frac{\partial \phi}{\partial z} , \quad \frac{\partial \phi}{\partial t}$$

are first-order small, while products of the dependent variables and their derivatives, and terms such as

$$\frac{\partial \phi}{\partial z} [x, h + \eta(x, t), t] - \frac{\partial \phi}{\partial z} (x, z, t) \Big|_{z=h}$$

are second-order small.

Equations (15), (17), (20), and (22) then become

$$-T \frac{\partial^2 \eta(x, t)}{\partial x^2} = \rho \left[\frac{\partial \phi(x, h, t)}{\partial t} - g\eta(x, t) \right] \quad (24)$$

$$\frac{\partial \eta(x, t)}{\partial t} = - \frac{\partial \phi}{\partial t} (x, z, t) \Big|_{z=h} \quad (25)$$

$$D \frac{\partial^2 w(x, t)}{\partial x^4} + m \frac{\partial^2 w(x, t)}{\partial t^2} = \rho \left[\frac{\partial \phi(x, 0, t)}{\partial t} + gw(x, t) + gh \right] \quad (26)$$

and

$$\frac{\partial w}{\partial t}(x, t) = \frac{\partial \phi}{\partial z}(x, z, t) \Big|_{z=0} \quad (27)$$

If the total floor deflection $w(x, t)$ is separated into a static deflection $\bar{w}(x)$ and dynamic deflection $\tilde{w}(x, t)$, and if a harmonic time dependence of the form

$$\begin{Bmatrix} \eta(x, t) \\ \tilde{w}(x, t) \\ \phi(x, z, t) \end{Bmatrix} = \begin{Bmatrix} \eta(x) \\ w(x) \\ \phi(x, z) \end{Bmatrix} e^{i\omega t} \quad (28)$$

is assumed, the initial value problem is converted to an eigenvalue problem of the form:

$$\frac{\partial^2 \phi}{\partial x^2} + \frac{\partial^2 \phi}{\partial z^2} = 0 \quad (29)$$

$$-T \frac{\partial^2 \eta}{\partial x^2} = \rho \left[i\omega \phi \Big|_{z=h} - g\eta \right] \quad (30)$$

$$i\omega \eta = - \frac{\partial \phi}{\partial z} \Big|_{z=h} \quad (31)$$

$$D \frac{\partial^4 w}{\partial x^4} - (m\omega^2 + \rho g)w = \rho i\omega \phi \Big|_{z=0} \quad (32)$$

$$i\omega w = \frac{\partial \phi}{\partial z} \Big|_{z=0} \quad (33)$$

$$\frac{\partial \phi}{\partial x} \Big|_{x=\pm a} = 0, \quad w(\pm a, t) = \frac{\partial^2 w(x, t)}{\partial x^2} \Big|_{x=\pm a} = 0 \quad (34)$$

where ω is the eigenvalue and

$$\begin{pmatrix} \eta(x) \\ w(x) \\ \phi(x, z) \end{pmatrix}$$

is the eigenvector.

2.6 Definition of Stability

The stability of the static equilibrium position denoted by $\tilde{w}(x, t) = \eta(x, t) = 0$ for a certain value of the net unidirectional body force magnitude g is defined in the paragraphs that follow.

The system governed by Eqs. (29) through (34) is stable (see Ref. 4) about the equilibrium position $\tilde{w}(x, t) = \eta(x, t) = 0$ if and only if, given $\epsilon > 0$, one can find $\gamma > 0$ so that

$$\left\{ [\tilde{w}(x, t)]^2 + [\eta(x, t)]^2 + \left[\frac{\partial \tilde{w}}{\partial t}(x, t) \right]^2 + \left[\frac{\partial \eta}{\partial t}(x, t) \right]^2 \right\}^{1/2} < \epsilon$$

for a given x and for all t whenever

$$\left\{ [\tilde{w}(x, 0)]^2 + [\eta(x, 0)]^2 + \left[\frac{\partial \tilde{w}}{\partial t}(x, 0) \right]^2 + \left[\frac{\partial \eta}{\partial t}(x, 0) \right]^2 \right\}^{1/2} < \gamma$$

Such a condition of stability can be assured if all the squares of the eigenfrequencies ω_k^2 , $k = 1, 2, 3, \dots$ are real and positive. Since the system is conservative, i.e., all the active forces can be derived from a potential function, the squares of the eigenfrequencies, ω_k^2 , will be real.

The stability criteria will then be defined as the set of values of g (assuming that all other parameters remain fixed) for which all the squares of the eigenfrequencies are positive.

2.7 Solution of the Eigenvalue Problem

The general solution of

$$\frac{\partial^2 \phi}{\partial x^2} + \frac{\partial^2 \phi}{\partial z^2} = 0$$

subject to

$$\left. \frac{\partial \phi}{\partial x} \right|_{x=\pm a} = 0$$

is

$$\begin{aligned} \phi(x, z) = & (C_0 + zD_0) + \sum_{\substack{n=1 \\ n \text{ odd}}}^{\infty} \sin(\alpha_n x) [C_n \cosh(\alpha_n z) + D_n \sinh(\alpha_n z)] \\ & + \sum_{\substack{n=2 \\ n \text{ even}}}^{\infty} \cos(\alpha_n x) [\bar{C}_n \cosh(\alpha_n z) + \bar{D}_n \sinh(\alpha_n z)] \quad (35) \end{aligned}$$

where $\alpha_n = n\pi/2a$ and $C_0, D_0, C_n, D_n, \bar{C}_n$, and \bar{D}_n are arbitrary constants to be determined.

The function $w(x)$ can be expressed as

$$w(x) = \sum_{n=1}^{\infty} U_n \psi_n(x) \quad (36)$$

where $\psi_n(x)$ constitute the set of orthonormal eigenfunctions of the problem

$$D \frac{d^4 \psi(x)}{dx^4} - m\sigma^2 \psi(x) = 0 \quad (37)$$

and

$$\psi(\pm a) = \left. \frac{d^2 \psi}{dx^2} \right|_{x=\pm a} = 0$$

and are given by

$$\psi_n(x) = \frac{1}{\sqrt{a}} \begin{cases} (-1)^{\frac{n-1}{2}} \cos\left(\frac{n\pi x}{2a}\right) & \text{for } n \text{ an odd integer} \\ (-1)^{\frac{n}{2}} \sin\left(\frac{n\pi x}{2a}\right) & \text{for } n \text{ an even integer} \end{cases} \quad (38)$$

with

$$\sigma_n^2 = \frac{D}{m} \left(\frac{n\pi}{2a} \right)^4$$

If the expressions given by Eqs. (35) and (36) are substituted into Eqs. (32) and (33), and use is made of the properties of the $\psi_n(x)$, the coefficients U_n may be eliminated. This gives rise to:

$$D_0 \left[m\sigma_k^2 - (m\omega^2 + \rho g) \right] P_k + C_0 \rho \omega^2 P_k + \sum_{\substack{n=2 \\ n \text{ even}}}^{\infty} \bar{D}_n \left[\alpha_n \left[m\sigma_k^2 - (m\omega^2 + \rho g) \right] P_{nk} \right] + \sum_{\substack{n=2 \\ n \text{ even}}}^{\infty} \bar{C}_n (\rho \omega^2 P_{nk}) = 0 \quad (39)$$

for k an odd integer, and

$$\sum_{\substack{n=1 \\ n \text{ odd}}}^{\infty} D_n \left[\alpha_n \left[m\sigma_k^2 - (m\omega^2 + \rho g) \right] Q_{nk} \right] + \sum_{\substack{n=1 \\ n \text{ odd}}}^{\infty} C_n (\rho \omega^2 Q_{nk}) = 0 \quad (40)$$

for k an even integer, where

$$P_{nk} = \int_{-a}^a \psi_k(x) \cos(\alpha_n x) dx = \frac{4ak(-1)^{\frac{n+2k-2}{2}}}{\pi(n^2 - k^2)}$$

for n , even, and k , odd,

$$Q_{nk} = \int_{-a}^a \psi_k(x) \sin(\alpha_n x) dx = \frac{4ak(-1)^{\frac{n+2k-1}{2}}}{\pi(n^2 - k^2)}$$

for n , odd, and k , even, and

$$P_k = \int_{-a}^a \phi_k(x) dx = \frac{4a}{\pi k}$$

Since the contact angle is assumed to be 90 deg for all motions of the free surface, no boundary conditions need be applied to $\eta(x, t)$ at $x = \pm a$. The function $\eta(x, t)$ may then be eliminated directly by substitution of Eq. (31) into Eq. (30). If use is made of the harmonicity of ϕ , there results

$$\left. \frac{T}{p} \frac{\partial^3 \phi}{\partial z^3} + g \frac{\partial \phi}{\partial z} - \omega^2 \phi \right|_{z=h} = 0 \quad (41)$$

Upon substitution of Eq. (35) into Eq. (41), with recognition of the fact that $[1, \cos(\alpha_n x), \sin(\alpha_n x)]$ form a complete set of orthogonal functions, we get

$$-\omega^2 C_0 + (g - \omega^2 h) D_0 = 0$$

$$\left[\alpha_n \left(g + \frac{T}{p} \alpha_n^2 \right) \tanh(\alpha_n h) - \omega^2 \right] \bar{C}_n + \left[\alpha_n \left(g + \frac{T}{p} \alpha_n^2 \right) - \omega^2 \tanh(\alpha_n h) \right] \bar{D}_n = 0 \quad (42)$$

for n , even, and

$$\left[\alpha_n \left(g + \frac{T}{p} \alpha_n^2 \right) \tanh(\alpha_n h) - \omega^2 \right] C_n + \left[\alpha_n \left(g + \frac{T}{p} \alpha_n^2 \right) - \omega^2 \tanh(\alpha_n h) \right] D_n = 0 \quad (43)$$

for n , odd.

The four infinite sets of linear homogeneous algebraic equations in the unknowns C_0 , D_0 , C_n , D_n , \bar{C}_n , and \bar{D}_n may be divided into two independent groups. The first is given by Eqs. (39) and (42), which govern symmetric oscillations of the free surface and the flexible floor; the second, by Eqs. (40) and (43), which govern the antisymmetric oscillations.

In each case a nontrivial solution can be obtained only if the determinant of the coefficients is equal to zero. This condition results in two equations of infinite order in ω^2 associated with the respective symmetric and antisymmetric oscillations of the system. These equations can be cast into the form

$$|[A]\omega^2 - [B]| = 0$$

where $[A]$ and $[B]$ are square matrices, and solved for the respective symmetric and antisymmetric frequencies of vibration of the system using digital computer techniques for any given order of $[A]$ and $[B]$.

2.8 Examination of the Stability Criteria

The necessary and sufficient conditions for the stability of the system as previously defined are $\omega_j^2 > 0$ for all ω_j^2 of the appropriate matrix equation. If all other parameters are held constant, then the boundaries of the set of values of the unidirectional net body force g for which all $\omega_j^2 > 0$ are those values of g for which one $\omega_j^2 = 0$. It does not follow, however, that, if there is a value of g , say g^* , for which one $\omega_j^2 = 0$, ω_j^2 is greater than 0 for g on one

side of g^* and ω_j^2 is less than 0 for g on the other side. Accordingly, the stability criteria are arrived at by setting ω^2 equal to zero. The resulting equation is then factored into the form

$$\prod_{k=1}^n (g - g_k) = 0$$

For a given root g_k , the value $g = g_k + \Delta$ is then substituted into the matrix equation, which is solved for ω^2 . The same is done for $g = g_k - \Delta$. The positive quantity Δ is taken small enough so that $\Delta < |g_{k+1} - g_k|$ and $\Delta < |g_k - g_{k-1}|$. After the resulting values of ω^2 have been examined, the region of g for stability is determined as that for which all ω_j^2 are greater than zero.

If ω^2 is set equal to zero then the symmetric and antisymmetric equations become, respectively:

$$|B'| \prod_{i=2}^n \left(g + \frac{T}{\rho} \alpha_i^2 \right) = 0 \quad (44)$$

where n is an even integer and

$$\prod_{i=2}^{n+1} (m\alpha_i^2 - \rho g) \prod_{j=1}^n \left(g + \frac{T}{\rho} \alpha_j^2 \right) = 0 \quad (45)$$

where n is an odd integer.

In Eq. (44), the following roots are of interest:

$$g_n = -\frac{T}{\rho} (\alpha_n)^2, \quad g_1 = \frac{m}{\rho} \alpha_1^2 \quad (5.212)$$

where g_1 is the smallest root of $|B'| = 0$.

where g_1 was solved for by digital computer techniques

and $n = 2, 4, 6, \dots$

Also, for Eq. (45) we have

$$g_n = -\frac{T}{\rho} \alpha_n^2, \quad g_j = \frac{m}{\rho} \sigma_j^2$$

where

$$n = 1, 3, 5, 7, \dots$$

$$j = 2, 4, 6, \dots$$

2.9 Stability Criteria for Antisymmetric Oscillations of the Free Surface and Flexible Floor

The negative values of g for which at least one value of ω^2 is zero in the antisymmetric case are

$$g = -\frac{T}{\rho a^2} \left(\frac{n\pi}{2} \right)^2 \quad (46)$$

where

$$n = 1, 3, 5, 7, \dots$$

The values of g are the same as would be encountered for the case of a rigid floor and are thus independent of the elastic and inertial properties of the flexible floor. The positive values of g , however, given by

$$g_j = \frac{m}{\rho} \sigma_j^2 = \frac{D}{\rho a^4} \left(\frac{j\pi}{2} \right)^4 \quad (47)$$

where

$$j = 2, 4, 6, 8, \dots$$

are dependent on the elastic properties of the flexible floor. Although the analysis has been done for the case of a flexible floor with simply supported edges, examination of the characteristic determinant shows that the equation $g_j = \frac{m}{\rho} \sigma_j^2$ is a general result applicable for the case of general identical homogeneous boundary conditions on the edges of the floor at $x = \pm a$. In such a case ω_j^2 will be the square of the $(j/2)^{\text{th}}$ eigenfrequency for antisymmetric free vibration of the floor associated with a given set of homogeneous boundary conditions of the same form at $x = \pm a$. The expressions for g_n and g_j for a given j and n are also valid if the characteristic determinant is not truncated but allowed to become a polynomial of infinite degree.

The solution of the matrix equation by means of a digital computer reveals that, with all other system parameters held fixed, the system is stable (i.e., all values of ω^2 are greater than 0) for antisymmetric initial disturbances for those values of the unidirectional body force magnitude g in the range

$$-\frac{T}{\rho(2a)^2} (\pi)^2 < g < \frac{D}{\rho(2a)^4} (2\pi)^4 \quad (48)$$

The results of the digital solution for the squares of the eigenfrequencies for the antisymmetric case are given below for the case of

$$\begin{aligned} a &= 5 \text{ ft} \\ h &= 0.5 \text{ ft} \\ D &= 6.2 \text{ ft-lb} \\ m &= 1.475 \times 10^{-2} \text{ slugs/ft}^2 \\ \rho &= 1.94 \text{ slugs/ft}^3 \\ \frac{T}{\rho} &= 2.64 \times 10^{-3} \text{ ft}^3/\text{sec}^2 \end{aligned}$$

The determinant was truncated at order 7. These parameters are characteristic of water at room temperature and a simply supported magnesium floor.

Figure 2 shows the squares of the first eight eigenfrequencies associated with anti-symmetric motions of the free surface and flexible floor plotted against values of g in the range of

$$-0.02 \text{ ft/sec}^2 < g < 32.2 \text{ ft/sec}^2$$

2.10 Stability Criteria for Symmetric Oscillations of the Free Surface and the Flexible Floor

The negative values of g for which at least one value of ω^2 is zero in the symmetric case are

$$g_n = -\frac{T}{\rho(a)^2} \left(\frac{n\pi}{2}\right)^2$$

where $n = 2, 4, 6, 8, \dots$

and are the same, as in the case of antisymmetric oscillations, as those associated with a rigid floor. The corresponding smallest non-negative value of g is given by.

$$g = 0$$

$$g_1 = \frac{m}{\rho} \sigma_1^2 = \frac{D}{\rho(a)^4} \left(\frac{1\pi}{2}\right)^4 \quad (5.212) \quad (49)$$

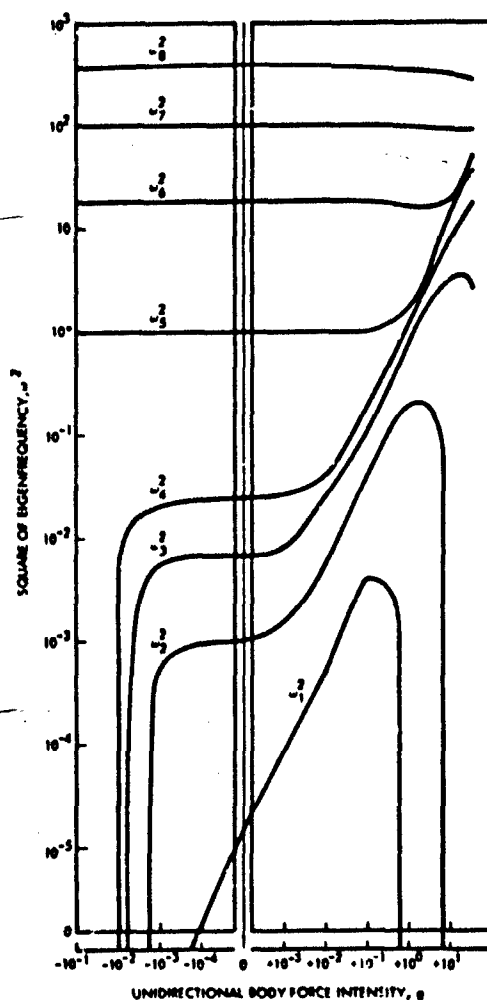


Fig. 2 Numerical Results

Again the result can be generalized to the case of general identical homogeneous boundary conditions on the edges of the floor at $x = \pm a$. In such a case ω_j^2 will be the square of the $[(j+1)/2]^{\text{th}}$ eigenfrequency of symmetric free vibration for the given homogeneous boundary conditions that are of the same form at $x = \pm a$.

In the case of the antisymmetric oscillations, the expressions for g_j and g_n remain the same for the case of an untruncated characteristic determinant.

Considerations similar to those associated with the antisymmetric case yield the following range of values for the unidirectional net body force intensity g for which all ω^2 are positive for the symmetric case:

$$-\frac{T}{\rho a^2} \pi^2 < g < \frac{D}{\rho(a)^4} \left(\frac{\pi}{2}\right)^4 \quad (5.212) \quad (50)$$

Since a general disturbance characterizable as an initial condition can be decomposed into symmetrical and antisymmetrical Fourier components that will excite the symmetrical and antisymmetrical modes of oscillation of the system, the general stability criteria for the system will be

$$-\frac{T}{\rho(2a)^2} \pi^2 < g < \frac{D}{\rho(a)^4} \left(\frac{\pi}{2}\right)^4 \quad (5.212) \quad (51)$$

For the case of a rigid floor, the general stability criterion is

$$-\frac{T}{\rho(2a)^2} (\pi)^2 < g < \infty \quad (52)$$

2.11 Discussion of the Stability Criteria

On an intuitive basis, the lower bound of the range of values of g for the stability of antisymmetric oscillations is acceptable. One can see that, for some negative value of g (i.e., the body force vector pointing in the $+z$ direction), the free surface of

the liquid will become unstable and the liquid will eventually undergo displacements of a magnitude comparable with the static equilibrium fluid depth h .

Regarding symmetrical oscillations of the system, one of the Fourier components of the free surface displacement function $\eta(x, t)$ is a constant. The coupling of this Fourier component with the Fourier components of the floor deflection gives rise to the transcendental equation $|B'| = 0$, as opposed to the simple infinite product in the antisymmetric case.

It is not intuitively obvious, however, that there should exist finite upper bounds for the stable regions in contrast to the infinite upper bound obtained for the case of the rigid tank. One might ask how the liquid can become unstable if it is in a state of static equilibrium in a container, with the net body force vector pointing into the liquid region.

As Eq. (51) shows clearly, if the bending stiffness parameter of the floor is increased indefinitely (i.e., the plate is made increasingly more rigid) the upper bound becomes positively unbounded and we have agreement with the case of the rigid floor. Since the analytic structure of the upper bound, $D/\rho(a)^4$, in Eq. (51) is similar to that given for the lower bound, $T/\rho(a)^2$, given in Eq. (49) for antisymmetric motions, it is conceivable that the upper bound would be associated with an instability in the flexible floor. This association would lead us to conclude, from the viewpoint of deflections sufficiently small to permit the linearization of the equations of motion, that the static equilibrium position of a Bernoulli-Euler type of plate with a hydrostatic fluid pressure field acting on its upper surface becomes unstable when the net body force intensity reaches a certain positive magnitude. This instability occurs because the total potential of the internal bending stress distribution in the beam, and of the external pressure field applied by the gas and the fluid, has a negative second variation with respect to a deflection parameter at the static equilibrium position. The linear equations characterize the instability in terms of "deflection without limit."

As the dynamic displacements of the flexible floor become larger, the simple Bernoulli-Euler representation that leads to the "deflection without limit" characterization becomes less valid.

A more realistic representation of an actual container floor undergoing dynamic deflections comparable to its thickness would include the effects of middle-surface stretching. These effects would involve, in terms of the physical model shown in Fig. 1, the removal of the roller support at $x = a$. Since the curvature of the unloaded floor is zero, the effects due to middle-surface stretching will be nonlinear. Such effects will also change the analytic structure of the total potential function, and will consequently lead to a modification of the "deflection without limit" characterization given to the instability by the linearized equations of motion.

3 CONSIDERATION OF NONLINEAR ELASTIC EFFECTS

3.1 Statement of the Problem

To assess the importance of nonlinear elastic effects, the edges of the flexible floor were characterized by fixed pin supports. Such a specification gives rise to nonlinear terms in the elastic restoring forces in the equations of dynamic equilibrium of an element of the flexible floor. These nonlinear terms contribute to the modification of the stability criteria given in section 2. To evaluate these modifications in a relatively uncomplicated manner, it was necessary to make some further simplifications. Since the finite upper bound for the stable range of values of g given in section 2 depends only on the elastic properties associated with the flexible floor and not on the surface tension T , the free surface was assumed constrained by a rigid flat surface at $z = h$, as shown in Fig. 3.

Another simplification was the specification of a static equilibrium position for the flexible floor involving zero static deflection. This simplification can be achieved by providing a constant gas pressure field, $p_1 = p_0 + \rho gh$, external to the flexible floor, which provides static balance to the weight of the liquid layer and the pressure p_0 , which is assumed to exist at $z = h$.

With the total displacements of an element of the free surface of the flexible floor in the $+x$ and $-z$ directions denoted as u and w respectively, the equations of equilibrium (Ref. 5) of the element, in the sense of D'Alembert, become:

$$EA \frac{\partial}{\partial x} \left[\frac{\partial u}{\partial x} + \frac{1}{2} \left(\frac{\partial w}{\partial x} \right)^2 \right] = m \frac{\partial^2 u}{\partial t^2} \quad (53)$$

$$D \frac{\partial^4 w}{\partial x^4} - EA \frac{\partial}{\partial x} \left[\left(\frac{\partial u}{\partial x} + \frac{1}{2} \left(\frac{\partial w}{\partial x} \right)^2 \right) \frac{\partial w}{\partial x} \right] - \rho g w + m \frac{\partial^2 w}{\partial t^2} - \rho \frac{\partial \Phi}{\partial t} \Big|_{z=0} = 0 \quad (54)$$

The linearized kinematic condition

$$\frac{\partial w}{\partial t} - \frac{\partial \Phi}{\partial z} \Big|_{z=0} = 0 \quad (55)$$

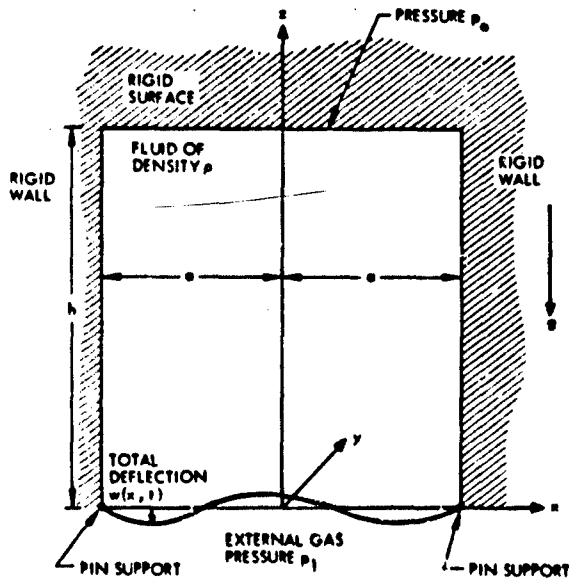


Fig. 3 Two-Dimensional Channel Analyzed To Determine Nonlinear Effects

will also be used. In addition, Φ must satisfy

$$\frac{\partial^2 \Phi}{\partial x^2} + \frac{\partial^2 \Phi}{\partial z^2} = 0$$

$$\left. \frac{\partial \Phi}{\partial x} \right|_{x=\pm a} = 0 \quad (56)$$

and

$$\left. \frac{\partial \Phi}{\partial z} \right|_{z=h} = 0$$

3.2 Approximate Solution

Because of the nonlinear terms in Eqs. (53) and (54), the methods used in section 2 involving a superposition of particular solutions is no longer valid. As an approximation, the simple one-term solution to be used in conjunction with Galerkin's method given below will be assumed

$$\begin{aligned} w(x, t) &= q_1(t) \cos\left(\frac{\pi x}{2a}\right) \\ u(x, t) &= q_2(t) \sin\left(\frac{\pi x}{a}\right) \\ \Phi(x, z, t) &= q_3(t) \cos\left(\frac{\pi x}{a}\right) \cosh\left[\frac{\pi}{a}(h-z)\right] \end{aligned} \quad (57)$$

where q_1 , q_2 , q_3 are arbitrary functions of time to be determined. The results of the nonlinear analysis indicate that the simplified nonlinear system is stable about the zero-deflection static equilibrium position for

$$0 < g < \frac{D}{\rho} \left(\frac{\pi}{2a}\right)^4$$

For

$$\frac{D}{\rho} \left(\frac{\pi}{2a} \right)^4 < g < \infty$$

the floor will deflect to a new stable equilibrium position given by:

$$w(x, t) = \pm \frac{\left[g - \frac{D}{\rho} \left(\frac{\pi}{2a} \right)^4 \right]^{1/2}}{\frac{1}{2} \sqrt{\frac{EA}{\rho}} \left(\frac{\pi}{2a} \right)^2} \cos \left(\frac{\pi x}{2a} \right)$$

$$u(x, t) = \frac{g - \frac{D}{\rho} \left(\frac{\pi}{2a} \right)^4}{\frac{2EA}{\rho} \left(\frac{\pi}{2a} \right)^3} \sin \left(\frac{\pi x}{a} \right)$$

These results, arrived at by an approximate method for the simplified system, give a qualitative picture of the behavior of the system, considered in section 2 for the range

$$\frac{D}{\rho} \left(\frac{\pi}{2a} \right)^4 < g$$

The nonlinear elastic restoring forces that arise because of the stretching of the middle surface enable the system to establish a new stable static equilibrium position. The new equilibrium configuration involves a different static stress distribution in the floor as well as different analytic representations of the natural frequencies associated with linear oscillations about the new static equilibrium configuration.

4 ANALYSIS OF THE CASE OF FLEXIBLE WALLS

4.1 Statement of the Problem

The system discussed in section 2 was modified to the extent that the floor was assumed rigid and the walls flexible. The flexible walls were Bernoulli-Euler plates of infinite extent in the y direction and had the same elastic properties as did the floor analyzed in section 2. For simplicity, the edges were considered simply supported, with the upper edge of each plate mounted on a roller support. This description neglects the importance of middle-surface stretching.

With the container empty, the width was $2a$, as shown in Fig. 4. In the static equilibrium position, the fluid had a flat free surface and a depth h . The sides of the container adjacent to $x = -a$ and $x = a$ had static deflections $\bar{w}_1(z)$ and $\bar{w}_2(z)$ respectively. The free surface and the exterior of the container were exposed to a gas pressure p_1 , which remained constant during undulations of the fluid free surface and the walls of the container.

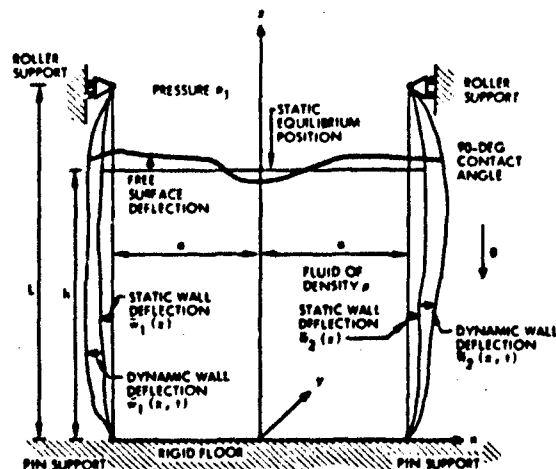


Fig. 4 Two-Dimensional Channel With Flexible Walls

Since the wall boundary conditions are much more involved than in the rigid wall case, a direct expansion of the velocity potential in "separation of variables" type product solution was not attempted. Rather, the present problem was recast into an integro-differential equation representation. Such a representation involves the use of a modified Green's function having the following properties:

$$\frac{\partial^2 G}{\partial x^2} + \frac{\partial^2 G}{\partial z^2} = -\delta(x - x')\delta(z - z') + \frac{1}{2ah} \quad (58)$$

$$\frac{\partial G}{\partial n(x, z)} = 0 \quad \text{for } x \text{ and } z \text{ on } C$$

$$\iint_D G \, dx \, dz = 0$$

where $n(x, z)$ denotes the direction of the normal on C pointing outward from D .

Application of Green's theorem to the functions $\phi(x, z, t)$ and $G(x, z, x', z')$ over the region D , together with the harmonicity of $\phi(x, z, t)$ and the reciprocity of G in (x, z) and (x', z') , yields the representation

$$\begin{aligned} \phi(x, z, t) = & \oint_C G(x, z, x', z') \frac{\partial \phi}{\partial n}(x', z', t) \, ds(x', z') \\ & + \frac{1}{2ah} \iint_D \phi(x', z', t) \, dx' \, dz' \end{aligned}$$

where ds' is a differential element of arc on C , the boundary of D . Application of the conditions of dynamic equilibrium (in the sense of D'Alembert) at the free surface and the flexible walls, as well as the kinematic conditions on C , yields a set of three integro-differential equations in the deflections of the free surface and

the walls. Expansion of these deflection functions in the appropriate sets of orthonormal eigenfunctions with nontrivial expansion coefficients yields a frequency equation associated with a determinant of infinite order. Solution for g with the condition that $\omega^2 = 0$ gives rise to the following range of values of g for the dynamic stability of the system:

$$0 < g < \infty$$

4.2 Discussion of the Stability Criteria

In contrast to the container with a flexible floor, there is no finite upper bound for the range of values of g for stability of the system about its static equilibrium position. The primary reason is that the walls can undergo deflection only in a direction perpendicular to that of the net body force. The lower bound $g = 0$ arises because of a constant (zero curvature) component in the Fourier expansion of the free surface deflection function. In an actual container there would be some degree of elastic coupling between the walls and the floor. This coupling would lead to a modification of the aforementioned range of values of g for stability about the static equilibrium position.

5 REFERENCES

1. M. Anliker and R. M. Beam, "On the Stability of Liquid Layers Spread Over Simple Curved Bodies," J. Aerospace Sci., Vol. 29, 1962, pp. 1196-1209
2. M. Anliker and W. S. Pi, Effects of Geometry and Unidirectional Body Forces on the Stability of Liquid Layers, SUDAER Report No. 150, Dept. of Aeronautics and Astronautics, Stanford University, Stanford, Calif., Mar 1963
3. W. C. Reynolds and H. M. Satterlee, The Dynamics of the Free Liquid Surface in Cylindrical Containers Under Strong Capillary and Weak Gravity Conditions, Report LG-2, Dept. of Mechanical Engineering, Stanford University, Stanford, Calif., May 1964

4. H. Ziegler, "Linear Elastic Stability," J. Applied Math. and Physics, Vol. IV, 1953
5. E. Mettler, "Dynamic Buckling," Handbook of Engineering Mechanics, Chapter 62, 1962

DISCUSSION

W. E. Jahsman, Lockheed

I share your desire to see the effect of flexibility on the stability criterion as determined experimentally, and I wonder if you don't already have that. After all, how do you differentiate between a flexible wall and a lucite wall which possesses finite modulus? Isn't this also flexible? It's interesting that when one uses a completely rigid solution, a negative lower bound for stability results, whereas if one admits any small but non-zero amount of flexibility, then the bound immediately comes up to zero.

Smith

The wall thickness of the fuel tanks used in space vehicles is much smaller in comparison to the other characteristic tank dimensions than is the case for the lucite tanks shown in the movies. Such model tanks will, in general, exhibit much less overall flexibility than will the actual fuel tanks. While it is true that any configuration utilized in a drop test will possess flexibility, it would be instructive to compare the results obtained from the drop test of the lucite configuration with those corresponding results obtained from a similar test of a more flexible tank.

P. G. Bhuta, TRW Systems Group

I share the view with you that there is more need for experimental work in this area. We did some experiments in which it was found that the shift in frequency due to flexibility was very small. In other words, take a completely rigid container and determine

the frequency experimentally. Now when the rigid walls are replaced by a flexible membrane, the frequency shift is very small. With a flexible wall the forced response was considerably larger than one might expect. This of course has got to do with the stability of the free surface. My feeling is that information on flexible containers is needed even in one-g. This would certainly be easier to do than drop testing.

Richard Warren, Lockheed

I was wondering how reasonable the boundary conditions are in comparison to the real case. You mentioned that the linearization limits the displacement of the bottom to the thickness of the bottom, and also in one of your cases you assume that the bottom was restrained such that it is less stiff in the radial direction than the walls of the container.

Smith

Since linearized equations of motion are of questionable validity for other than small motions, and analysis was made of the non-linear effect of middle surface stretching in the flexible floor. For small oscillations, instability is characterized by the condition $\omega^2 < 0$, which is indicative of an exponential growth of the system response. In actuality the non-linear effects become dominant for larger amplitudes, and the system assumes a new configuration. For the problem considered this configuration consisted of a new finite deflected static equilibrium position.

BLANK PAGE

PAPER 10

SLOSHING OF A LIQUID IN A DRAINING OR FILLING TANK UNDER VARIABLE G CONDITIONS

By P. G. Dhata* and L. R. Keval*
TRW SPACE TECHNOLOGY LABORATORIES

ABSTRACT

The sloshing of a liquid in a tank which is subjected to variable accelerations along its axis in a gravitational field, and which may be in the process of being filled or drained, is studied in this paper. The complete formulation pertaining to the linearized problem of the free-surface oscillations in such a tank is given. The effects due to surface tension are included. It is shown that the equations reduce to the proper results in the limiting cases.

The solutions of initial value problems for certain specific examples are given and the results for a draining tank indicate the possibility of a blowthrough of the vapor during zero-g draining. The results for a filling tank in a low-g environment show the need for the provision of adequate baffles to damp the free surface motion.

*Also, University of Southern California.

NOMENCLATURE

a	Outer radius of tank
$\dot{A}_o(t)$	Function of time, Eq. (14)
$\dot{A}_n(t)$	Function of time, Eq. (13)
$\dot{B}_o(t)$	Function of time, Eq. (14)
$\dot{B}_n(t)$	Function of time, Eq. (13)
$C_n(t)$	Generalized coordinate for free-surface distortion, Eq. (16)
$f(t)$	Time variation of outlet velocity
$\hat{f}(t)$	Acceleration of tank along z axis
g	Gravitational acceleration
$h(t)$	Mean free surface height
h_o	Initial mean free surface height
J_m	Bessel function of first kind and order m
k_n	Separation constant for Laplace's equation
m	Number of nodal diameters, Eq. (27)
p	Pressure
(r, θ, z)	Cylindrical coordinates
t	Time
u, v, w	Components of liquid velocity
W_o	Amplitude of outlet velocity
α	Constant rate of draining, Eq. (39)
δ	Radius of outlet
ζ	Free surface displacement
ρ	Liquid density
σ	Surface tension
ϕ	Velocity potential

SLOSHING OF A LIQUID IN A DRAINING OR FILLING TANK UNDER VARIABLE G CONDITIONS

1 INTRODUCTION

Considerable interest in the dynamic behavior of liquids with a free surface has arisen because of the use of liquid propellants in space launch vehicles. Recently attention has been devoted to the behavior of the liquids under low-gravitational conditions because of the long periods of weightlessness or near-weightlessness which will be encountered during longer missions of planet explorations. A problem of particular concern is the draining and filling of tanks under low- or zero-gravitational conditions. Filling of a tank is of concern for refuelling of spacecraft or space stations. In this paper the problem of draining or filling under low-g conditions is studied. Since extensive bibliographies (Ref. 1, 2, 3) are available in the literature, no attempt will be made to reproduce them here. Rather, only pertinent references are cited.

Axisymmetric sloshing of a liquid due to the outlet velocity fluctuations at the bottom of a circular cylindrical tank was studied by Bhuta and Yeh (Ref. 4) with the object of determining the forces rather than the stability of the free-surface motion. They assumed that there was no net outflow from the tank - i.e., the amount of liquid in the tank remained unchanged. Miles (Ref. 5) studied the free oscillations of a liquid in a cylindrical tank and analyzed the decrement of motion caused by laminar boundary layer friction and time varying depths. Miles also studied (Ref. 6) the effect of damping on free-surface oscillations due to drainage. Although the mean free surface height, $h(t)$, was permitted to vary slowly with time the variation of h in averaging over one cycle was neglected, and the motion of the free surface was assumed to be approximately simple harmonic. It should be emphasized that the objective of the work of Refs. 5 and 6 appears to be to study the nature of damping provided by drainage, rather than to study drainage-induced disturbances; also, zero- or low-g conditions were of no concern. It may be remarked that the report of the experimental investigation of Ref. 7 states, "For tanks of practical size, the incremental damping

as given by Equation (11) is extremely small and no experimental data have been published to either substantiate or refute these theoretical predictions." In the present investigation the problem is studied with the object of studying the draining- or filling-induced free-surface distortions, and it is found that considerable distortion of the free surface without oscillations can occur during drainage under zero-g conditions and that the free surface can continue to oscillate during filling under low-g conditions.

Saad and Oliver (Ref. 8) studied the motion caused by draining or filling of a tank in the presence of surface-tension forces. The present paper considers a more general problem than the one they treated and takes into account in the formulation the effects of varying the acceleration along the axis of the tank. It is found in the limiting case that an incorrect linearized free-surface condition was used in Ref. 8 and that the initial value problem was not well formulated. It was concluded in Ref. 8 that "... the oscillation may be either damped (in the case of the filling container) or exponentially enhanced (in the case of the emptying container)." Computer solutions of the governing differential equation given in the present paper do not show a damping of the free-surface oscillations during filling of a tank. The results obtained here for a tank draining in a zero-g condition indicate a significant distortion of the free-surface interface and a possibility of a vapor blowthrough. These results are in general agreement with the experimental observations of Nussle, Derdul, and Petrash (Ref. 9).

2 MATHEMATICAL FORMULATION

Consider the cylindrical coordinate system (r, θ, z) attached to the bottom of the tank as shown in Fig. 1. The mean free surface height is denoted by $h(t)$. The radii of the tank and the outlet are taken to be a and δ , respectively. It is assumed the liquid is inviscid and incompressible and that the magnitude of the free surface wave height, ζ , is much smaller than h . Within the liquid a velocity potential ϕ exists and satisfies Laplace's equation

$$\frac{\partial^2 \phi}{\partial r^2} + \frac{1}{r} \frac{\partial \phi}{\partial r} + \frac{1}{r^2} \frac{\partial^2 \phi}{\partial \theta^2} + \frac{\partial^2 \phi}{\partial z^2} = 0 \quad (1)$$

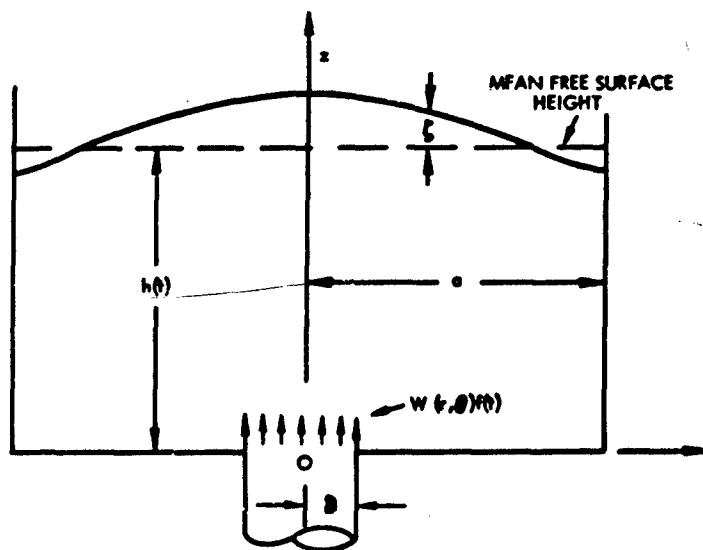


Fig. 1 Geometry of the Problem

The components of the velocity relative to the tank in the radial, tangential, and axial directions are obtained from

$$u = \frac{\partial \varphi}{\partial r}, \quad v = \frac{1}{r} \frac{\partial \varphi}{\partial \theta} \quad \text{and} \quad w = \frac{\partial \varphi}{\partial z} \quad (2)$$

The requirement that the normal component of the velocity vanishes at the wall gives

$$\left. \frac{\partial \varphi}{\partial r} \right|_{r=a} = 0 \quad (3)$$

The boundary condition to be satisfied at the bottom of the tank is

$$\frac{\partial \varphi}{\partial z} = \begin{cases} W(r, \theta) f(t) & , \quad 0 \leq r \leq \delta \\ 0 & , \quad \delta < r \leq a \end{cases} \quad (4)$$

The kinematic free-surface condition which requires that a particle on the free surface moves with the velocity of the free surface in the vertical direction (Ref. 10) yields

$$\dot{h} + \frac{\partial \zeta}{\partial t} + u \frac{\partial \zeta}{\partial r} + \frac{v}{r} \frac{\partial \zeta}{\partial \theta} = w \quad (5)$$

where ζ is the free-surface wave height measured from the mean free-surface height $h(t)$, t is the time, and the components of velocity (u, v, w) are evaluated on the free surface. The dynamic condition to be satisfied on the free surface is obtained from the integral of the equations of motion, viz.

$$\frac{p}{\rho} + \frac{\partial \varphi}{\partial t} + \frac{1}{2}(u^2 + v^2 + w^2) + [g - \hat{f}(t)]z = F(t) \quad (6)$$

where p is the pressure, $\hat{f}(t)$ denotes the prescribed vertical acceleration of the tank along its axis, and $F(t)$ is an arbitrary function of time. Following Benjamin and Ursell (Ref. 11), the quantity $\hat{f}(t)$ is included to account for the acceleration of the tank. If surface-tension effects are included, the pressure on the free surface is related to the surface-tension forces in the linear theory by

$$p = -\sigma \nabla^2 \zeta = -\sigma \left(\frac{\partial^2 \zeta}{\partial r^2} + \frac{1}{r} \frac{\partial \zeta}{\partial r} + \frac{1}{r^2} \frac{\partial^2 \zeta}{\partial \theta^2} \right) \quad (7)$$

where σ is the surface tension force per unit length. On the free surface

$$z = h(t) + \zeta(r, \theta, t) \quad (8)$$

and the kinematic free-surface conditions, Eq. (5), when linearized under the assumption that slopes of the free-surface waves and radial and tangential components of the velocity on the free surface are small, takes the form

$$\left. \frac{\partial \varphi}{\partial z} \right|_{z=h} = \dot{h} + \frac{\partial \zeta}{\partial t} \quad (9)$$

where the dot denotes differentiation with respect to time and $\partial \varphi / \partial z$ is evaluated on the mean free-surface height, $h(t)$. Substituting from Eqs. (7) to (9) into Eq. (6) gives

$$\left\{ -\frac{\sigma}{\rho} \nabla^2 \zeta + \frac{\partial \varphi}{\partial t} + \frac{1}{2} \left[\left(\frac{\partial \varphi}{\partial r} \right)^2 + \left(\frac{1}{r} \frac{\partial \varphi}{\partial \theta} \right)^2 + \left(h + \frac{\partial \zeta}{\partial t} \right)^2 \right] + [g - \hat{f}(t)] \zeta \right\}_{z=h+\zeta} = F(t) \quad (10)$$

Neglecting squares of $\frac{\partial \varphi}{\partial r}$, $\frac{1}{r} \frac{\partial \varphi}{\partial \theta}$ and $\frac{\partial \zeta}{\partial t}$ in Eq. (10) gives

$$\left(\frac{\partial \varphi}{\partial t} \right)_{z=h} + h \frac{\partial \zeta}{\partial t} - \frac{\sigma}{\rho} \nabla^2 \zeta + [g - \hat{f}(t)] \zeta = F(t) - \frac{1}{2} \dot{h}^2 - [g - \hat{f}(t)] h \quad (11)$$

where $\partial \varphi / \partial t$ is evaluated at $z=h$ due to the linearization. Since the right-hand member of Eq. (11) is a function of time alone, it may be set equal to zero by incorporating it into the definition of φ . Hence the dynamic free-surface condition of Eq. (11) becomes

$$\left(\frac{\partial \varphi}{\partial t} \right)_{z=h} + h \frac{\partial \zeta}{\partial t} - \frac{\sigma}{\rho} \nabla^2 \zeta + [g - \hat{f}(t)] \zeta = 0 \quad (12)$$

Equations (1), (3), (4), (9), and (12) define the boundary-value problem to be solved. The initial-value problem is formulated in a later section.

It may be noted from Eqs. (3) and (9) that

$$\left. \frac{\partial^2 \zeta}{\partial t \partial r} \right|_{r=a} = 0$$

Hence, $\partial \zeta / \partial r$ equals a constant (its initial value). If, further, one assumes for ζ the same functional dependence in r and θ as for ϕ , then as a consequence of Eqs. (3) and (9) the angle of contact of the free surface with the tank wall is 90 deg. Such an assumption will be made in what follows and hence the contact angle will be restricted to 90 deg.

It is appropriate to remark at this point that if we neglect the acceleration $\hat{f}(t)$ due to the motion of the tank itself in Eq. (12), we notice that $h \frac{\partial \zeta}{\partial t}$ does not appear in Eq. (1.8) of Ref. 8. The contribution of this term will be small only when h is of the order of magnitude of $\partial \zeta / \partial t$.

3 SOLUTION OF THE BOUNDARY VALUE PROBLEM

In this section the differential equations governing the time variation of the free-surface waves and the velocity potential are derived for the axisymmetric case, and the procedure for obtaining similar equations for the asymmetric case is outlined.

The derivation of the equations will involve Bessel functions of the first kind and all orders and expansions of these functions into Fourier-Bessel series. The axisymmetric case will be treated first because it is an exceptional case (Ref. 11) in the Fourier-Bessel expansion, and as such it must be treated separately.

3.1 Axisymmetric Solution

For the axisymmetric case a solution of Eq. (1) which is regular at the origin may be written as

$$\varphi_n = J_0(k_n r) \left[\dot{A}_n(t) \cosh k_n z + \dot{B}_n(t) \sinh k_n z \right] \quad , \quad k_n \neq 0 \quad (13)$$

where $\dot{A}_n(t)$ and $\dot{B}_n(t)$ are undetermined functions of time. k_n is a constant, and J_0 is the Bessel function of the first kind and order zero. When $k_n = 0$, a solution of Eq. (1) which is regular at $r = 0$ is

$$\varphi_0 = \dot{A}_0(t) + \dot{B}_0(t) z \quad (14)$$

where $\dot{A}_0(t)$ and $\dot{B}_0(t)$ are to be determined. The total potential φ is given by summation of φ_0 and φ_n over n from one to infinity. Application of the boundary condition of Eq. (3) to Eq. (13) yields

$$J_1(k_n a) = 0 \quad (15)$$

which determines the values of k_n . It should be noted that $k_n = 0$ is a solution of Eq. (15), and this requires a treatment of the axisymmetric case separate from the asymmetric case. Equation (14) identically satisfies the condition of Eq. (3). Let the free-surface wave height ζ be given by

$$\zeta(r, t) = \sum_{n=1}^{\infty} C_n(t) J_0(k_n r) \quad (16)$$

For the axisymmetric case, the boundary condition of Eq. (4) takes the form

$$\left. \frac{\partial \varphi}{\partial z} \right|_{z=0} = \begin{cases} W_0 f(t) & , \quad 0 \leq r \leq \delta \\ 0 & , \quad \delta < r \leq a \end{cases} \quad (17)$$

To satisfy the boundary condition of Eq. (17) we expand $\frac{\partial \phi}{\partial z} \Big|_{z=0}$ in a Fourier-Bessel series:

$$W_o f(t) = \frac{W_o}{a^2} f(t) \delta^2 + \frac{2W_o f(t) \delta}{a^2} \sum_{n=1}^{\infty} \frac{J_1(k_n \delta) J_0(k_n r)}{k_n [J_0(k_n a)]^2} \quad (18)$$

Use of Eq. (17) yields

$$\dot{B}_o(t) = W_o f(t) \frac{\delta^2}{a^2} \quad (19)$$

and

$$\dot{B}_n(t) = \frac{2W_o f(t) \delta J_1(k_n \delta)}{k_n^2 a^2 [J_0(k_n a)]^2} \quad (20)$$

Use of the kinematic free-surface condition of Eq. (9) yields

$$\dot{B}_o(t) = \dot{h} \quad (21)$$

and

$$\dot{A}_n k_n \sinh k_n h + \dot{B}_n k_n \cosh k_n h = \dot{C}_n \quad (22)$$

Equations (19) and (21) show that the continuity requirement relating the rate of change of mean free-surface height, $\dot{h}(t)$, to the outlet velocity is satisfied. The dynamic free-surface condition of Eq. (12) requires

$$\ddot{A}_o = -\ddot{B}_o h \quad (23)$$

and

$$\ddot{A}_n \cosh k_n h + \ddot{B}_n \sinh k_n h + h \dot{C}_n + \left[\frac{\sigma}{\rho} k_n^2 + g - \hat{f}(t) \right] C_n = 0. \quad (24)$$

Eliminating A_n in Eqs. (22) and (24) results in an uncoupled equation for C_n , viz.

$$\ddot{C}_n - \frac{2k_n h \dot{C}_n}{\sinh 2k_n h} + \left[\frac{\sigma}{\rho} k_n^3 + [g - \hat{f}(t)] k_n \right] \tanh k_n h C_n = \frac{k_n \ddot{B}_n}{\cosh k_n h} - \frac{\dot{B}_n k_n^2 h}{\sinh k_n h} \quad (25)$$

By the use of Eqs. (19) to (21), Eq. (25) may be written as

$$\ddot{C}_n - \frac{2k_n h \dot{C}_n}{\sinh 2k_n h} + \left[\frac{\sigma}{\rho} k_n^3 + [g - \hat{f}(t)] k_n \right] \tanh k_n h C_n = \frac{2h J_1(k_n \delta)}{k_n \delta \cosh k_n h [J_0(k_n a)]^2} - \frac{2h^2 J_1(k_n \delta)}{\delta \sinh k_n h [J_0(k_n a)]^2} \quad (26)$$

To evaluate the free-surface distortion ζ one needs to solve Eq. (26) for given initial conditions, for various values of k_n given by Eq. (15), and for the prescribed outlet velocity. One then uses Eq. (16) to sum the modes. The formulation of the initial value problem is discussed in a later section. If surface tension and drainage effects are neglected, the present problem reduces to that of Yeh (Ref. 12). It may easily be verified that the present formulation reduces to that of Ref. 12 in the appropriate limiting case.

One also notices that in Eq. (6) of Ref. 6 the right-hand member of our Eq. (26) is absent - because the problem in Ref. 6 is formulated in terms of a sloshing potential only. In such a formulation our boundary condition of Eq. (4) is replaced by a

homogeneous boundary condition, and hence the homogeneous equation for the generalized coordinate was obtained. In the present paper the problem is formulated in terms of the total potential.

3.2 Asymmetric Case

If the outlet hole is located eccentrically, or if the outlet flow is dependent on θ , the asymmetric modes will be excited. Hence an outline of a procedure that may be followed is given here. One proceeds in the same manner as for the axisymmetric case except that φ_{mn} and ζ_{mn} now are taken in the form

$$\varphi_{mn} = \left[\dot{A}_{mn}(t) \cosh k_{mn} z + \dot{B}_{mn}(t) \sinh k_{mn} z \right] J_m(k_{mn} r) \cos m \theta \quad (27)$$

and

$$\zeta_{mn} = C_{mn}(t) J_m(k_{mn} r) \cos m \theta \quad (28)$$

In obtaining the potential φ or the free-surface wave height, ζ , one sums over m from 1 to infinity and over n from 0 to infinity.

4 THE INITIAL VALUE PROBLEM

To solve the initial value problem for wave height, ζ , or velocity potential, φ , we need to prescribe the initial conditions over the entire field. In Ref. 8, Saad and Oliver concluded, "The condition on velocity is more readily formulated in terms of the potential function since it is not obvious that the initial surface velocity can be prescribed arbitrarily; in fact, it cannot." The initial value problem for surface waves is a classical one and is discussed in an expository article by Wehausen and Laitone (Ref. 13), which refers to the early work of Cauchy and Poisson. In the problems discussed in Ref. 13 it is shown that one needs only to prescribe at the instant $t = 0$ the shape of the free surface and its vertical velocity to describe the subsequent motion.

In the present problem the fluid is of finite extent and we have an inflow or outflow through the circular hole in the bottom of the tank. Since some of the recent experimental investigations of Nussle, Derdul, and Petrash (Ref. 9) concern drainage from quiescent initial conditions, the formulation is given for these initial conditions. The formulation may be extended easily to other arbitrary initial conditions. It will be shown that for the draining or filling problem it is also necessary to prescribe the outlet liquid velocity and the outlet liquid acceleration.

For the flow starting from rest

$$\zeta(r, 0) = 0 \quad (29)$$

and

$$\frac{\partial \zeta}{\partial t}(r, 0) = 0 \quad (30)$$

Using Eq. (16), one then obtains

$$C_n(0) = 0 \quad (31)$$

and

$$\dot{C}_n(0) = 0 \quad (32)$$

From Eqs. (19) and (20), one requires

$$\dot{B}_0(0) = W_0 f(0) \frac{\delta^2}{a^2} \quad (33)$$

and

$$\dot{B}_n(0) = \frac{2W_o f(0) \delta J_1(k_n \delta)}{k_n^2 a^2 [J_o(k_n a)]^2} \quad (34)$$

It also follows from Eqs. (19) and (20) that

$$\ddot{B}_o(0) = W_o \dot{f}(0) \frac{\delta^2}{a^2} \quad (35)$$

and

$$\ddot{B}_n(0) = \frac{2W_o \dot{f}(0) \delta J_1(k_n \delta)}{k_n^2 a^2 [J_o(k_n a)]^2} \quad (36)$$

To obtain the initial condition on \dot{A}_n one uses Eqs. (32) and (22) to obtain

$$\dot{A}_n(0) = \frac{-2W_o f(0) \delta J_1(k_n \delta)}{k_n^2 a^2 [J_o(k_n a)]^2} \coth k_n h(0) \quad (37)$$

The corresponding initial value of \ddot{A}_n is obtained by making use of Eqs. (31), (32), and (24), and is given by

$$\ddot{A}_n(0) = - \frac{2W_o \dot{f}(0) \delta J_1(k_n \delta)}{k_n^2 a^2 [J_o(k_n a)]^2} \tanh k_n h(0) \quad (38)$$

Hence the initial conditions for the entire field are prescribed. It is clear that the same procedure applies also for any arbitrary initial conditions.

5 NUMERICAL EXAMPLES

In this section, digital computer solutions of Eq. (26) are given for certain specific examples (for the first-mode contribution ($n = 1$), and for $\hat{f}(t) \equiv 0$) to illustrate the method. For any specific application it will be necessary to evaluate the contribution from higher modes also. It is possible to obtain asymptotic solutions of Eq. (26) for certain values of the parameters involved. However, the regimes where such solutions are valid are not necessarily the ones where principal physical interest lies, and hence such solutions will not be given here. In all the examples presented, quiescent initial free-surface conditions are assumed.

In Fig. 2, the free-surface distorted shapes are given for various values of time during zero-g drainage of a liquid at a constant rate from a tank of radius $a = 60$ in. through an outlet radius $\delta = 6$ in. For drainage at a constant rate, $\ddot{h} = 0$ in Eq. (26) and h is given by

$$\frac{h}{a} = \frac{h_0}{a} + \frac{\alpha}{a} t \quad (39)$$

where h_0 is the value of h at $t = 0$ and α denotes the constant rate at which h changes.* For the example considered in Fig. 2, $\alpha/a = -0.015$, $g = 0$, $\sigma/\rho = 0.446 \text{ in.}^3/\text{sec}^2$, and $h_0/a = 1.0$. The right-hand portion of the figure shows that (based on the contribution from the first mode) the possibility of the vapor blowing through exists since the free-surface distortion is rapidly increasing. Such results were obtained in the experimental investigations given in Ref. 9.

In Fig. 3, the time history of the free-surface distortion at the center of the tank during drainage at a constant rate is given for $g = 38.6 \text{ in./sec}^2$. In this example, again $a = 60 \text{ in.}$, $\delta = 6.0 \text{ in.}$, $\alpha/a = -0.015$, $\sigma/\rho = 463.2 \text{ in.}^3/\text{sec}^2$, and $h_0/a = 1.0$.

*For draining, α is negative.

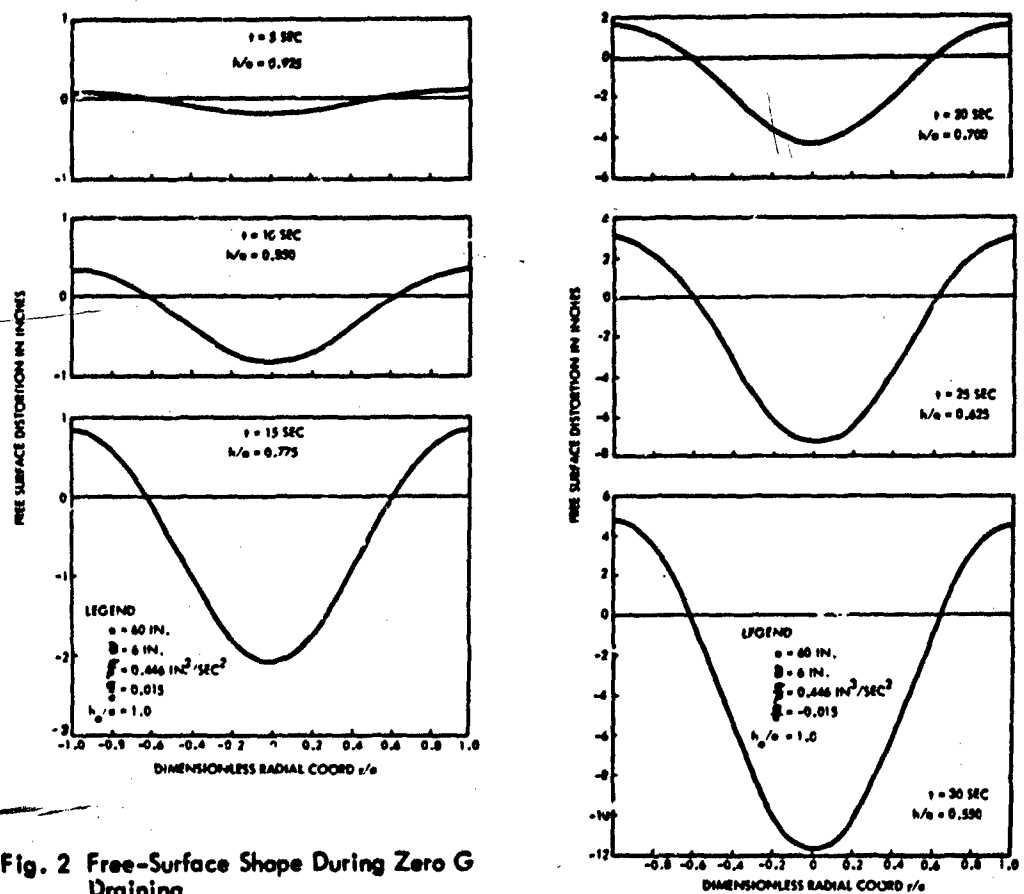


Fig. 2 Free-Surface Shape During Zero G Draining

Figure 3 shows that oscillations of the free-surface excited by the drainage are damped out and that free-surface distortion increases as the drainage proceeds.

In Fig. 4 the time history of free-surface distortion at the center of the tank is given for gravity-induced drainage at the 0.1 g level. For gravity drainage governed by Torricelli's law

$$h = \frac{g}{2} \left(\frac{\delta}{a} \right)^4 t^2 - (2gh_0)^{1/2} \frac{\delta^2}{a^2} t + h_0 \quad (40)$$

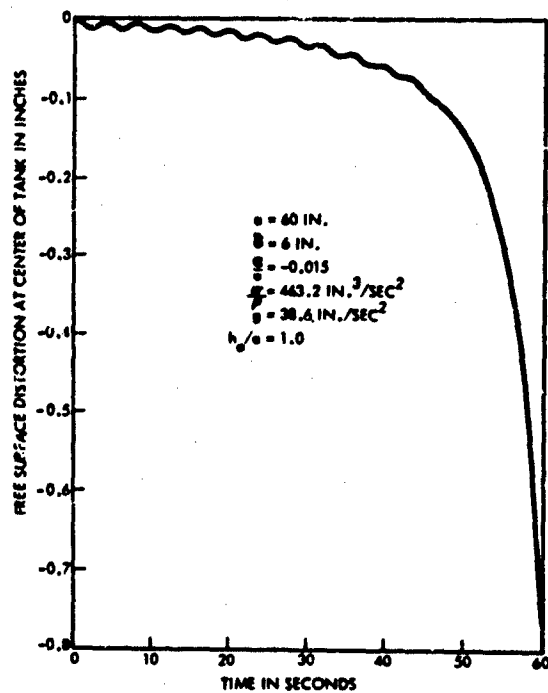


Fig. 3 Time History of Free-Surface Distortion at Center of Tank During Draining

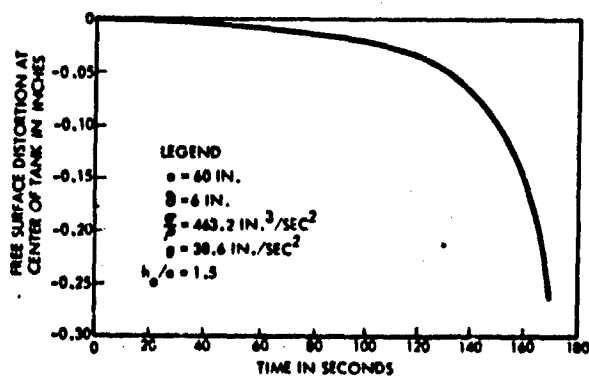


Fig. 4 Time History of Free-Surface Distortion at Center of Tank During Gravity (0.1 g) Draining

$$\dot{h} = -\frac{\delta^2}{a^2} (2gh)^{1/2} \quad (41)$$

and

$$\ddot{h} = -\frac{\delta^2}{a^2} \frac{g}{2} (h)^{-1/2} \dot{h} \quad (42)$$

where for simplicity the coefficient of the vena contracta has been assumed to be unity. The values of the various physical constants used are given in the legend of Fig. 4.

Figure 5 gives the time history of the free-surface distortion at the center of the tank during filling at a constant rate. It will be noted that during filling the oscillations are

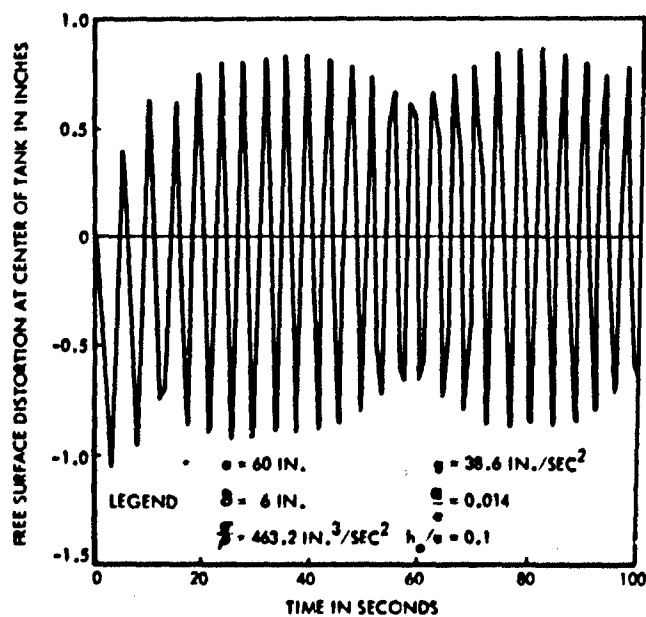


Fig. 5 Time History of Free-Surface Distortion at Center of Tank During Filling

not damped. This fact is explained by examination of the terms in Eq. (26). One observes that the damping-like term (second term in the left-hand member) and the forcing term (second term in the right-hand member) approach zero as h increases, whereas the coefficient of the $\frac{C_n}{h}$ term approaches a constant value - since $\tanh k_n h \approx 1.0$ as h increases. Hence one would expect that free oscillations, once started, would persist unless adequate damping is provided.

On the other hand, during drainage at a constant rate, the forcing term in the right-hand member of Eq. (26) appears to dominate the damping term containing \dot{C}_n as h decreases. It is this domination which gives rise to large free-surface distortion and the possibility of a vapor blowthrough during zero-g drainage.

6 SUMMARY AND CONCLUSIONS

This paper presents a formulation for studying the distortions of the free surface of a liquid, during variable low-g conditions induced by draining or filling of a tank. The formulation also provides the appropriate conditions for the solution of the initial-value problem. It is shown that the equations derived reduce to the appropriate results in the corresponding limiting cases. Several specific examples illustrate the method to be used in the solution of the drainage- or filling-induced disturbances of the free surface during variable zero- or low-g conditions. The stability of the free surface may also be studied using the given formulation.

One of the examples considered for drainage at a constant rate under zero-g conditions indicates the possibility of a vapor blowthrough such as the ones reported in Ref. 3. An interesting result of this study, of concern for refueling of spacecraft or space stations, points to the necessity of providing suitable baffles in tanks to damp the motion of the liquid free surface induced by the refueling operation. Unless such motion is damped adequately, it may adversely affect the attitude stabilization of the spacecraft or space station.

Only a limited number of examples are presented to illustrate the method and the trends predicted by the present study. It is recommended that additional specific

examples be studied to delineate the problems which may be encountered by spacecraft during periods of weightlessness or near-weightlessness. The present analysis also provides a means of studying the problems theoretically to supplement the current experimental work using a drop tower facility where only relatively short periods of weightlessness are available.

7 REFERENCES

1. R. M. Cooper, "Dynamics of Liquids in Moving Containers," ARS J., 8, 1960, pp. 725-729
2. H. N. Abramson, "Dynamic Behavior of Liquid in Moving Containers," Appl Mech Rev, Vol. 16, No. 7, Jul 1963, pp. 501-506
3. TRW Space Technology Laboratories, Bibliography on Liquid Sloshing, by G. C. K. Yeh, TRW Report No. 64-9713. 6-61, Aug 1964
4. P. G. Bhuta, and G. C. K. Yeh, "Liquid Sloshing Due to a Time Dependent Discontinuous Boundary," to be published in Intern. J. Mech. Sci.
5. Ramo-Wooldridge Corporation (TRW Space Technology Laboratories), On the Sloshing of a Liquid in a Cylindrical Tank, by J. W. Miles, Report No. AM 6-5, 20 Apr 1956
6. J. W. Miles, "Note on the Damping of Free-Surface Oscillations Due to Drainage," J. Fluid Mech., Vol. 12, Part 3, 1962, pp. 438-440. Also available as Aerospace Corp. Report No. TDR-930 (2270-20) TN-1, Sep 1961
7. National Aeronautics and Space Administration, Investigation of the Damping of Liquids in Right-Circular Cylindrical Tanks, Including the Effects of a Time-Variant Liquid Depth, by D. G. Stephens, H. W. Leonard, and T. W. Perry, Jr., NASA TN D-1367, Jul 1962
8. M. A. Saad and D. A. Oliver, "Linearized Time Dependent Free Surface Flow in Rectangular and Cylindrical Tanks," Proc. 1964 Heat Transfer and Fluid Mechanics Institute, Stanford University Press, Stanford, Calif., pp. 81-99

9. National Aeronautics and Space Administration, Photographic Study of Propellant Outflow from a Cylindrical Tank During Weightlessness, by R. C. Nussle, J. D. Derdul, and D. A. Petrash, NASA Technical Note No. TN-D-2572, Jan 1965
10. H. Lamb, Hydrodynamics, 6th ed., Chapter IX, Dover Publications, New York, 1945, p. 364
11. T. B. Benjamin and F. Ursell, "The Stability of the Plane Free Surface of a Liquid in Vertical Periodic Motion," Proc. Roy. Soc. (London), Series A, Vol. 225, 1954, pp. 505-515
12. TRW Space Technology Laboratories, Liquid Sloshing in a Moving Tank with a Time Dependent Discontinuous Boundary, by G. C. K. Yeh, Redondo Beach, Calif., Report EM 14-12, Jun 1964
13. J. Wehausen and E. V. Laitone, "Surface Waves," in Handbuch Der Physik, Fluid Dynamics III, Springer-Verlag, Berlin, 1960, pp. 603-631

ACKNOWLEDGEMENT

The authors wish to thank R. N. Schreiner for his help with the numerical examples.

DISCUSSION

Michel Saad, University of Santa Clara

I have three comments. I would like to call attention to the following equation:

$$\omega_m^2 = p_m^2 \tanh k_m \bar{h}_o \left[1 - \frac{(k_m \bar{A} \bar{v})^2 \tanh k_m \bar{h}_c}{4 p_m^2} \right]$$

$$\frac{d\bar{h}}{dt} = \bar{v} \bar{A}$$

This is an equation for the frequency of oscillation. It is equation 4-4, page 90 in our paper last year*. The velocity of the surface is \bar{v} . The bars indicate nondimensional quantities. We note from this equation that if \bar{h} is large we have damping. The statement was made that by filling and draining the tank we could enhance or damp the oscillation. This is not true, and this statement should be deleted. Our paper was restricted to small \bar{h} and the alledged damping term is of higher order in \bar{h} 's, hence to the order of approximation in our work, the oscillation frequency is purely real.

*Proceedings of the 1964 Heat Transfer and Fluid Mechanics Institute, Stanford University Press.

Now, as to the comment on page 10 of your paper that the initial surface velocity can be arbitrarily specified. The velocity of the free surface should be consistent with the continuity equation. In other words you cannot take any velocity at the free surface. You have to specify a velocity distribution consistent with the continuity equation in which the mass flux at the outlet is explicitly included, which I think is what you had in mind there.

Now, the third comment is that the problems of filling the tank and draining the tank are quite different. One cannot just take a tank and assume a general velocity, V , at the exit, obtain a solution, and then just write minus V and think that this solution will be applicable. One may assume irrotational flow while draining a tank, but this assumption is not acceptable when filling the tank. In draining a tank one can assume isentropic flow, but filling a tank involves dissipative effects and one cannot assume isentropic conditions.

P. G. Bhuta, TRW Systems Group

I would like to thank you for your paper because that is what gave us the impetus for doing this particular investigation; without that I probably wouldn't have ever done it myself. The assumption of irrotationality for draining the tank is not strictly valid either. We know this because we have to install anti-vortex baffles in tanks.

Saad

I have one other comment. The curves at the end of our paper are correct since they do not involve the oscillatory part of the surface displacement, but only the non-oscillatory part of the motion.

Bhuta

Oh, sure, I didn't mean to imply that they weren't — what I said was that those solutions are valid; however, they are not applicable in practical situations because more interesting things happen like, as you point out, when h is small. Unfortunately, you can't find analytical solutions when h is real small, anyway.

Robert Smith, Lockheed

In practical applications in the space vehicle is there coupling between, say, the pump and this oscillation?

Bhuta

For the examples considered in our paper $f(t)$ is equal to zero, but $\dot{f}(t)$ does not have to be zero and this would have definite effects on stability. The formulation given in the paper permits one to consider such effects. The paper by Tong and Fung considered this aspect; not the draining case, but the stability aspect when you do shake the tank. Of course, you have an additional damping-like term now which might cause additional instability or stability depending upon whether you're filling or draining the tank.

PAPER 11

THE EFFECT OF WALL ELASTICITY AND SURFACE
TENSION ON THE FORCED OSCILLATIONS OF A
LIQUID IN A CYLINDRICAL CONTAINER

By P. Tong and Y. C. Fung
CALIFORNIA INSTITUTE OF TECHNOLOGY

ABSTRACT

The stability of a fluid contained in a circular cylindrical tank with a flat, flexible bottom under a periodic axial excitation is studied. A variational approach is formulated. An approximate solution results in a pair of coupled ordinary differential equations with periodic coefficients. A method of handling the stability of the solutions of such a system of equations is presented. Numerical results are discussed.

NOMENCLATURE

English Symbols

A_n, B_n

B_M

B_σ

Constants

Membrane number

Bond number

$c_n \cdot d_n$	Amplitude of the n^{th} sloshing mode
F_1	Potential of the solid-liquid-gas interface
F_3	Potential of the edge load acting on the rim of the tank bottom
$g(t)$	Gravitational acceleration, time dependent
g_0	Mean local gravitational acceleration
g_1	Amplitude of the imposed axial acceleration
$G(\tau)$	Nondimensional gravitational acceleration
h	Membrane thickness
H	Nondimensional free surface shape
I, I_1, I_2, I_3, I_4	Functionals
J_0, J_1	Bessel functions of first kind
k_n	n^{th} root of the equation $J_1(k_n) = 0$
l	Depth of liquid
L	Nondimensional depth of liquid
L_1	Pressure energy in nondimensional form
L_2, L_3	Lagrangians in nondimensional form
$\underline{M}_1, \underline{M}_2, \underline{M}_3$	Matrix
N_r	Midplane stress resultant
$p_n \omega$	n^{th} sloshing frequency for rigid tank
p	Pressure
P	Nondimensional pressure
r_0	Radius of the tank
(r, θ, z)	Cylindrical coordinates
(R, ϵ, Z)	Nondimensional cylindrical coordinates

S_1, S_2, S_3

Surfaces

t

Time

\underline{U}

Modal matrix

w

Transverse deflection of membrane

W

Nondimensional transverse deflection of membrane

z

Vertical coordinate

Z

Nondimensional vertical coordinate

Greek Symbols

α

Nondimensional imposed axial acceleration

γ_n

Constants

Γ_1, Γ_3

Boundary curves of S_1, S_3 respectively

$\delta_1, \delta_2, \delta_3$

Constants

η

Free surface shape

θ

Azimuthal coordinate

λ

Mass ratio

Λ_n

Constants

μ_n, ν_n

Constants

ρ

Density of membrane

ρ_0

Density of liquid

σ

Surface tension

τ

Nondimensional time

ϕ

Velocity potential

Φ

Nondimensional velocity potential

ω

Forcing frequency

Ω

Nondimensional frequency

$\Omega_1^2, \Omega_2^2, \dots (n=m, \dots, N)$

Eigenvalues of Ω^2 where M, \dots, N indicate the fluid modes which are chosen for the approximate solution

Ω_M^2

Frequency parameter for the membrane

Ω_σ^2

Frequency parameter for surface tension

$\nabla^2, \bar{\nabla}^2$

Two-dimensional Laplace operator

$\left(\frac{1}{r_0^2} \nabla^2 = \bar{\nabla}^2 = \frac{1}{r} \frac{\partial}{\partial r} r \frac{\partial}{\partial r} + \frac{1}{r^2} \frac{\partial^2}{\partial \theta^2} \right)$ in cylindrical coordinates)

$\nabla, \bar{\nabla}$

Three-dimensional gradient operator

$\left(\frac{1}{r_0} \nabla = \bar{\nabla} = \bar{e}_r \frac{\partial}{\partial r} + \frac{\bar{e}_\theta}{r} \frac{\partial}{\partial \theta} + \bar{e}_z \frac{\partial}{\partial z} \right)$

in cylindrical coordinates; for the free surface and the membrane, ignore the $\bar{e}_z \frac{\partial}{\partial z}$ term)

THE EFFECT OF WALL ELASTICITY AND SURFACE TENSION ON THE FORCED OSCILLATIONS OF A LIQUID IN A CYLINDRICAL CONTAINER

1 INTRODUCTION

Dynamics of large liquid-fuel rockets naturally involve the motion of a liquid in a flexible container. The symmetric modes of the fluid motion, which influences the pressure at the tank bottom, and therefore influences the pressure in the pump and in the combustion chamber, as well as thrust and rocket acceleration, have an important effect on the structural dynamics of a rocket. In some instances the longitudinal oscillations were so serious as to affect the safety of the vehicle. For this reason, the analysis of the forced oscillations of the liquid container is important.

At ground level, perhaps the effects on fuel sloshing of the flexibility of the tank wall and the surface tension of the free surface are negligible. At reduced gravity conditions, these effects become more evident. It is the purpose of this article to evaluate the effects of tank flexibility and surface tension on the stability of liquid motion in the symmetric modes.

Sloshing of liquids has been studied by many authors. Although most of them considered rigid containers (Ref. 1), Miles (Ref. 2) considered bending modes of a flexible container, and Bleich (Ref. 3) investigated the longitudinal modes. Recently, Bhuta and Koval (Refs. 4 and 5) studied the coupled oscillations of a liquid in a tank with a flexible bottom. They defined the normal modes of the system, and treated the orthogonality and expansion theorems. Bhuta and Yeh (Refs. 6 and 7) considered the problem of arbitrarily assigned velocity distribution on the tank bottom.

On the other hand, there is substantial literature about the influence of surface tension on sloshing, e.g., Yeh's bibliography (Ref. 8) and papers by Bond and Newton (Ref. 9) and Reynolds (Ref. 10). Most of these studies, however, are concerned with free oscillations. Very little has been done about the influence of surface tension on forced oscillations, and no work seems to have been done on coupling with the flexibility of the tank.

In the present paper, a circular tank with a flexible bottom under vertical periodic excitation is studied. The problem is first formulated in the form of differential equations and then in the form of a variational principle. An approximate solution is presented, which results in a pair of coupled ordinary differential equations with periodic coefficients. The stability of the solutions of these equations is discussed.

2 STATEMENT OF THE PROBLEM

A circular cylindrical container with rigid side walls and a flat, flexible, bottom contains a liquid with a free surface. The tank walls are subjected to an oscillatory axial acceleration, in addition to a constant mean-local-gravitational acceleration directed along the axis of the cylinder. Above the liquid surface is a gas with constant pressure. No external force acts underneath the tank bottom. The situation is pictured in Fig. 1. The problem is to determine the motion of the liquid and, in particular, its stability.

The fluid properties, including the surface tension, are assumed to be uniform, constant, incompressible, and inviscid.

The mean free surface of the liquid is assumed to be a plane perpendicular to the cylinder axis. In low-gravity and finite surface tension, one may have to consider a curved mean free surface. The governing criterion is the Bond number defined below. In this paper, we assume that the Bond number is sufficiently large so that the free surface is approximately a plane. The case of low Bond number is discussed later.

As a further simplification, we assume that the deviation from the static equilibrium condition is small, so that the deflections of the free surface and of the tank bottom, the fluid velocity, and hence the velocity potential,

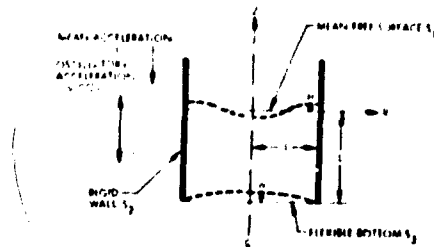


Fig. 1 Geometry of the Problem in Nondimensional Variables

may be considered infinitesimal quantities of the first order. Under this assumption, all the equations can be linearized, and the mathematical problem is relatively simple. A number of interesting nonlinear problems are ruled out by this assumption. But, as an investigation of the initial tendency toward instability, the linearized theory should be adequate.

3 MATHEMATICAL FORMULATION

Consider a quantity of inviscid liquid situated in a cylindrical container of radius r_0 as is shown in Fig. 1. The cylindrical polar coordinate system is chosen so that the $+z$ direction is directed upward away from the liquid, the zero on this axis being fixed on the mean free surface. If the fluid is assumed inviscid and incompressible, and the motion irrotational, the equation of continuity may be expressed in terms of the velocity potential ϕ ,

$$\left(\frac{1}{r} \frac{\partial}{\partial r} r \frac{\partial}{\partial r} + \frac{1}{r^2} \frac{\partial^2}{\partial \theta^2} + \frac{\partial^2}{\partial z^2} \right) \phi = 0 \quad (1)$$

and the velocity components \bar{u} , \bar{v} , \bar{w} are

$$\bar{u} = \phi_r, \quad \bar{v} = \frac{1}{r} \phi_\theta, \quad \bar{w} = \phi_z \quad (2)$$

The usual subscript notation is used to denote partial differentiation.

The kinematic conditions at the tank walls and the free surface are

$$\bar{u} = \frac{\partial \phi}{\partial r} = 0 \quad \text{on} \quad r = r_0 \quad (3)$$

$$\bar{w} = \frac{\partial \phi}{\partial z} = \frac{\partial \eta}{\partial t} \quad \text{on} \quad z = -l \quad (4)$$

$$\bar{w} = \frac{\partial \phi}{\partial z} = \frac{\partial \eta}{\partial t} \quad \text{on} \quad z = 0 \quad (5)$$

where w denotes the deflection of the tank bottom, and η denotes the deflection of the free surface, both positive in the $+z$ direction, and both assumed to be infinitesimal.

Since the motion is irrotational, Bernoulli's equation is satisfied throughout the liquid domain. In particular, at the free surface, we have

$$\frac{p}{\rho_0} = -\frac{1}{2}(\nabla\phi)^2 - g(t)\eta - \phi_t + c(t) \quad (6a)$$

$$g(t) = g_0 + g_1 \cos \omega t \quad (6b)$$

where

- | | | | |
|---------------------|---|---------------------------------------|---------------------------------------------------------------------------------------------------|
| $c(t)$ | = | arbitrary function of time | } Taken as positive if they
are directed toward the
tank bottom (along the
-z direction) |
| g_0 | = | mean local gravitational acceleration | |
| $g_1 \cos \omega t$ | = | imposed axial acceleration* | |
| p | = | pressure just inside the interface | |

The pressure p is related to the pressure just outside the liquid, p_G , by the relation

$$p_G - p = \sigma K \quad (7)$$

where

- σ = surface tension
 K = total curvature of the free surfaces

*Here we just write out a special form of imposed axial acceleration. The method developed later can be applied to a general periodic imposed axial acceleration.

In linearized form, under the assumptions that $\eta/r_0 \ll 1$ and $|\text{grad } \eta| < 1$, we have

$$K = \bar{\nabla}^2 \eta = \frac{1}{r} \frac{\partial}{\partial r} \left(r \frac{\partial \eta}{\partial r} \right) + \frac{1}{r^2} \frac{\partial^2 \eta}{\partial \theta^2} \quad (8)$$

If the pressure of the gas p_G is a constant, then without loss of generality we may set $p_G = 0$. The function $c(t)$ can be absorbed in ϕ_t . We can also neglect $|\bar{\nabla} \phi|^2$ in Eq. (6) and evaluate ϕ_t on the surface $z = 0$ under the scheme of linearization. Thus we obtain the linearized free surface condition,

$$\frac{\sigma}{\rho_0} \bar{\nabla}^2 \eta = \left(\frac{\partial \phi}{\partial t} \right)_{z=0} + g(t) \eta \quad (9)$$

Similarly, Bernoulli's equation gives the pressure on top of the bottom wall

$$(p)_{z=-l+w} = \rho_0 \left[- \left(\phi_t \right)_{z=-l} - g(t) (-l + w) \right] \quad (10)$$

No other forces are assumed to be acting on the tank bottom. If the tank bottom is very thin and is prestressed so that it behaves like a membrane, then the equation of motion of the bottom is

$$N_r \bar{\nabla}^2 w = \rho h \left[\frac{\partial^2 w}{\partial t^2} + g(t) \right] + (\rho)_{z=-l+w} \quad (11)$$

where

- N_r = tensile stress resultant in the tank bottom (assumed to be a constant)
- ρ = density of the tank bottom material
- h = tank bottom wall thickness
- ρh = mass per unit area of the tank bottom

A combination of Eqs. (10) and (11) gives the linearized equation of motion of the elastic bottom as a membrane:

$$N_r \nabla^2 w = \rho h \frac{\partial^2 w}{\partial t^2} - \rho_0 g(t) w - \rho_0 \left(\frac{\partial \phi}{\partial t} \right)_{z=-l} + (\rho h + \rho_0 l) g(t) \quad (12)$$

In reality, a tank with flat bottom develops both bending and stretching stresses under fluid pressure. Equation (12) is a good approximation only if a membrane tension is built in at the edges by stretching the bottom onto a rigid cylinder before the two are welded together.

It is necessary to specify the boundary conditions for η and w at the edge $r = r_0$. We choose

$$w = 0 \quad \text{when} \quad r = r_0 \quad (13)$$

$$\frac{\partial \eta}{\partial r} = 0 \quad \text{when} \quad r = r_0 \quad (14)$$

The last condition is a special case of zero capillary-hysteresis. It is consistent with the simplifying assumption that the undisturbed free surface is a plane $z = 0$. In a very-low-gravity condition, the mean free surface is curved, and Eq. (14) should be replaced by the condition $\partial \eta / \partial r = \gamma \eta$ at the wall where γ is a physical constant.

These equations define the linear, inviscid problem of sloshing under appropriate initial or periodicity conditions.

4 DIMENSIONLESS EQUATIONS

Taking the radius of the cylinder r_0 as the characteristic length, the gravitational acceleration g_0 as the characteristic acceleration, and ω as the characteristic frequency, we define the dimensionless variables as follows:

$$\begin{aligned}
 R &= \frac{r}{r_0} & Z &= \frac{z}{r_0} \\
 L &= \frac{l}{r_0} & \tau &= \omega t \\
 \Phi &= \frac{\phi}{\omega r_0^2} & H &= \frac{\eta}{r_0} \\
 W &= \frac{w}{r_0} & \alpha &= \frac{s_1}{s_0} \\
 G(\tau) &= \frac{s_0 + s_1 \cos \omega t}{s_0} & P &= \frac{p}{\rho_0 \omega^2 r_0^2}
 \end{aligned} \tag{15}$$

We define the dimensionless parameters as follows:

$$\begin{aligned}
 \text{Bond number} &= B_\sigma = \rho_0 s_0 r_0^2 / \sigma \\
 \text{Membrane number} &= B_M = \rho_0 s_0 r_0^2 / N_r \\
 \text{Frequency parameter for surface tension} &= \Omega_\sigma^2 = \rho_0 r_0^3 \omega^2 / \sigma \\
 \text{Frequency parameter for the membrane} &= \Omega_M^2 = \rho_0 r_0^3 \omega^2 / N_r \\
 \text{Mass ratio} &= \lambda = \frac{\rho h}{\rho_0 r_0}
 \end{aligned} \tag{16}$$

and the operator

$$\nabla^2 = 1/R \partial/\partial R (R \partial/\partial R) + 1/R^2 \partial^2/\partial \theta^2 = r_0^2 \bar{\nabla}^2 \tag{17}$$

Then the equations become

$$\left(\frac{\partial^2}{\partial Z^2} + \nabla^2 \right) \Phi = 0 \tag{18}$$

$$\nabla^2 H - \Omega_\sigma^2 \left(\frac{\partial \Phi}{\partial \tau} \right)_{Z=0} - B_\sigma G H = 0 \quad (19)$$

$$\nabla^2 W - \lambda \Omega_M^2 \frac{\partial^2 W}{\partial \tau^2} + \Omega_M^2 \left(\frac{\partial \Phi}{\partial \tau} \right)_{Z=-L} + B_M G(\tau) W - (\lambda + L) B_M G(\tau) = 0 \quad (20)$$

with the boundary conditions

$$\frac{\partial \Phi}{\partial R} = 0 \quad \text{on } R = 1 \quad (21)$$

$$\frac{\partial \Phi}{\partial Z} = \frac{\partial W}{\partial \tau} \quad \text{on } Z = -L \quad (22)$$

$$\frac{\partial \Phi}{\partial Z} = \frac{\partial W}{\partial \tau} \quad \text{on } Z = 0 \quad (23)$$

$$W = 0 \quad \text{on } R = 1 \quad (24)$$

and

$$\frac{\partial H}{\partial R} = 0 \quad \text{on } R = 1 \quad (\text{assuming } \gamma = 0) \quad (25)$$

Equations (18) through (25) show that the problem of sloshing depends on the parameters Ω_σ^2 , B_σ , α , Ω_M^2 , B_M , λ , and L .

These dimensionless parameters are not all independent; since

$$\Omega_M^2 = \frac{\sigma}{N_r} \Omega_\sigma^2 \quad \text{and} \quad B_M = \frac{\sigma}{N_r} B_\sigma \quad (26)$$

therefore

$$\frac{B_M}{B_\sigma} = \frac{\Omega_M^2}{\Omega_\sigma^2} \quad (27)$$

However, we retain the sets of symbols Ω_J^2 , B_σ and Ω_M^2 , B_M because these two pairs of parameters are not both likely to be important. The conditions are:

- Ω_M^2 , $B_M \rightarrow 0$ if the tank bottom is rigid
- Ω_σ^2 , $B_\sigma \rightarrow \infty$ if the surface tension has no effect

5 DISCUSSION OF ANALYTICAL SOLUTIONS

Consider symmetric modes of motion in which ϕ , H , W are independent of the angular coordinates θ . A solution of Eq. (18) may be posed as

$$\phi = \dot{d}_0(\tau)Z + c_0(\tau) + \sum_{n=1}^{\infty} J_0(k_n R) \left[\dot{d}_n(\tau) \frac{\cosh k_n Z}{\sinh k_n L} + \dot{c}_n(\tau) \frac{\sinh k_n Z}{\cosh k_n L} \right] \quad (28)$$

Then Eqs. (22) and (23) give

$$H = d_0(\tau) + \sum_{n=1}^{\infty} d_n(\tau) \frac{k_n J_0(k_n R)}{\cosh k_n L} \quad (29)$$

and

$$W = d_0(\tau) + f(R) + \sum_{n=1}^{\infty} k_n [d_n(\tau) - c_n(\tau)] J_0(k_n R) \quad (30)$$

Both Eqs. (21) and (25) are satisfied if the k_n 's are the roots of the equation

$$J_1(k_n) = 0 \quad n = 1, 2, 3, \dots \quad (31)$$

Eq. (24) is satisfied by taking

$$d_0(\tau) + \sum_{n=1}^{\infty} k_n [d_n(\tau) - c_n(\tau)] J_0(k_n) = 0 \quad (32)$$

and

$$f(R) = (\lambda + L) \left[1 - \frac{J_0(\sqrt{B_M} R)}{J_0(\sqrt{B_M})} \right]$$

Here, $f(R)$ is the static deflection of the membrane. We assume that, if B_M is positive, $\sqrt{B_M}$ is less than the first root of $J_0(x) = 0$, namely, 2.4048. To satisfy Eqs. (19) and (20), we substitute ϕ , H , W from Eqs. (28) through (30), collect terms, and represent the lefthand side as a Fourier-Bessel series in $J_0(k_n R)$. Since the series vanishes, every coefficient of $J_0(k_n R)$, $n = 1, 2, \dots$, must vanish. Thus, from Eq. (19) we obtain the necessary conditions

$$\Omega_\sigma^2 \ddot{c}_0(\tau) + B_\sigma G(\tau) d_0(\tau) = 0 \quad (33a)$$

and

$$\Omega_\sigma^2 \ddot{c}_n(\tau) + k_n \tanh k_n L [k_n^2 + B_\sigma G(\tau)] d_n(\tau) = 0 \quad (33b)$$

To avoid the divergent difficulty, we modify Eq. (20) by multiplying by R ; integrating with respect to R from 0 to R , we get

$$R \frac{\partial W}{\partial R} + B_M G \int_0^R R W(R, \tau) dR - \lambda \Omega_M^2 \frac{\partial^2}{\partial \tau^2} \int_0^R W(R, \tau) R dR - \frac{(\lambda + L)}{2} B_M G R^2 + \Omega_M^2 \int_0^R \frac{\partial \Phi}{\partial \tau} \Big|_{Z=-L} R dR = 0 \quad (34)$$

Any function $W(R, \tau)$ of class C^2 in the closed interval 0 to 1 for R satisfying the above equation will satisfy Eq. (20). A substitution of Eqs. (28), (29), and (30) into it gives

$$\sum_{n=1}^{\infty} k_n^2 (c_n - d_n) J_1(k_n R) + B_M G \left[\frac{d_0 R}{2} + \sum_{n=1}^{\infty} (d_n - c_n) J_1(k_n R) \right] - \lambda \Omega_M^2 \left[\frac{d_0 R}{2} + \sum_{n=1}^{\infty} (\ddot{d}_n - \ddot{c}_n) J_1(k_n R) \right] + \Omega_M^2 \left[\frac{-\lambda \ddot{d}_0 + \ddot{c}_0}{2} R + \sum_{n=1}^{\infty} \frac{J_1(k_n R)}{k_n} (\ddot{c}_n \coth k_n L - \ddot{d}_n \tanh k_n L) \right] - \alpha \frac{(\lambda + L) \sqrt{B_M}}{J_0(\sqrt{B_M})} J_1(\sqrt{B_M} R) = 0 \quad (35)$$

By expanding R and $J_1(\sqrt{B_M} R)$ in terms of $J_1(k_n R)$, we can collect the coefficients of $J_1(k_n R)$ and set them equal to zero, to obtain

$$\frac{\Omega_M^2}{k_n} \left[\ddot{c}_n (\coth k_n L + \lambda k_n) - \ddot{d}_n (\tanh k_n L + \lambda k_n) \right] + (k_n^2 - B_M G) (c_n - d_n) = - \frac{\Omega_M^2}{k_n J_0(k_n)} \left[(\lambda + L) \ddot{d}_0 + \ddot{c}_0 + \frac{B_M G}{\Omega_M^2} d_0 \right] + \frac{2\alpha (\lambda + L) \sqrt{B_M} J_1(\sqrt{B_M})}{k_n J_0(k_n) J_0(\sqrt{B_M})} \frac{k_n^2}{B_M - k_n^2} \quad (36)$$

Now, if we want to truncate the infinite series in Eqs. (28) through (30) by taking $n = m, \dots, N$, we see that Eqs. (32), (33), and (36) always involve $2(N - m + 2)$ unknowns and $2(N - m + 2)$ equations, which in general have solutions.

Of course, we can do the same thing for Eq. (19) to obtain

$$i_{\sigma}^2 \ddot{c}_n + (k_n^2 + B_{\sigma} G) k_n (\tanh k_n L) d_n = \frac{\sinh k_n L}{J_0(k_n)} (\Omega_{\sigma}^2 \ddot{c}_0 + B_{\sigma} G d_0) \quad (37)$$

However, since we have assumed $\partial H / \partial R = 0$ at $R = 1$, the series of Eq. (29), after twice term-by-term differentiation, is still convergent. Thus Eq. (37) coincides with Eq. (33).

We shall now discuss the solution for Eqs. (32), (33), and (36). For the case of free vibration, i.e. $G = 1$ or $\alpha = 0$, solutions for c_n , d_n can be obtained rather easily. If we let

$$c_n = C_n e^{i\Omega \tau}$$

and

(33)

$$d_n = D_n e^{i\Omega \tau}$$

then, from Eq. (33), we obtain

$$C_0 = \frac{B_{\sigma}}{\Omega_{\sigma}^2 \Omega^2} D_0$$

and

(39)

$$C_n = \frac{k_n (k_n^2 + B_{\sigma}) \tanh k_n L}{\Omega_{\sigma}^2 \Omega^2} D_n = \frac{p_n^2}{\Omega^2} D_n$$

and from Eqs. (36) and (39),

$$\Omega_M^2 \Omega^2 \frac{(L + \lambda)}{J_0(k_n)} D_0 = \beta_n D_n \quad (40)$$

where

$$\beta_n = - \left[\Omega_M^2 p_n^2 (\coth k_n L + \lambda k_n) - \Omega_M^2 \Omega^2 (\tanh k_n L + \lambda k_n) + k_n (k_n^2 - B_M) \left(\frac{p_n^2}{\Omega^2} - 1 \right) \right] \quad (41)$$

Substituting into Eq. (30), we have

$$W = e^{i\Omega\tau} D_0 \left[1 + \sum_{n=1}^{\infty} k_n \frac{\Omega_M^2 \Omega^2 (L + \lambda)}{\beta_n} \left(1 - \frac{p_n^2}{\Omega^2} \right) \frac{J_0(k_n R)}{J_0(k_n)} \right] + f(R) \quad (42)$$

Now we can easily see that the coefficient of $J_0(k_n R)$ in the above series is of order $1/(k_n^{3/2})$ for large n ; so the series is actually divergent after twice term-by-term differentiation with respect to R . At $R = 1$, $W = 0$, we have $D_0 = 0$ for $\Omega_M^2 \neq 0$ ($\Omega_M^2 = 0$ corresponds to rigid tank); therefore,

$$\xi(\Omega^2) = 1 + \sum_{n=1}^{\infty} \frac{\Omega_M^2 (L + \lambda) k_n}{\beta_n} (\Omega^2 - p_n^2) = 0 \quad (43)$$

This equation will determine the eigenvalue Ω . It can be shown that, for $p_n^2 \geq 0$, $\chi_n \geq 0$, all the roots Ω are real, and no double roots exist. In the case $\Omega_M^2 \rightarrow 0$, some Ω 's can be obtained asymptotically in a rather simple fashion. Let

$$\Omega^2 = \Omega_I^2 = p_I^2 (1 - \delta_1 \Omega_M^2 - \delta_2 \Omega_M^4 - \delta_3 \Omega_M^6 \dots) \quad (44)$$

Then we have

$$\begin{aligned} \beta_I &= -\Omega_M^2 \left[p_I^2 (\coth k_I L + \lambda k_I) - p_I^2 (1 - \delta_1 \Omega_M^2 - \delta_2 \Omega_M^4 \dots) (\tanh k_I L + \lambda k_I) \right. \\ &\quad \left. + \chi_I \delta_1 \Omega_M^2 + (\delta_2 + \delta_1^2) \Omega_M^4 + \dots \right] \\ &= \left[\delta_1 \chi_I - p_I^2 (\coth k_I L - \tanh k_I L) \right] \Omega_M^2 \\ &\quad + \left[(\delta_1^2 + \delta_2) \chi_I - p_I^2 \delta_1 (\tanh k_I L + \lambda k_I) \right] \Omega_M^4 \\ &\quad + \left[(\delta_1^2 + 2\delta_1 \delta_2 + \delta_3) \chi_I - p_I^2 \delta_2 (\tanh k_I L + \lambda k_I) \right] \Omega_M^6 + o(\Omega_M^8) \quad (45) \end{aligned}$$

where

$$\chi_I = k_I (k_I^2 - B_M) \quad (46)$$

Equation (43) becomes

$$\begin{aligned} 1 - \frac{p_I^2 (L + \lambda) (\delta_1 + \delta_2 \Omega_M^2 + \dots) \Omega_M^2}{\delta_1 \chi_I - p_I^2 (\coth k_I L - \tanh k_I L) + \left[(\delta_1^2 + \delta_2) \chi_I - p_I^2 \delta_1 (\tanh k_I L + \lambda k_I) \right] \Omega_M^2 + \dots} \\ - \Omega_M^2 p_I^2 (L + \lambda) \left[\sum_{n=1}^{\infty} \frac{1}{k_n^2 - B_M} - \frac{1}{k_I^2 - B_M} \right] + o(\Omega_M^4) = 0 \quad (47) \end{aligned}$$

In order that the above equation be valid as $\Omega_M^2 \rightarrow 0$, we must have

$$\delta_1 = \frac{\coth k_l L - \tanh k_l L}{k_l} p_l^2 \quad (48)$$

and, since

$$\sum_{n=1}^{\infty} \frac{1}{k_n^2 - B_M} = \frac{1}{B_M} - \frac{J_0(\sqrt{B_M})}{2\sqrt{B_M} J_1(\sqrt{B_M})} \quad (49)$$

Eq. (43) becomes

$$1 - \frac{p_l^2 (L + \lambda) (\delta_1 + \delta_2 \Omega_M^2 + \dots)}{(\delta_1^2 + \delta_2) x_l - p_l^2 \delta_1 (\tanh k_l L + \lambda k_l) + [x_l (\delta_1^2 + 2\delta_1 \delta_2 + \delta_3) - p_l^2 \delta_2 (\tanh k_l L + \lambda k_l)] \Omega_M^2 + \dots} - \Omega_M^2 p_l^2 (L + \lambda) \left[\frac{1}{B_M} - \frac{J_0(\sqrt{B_M})}{2\sqrt{B_M} J_1(\sqrt{B_M})} - \frac{1}{k_l^2 - B_M} \right] + o(\Omega_M^4) = 0 \quad (50)$$

Expanding the lefthand side in power series of Ω_M^2 , and putting the coefficient of Ω_M^{2n} equal to zero, we get

$$1 - \frac{p_l^2 (L + \lambda) \delta_1}{(\delta_1^2 + \delta_2) x_l - p_l^2 \delta_1 (\tanh k_l L + \lambda k_l)} = 0 \quad (51)$$

and

$$p_l^2 (L + \lambda) \delta_2 - (\delta_1^2 + 2\delta_1 \delta_2 + \delta_3) x_l + p_l^2 \delta_2 (\tanh k_l L + \lambda k_l) + [p_l^2 (L + \lambda)]^2 \left[\frac{1}{B_M} - \frac{J_0(\sqrt{B_M})}{2\sqrt{B_M} J_1(\sqrt{B_M})} - \frac{1}{k_l^2 - B_M} \right] \delta_1 = 0$$

Then

$$\delta_2 = \frac{\delta_1 p_l^2 \nu_l - \delta_1^2 \chi_l}{\chi_l}$$

and

(52)

$$\delta_3 = \frac{1}{\chi_l} \left\{ \delta_2 p_l^2 \nu_l - (\delta_1^2 + 2\delta_1 \delta_2) \chi_l + [p_l^2 (L + \lambda)]^2 \left[\frac{1}{\sqrt{B_M}} - \frac{J_0(\sqrt{B_M})}{2\sqrt{B_M} J_1(\sqrt{B_M})} - \frac{1}{k_l^2 - B_M} \right] \delta_1 \right\}$$

Therefore, after some rearrangement, we get

$$\Omega_l^2 = p_l^2 \left[1 - \left(\frac{\mu_l}{\nu_l} - 1 \right) \left(\frac{\nu_l p_l^2}{\Lambda_l} \right) - \left(2 - \frac{\mu_l}{\nu_l} \right) \left(\frac{\mu_l}{\nu_l} - 1 \right) \left(\frac{\nu_l p_l^2}{\Lambda_l} \right)^2 + o\left(\frac{1}{\Lambda_l^3} \right) \right] \quad (53)$$

where

$$\Lambda_l = \frac{\chi_l}{\Omega_M^2} \quad (54)$$

From Eq. (53) we make two interesting observations:

- The term p_l is the l^{th} nondimensional natural sloshing frequency of the liquid in a rigid tank. Since $(\mu_l/\nu_l) > 1$, we conclude that $\Omega_l^2 < p_l^2$.
- The elastic effect is at least of order

$$\frac{\Omega_M^2}{\sinh 2k_l L} \left[= 2 \frac{\chi_l}{\Lambda_l} (\mu_l - \nu_l) \right]$$

Because of the presence of the elastic bottom, the sloshing mode shapes are no longer as simple as those in a rigid tank; but, in rigid tanks, the influence of cross coupling of different fluid modes on the natural frequency is of order Ω_M^6 .

The other limiting case is: ρ_0 , the density of the fluid, tends to zero while $B_\sigma \cdot \Omega_\sigma^2$ are bounded away from zero; then Eq. (43) will tend to the free-vibration frequency equation for a circular membrane - i.e.,

$$\epsilon(\Omega^2) = 1 + \sum_{n=1}^{\infty} \frac{k^2 \Omega^2}{k_n^2 \Omega^2 - k_n^2} \quad (55)$$

$$-\frac{k \Omega J_0(k \Omega)}{2 J_1(k \Omega)} = 0$$

or

$$J_0(k \Omega) = 0$$

where

$$k^2 = \frac{\rho h r_0^2 \omega^2}{N r}$$

6 STABILITY OF THE SOLUTION

To study the stability of the solution (Refs. 11 and 12), we shall consider the following more general system of equations:*

$$\ddot{y}_1 + \sum_{n=-\infty}^{\infty} A_{2n} e^{i2nt} y_1 + \sum_{n=-\infty}^{\infty} A_{2n-1} e^{i2nt} y_2 = 0 \quad (56)$$

$$\ddot{y}_2 + \sum_{n=-\infty}^{\infty} B_{2n} e^{i2nt} y_2 + \sum_{n=-\infty}^{\infty} B_{2n+1} e^{i2nt} y_1 = 0$$

*This is an extension of Hill's method (see Ref. 12, p. 413) to a system of two equations.

where $B_0 = A_0$, $A_0 > 0$, $B_0 > 0$, $A_{-1} = B_1 = 0$, $\sum_{n=-\infty}^{\infty} \beta_n$ (where $\beta_n = |A_n|$ or $|B_n|$) is an absolutely convergent series. Equations (56) are invariant when t is changed to $t + \pi$; therefore if $y(t)$ is a solution of Eqs. (58), $y(t + \pi)$ is also a solution. By the Floquet theorem (Ref. 13), Eqs. (56) have solutions of the following form:

$$\underline{y}(t) = e^{\xi t} \underline{\psi}(t)$$

where

$$\underline{y} = \begin{pmatrix} y_1 \\ y_2 \end{pmatrix} \quad \dots \quad \underline{\psi} = \begin{pmatrix} \psi_1 \\ \psi_2 \end{pmatrix}$$

The term $\underline{\psi}(t)$ is periodic function mod(π). If $\text{Re } \xi > 0$, $y \rightarrow \infty$ as $t \rightarrow \infty$ an unbounded solution exists, which is said to be unstable. For a periodic solution mod(π) to exist, $\text{Im } \xi$ must be equal to an integer, whereas $\text{Re } \xi = 0$.

Let us assume a solution of the following form:

$$y_1(t) = e^{\xi t} \sum_{n=-\infty}^{\infty} \gamma_{2n} e^{i2nt}$$

$$y_2(t) = e^{\xi t} \sum_{n=-\infty}^{\infty} \gamma_{2n+1} e^{i2nt}$$

where $\sum_{n=-\infty}^{\infty} n^2 \gamma_{2n}$, $\sum_{n=-\infty}^{\infty} n^2 \gamma_{2n+1}$ are absolutely convergent series.

Substituting into Eqs. (56), we get

$$\begin{aligned} \sum_{n=-\infty}^{\infty} \gamma_n (2n + \xi)^2 e^{(2n+\xi)t} + \sum_{m=-\infty}^{\infty} A_{2m} e^{2mt} \sum_{n=-\infty}^{\infty} \gamma_{2n} e^{(2n+\xi)t} \\ + \sum_{m=-\infty}^{\infty} A_{2m-1} e^{2mt} \sum_{n=-\infty}^{\infty} \gamma_{2n+1} e^{(2n+\xi)t} = 0 \end{aligned} \quad (57)$$

$$\begin{aligned} \sum_{n=-\infty}^{\infty} \gamma_{2n+1} (2n + \xi)^2 e^{(2n+\xi)t} + \sum_{m=-\infty}^{\infty} B_{2m} e^{2mt} \sum_{n=-\infty}^{\infty} \gamma_{2n+1} e^{(2n+\xi)t} \\ + \sum_{m=-\infty}^{\infty} B_{2m+1} e^{2mt} \sum_{n=-\infty}^{\infty} \gamma_{2n} e^{(2n+\xi)t} = 0 \end{aligned}$$

On rearranging the terms of the absolute convergent series, and equating the coefficients of $e^{(2n+\xi)t}$ to zero, we obtain

$$\begin{aligned} -\gamma_{2n} \frac{(1\xi - 2n)^2}{A_0 - 4n^2} + \sum_{m=-\infty}^{\infty} \frac{A_m}{A_0 - 4n^2} \gamma_{2n-m} = 0 \\ -\gamma_{2n+1} \frac{(1\xi - 2n)^2}{B_0 - 4n^2} + \sum_{m=-\infty}^{\infty} \frac{B_m}{B_0 - 4n^2} \gamma_{2n+1-m} = 0 \end{aligned} \quad (58)$$

provided that $A_0 - 4n^2 \neq 0$, $B_0 - 4n^2 \neq 0$. The divisors $A_0 - 4n^2$ and $B_0 - 4n^2$ are introduced in order to make an infinite determinant, which will be formed below, to be convergent.

Equations (58) are a set of homogeneous equations. For γ_n to have nontrivial solutions, the determinants formed by the coefficients of the equations must vanish. Call this determinant $\Delta(\xi)$; then

$$\Delta(\xi) = |\alpha_{ij}| = 0 \quad (59)$$

where

$$\alpha_{2m, 2m} = \frac{A_0 - (\xi - 2m)^2}{A_0 - 4m^2}$$

$$\alpha_{2m+1, 2m+1} = \frac{B_0 - (\xi - 2m)^2}{B_0 - 4m^2}$$

$$\alpha_{2m, n} = \frac{A_{2m-n}}{A_0 - 4m^2} \quad \text{for } 2m - n \neq 0$$

$$\alpha_{2m+1, n} = \frac{B_{2m+1-n}}{B_0 - 4m^2} \quad \text{for } 2m+1 - n \neq 0$$

$$m, n = 0, \pm 1, \pm 2, \dots$$

We consider another infinite determinant $\Delta_1(\xi) = |\beta_{ij}|$ where

$$\beta_{m, m} = 1 \quad (60a)$$

$$\beta_{2m, n} = \frac{\alpha_{2m, n}}{\alpha_{2m, 2m}} = \frac{A_{2m-n}}{A_0 - (\xi - 2m)^2} \quad \text{for } 2m - n \neq 0 \quad (60b)$$

$$\beta_{2m+1, n} = \frac{\alpha_{2m+1, n}}{\alpha_{2m+1, 2m+1}} = \frac{B_{2m+1-n}}{B_0 - (\xi - 2m)^2} \quad \text{for } 2m+1 - n \neq 0 \quad (60c)$$

Since

$$\prod_{m=-\infty}^{\infty} \beta_{m,m} = 1, \quad \sum_{\substack{m,n=-\infty \\ m \neq n}}^{\infty} |\beta_{m,m}|$$

converges, provided ξ does not have such a value that one of the denominators of $\beta_{m,n}(\xi)$ vanishes. Thus, the infinite determinant $\Delta_1(\xi)$ is absolutely convergent. Then (Ref. 14),

$$\begin{aligned} \Delta(\xi) &= \Delta_1(\xi) \lim_{m \rightarrow \infty} \prod_{n=-m}^m \frac{[A_0 - (\xi - 2n)^2][B_0 - (\xi - 2n)^2]}{(A_0 - 4n^2)(B_0 - 4n^2)} \\ &= \Delta_1(\xi) \frac{\sin \frac{\pi}{2}(\xi - \sqrt{A_0}) \sin \frac{\pi}{2}(\xi + \sqrt{A_0}) \sin \frac{\pi}{2}(\xi - \sqrt{B_0}) \sin \frac{\pi}{2}(\xi + \sqrt{B_0})}{\sin^2 \left(\frac{\pi}{2} \sqrt{A_0} \right) \sin^2 \left(\frac{\pi}{2} \sqrt{B_0} \right)} \end{aligned} \quad (61)$$

We note some interesting properties of $\Delta_1(\xi)$: (1) $\Delta_1(\xi)$ is a meromorphic function of ξ and tends to 1 as $\text{Re } \xi \rightarrow \pm \infty$; (2) $\Delta_1(\xi)$ is a periodic function of ξ with period $2i$. If we form another function,

$$\begin{aligned} F(\xi) &= \Delta_1(\xi) - K_1 \left[\cot \frac{\pi}{2}(\xi + \sqrt{A_0}) - \cot \frac{\pi}{2}(\xi - \sqrt{A_0}) \right] \\ &\quad - K_2 \left[\cot \frac{\pi}{2}(\xi + \sqrt{A_0}) + \cot \frac{\pi}{2}(\xi - \sqrt{A_0}) \right] \\ &\quad - K_3 \left[\cot \frac{\pi}{2}(\xi + \sqrt{B_0}) - \cot \frac{\pi}{2}(\xi - \sqrt{B_0}) \right] \\ &\quad - K_4 \left[\cot \frac{\pi}{2}(\xi + \sqrt{B_0}) + \cot \frac{\pi}{2}(\xi - \sqrt{B_0}) \right] \end{aligned} \quad (62)$$

where K_j 's are so chosen that $F(\xi)$ has no poles at $i\xi = \pm\sqrt{A_0}, \pm\sqrt{B_0}$. then, since $\Delta_1(i\xi)$ is a periodic function of ξ , it follows that $F(\xi)$ has no poles at

$$i\xi = 2n \pm \sqrt{A_0}, \quad 2n \pm \sqrt{B_0}, \quad n = \pm 1, \pm 2, \dots$$

Thus, $F(\xi)$ is a meromorphic function with no pole on the entire plane. $F(\xi)$ is certainly bounded, therefore, by Liouville's theorem, $F(\xi)$ must be a constant, say C . As $\operatorname{Re} \xi \rightarrow \pm\infty$, $\Delta_1(i\xi) = 1$. Therefore,

$$C = 1 + 2(K_2 + K_4)i \text{ as } \operatorname{Re} \xi \rightarrow \infty$$

$$= 1 - 2(K_2 + K_4)i \text{ as } \operatorname{Re} \xi \rightarrow -\infty$$

Hence, $K_2 + K_3 = 0$, and $F(\xi) = 1$ for all ξ . Using this result and Eqs. (61) and (62), we get

$$\Delta(i\xi) = \frac{\sin^4 \frac{\pi \xi i}{2} - 2\delta_2 \sin^2 \frac{\pi \xi i}{2} + \delta_1 + \delta_3 \sin \frac{\pi \xi i}{2}}{\sin^2 \left(\frac{\pi}{2} \sqrt{A_0} \right) \sin^2 \left(\frac{\pi}{2} \sqrt{B_0} \right)} \quad (63)$$

where δ_i are some constants relating to K_j 's, A_0 , and B_0 . Put $i\xi = 0, 1/2$ and 1 in Eq. (63) and we get

$$\delta_1 = \Delta(0) \sin^2 \left(\frac{\pi}{2} \sqrt{A_0} \right) \sin^2 \left(\frac{\pi}{2} \sqrt{B_0} \right)$$

$$2\delta_2 = 1 + \sin^2 \left(\frac{\pi}{2} \sqrt{A_0} \right) \sin^2 \left(\frac{\pi}{2} \sqrt{B_0} \right) [\Delta(0) - \Delta(1)] \quad (64)$$

and

$$2\delta_3 = \frac{1}{2} + \sin^2 \left(\frac{\pi}{2} \sqrt{A_0} \right) \sin^2 \left(\frac{\pi}{2} \sqrt{B_0} \right) \left[2\Delta\left(\frac{1}{2}\right) - \Delta(0) - \Delta(1) \right]$$

In a special case, if the coefficients of Eq. (56) are even functions of t , then Eq. (56) is unchanged when we change t to $-t$; we see that, if ξ is a solution, then $-\xi$ is also a solution. Therefore, if $\Delta(i\xi_0) = 0$ and $\sin(i\xi_0\pi) = 0$, then $\delta_3 = 0$. Therefore, when we want to find the roots for $\Delta(i\xi) = 0$, we always have $\delta_3 \sin(\pi_1 \xi) = 0$ and the roots of Eq. (63) can be written out in a simple form,

$$\sin^2 \frac{\pi_1 \xi}{2} = \delta_2 \pm \sqrt{\delta_2^2 - \delta_1^2} \quad (65)$$

For a bounded solution, i.e. for $\text{Re} \xi = 0$, we must have

$$1 \geq \delta_2 \pm \sqrt{\delta_2^2 - \delta_1^2} \geq 0 \quad (66)$$

In Eq. (63), by putting $\Delta(i\xi) = 0$, we can compute ξ , and determine whether this is an unbounded solution or not. Then, from Eq. (53), we can compute γ_n , and obtain the complete solution of Eqs. (56). For a periodic solution, we must have $\Delta(0) = 0$ or $\Delta(1) = 0$.

If a periodic solution of an inhomogeneous counterpart of Eqs. (56) is considered, e.g.

$$\ddot{\underline{X}} + \underline{A}(t)\underline{X} = \underline{B}(t)$$

where $\underline{B}(t)$ is a column matrix with its elements as periodic function, we can use Eq. (57) (with non-zero righthand side) by putting $\xi = 0$, whereas Eqs. (58) become inhomogeneous. If $\Delta(0)$ is not equal to 0, we can solve for γ_n uniquely. If $\Delta(0) = 0$ we are on the boundary where Eqs. (56) have an unbounded solution. Therefore, for such an inhomogeneous equation as in our problem, the zone of instability is determined by the homogeneous solution.

7 APPROXIMATE SOLUTIONS

We choose

$$\phi = d_0(\tau)Z + c_0(\tau) + \sum_{n=m}^N J_0(k_n R) \left[\dot{c}_n(\tau) \frac{\cosh k_n Z}{\sinh k_n L} + \dot{d}_n(\tau) \frac{\sinh k_n Z}{\cosh k_n L} \right] \quad (67)$$

$$H = d_0(\tau) + \sum_{n=m}^N d_n(\tau) \frac{k_n J_0(k_n R)}{\cosh k_n L} \quad (68)$$

and

$$W = d_0(\tau) + \sum_{n=m}^N k_n [d_n(\tau) - c_n(\tau)] J_0(k_n R) + f(R) \quad (69)$$

where

$$d_0(\tau) = \sum_{n=m}^N k_n [c_n(\tau) - d_n(\tau)] J_0(k_n) \quad (70)$$

These equations satisfy Eqs. (18), (19), and (21) through (25). Then the equations

$$\Omega_\sigma^2 \ddot{c}_0(\tau) + B_\sigma G(\tau) d_0(\tau) = 0 \quad (71a)$$

$$\Omega_\sigma^2 \ddot{c}_n(\tau) + k_n \tanh k_n L [k_n^2 + B_\sigma G(\tau)] d_n(\tau) = 0 \quad (71b)$$

hold for $n = m, m+1, \dots, N$. Now, $N - (m-1)$ of the c_n, d_n are left arbitrary. To determine these arbitrary functions, we use the Ritz method by substituting ϕ , H , and W of Eqs. (67) through (70) into the variational equation

$$\delta \int_{\tau_1}^{\tau_2} I(\Phi, H, W; \tau) d\tau = 0 \quad (72)$$

where

$$I = - \int_V P dv + \frac{1}{\Omega_M^2} \int_{S_1} \sqrt{1 + (\nabla H)^2} dS_1$$

$$+ \frac{1}{2\Omega_M^2} \int_{S_3} \left[\frac{1}{2} (\nabla W)^2 - \frac{\lambda}{2} \Omega_M^2 \left(\frac{\partial W}{\partial \tau} \right)^2 + \lambda B_M G(\tau) W \right] dS_3$$

and

V = actual volume occupied by the fluid

P = nondimensional pressure in the fluid

The Euler equations are exactly Eq. (36) for $N = m \dots N$, with c_0, d_0 satisfying Eq. (71a).

For free vibration, by taking a single term $m = N$, we get the "one-term approximation":

$$1 + \frac{\Omega_M^2 (L + \lambda) (\Omega^2 - p_m^2) k_m}{\beta_m} = 0 \quad (73a)$$

or

$$\frac{\Omega_1}{\Omega_2} = \frac{1}{2} p_m^2 \left\{ \frac{\Lambda_m}{\nu_m p_m^2} + \frac{\mu_m}{\nu_m} + \sqrt{\left(\frac{\Lambda_m}{\nu_m p_m^2} + \frac{\mu_m}{\nu_m} \right)^2 - \frac{4 \Lambda_m}{\nu_m p_m^2}} \right\} \quad (73b)$$

which is the same as neglecting all the terms in the summation of Eq. (43) except the m^{th} term. If we take two terms, i.e., $N = m + 1$ ("two-term approximation"), we get the following characteristic equation for Ω :

$$1 + \sum_{n=m}^{m+1} \frac{\alpha_M^2 (L + \lambda) (\Omega^2 - p_n^2) k_n}{\beta_n} = 0$$

8 NUMERICAL RESULTS

Some numerical results are obtained using the method discussed above. In Figs. 2 through 5, the first three natural frequencies normalized by the first sloshing frequency p_1 , which equals

$$\left[\frac{k_1 (k_1^2 + B_\sigma) \tanh k_1 L}{\Omega_\sigma^2} \right]^{1/2}$$

of the corresponding rigid tank, versus the membrane number B_M , which equals $(\rho_o g_o r_o^2)/N_r$, were plotted for parameters B_o, L, λ . Since Ω is normalized by p_1 , the parameters Ω_o^2 and Ω_M^2 , which equals $\Omega_o^2 (B_M/B_o)$ can be eliminated. The computation was based on Eq. (73) (one-term approximation), with $m = 1$, and on Eq. (43). In most of the calculations, the one-term approximation and exact solution gave almost identical results for the lowest frequency, which cannot be distinguished in the figures shown.

From these figures, we see the general trend clearly that frequencies decrease as B_M increases. In Fig. 2, the Bond number is large ($B_o = 10$), and B_M does not have much effect on the lowest frequency. As B_o decreases (see Figs. 3 and 4, $B_o = 1, 0.1$), the great effect of B_M can be seen. At certain ranges of B_M , the lowest frequency decreases sharply as B_M increases; and the range is approximately determined by the ratio of B_o to B_M , and the depth of liquid L . This relationship can be seen clearly from Eq. (43), if the terms in the summation sign are normalized in a slightly different form, i.e., for B_o, B_M small,

$$1 + \sum_{n=1}^{\infty} \frac{k_n (L + \lambda) \left[1 - \left(\frac{\Omega}{p_1} \right)^2 \frac{(k_1^2 + B_o) k_1 \tanh k_1 L}{(k_n^2 + B_o) k_n \tanh k_n L} \right]}{\coth k_n L + \lambda k_n - \frac{\Omega^2 (k_1^2 + B_o) k_1 \tanh k_1 L}{p_1^2 (k_n^2 + B_o) k_n \tanh k_n L} (\tanh k_n L + \lambda k_n) + \frac{k_n^2 - B_M}{(k_n^2 + B_o) \tanh k_n L} \frac{B_o}{B_M} \left(\frac{\Omega^2}{p_1^2} - 1 \right)}$$

$$\approx 1 + \sum_{n=1}^{\infty} \frac{k_n (L + \lambda) \left[1 - \left(\frac{\Omega}{p_1} \right)^2 \frac{k_1^2 \tanh k_1 L}{k_n^3 \tanh k_n L} \right]}{\coth k_n L + \lambda k_n - \frac{\Omega^2 k_1^3 \tanh k_1 L}{p_1^2 k_n^3 \tanh k_n L} (\tanh k_n L + \lambda k_n) + \frac{1}{\tanh k_n L} \frac{B_o}{B_M} \left[\left(\frac{\Omega}{p_1} \right)^2 \frac{k_1^3 \tanh k_1 L}{k_n^3 \tanh k_n L} - 1 \right]}$$

= 0

(75)

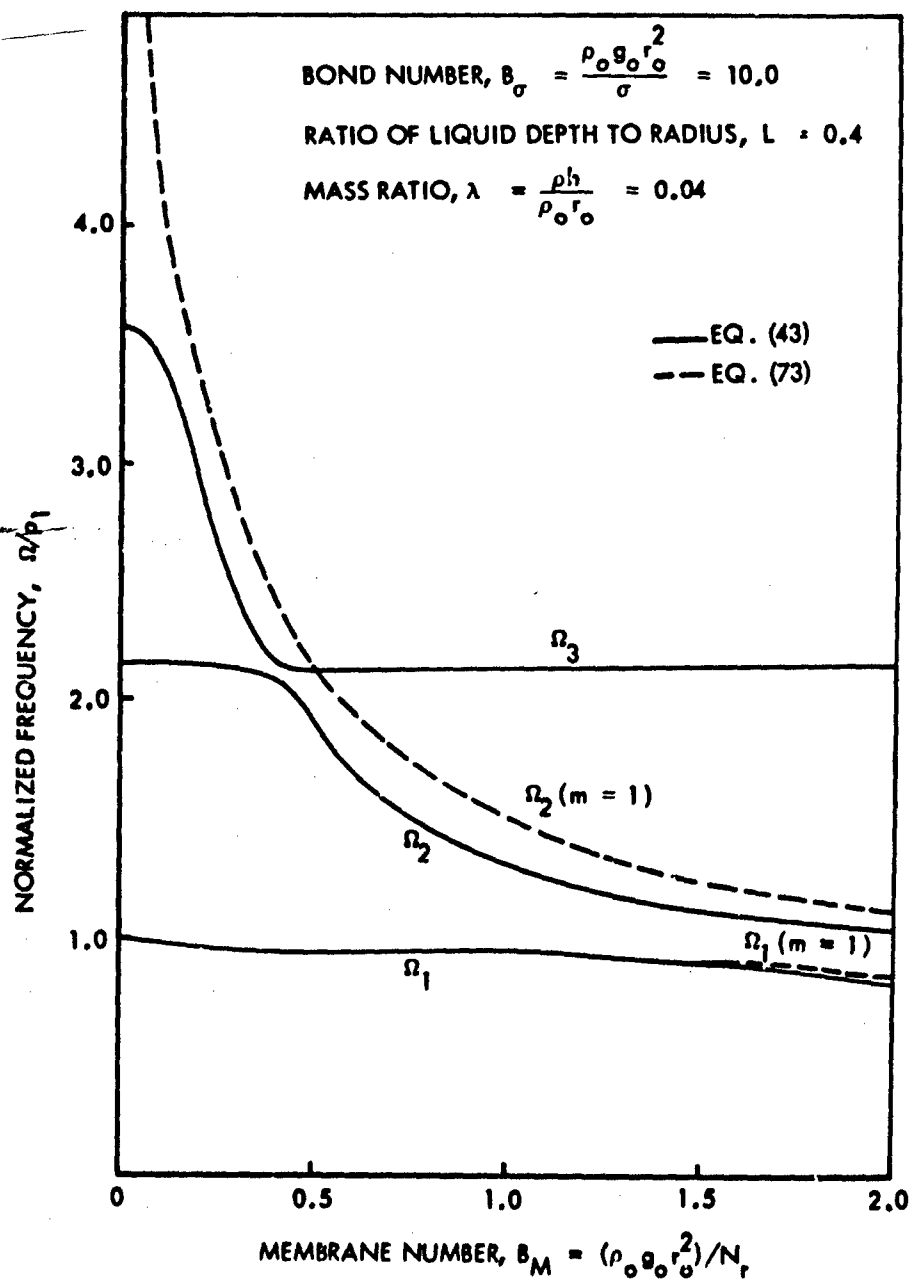


Fig. 2 Frequencies Computed From Eqs. (43) and (73), With Bond Number 10

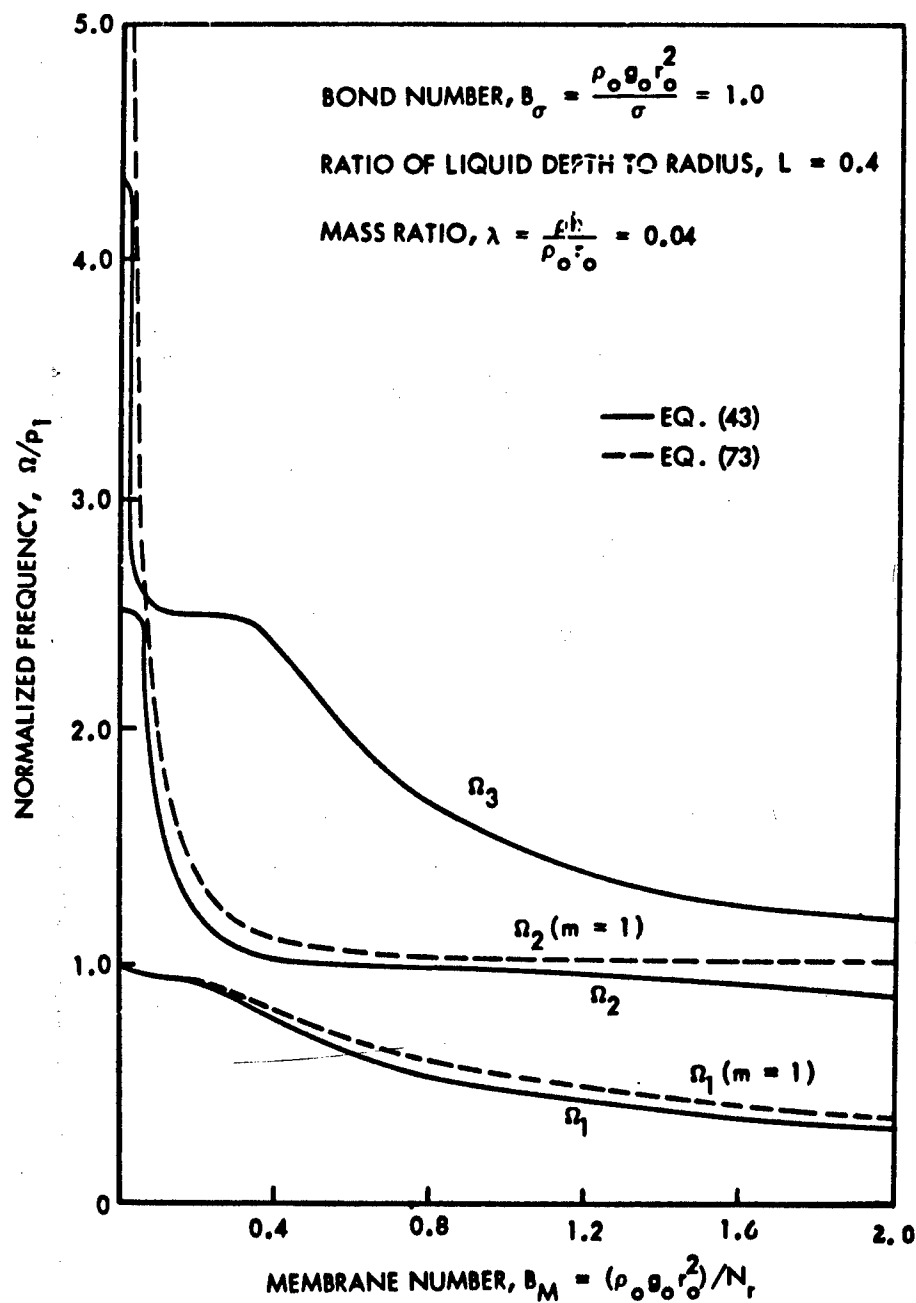


Fig. 3 Frequencies Computed From Eqs. (43) and (73), With Bond Number 1.0

Apparently the roots for Ω/p_1 depend on B_σ/B_M only for fixed L, λ . Physically it says that, at low Bond number, the surface tension plays an important role; its effect depends mainly on B_M/B_σ (the ratio of the surface tension to midplane stress resultant of the membrane). The argument holds for any N-term approximation.

In Figs. 4 and 5 we can see the effect of the depth of the liquid to radius ratio L . It causes the sharp decrease of frequency occurring at smaller B_M for larger L .

In Fig. 6 (a and b), the stability boundary with $\alpha (=g_1/g_0)$ is plotted versus forcing frequency normalized by the rigid tank first sloshing frequency, according to Eq. (A-9) in the Appendix, with $i = j = 1$ for one-term approximation only.

9 CONCLUSIONS

From the exact solution for free vibration, we make four conclusions for the eigenvalue Ω : (1) Ω is always real, for $p_n^2, \chi_n > 0$; (2) the elastic effect lowers the natural vibration frequency; (3) the elastic effect on each sloshing frequency is of order $\Omega_M^2/\sinh 2k_n L$; (4) because of the presence of the elastic bottom, coupling of different sloshing modes occurs, and the effect of one sloshing mode on the natural frequency of another due to this elastic coupling is of order Ω_M^6 .

Numerical results indicate a great effect of surface tension on the natural frequency and stability boundary at low Bond numbers. If B_σ, B_M are both small (<1), then the frequency depends on the combination of parameters B_M/B_σ .

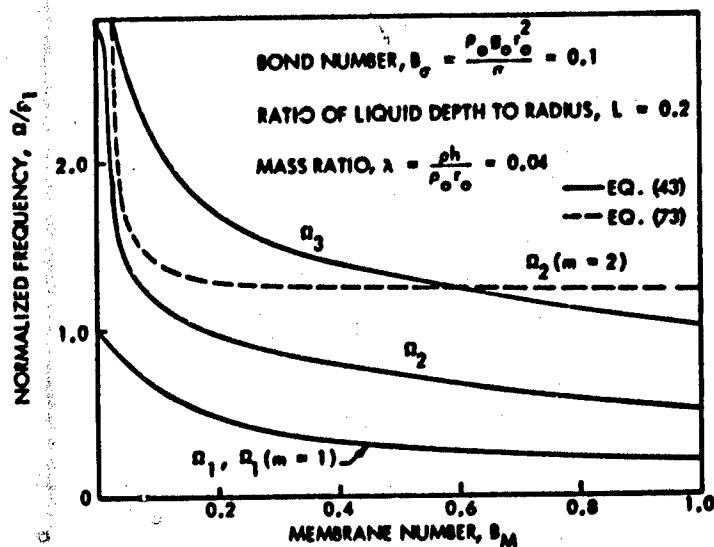


Fig. 4 Frequencies Computed From Eqs. (43) and (73), With Bond Number 0.1 and Lower Ratio of Liquid Depth to Radius

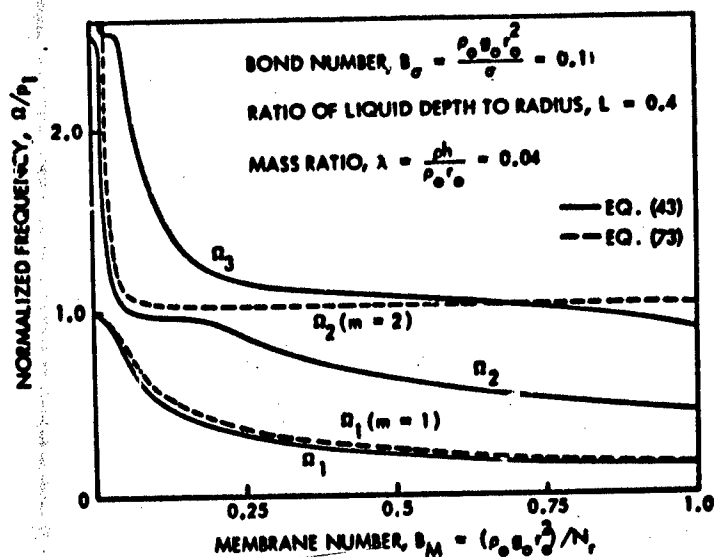


Fig. 5 Frequencies Computed From Eqs. (43) and (73), With Bond Number 0.1

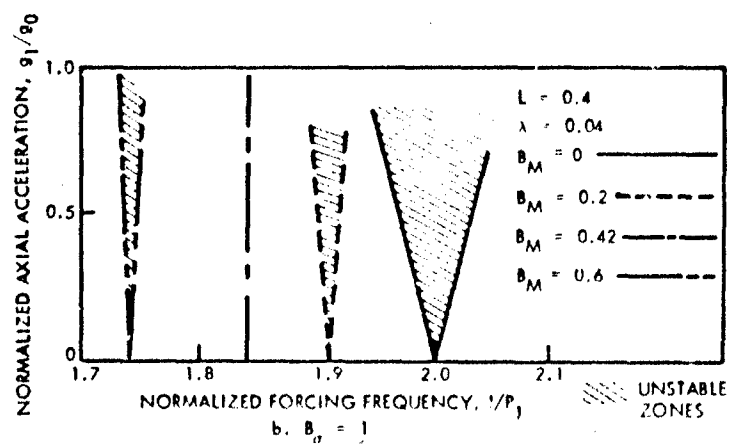
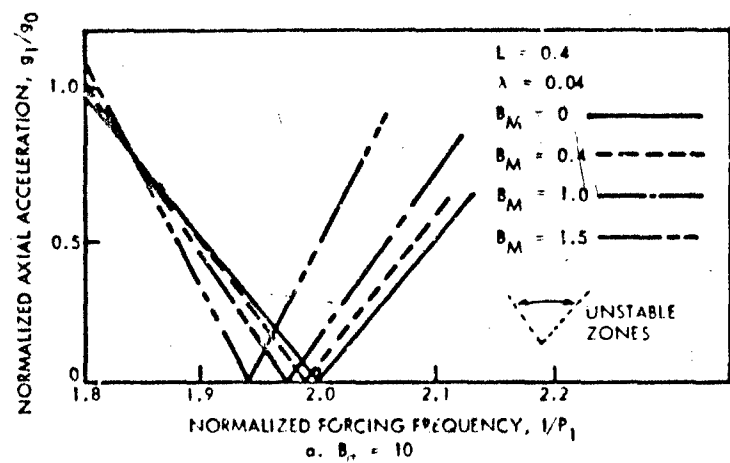


Fig. 6 Stability Boundary Computed From Eq. (75), for Various Values of B_σ and B_M

10 CITED REFERENCES

1. Benjamin, T. B. and Ursell, F., "The Stability of the Plane Free Surface of a Liquid in Vertical Periodic Motion," Proc. Roy. Soc., Series A, Vol. 225, 1954, p. 505
2. Miles, J. W., "On Sloshing of Liquid in a Flexible Tank," J. Applied Mechanics, Vol. 25, Jun 1958, pp. 277-283
3. Bleich, H. H., "Longitudinal Forced Vibration of Cylindrical Fuel Tanks," Jet Propulsion, Vol. 26, No. 2, Feb 1956, pp. 109-111
4. Bhuta, P. G. and Koval, L. R., Coupled Oscillation of Liquid With a Free Surface in a Tank Having a Flexible Bottom, EM 13-19, STL, Aug 1963
5. -----, Hydroelastic Solution of the Sloshing of a Liquid in a Cylindrical Tank, TRW Space Technology Lab., Report 13-22, (6110-8792-RU000), Oct 1963
6. Bhuta, P. G. and Yeh, G. C. K., Liquid Sloshing Due to a Time Dependent Discontinuous Boundary, TRW Space Technology Lab., Report EM 13-16, (6110-8692-RU000), Aug 1963
7. Yeh, G. C. K., Liquid Sloshing in a Moving Tank With a Time Dependent Discontinuous Boundary, TRW Space Technology Lab., Report EM 14-12, (6438-6002-RU000), Jun 1964
8. -----, "Bibliography on Liquid Sloshing," TRW Space Technology Lab., Interoffice Corresp. 64-9713.6-61, Aug 1964
9. Bond, W. N. and Newton, D. A., "Bubbles, Drops, and Stokes' Law," Phil. Mag. Vol. 5, 1928, pp. 794-800
10. Reynolds, W. C., Hydrodynamic Considerations for the Design of Systems for Very Low Gravity Environments, Dept. of Mech. Eng., Rept. LG-1, Stanford Univ., 1963
11. Hsu, C. S., "Further Results on Parametric Excitation of a Dynamic System," (paper presented at the ASME Applied Mechanics Conference, Boulder, Colorado, Jun 1964)

12. Whittaker, E. T. and Watson, G. N., Modern Analysis, Cambridge, at the Univ. Press (New York, The Macmillan Company), p. 413
13. Cesari, L., Ergebnisse der Math. und Ihrer Grenzgebiete, New Series No. 16-20, 1955-59, Heft 16, p. 55
14. Gibson, G. A., Advanced Calculus, Macmillan and Co., Ltd., London, 1931, p. 236

11 UNCITED REFERENCES

- Bateman, H., "Notes on a Differential Equation Which Occurs in the Two Dimensional Motion of a Compressible Fluid and the Associated Variational Principle," Proc. Royal Soc., London, A125, Nov 1929, pp. 598-618
- Hsu, C. S., "On the Parametric Excitation of a Dynamic System Having Multiple Degrees of Freedom," J. Applied Mechanics, Vol. 30, 1963, p. 367
- Lamb, H., Hydrodynamics, 6th Ed., N. Y., Dover Publications
- Landau, L. D. and Lifshitz, E. M., Fluid Mechanics, Pergamon Press
- Wang, C. T., "Variational Method in the Theory of Compressible Fluid," J. Aero. Sciences, Vol. 15, 1948, p. 675

Appendix A

APPROXIMATE BOUNDARY FOR A SYSTEM OF DIFFERENTIAL EQUATIONS WITH PERIODIC COEFFICIENTS TO HAVE UNBOUNDED SOLUTION

Following Struble's (Ref. 15) approximate stability boundary for Mathieu's equation, we extend it to a system of N equations:

$$\ddot{\underline{y}} + \underline{D}\dot{\underline{y}} = \alpha \cos t \underline{A}\underline{y} \quad (\text{A-1})$$

where

$$\underline{y} = \begin{bmatrix} y_1 \\ y_2 \\ \vdots \\ y_n \end{bmatrix}$$

$$\underline{D} = \begin{bmatrix} \Omega_1^2 & & & 0 \\ & \Omega_2^2 & & \\ & & \ddots & \\ 0 & & & \Omega_n^2 \end{bmatrix} \quad (\text{A-2})$$

$$\underline{A} = (a_{ij})$$

and Ω_i 's are different from zero, α is a small parameter, a_{ij} are constants. We assume that y_i 's have the expansions

$$y_i = E_i(t) \cos(\Omega_i t - \theta_i t) + \alpha y_i^{(1)} + \alpha^2 y_i^{(2)} + \dots \quad (\text{A-3})$$

where $E_i(t)$, $\theta_i(t)$ are slowly varying parameters, and that \dot{E}_i^2 , $\dot{\theta}_i^2$, \ddot{E}_i , $\dot{\theta}_i \dot{E}_i$, $\ddot{\theta}_i$ can be neglected as compared with \dot{E}_i , $\dot{\theta}_i$. Substituting (A-3) into (A-1), we get

$$2\Omega_i [E_i \dot{\theta}_i + 0(\dot{\theta}_i^2, \dot{E}_i^2, \dots)] \cos(\Omega_i t - \theta_i) - 2\Omega_i (\dot{E}_i + \dots) \sin(\Omega_i t - \theta_i) + \alpha [\ddot{y}_i^{(1)} + \Omega_i^2 y_i^{(1)}]$$

$$= \frac{\alpha}{2} \sum_{j=1}^n a_{ij} E_j \left\{ \cos[(1 + \Omega_j)t - \theta_j] + \cos[(1 - \Omega_j)t + \theta_j] \right\} + 0(\alpha^2) \quad i = 1, 2, \dots, n \quad (\text{A-4})$$

For $\Omega_i = 1 \pm \Omega_j$, we may solve for $y_i^{(1)}$ immediately by taking E_i, θ_i to be constants. But there is a possibility that the expansion for $y_i^{(1)}$ breaks down because of zero or small divisors for the solution of $y_i^{(1)}$.* In order to avoid this difficulty, we can use E_i, θ_i to cancel those terms that cause trouble. We shall consider the case that $\Omega_i + \Omega_j = 1 + O(\alpha)$ for only one pair of specific i, j .

In this case, we remove the troublesome terms in (A-4) by putting

$$\begin{aligned} 2\Omega_i \dot{\theta}_i E_i \cos(\Omega_i t - \theta_i) - 2\Omega_i \dot{E}_i \sin(\Omega_i t - \theta_i) \\ = \frac{\alpha}{2} a_{ij} E_j \cos[(1 - \Omega_j)t + \theta_j] \\ = \frac{\alpha}{2} a_{ij} E_j \left\{ \cos[(1 - \Omega_i - \Omega_j)t + \theta_i + \theta_j] \cos(\Omega_i t - \theta_i) \right. \\ \left. - \sin[(1 - \Omega_i - \Omega_j)t + \theta_i + \theta_j] \sin(\Omega_i t - \theta_i) \right\} \end{aligned} \quad (A-5)$$

and a similar equation with the subscripts i, j interchanged. Then by equating the coefficients of $\cos(\Omega_r t - \theta_r)$, $\sin(\Omega_r t - \theta_r)$, $r = i, j$ we get

$$\begin{aligned} 2\Omega_i \dot{\theta}_i E_i &= \frac{\alpha}{2} a_{ij} E_j \cos[(1 - \Omega_i - \Omega_j)t + \theta_i + \theta_j] \\ 2\Omega_i \dot{E}_i &= \frac{\alpha}{2} a_{ij} E_j \sin[(1 - \Omega_i - \Omega_j)t + \theta_i + \theta_j] \\ 2\Omega_j \dot{\theta}_j E_j &= \frac{\alpha}{2} a_{ji} E_i \cos[(-\Omega_i - \Omega_j)t + \theta_i + \theta_j] \\ 2\Omega_j \dot{E}_j &= \frac{\alpha}{2} a_{ji} E_i \sin[(1 - \Omega_i - \Omega_j)t + \theta_i + \theta_j] \end{aligned} \quad (A-6)$$

*Struble, R. A., Nonlinear Differential Equations, New York, McGraw-Hill Book Company, 1962, Chapter 8, pp. 221-227

It can be easily shown that

$$\begin{aligned}\Omega_i a_{ji} E_i^2 &= \Omega_j a_{ij} E_j^2 \\ \theta_i &= \theta_j\end{aligned}\tag{A-7}$$

Substituting into Eq. (A-6), it becomes

$$\begin{aligned}2\Omega_i \dot{\theta}_i &= \frac{\alpha}{2} \left(\frac{a_{ij} a_{ji} \Omega_i}{\Omega_j} \right)^{1/2} \cos \left[(1 - \Omega_i - \Omega_j)t + 2\theta_i \right] \\ 2\Omega_i \dot{E}_i &= \frac{\alpha}{2} \left(\frac{a_{ij} a_{ji} \Omega_i}{\Omega_j} \right)^{1/2} E_i \cos \left[(1 - \Omega_i - \Omega_j)t + 2\theta_i \right]\end{aligned}\tag{A-8}$$

The values of $\Omega_i, \Omega_j, a_{ij}, a_{ji}, \alpha$ will determine whether E_i, E_j in the above equation, has unbounded solutions or not. We note that Eq. (A-8) has exactly the same form as that obtained by Struble for a single Mathieu's equation. If $a_{ij} a_{ji} \Omega_i / \Omega_j$ is less than 0 from Struble's result, all solutions of E_i are bounded; if $a_{ij} a_{ji} \Omega_i / \Omega_j$ is greater than 0, its stability criterion is

$$\begin{aligned}|1 - \Omega_i - \Omega_j| &> \left| \frac{\alpha}{2} \left(\frac{a_{ij} a_{ji}}{\Omega_i \Omega_j} \right)^{1/2} \right| && \text{Stable} \\ &< && \text{Unstable}\end{aligned}\tag{A-9}$$

DISCUSSION

P. G. Bhuta, TRW Systems Group

Do you have a physical explanation for the line you get for instability? Generally there is a region of instability.

Tong

These curves are computed using Hsu's first order approximation. In the case of very large forcing amplitude you cannot use that approximation for the coupled Mathieu equation. This is only the initial trend. Physically, it says that the stability zone is narrow for relatively small forcing amplitude.

PAPER 12

**SHAPE AND STABILITY OF THE LIQUID-GAS INTERFACE
IN A ROTATING CYLINDRICAL TANK AT LOW g**

By J. G. Seebold* and W. C. Reynolds
STANFORD UNIVERSITY

ABSTRACT

The equilibrium liquid-gas interface in a cylindrical tank rotating at constant angular velocity about its axis in an axial body force field is discussed. A variational principle leads to a boundary value problem associated with the equilibrium free surface and an eigenvalue problem associated with the stability of that surface. The principle results are a parametric stability map governing the existence of stable menisci and shape parameters of the possible equilibrium interface configurations. Experimental results provide quantitative support for the analysis.

*Presently with Lockheed Missiles & Space Company.

SHAPE AND STABILITY OF THE LIQUID-GAS INTERFACE IN A ROTATING CYLINDRICAL TANK AT LOW g

1 THE PROBLEM

This paper presents a description of a study of the shape and stability of the axis-symmetric liquid-gas interface in a cylindrical container rotating at constant angular velocity about its axis in an axial force field. The objective of this study was to determine the influence of rotation on the capillary hydrostatics of the system, particularly in a low-gravity environment.

The relative importance of capillary and body forces is indicated by the Bond number, $Bo = \rho g L^2 / \sigma$.^{*} When the Bond number is very large, as usually is the case on earth, capillary forces can be neglected. But in a low-gravity (low Bond number) environment, or when the characteristic dimension of the system is small, such forces must be considered. This is the regime of capillary hydrostatics.

Rotational effects are of interest, not only for their own sake and for the sake of a more complete understanding of capillary hydrostatics, but also because many systems do rotate or could be made to rotate if this would prove advantageous. Applications that immediately come to mind are liquid-vapor separation, positive liquid positioning and expulsion, and optimum-position storage of volatile liquids.

^{*} ρ is liquid density, σ is surface tension, g is the acceleration of a free particle in the body force field, and L is a characteristic dimension of the system.

2 METHOD OF ANALYSIS

There are three principle idealizations associated with the analysis upon which this paper is based.* Perhaps the most restrictive is the assumption that the contained liquid is in a state of solid body rotation. The importance of this idealization depends upon when, after initiation of rotation, one chooses to apply the results.†

A second assumption is that all liquid properties, including ρ and σ , are uniform throughout the system and constant in time. It is also assumed that the liquid-solid contact angle, θ , is uniform and constant in time. The contact angle is sensitive to changes in surface and environmental conditions, and some dynamic hysteresis of the contact angle is commonly observed except in the case of very pure liquids on clean surfaces.

Constancy of the contact angle then implies that the liquid is pure and uncontaminated, the surface is clean and homogeneous, and the environment is constant.

The third important assumption is that the meniscus stability may be determined from an inviscid treatment. There are theoretical results indicating that static and dynamic stability analyses yield the same results for the inviscid case and that viscous forces do not appreciably influence the stability limit in a dynamic analysis.‡ Hence, this assumption is felt to be both legitimate and expedient.

*The study upon which this paper is based was supported by the National Science Foundation under grant NSF-GP-2720; the results are reported in complete detail in: Stanford University, Configuration and Stability of a Rotating Axisymmetric Meniscus at Low-g, by J. G. Seebold and W. C. Reynolds, Mech. Engrg. Dept. Report No. LG-4, Stanford, Calif., 1965

†Development time for solid-body rotation cannot be predicted by simple viscous diffusion theory. Estimates based on viscous diffusion are found experimentally to be over-predictive by orders of magnitude. A much better estimate is given by: H. P. Greenspan and L. N. Howard, "On a Time-Dependent Motion of a Rotating Fluid," J. Fl. Mech., Vol. 17, Part 3, 1963

‡See, for example: P. Concus, "Capillary Stability in an Inverted Rectangular Tank," Symposium on Physical and Biological Phenomena in a Weightless State, Vol. 14, American Astronautical Society, edited by E. T. Benedikt and R. W. Halliburton; Stanford University, The Dynamics of the Free Liquid Surface in Cylindrical Containers Under Strong Capillary and Weak Gravity Conditions, by H. M. Satterlee and W. C. Reynolds, Mech. Engrg. Dept. Report No. LG-2, Stanford, Calif., 1964

In addition, we neglect the density of the covering gas in describing both the shape and stability of the surface. The gas density can be included by replacing the liquid density by $\rho_{\text{liq}} - \rho_{\text{gas}}$ in the results of the present analysis.*

There are two methods by which one might formulate the theory. One method, which might be termed the direct approach, is to set up the differential equation of the free surface by considering a force balance on an infinitesimal annular ring of the surface. The meniscus shape is obtained by integrating this equation. Stability can be investigated by formulating the dynamic problem for infinitesimal motion within the liquid in terms of the velocity potential. If a periodic time variation of the velocity potential is assumed, characteristic frequencies can be obtained from the resulting eigenvalue problem. The resulting normal modes of vibration possess either real or imaginary frequencies. If the frequency is real, the disturbance simply oscillates in time and the surface is stable. An imaginary frequency implies that the disturbance amplitude will grow in time, hence, that the surface is unstable. A system with no unstable modes is considered to be stable to small disturbances.†

An alternative method, which may be termed the indirect approach, is to formulate the problem in terms of a variational principle,‡ in this case Hamilton's principle. This principle is an extension of the familiar proposition that a conservative mechanical system is in a condition of stable equilibrium when its total potential energy is a minimum. In this circumstance, a small perturbation produces only small-order changes in the potential energy of the system, and the small forces that are developed are of restoring tendency. Hamilton's principle allows consideration of kinetic, as well as potential, energy terms. It asserts that the motion must be such that the integral over

*This gives an "exact" correction for shape, and a good approximate correction for stability.

†For an example of this type of analysis, see: Stanford University, The Dynamics of the Free Liquid Surface in Cylindrical Containers Under Strong Capillary and Weak Gravity Conditions, by H. M. Satterlee and W. C. Reynolds, Mech. Engrg. Dept. Report No. LG-2, Stanford, Calif., 1964

‡P. Concus, "Capillary Stability in an Inverted Rectangular Tank", Symposium on Physical and Biological Phenomena in a Weightless State, Vol. 14, American Astronautical Society, edited by E. T. Benedikt and R. W. Halliburton

time of the difference of the kinetic energy and potential energy functions is minimized. This difference is called the "Lagrangian" of the variational problem. The necessary condition for minimization yields the Euler-Lagrange equation of the variational problem, which is identical with the differential equation for the equilibrium free surface. The Euler-Lagrange equation can be integrated to obtain the surface shape, as before. The sufficient condition for minimization is that the second variation of the difference integral be positive. The critical condition of "neutral" or "marginal" stability is then obtained by setting the second variation equal to zero. The result is the Jacobi equation of the variational problem, and an eigenvalue problem for the stability limit.*

The important contrast between these two approaches lies in the difference in stability analyses. In the direct approach, a dynamic analysis is employed that must yield dynamic stability limits. In the indirect approach, stability is investigated by means of a variational principle which can give only static results. The crucial link between the two stability analyses is that, under certain circumstances, the eigenvalue problems for the stability limits that result from each of the two methods are identical.† In this circumstance, static stability implies dynamic stability, a condition not commonly found in mechanics. When this is the case, one can determine stability limits by either method, preferably by the easier. In this study, the indirect approach was employed for stability analysis. The equivalence of static and dynamic stability criteria for the nonrotating cylinder has been established analytically.‡ This correspondence is assumed to hold with rotation, and the results of a companion experiment appear to justify this assumption.†

*For a thermodynamic formulation, see: Stanford University, Capillary Hydrostatics and Hydrodynamics at Low g, by W. C. Reynolds, M. A. Saad, and H. M. Satterlee, Mech. Engrg. Dept. Report No. LG-3, Stanford, Calif., 1964

† P. Concus, "Capillary Stability in an Inverted Rectangular Tank", Symposium on Physical and Biological Phenomena in a Weightless State, Vol. 14, American Astronautical Society, edited by E. T. Benedikt and R. W. Halliburton

‡ Stanford University, The Dynamics of the Free Liquid Surface in Cylindrical Containers Under Strong Capillary and Weak Gravity Conditions, by H. M. Satterlee and W. C. Reynolds, Mech. Engrg. Dept. Report No. LG-2, Stanford, Calif., 1964

† Stanford University, Configuration and Stability of a Rotating Axisymmetric Meniscus at Low-g, by J. G. Seebold and W. C. Reynolds, Mech. Engrg. Dept. Report No. LG-4, Stanford, Calif., 1965

3 NATURE OF RESULTS

The result of integrating the surface equation is the shape of the interface. The result can be presented in a number of ways. The most useful information for design purposes appears to be the height of rise of the liquid up the wall of its container and the depth of penetration of the meniscus toward the bottom. In order to make feasible the graphical presentation of such information, at least one of the parameters of the problem should be fixed. Since the case of zero g is of particular interest, we have presented the height ratios (height/tank-diameter) for the case of zero axial body force.

The result of the stability analysis is a stability map that one can enter with the parameters of a particular situation and find out if a stable rotating meniscus can exist. The most commonly observed type of instability is the "falling out" type. In a small enough system, such as a thermometer at 1 g , the liquid can be maintained at the top of an inverted cylinder and stabilized by the capillary forces. Now, suppose we are able to dilate the cylinder very slowly in some way. Intuition tells us that eventually the interface would fail and the liquid would fall. Instabilities in which the fluid on top displaces the lighter fluid on which it rests are often called "Taylor" instabilities.* We will adopt this designation in order to distinguish the "falling out" type of instability from another that will be discussed presently.

When the cylinder is not rotating, instabilities are of the Taylor type; whenever the critical Bond number is exceeded, the heavier fluid on top displaces the lighter fluid upon which it rests. Thus, if we have a tube partially filled with some liquid, whenever the Bond number is less than the critical value we will be able to invert the tube without disturbing the meniscus.† This can be done rather easily with a 1/4-in.

*Even though his name is often used in connection with this kind of instability, Taylor did not consider surface tension effects.

† Provided that the inversion process does not itself destroy the meniscus.

diameter tube and water, for example, while it cannot be done with a 1/2-in. diameter tube. The inverted configuration is impossible in the 1/2-in. tube because the magnitude of the Bond number associated with the inverted meniscus is too great. The dependence of the critical Bond number on the contact angle θ of the liquid-solid system in a nonrotating cylinder has been thoroughly investigated.* The curve of critical Bond number versus contact angle is symmetrical about the most stable case, which occurs for the flat interface ($\theta = 90$ deg).

The stability results presented in this paper show that, when rotation is introduced, two important differences arise. First, the curve of critical Bond number for Taylor instability is no longer symmetrical; wetting liquids become unstable at smaller negative Bond numbers, and nonwetting liquids become unstable at larger negative Bond numbers.[†] Thus, in general, rotation tends to destabilize the wetting liquids and to stabilize the nonwetting liquids. A second effect of rotation is to introduce another type of instability. Suppose we have a specific container and a specific liquid so that θ and B_0 are fixed; it can happen that as we increase rotation no instability of the Taylor type will be encountered, but that as soon as the rotation exceeds a critical value a solution to the meniscus equation cannot be obtained. We interpret this as implying that there is no meniscus that will span the cylinder. The rotational instability is one of nonexistence. The results of this study show that when the limit of rotational stability is exceeded, no meniscus can exist and the liquid-gas interface undergoes a transition to a bubble or pseudoannular configuration. The limit of rotational stability depends on the contact angle of the liquid-solid system, the systems with small contact angles being the most easily disturbed.

*In the latter half of the 19th century. Bashforth and Adams were already conducting investigations on this subject.

[†]We regard wetting liquids as those that exhibit contact angles less than 90 deg, and nonwetting liquids as those exhibiting greater contact angles. Bond number is considered to be negative when the liquid is on top.

4 SUMMARY OF RESULTS

Numerical integration of the differential equations obtained from the variational formulation leads, in principle, to a description of all possible neutrally stable menisci. For the nonrotating cylinder, the Bond number (Bo) and the contact angle (θ) suffice to completely determine both the shape and stability of the meniscus. The introduction of rotation has the concomitant effect of requiring an additional descriptive parameter. We call this parameter the "rotational Weber number", $\Omega^2 = (\rho r_1^3 / \sigma) \omega^2$, where r_1 is the radius of the cylinder and ω is the speed of rotation. To each neutrally stable meniscus there belongs a Bond number, a contact angle, and a critical rotational Weber number. In Fig. 1, the lines of constant critical Ω^2 on a $Bo - \theta$ plane are shown. The line $\Omega^2 = 0$ represents the familiar relation between critical Bond number and contact angle for Taylor instability in the nonrotating cylinder. The dashed

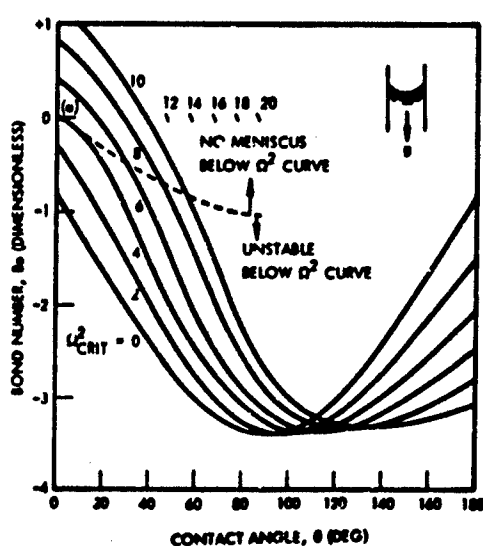


Fig. 1 Stability Map

line separates the regions in which Taylor instability and nonexistence instability of the meniscus occur. In the region above the dashed line, where no Taylor instabilities occur, solutions to the meniscus equation can be found only if the rotational speed is not too great. Thus, the lines of constant Ω^2 above the dashed line mark the regions in the $Bo - \theta$ plane in which no solutions of the meniscus equations can be found. This region includes two special cases of interest, zero Bond number and zero contact angle, which are shown separately in Figs. 2 and 3.

Consider, for example, rotation with $\Omega^2 = 8$. The curve $\Omega^2 = 8$ in Fig. 1 defines the critical Bond number as a function of contact angle for the given rotational condition.

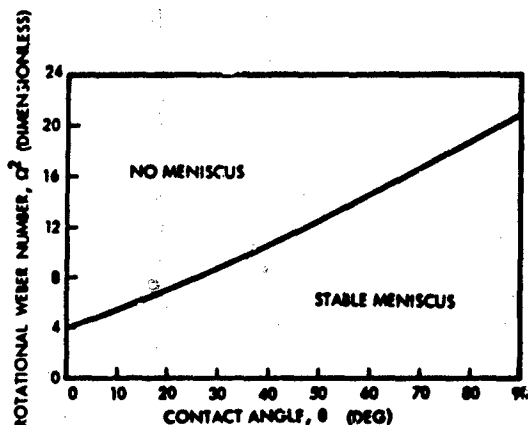


Fig. 2 Existence Map (Zero Bond Number)

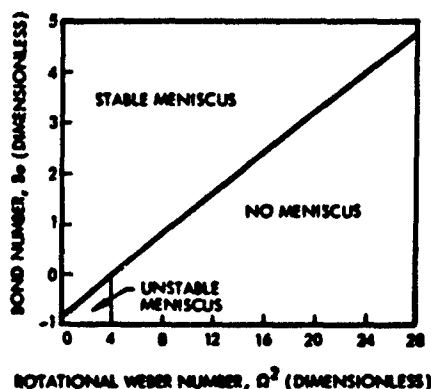


Fig. 3 Existence Map (Zero Contact Angle)

For $Bo - \theta$ combinations above the curve, menisci exist and are stable to small disturbances. Below the curve and below the dashed line the meniscus exists, but it will exhibit Taylor instability. Below the curve and above the dashed line no solution to the meniscus equation exists, and a shape transition will occur.

Point (a) of Fig. 1 can be calculated by considering the differential equation of the interface and a perturbation about the zero contact angle point. Since the surface slope at the wall is positive infinite and the curvature is non-negative for rotational surfaces that exhibit zero contact angle, one finds that $\Omega^2 \geq 4$ is required for existence of zero-gravity zero-contact angle solutions. The procedure for calculating this existence limit was extended to include annular tanks. The result is

$$\Omega^2 = \frac{\rho r_o^3 \omega^2}{\sigma} \leq \frac{4}{(1 - r_i/r_o)^2}$$

where r_i and r_o are the inner and outer radii of the tank.

A convenient means of characterizing the zero-g meniscus shape is to present the extreme dimensions of the meniscus (the height of rise at the wall and depth of fall at the center) normalized by dividing by tank diameter. These height ratios as functions of the other pertinent parameters are probably the most significant aspects of the meniscus shape from the standpoint of tank design. This information is presented in Fig. 4, where L_1 is the height of rise of the liquid up the tank wall, and L_2 is the depth of penetration of the meniscus toward the tank bottom. Both distances are measured from the mean liquid level and normalized on tank diameter. The dashed lines correspond to the nonexistence limit discussed previously.

The stability analysis shows that as long as rotational speed is below a certain critical value a stable zero-g meniscus will exist. As the rotational speed is increased, the meniscus becomes more distended and may eventually reach the top or bottom of a tank of finite length. This contact with tank top or bottom leads to destruction of the meniscus, so it is of considerable importance.

For example, even in the regime of subcritical rotation, the meniscus will fail to exist when the mean liquid level is too high. In such a case, a meniscus that could span the tank does exist, but the presence of the tank top prevents the liquid from rising to its equilibrium height. It seems inevitable that a bubble, possibly attached at the tank top, will be formed. This condition is characterized by lack of sufficient ullage.

If we define a factor that is descriptive of tank loading and geometry, $\gamma = L(1 - f)/D$, we can obtain from the

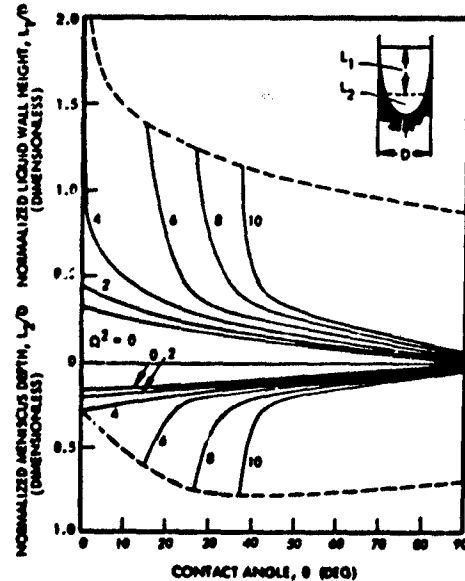


Fig. 4 Meniscus Configuration
($B_0 = 0$)

surface integrations an "insufficient ullage criterion."* This criterion is shown in Fig. 5. Points above the applicable γ -line represent "topped-out" menisci resulting from insufficient ullage.

As an example of the use of Fig. 5, suppose we have a liquid that exhibits a contact angle of 4-1/2 deg contained in a tank of $L/D = 3$. Suppose that this tank will be rotated at such a speed that $\Omega^2 = 2$, and we want to know how high we can fill the tank and still maintain a meniscus. Figure 5 shows that, at $\theta = 4\frac{1}{2}$ deg and $\Omega^2 = 2$ (since $L/D = 3$), f should not be greater than about 0.867 if a meniscus is to be maintained. Consequently, if the tank were filled to 90 percent we should expect to see a bubble, and if filled to 80 percent we should expect to see a meniscus. Photographs of zero-g drop-tower experiments involving methanol in a tank (with $L/D = 3$), which gives a contact angle of about 4-1/2 deg, are shown in Fig. 6. In the bottom row, the tanks are rotating at a speed such that $\Omega^2 = 2$. Thus, all the conditions of this example are fulfilled, and we see that the 80 percent surface is indeed a meniscus while the 90 percent surface is a bubble.

Destruction of the meniscus will also occur, even for subcritical rotation, if the mean liquid level is too low. In this case, the meniscus is prevented from falling to its equilibrium depth by the presence of the tank bottom. The bottom must then be partially exposed, and the liquid must form a sort of pseudoannulus. We have coined the term "annuloid" to describe this surface because, while it is not an annulus, it is

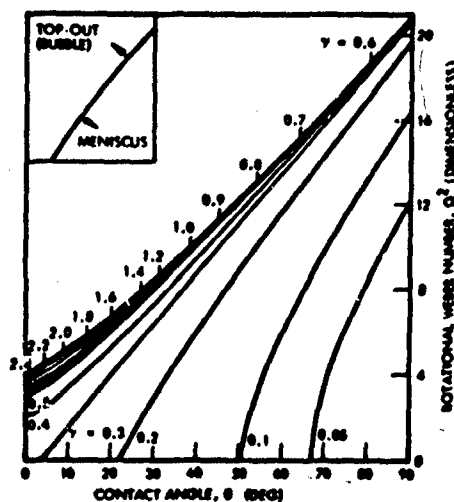


Fig. 5 Insufficient Ullage Criterion for Subcritical Rotation ($Bo = 0$)

* L is the length of the tank. D is its diameter, and f is the fraction of tank volume that is filled with liquid.

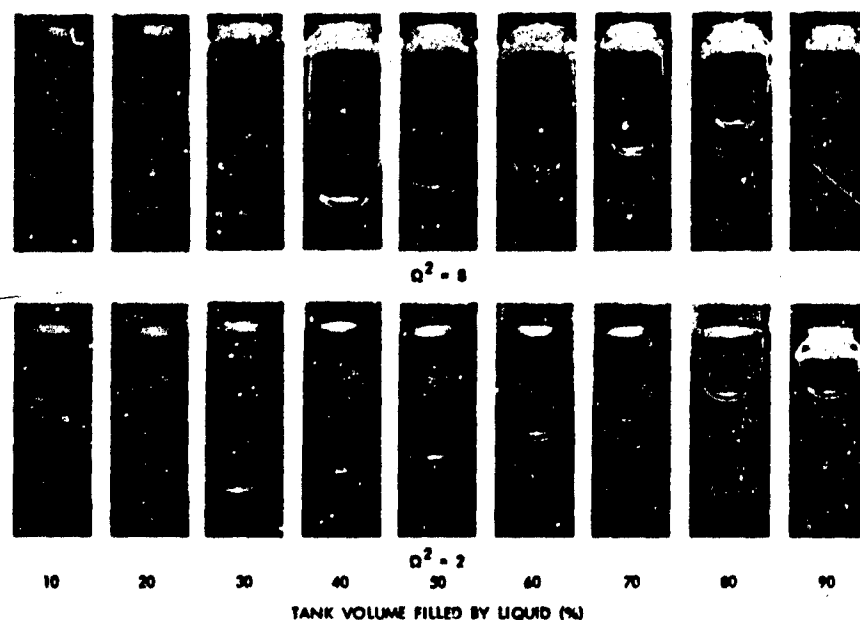


Fig. 6 Zero-Gravity Test-Run Photographs

like an annulus since both ends of the tank are at least partially exposed. If we define another tank loading and geometry factor, $\delta = fL/D$, we can obtain an "insufficient liquid criterion" from the surface integrations. This criterion is shown in Fig. 7. Points above the applicable δ -line represent "bottomed-out" menisci due to insufficient liquid.

Consider an example in which a tank of $L/D = 3$ contains a liquid that exhibits a contact angle of $4\frac{1}{2}$ deg. This tank will be rotated at a constant speed such that $\Omega^2 = 2$, and we want to know how little liquid should be present so that the tank bottom will not be exposed. Figure 7 shows that, at $\Omega^2 = 2$ and $\theta = 4\frac{1}{2}$ deg (since $L/D = 3$), as long as f exceeds about 0.07 a meniscus should exist and no part of the tank bottom should be exposed. This example has been chosen to correspond to the parameters of Fig. 6: methanol exhibits a contact angle of about $4\frac{1}{2}$ deg, the tanks have $L/D = 3$,

and in the bottom row the tanks are rotating with $\Omega^2 = 2$.

We see that, even when the tank loading is reduced to 10 percent, the tank bottom remains unexposed as this example would lead us to expect.

No meniscus can exist in the region of supercritical rotation. The evidence of Fig. 6 and many similar observations seems to indicate a bubble or an annuloid is produced. The bubble forms, as expressed in oversimplified terms, when liquid is forced up the wall in order to reduce the effective diameter that must be spanned by the liquid-gas interface.

If a sufficient reserve of liquid is available, the annular layer thus created becomes sufficiently thick that an equilibrium meniscus can span the reduced diameter. If not, the bottom of the tank is exposed and an annuloid results. The bubble configuration falls when the length of the required bubble exceeds the length of the tank. By examining the zero-g surface integrations that exhibit zero contact angle, we can obtain both the configuration characteristics of rotating zero-g bubbles and an insufficient length criterion for the existence of such bubbles. The bubble major and minor axes normalized on tank diameter are presented in Fig. 8. The insufficient length criterion for the supercritical rotation region is shown in Fig. 9. Above the appropriate line corresponding to tank L/D , we find the annuloid regime; below the line lies the bubble regime.

As an example of the use of Fig. 9, suppose we have a tank of $L/D = 3$ rotating at such a speed that $\Omega^2 = 8$. We wish to know how little liquid can be present so that a

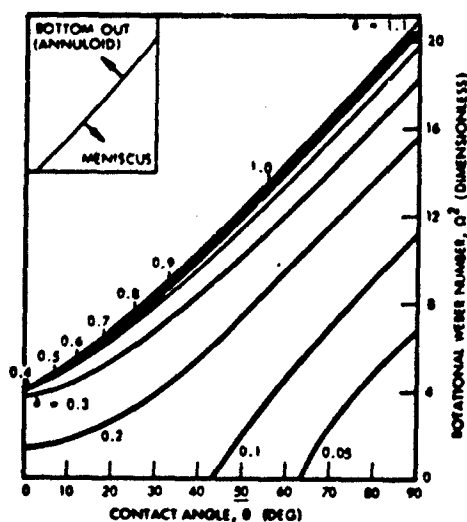


Fig. 7 Insufficient Liquid Criterion for Subcritical Rotation ($Bo = 0$)

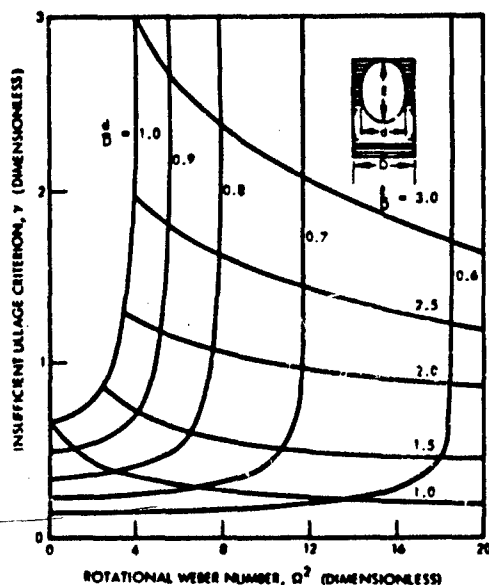


Fig. 8 Bubble Configuration ($Bo = 0$)

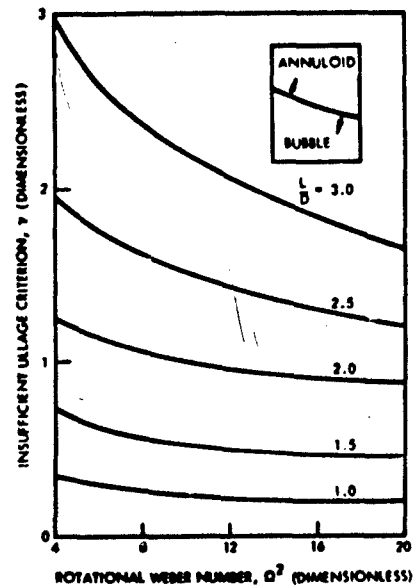


Fig. 9 Insufficient Length Criterion for Supercritical Rotation ($Bo = 0$)

bubble is still maintained. Figure 9 shows that, when $\Omega^2 = 8$ and $L/D = 3$, as long as f exceeds about 0.2 the bubble length should be contained in the tank and an annuloid should not result. The experiments shown in the top row in Fig. 6 correspond to the stipulations of this example ($\Omega^2 = 8$ and $L/D = 3$). We see that when the tank loading is reduced to 20 percent, a bubble is no longer contained and the annuloid configuration results.

5 CONCLUSION

While we tend to think of the liquid-gas equilibrium interface as a meniscus, it has become clear that two other interface shapes may arise, either inadvertently or intentionally, in rotating tanks at zero g. All three classes of shapes are represented in Fig. 6. The classes are menisci, bubbles, and a third shape in which both the top and

bottom of the tank are at least partially exposed. Though this shape is not an annulus, it is like an annulus, and we have coined the term "annuloid" to describe it.

There are three regimes in an $\Omega^2 - f$ plane in which these distinctly different liquid-gas equilibrium interfaces should be expected. In the region of subcritical rotation, a meniscus, annuloid, or bubble may appear; in the region of supercritical rotation only the latter two shapes may be expected. An example of the location of these three regimes is given in Fig. 10 for a liquid that exhibits a contact angle of zero deg (a perfect wetter) and a tank of $L/D = 2$. This example is obtained directly from the three criteria presented in the foregoing section (Figs. 5, 7, and 9). Interface shape characteristics are given for zero-g menisci and bubbles in Figs. 4 and 8. The characteristics of the annuloids are that both ends of the tank are at least partially exposed, and all the liquid is on the wall of the tank.

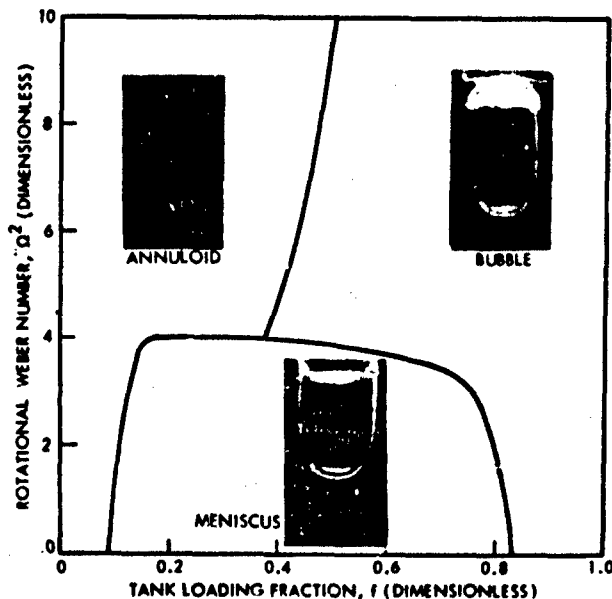


Fig. 10 Regime Graph With $L/D = 2$, $\theta = 0$ deg, and $Bo = 0$

DISCUSSION

Paul Concus, Lockheed

You pointed out that when the liquid is rotating, wetting and non-wetting liquids would be affected differently. Did you try any experiments with non-wetting liquids?

Seebold

We didn't try non-wetting liquids. We were not interested in them because spacecraft propellants are typically very good wetters. The non-wetting results were included simply to complete the presentation of the theory.

W. E. Jahsman, Lockheed

Why did you choose to characterize your results in terms of a rotational Weber number rather than a Bond number?

Seebold

If we interpret ωr_0 as a velocity, the dimensionless grouping Ω^2 looks like a Weber number. By regrouping the factors, a radial Bond number would be obtained. What is important is that Ω^2 is a number that compares the importance of radial body forces with surface forces.

Jahsman

In a practical case for large tanks such as the Saturn where a small thruster is employed to generate axial Bond numbers of the order of 200, wouldn't these large axial Bond numbers overpower the destabilizing effect of the small rotational rates you spoke of?

Seebold

I'm sure they would. I pointed out that in a zero-g environment, the critical rotational rates for large tanks would be quite low, being measured in terms of a few revolutions per hour. When the net axial acceleration is not zero, as is usually the case, the important comparison would be between the resulting axial Bond number and the radial Bond number you spoke of in your first question. There are parametric stability data in the paper for the low axial Bond number range. If the axial Bond number were not small, then the rotational rate required to overpower the axial acceleration would also not be small.

Merte, University of Michigan

In your presentation you referred to the simple viscous theory for predicting time to achieve solid body rotation. Were you referring to pure radial diffusion or do you include the axial diffusion to calculate this time?

Seebold

No, I only refer to the propagation of a viscous boundary layer inward from the wall in order to illustrate the absurd development time that results, but I'm sure the estimate will still be far off if you consider propagation from the bottom of the tank as well. A much closer estimate, referenced in the paper, is given by Greenspan and Howard. Viscous processes lead to the formation of an Ekman layer, which promotes a torroidal circulation that seems to be the primary development mechanism of solid body rotation.

BLANK PAGE

PAPER 13

MENISCUS SHAPE UNDER REDUCED-GRAVITY CONDITIONS

By H. M. Satterlee and J. N. Chin
LOCKHEED MISSILES & SPACE COMPANY

ABSTRACT

The shape of the capillary surface in a right circular cylinder is a function of the Bond number, B (ratio of gravitational forces to surface tension forces acting on the liquid), and the contact angle, θ (measured from the solid surface to the limiting tangent to the liquid-gas interface). The derivation of the differential equation for this capillary surface is given along with the results of numerical calculations for $0 \leq B < 81$ and $0 \text{ deg} \leq \theta \leq 90 \text{ deg}$. An ellipsoid of revolution approximation to the capillary surface shape is also developed. Experimental data regarding the shape of the capillary surface are reported together with the experimental techniques.

Comparison of experimental data with numerical solutions indicates good agreement. Comparison of the ellipsoidal approximation to the numerical solutions indicates that the ellipsoidal approximation can be used for engineering calculations in the range $0 \leq B \leq 10$.

MENISCUS SHAPE UNDER REDUCED-GRAVITY CONDITIONS

1 INTRODUCTION

The design of a rocketship for operation in space nearly always involves consideration of liquid behavior under nearly weightless conditions. Because the body forces that act on liquids under normal conditions on the earth are very much reduced, the liquids will behave quite differently. Liquid motions will ordinarily be much slower and the interface shapes will be highly curved. The shape of the liquid-gas interface in cylindrical rocket tanks under reduced gravity is the subject of this paper.

Knowledge of the shape of liquid masses in rocketships in flight is necessary for several reasons. For example, the different shape of the liquid in the tank results in a different wetted area from that under ordinary high-gravity conditions. In addition, the distorted free surface will ordinarily have a larger area. In the first example, knowledge of the difference in wetted area can be used to calculate the heat transfer between the tank walls and the liquid. In the second, the larger surface area can change the calculated heat and mass transfer between the liquid and the ullage space.

The differential equation for the shape of liquid masses when surface tension is important has been known for some time. In fact, knowledge of the properties of the solution of this differential equation has been used as a means for measuring the surface tension of liquids from measured heights of sessile drops.

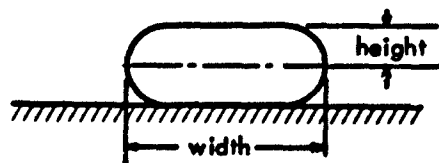
Long ago, Rayleigh* reported a number of theoretical observations concerning the meniscus shape in cylindrical containers. This effort grew out of discussions of corrections of surface-tension measurements made by the capillary rise method. Rayleigh, in fact, studied the capillary shape under what would today be considered very low- and high-gravity conditions. In his works, he refers to a suggestion of Hagen and Desains that the capillary surface in a cylinder is similar in shape to an

*Baron Rayleigh (J. W. Strutt), "On the Theory of the Capillary Tube," Scientific Papers, Vol VI, Cambridge Univ. Press, 1920, p. 355

oblate spheroid. The work of Bashforth and Adams* is often quoted by workers in surface chemistry in connection with precise surface-tension measurements. More recently Jahsman† used a series expansion method applicable for low Bond numbers.‡ The work of all of these researchers can be used to provide insight into the shape of a meniscus under low-gravity conditions. However, the results of these efforts have not been presented in such a way as to be readily useful. Recently, Reynolds§ presented the results of a large number of calculations on the shape of capillary surfaces in a more useful manner. However, only the volume contained within the curve and its rise height at the container wall were presented.

Use of the capillary shape in measuring surface tension is an adequate verification of the differential equation of the free surface. However, experimental confirmation has been limited to examination of nonwetting drops of liquid on top of horizontal surfaces or of bubbles in a wetting liquid on the lower side of horizontal surfaces. In other words, previous observations have been made with drop or bubble shapes that are double valued with respect to the vertical coordinate. Measurements are made more easily when referenced to the width of the drop or bubble measured where the slope is vertical (see sketch at right).

In the remainder of this paper, the differential equation of the capillary surface is



*It is interesting to note that many famous investigators of the last century were interested in this subject. Among these were Poincaré, Mathieu, and Bashforth and Adams. See: F. Bashforth and J. C. Adams, An Attempt to Test the Theories of Capillary Action, Cambridge Univ. Press, 1883

†W. E. Jahsman, "The Equilibrium Shape of the Surface of a Fluid in a Cylindrical Tank," Developments in Mechanics, Vol. 1, Eds. J. E. Lay and L. E. Malvern, Plenum Press, New York, pp 603-612

‡The ratio of gravitational forces to surface tension forces.

§Stanford University, Capillary Hydrostatics and Hydrodynamics at Low g, by W. C. Reynolds, M. A. Saad, and H. M. Satterlee, Mech. Engr. Dept. Report LG-3, Stanford, Calif., 1 Sep 1964, p. 34

briefly outlined and successful techniques for numerical integration are described. An approximation to the capillary surface using the ellipsoid suggestion of Hagen and Desains is developed. The experimental data are compared with both exact and approximate theories.

2 DEVELOPMENT AND SOLUTION OF DIFFERENTIAL EQUATION FOR FREE-SURFACE SHAPE

The shape of the free surface of a liquid may be determined from Bernoulli's equation:

$$\frac{v}{\rho} + g\bar{z} = \text{constant} \quad (1)$$

The individual terms of this equation may be recognized as the pressure head and gravity head, respectively.

Consider a liquid resting in a right-circular cylinder of radius R as shown in Fig. 1.

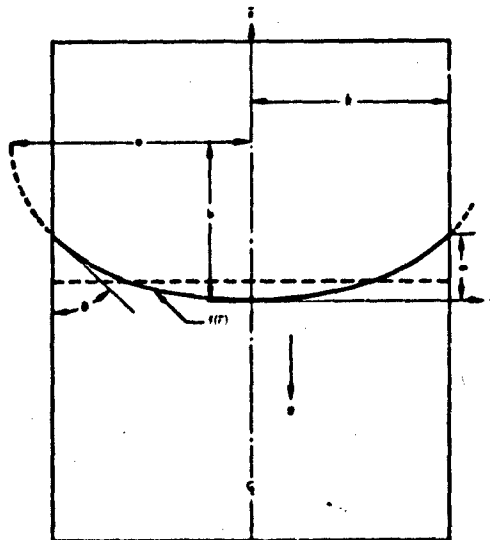


Fig. 1 Geometry Used for Analysis of Liquid Surface Under Reduced Gravity Conditions

The coordinate system is chosen so that the vertex of the surface is, for convenience, at the origin. Replacing z by $f(\bar{r})$ and assuming the pressure above the free surface is uniform, Eq. (1) yields

$$p = p_g - (p_g - p_o) - \rho g f \quad (2)$$

In this equation, p_g is the pressure in the space above the capillary surface and p_o is the liquid pressure in the free surface at the vertex. The quantities ρ and g are the liquid density and the local acceleration directed as indicated in the figure. The pressure difference across

an axisymmetric capillary surface can be written in terms of the surface derivative and the surface tension, assuming constant surface tension:

$$p_g - p = \frac{\sigma}{\bar{r}} \frac{d}{d\bar{r}} \left[\frac{\bar{r} f_{\bar{r}}}{(1 + f_{\bar{r}}^2)^{1/2}} \right] \quad (3)$$

Here, σ is the surface tension. The subscript notation indicates differentiation with respect to the subscript coordinate. The complete differential equation in dimensional form can be obtained by substituting Eq. (3) into Eq. (2):

$$\frac{\sigma}{\bar{r}} \frac{d}{d\bar{r}} \left[\frac{\bar{r} f_{\bar{r}}}{(1 + f_{\bar{r}}^2)^{1/2}} \right] - \sigma \left\{ \frac{1}{\bar{r}} \frac{d}{d\bar{r}} \left[\frac{\bar{r} f_{\bar{r}}}{(1 + f_{\bar{r}}^2)^{1/2}} \right] \right\}_{\bar{r}=0} - \rho g \bar{r} = 0 \quad (4)$$

This equation can be made nondimensional by defining the following dimensionless quantities:

$$r = \frac{\bar{r}}{R} \quad , \quad F = \frac{f}{R} \quad , \quad B = \rho g R^2 / \sigma \quad (5)$$

where R is the tank radius and B the Bond number. The result is

$$\frac{1}{r} \frac{d}{dr} \left[\frac{r F_r}{(1 + F_r^2)^{1/2}} \right] - \left\{ \frac{1}{r} \frac{d}{dr} \left[\frac{r F_r}{(1 + F_r^2)^{1/2}} \right] \right\}_{r=0} - B F = 0 \quad (6)$$

The boundary conditions for Eq. (6) are:

$$F_r(1) = \cot \theta \quad (7)$$

$$F_r(0) = 0 \quad (8)$$

where θ is the contact angle defined in the conventional way. By expanding the derivative, which is evaluated at $r = 0$, and using Eq. (8), the following equation is obtained:

$$\frac{1}{r} \frac{d}{dr} \left[\frac{r F_r}{(1 + F_r^2)^{1/2}} \right] - 2 F_{rr}(0) - B F = 0 \quad (9)$$

Two numerical methods, the integral method and the Runge-Kutta method, were developed to integrate Eq. (9) with boundary conditions (7) and (8). These methods are described in the following subsections.

2.1 Integral Method

Multiplying each term of Eq. (9) by $r dr$ and integrating from $r = 0$ to $r = r$ with boundary condition (8) gives:

$$\frac{r F_r}{(1 + F_r^2)^{1/2}} = E(r) \quad (10)$$

where

$$E(r) = F_{rr}(0) r^2 + B \int_0^r F r dr \quad (11)$$

With boundary condition (7), the constant $F_{rr}(0)$ in Eq. (11) may be eliminated to yield:

$$E(r) = r^2 \cos \theta + B \left(\int_0^r F r dr - r^2 \int_0^1 F r dr \right) \quad (12)$$

Solving for F_r from Eq. (10) and then integrating from $r = 0$ to $r = r$, yields:

$$F = \int_0^r \frac{E(r) dr}{[r + E(r)]^{1/2} [r - E(r)]^{1/2}} \quad (13)$$

where $F = 0$ at $r = 0$ has been used for a convenient datum. Equations (12) and (13) are the basic integrals for successive approximations. An assumed initial F distribution, based on the ellipsoidal approximation to be discussed later, is used to calculate $E(r)$ which is then used to calculate F . The process is continued until the relative difference between two consecutive approximations of F is reduced to a small value. Experience in using this method with a computer program indicates that the convergence is very rapid for small Bond numbers ($B < 10$). However, instability was encountered with large Bond numbers.

When $B = 0$, Eq. (13) may be integrated directly to yield

$$F = \frac{1}{\cos \theta} \left[1 - (1 - r^2 \cos^2 \theta)^{1/2} \right] \quad (14)$$

which is an equation of a circle with radius $1/\cos \theta$ and center at $(r = 0$,

~~$F = 1/\cos \theta$~~). The meniscus rise for this case is

$$\frac{m}{R} = F(1) = \frac{1 - \sin \theta}{\cos \theta} \quad (15)$$

2.2 Runge-Kutta Integration

A fourth-order Runge-Kutta numerical scheme of integrating a second-order ordinary differential equation was also used to integrate Eq. (9). An iteration procedure is required which involves assuming a value for $F_{rr}(0)$ and checking the resulting contact angle at the wall. The Runge-Kutta method has the advantage over other numerical methods, since no special techniques are required to start the computation. Experience in using the computer program based on this approach indicates that convergence is very rapid at all Bond numbers.

3 APPROXIMATION OF FREE-SURFACE SHAPE BY ELLIPSOIDS OF REVOLUTION

This approach is suggested by reference to the work of Hagen and Desains in one of Rayleigh's papers.* These workers approximated the free surface in a narrow capillary tube with a segment of an ellipsoid.

*Baron Rayleigh (J. W. Strutt). "On the Theory of the Capillary Tube." Scientific Papers, Vol VI. Cambridge Univ. Press. 1920, p. 355

3.1 Ellipsoidal Approximation for Meniscus

In a nondimensional form, the ellipsoidal approximation to the free surface is (Fig. 1):

$$F = \beta \left\{ 1 - \left[1 - \left(\frac{r}{\alpha} \right)^2 \right]^{1/2} \right\} \quad (16)$$

where $\alpha = a/R$ and $\beta = b/R$, the nondimensional semimajor and semiminor axes, respectively, of the ellipsoid of revolution. When $\alpha = \beta = 1/\cos \theta$, Eq. (16) reduces to Eq. (14).

Differentiating Eq. (16) and satisfying the results with the contact-angle boundary condition, Eq. (7) yields

$$\alpha^2 = \frac{1}{2} \left[1 + (1 + 4\beta^2 \tan^2 \theta)^{1/2} \right] \quad (17)$$

A second relationship may be obtained by substituting Eq. (16) into Eq. (9) and evaluating the result at $r = 1$:

$$B = \frac{\left[1 + \left(\frac{\beta^2}{\alpha^2} - 1 \right) \frac{1}{\alpha^2} \right]^{-3/2} + \left[1 + \left(\frac{\beta^2}{\alpha^2} - 1 \right) \frac{1}{\alpha^2} \right]^{-1/2} - 2}{\alpha^2 \left[1 - \left(1 - \frac{1}{\alpha^2} \right)^{1/2} \right]} \quad (18)$$

From Eq. (17), the following relationship may be derived:

$$\xi = \frac{\alpha^2 \cos \theta}{\beta} = \left[1 + \left(\frac{\beta^2}{\alpha^2} - 1 \right) \frac{1}{\alpha^2} \right]^{-1/2} \quad (19)$$

Therefore.

$$B = \frac{\xi^3 + \xi - 2}{\alpha^2 \left[1 - \left(1 - \frac{1}{\alpha^2} \right)^{1/2} \right]} \quad (20)$$

Equations (17) and (20) may be used to define a Bond number in terms of θ , β , and α .

Manipulation of Eq. (19) yields

$$\left(1 - \frac{1}{\alpha^2} \right)^{1/2} = \frac{\sin \theta}{\xi} \quad (21)$$

Therefore, Eq. (20) may be written as

$$\xi^4 + \sin \theta \xi^3 + \xi^2 - (2 + B - \sin \theta) \xi - 2 \sin \theta = 0 \quad (22)$$

which may be solved for ξ . Once ξ is obtained, α and β may be calculated from Eqs. (21) and (19). When $\theta = 0$, Eq. (22) reduces to

$$\xi^3 + \xi - (2 + B) = 0 \quad (23)$$

which may be solved analytically. Note, for this case,

$$\alpha = 1 \quad \text{and} \quad \beta = 1/\xi$$

Once α and β are obtained, the nondimensional meniscus rise is simply calculated by

$$\frac{m}{R} = F(1) = \beta \left[1 - \left(1 - \frac{1}{\alpha^2} \right)^{1/2} \right] \quad (24)$$

Figure 2 shows the results of parametric calculations based on the ellipsoidal approximation.

It may be desirable to calculate the wetted area in the tank. This may be done by integrating the volume under the meniscus and comparing it with a known volume of liquid. However, in order to make the calculations in this paper most useful, the volume contained within the meniscus (as if it were a cup) is presented. This is given in dimensionless form by

$$\frac{V}{\frac{2}{3}\pi R^3} = \beta \left[\alpha^2 - \left(\alpha^2 + \frac{1}{2} \right) \left(1 - \frac{1}{\alpha^2} \right)^{1/2} \right] \quad (25)$$

The ratio of the increased wetted side wall height to tank radius is simply (2/3) of the foregoing dimensionless volume. Another quantity of interest is the free-surface area. This also may be obtained by integration. The result in dimensionless form is given by

$$\begin{aligned} \frac{A}{2\pi R^2} = & \frac{\alpha^2}{2} \left\{ 1 - \left(1 - \frac{1}{\alpha^2} \right)^{1/2} \left[1 - \left(1 - \frac{\beta^2}{\alpha^2} \right) \frac{1}{\alpha^2} \right]^{1/2} \right. \\ & \left. + \left(\frac{\beta}{\alpha} \right)^2 \left(1 - \frac{\beta^2}{\alpha^2} \right)^{-1/2} \ln \frac{\left[1 - \left(1 - \frac{\beta^2}{\alpha^2} \right) \frac{1}{\alpha^2} \right]^{1/2} - \left[\left(1 - \frac{1}{\alpha^2} \right) \left(1 - \frac{\beta^2}{\alpha^2} \right) \right]^{1/2}}{1 - \left(1 - \frac{\beta^2}{\alpha^2} \right)^{1/2}} \right\} \end{aligned} \quad (26)$$

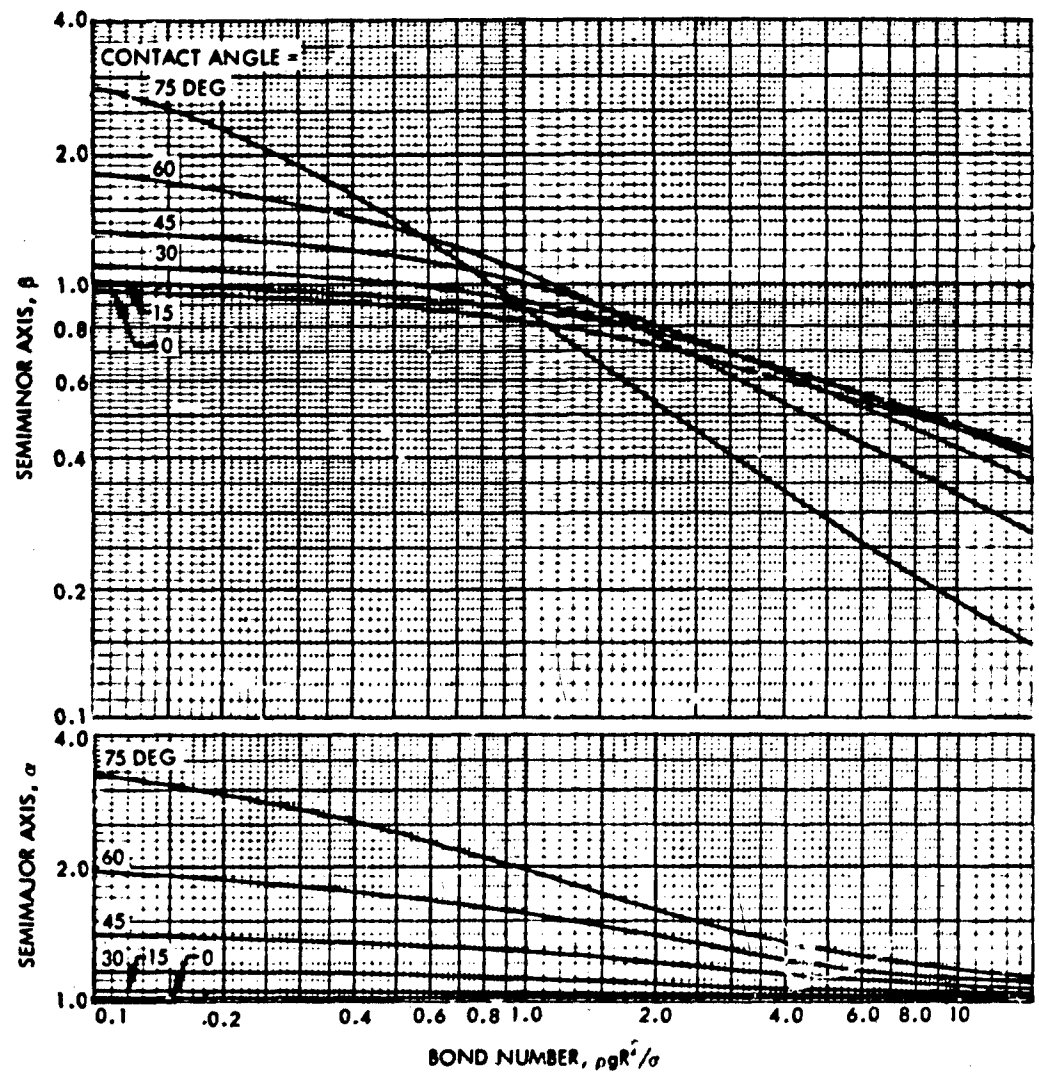


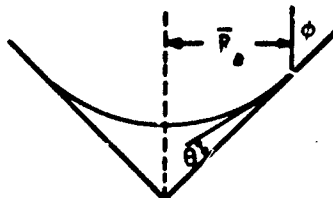
Fig. 2 Ellipsoid Configuration Curves

Introducing the ellipse eccentricity, $e \equiv (1 - \beta^2/\alpha^2)^{1/2}$, so that $\beta^2/\alpha^2 = 1 - e^2$ and $\alpha^2 = 1 + (1 - e^2) \tan^2 \theta$, Eq. (26) may be manipulated to yield,

$$\frac{A}{2\pi R^2} = \frac{1}{2} \alpha^2 \left[1 - \frac{(1 - e^2) \sin \theta}{1 - e^2 \cos^2 \theta} + \frac{1 - e^2}{2e} \ln \left(\frac{1 + e}{1 - e} \right) \left(\frac{1 - e \sin \theta}{1 + e \sin \theta} \right) \right] \quad (27)$$

Figure 3 shows the results calculated with Eqs. (25) and (27).

The preceding results are derived for liquids inside a cylindrical container. However, with appropriate transformations, these results may be applied to other axisymmetric containers. For instance, consider liquid in a conical tank of half-angle ϕ and contact angle θ . Then, by using an effective tank radius R_e (see sketch to the right) in defining the Bond number and an effective contact angle $\theta_e = \theta + \phi$, the foregoing results become directly applicable.



3.2 Ellipsoidal Approximation for "Swallowed Bubbles"

If the ullage volume is small, the liquid may wet the top of the tank. The result is that the vapor bubble will be "swallowed" and will rest against the top of the tank in an undetermined location. The ellipsoidal approximation may be extended to cover this case as well.

The differential equation of the free surface and the ellipsoidal approximation can be used again to obtain relations to describe the swallowed bubble. Equation (4) is non-dimensionalized in a different manner that is based on the semimajor axis of the bubble. Here,

$$r_b = \frac{\bar{r}}{a}, \quad F_b = \frac{f}{a}, \quad \beta_b = \frac{b}{a}, \quad B_b = \rho g a^2 / \sigma \quad (28)$$

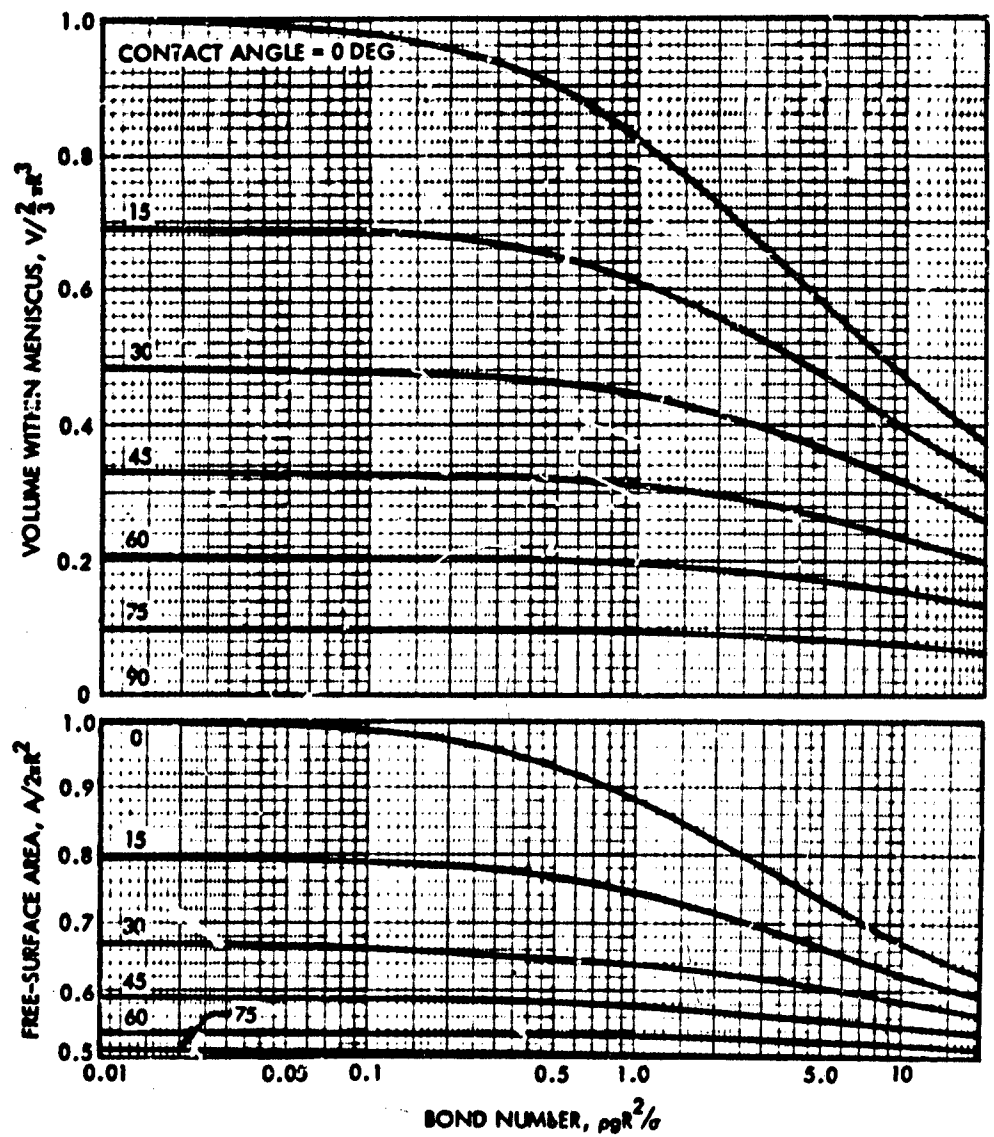


Fig. 3 Ellipsoid Area and Volume Curves

The results are

$$\frac{1}{r_b} \frac{d}{dr_b} \left[\frac{r_b F_b r_b}{(1 + F_b^2)^{1/2}} \right] - 2 F_b r_b r_b^{(0)} - B_b F_b = 0 \quad (29)$$

$$F_b = \beta_b \left[1 \pm (1 - r_b^2)^{1/2} \right] \quad (30)$$

The plus sign refers to the upper limb of the ellipse and the minus to the lower. Equation (30) is substituted into Eq. (29) and the result, evaluated at $r_b = 1$, is

$$B_b = \left(\frac{1}{\beta_b} \right)^3 - \frac{1}{\beta_b} - 2 \quad (31)$$

The contact angle constraint in this case is

$$\tan \theta = \frac{\beta_b r_o}{(1 - r_o^2)^{1/2}} \quad (32)$$

where $r_o = r_s/a$, and r_s is the radius of the dry area at tank top. This equation can be used to find an initial value of r_o for calculation purposes:

$$r_o^2 = \frac{\tan^2 \theta}{\tan^2 \theta + \beta_b^2} \quad (33)$$

The volume of the bubble in dimensionless form is

$$\frac{V}{(4\pi/3)a^3} = \frac{1}{4} \beta_b \left[2 + (2 + r_o^2) (1 - r_o^2)^{1/2} \right] \quad (34)$$

Since a is usually not known, it may be eliminated from Eqs. (31) and (34) to yield:

$$B_V = \frac{\rho g}{\sigma} \left(\frac{3V}{4\pi} \right)^{2/3} \\ = \left(\frac{1}{\beta_b^3} + \frac{1}{\beta_b} - 2 \right) \left\{ \frac{1}{4} \beta_b \left[2 + (2 + r_o^2) (1 - r_o^2)^{1/2} \right] \right\}^{2/3} \quad (35)$$

Where B_V is a Bond number based on the bubble volume. Equations (33) and (35) determine r_o and β_b for given θ and B_V . Since V is also known, a may be calculated from Eq. (34).

From the foregoing results, the following quantities may be derived: dimensionless depth of bubble,

$$\frac{d}{a} = \beta_a \left[1 + (1 - r_o^2)^{1/2} \right] \quad (36)$$

and dimensionless free-surface interface area of bubble,

$$\frac{A}{4\pi a^2} = \frac{1}{4} \left\{ 1 + \frac{(1 - e_b^2) \cos \theta}{1 - e_b^2 \cos^2 \theta} + \frac{1 - e_b^2}{2e_b} \ln \left(\frac{1 + e_b}{1 - e_b} \right) \left(\frac{1 + e_b \cos \theta}{1 - e_b \cos \theta} \right) \right\} \quad (37)$$

where $e_b = (1 - \beta_b^2)^{1/2}$, the bubble eccentricity. Graphs of bubble eccentricity versus bubble-volume Bond number and other useful ratios such as r_g/a , d/a , $3V/4\pi a^3$, and $A/4\pi a^2$ may be easily prepared. However, experimental data with "swallowed bubble" conditions were not obtained. Graphs of parameters calculated from these relations (as in Figs. 2 and 3) have, therefore, not been presented.

4 EXPERIMENTAL PROCEDURES AND RESULTS

The following paragraphs indicate the procedures followed in the subject experiments of this paper and the results of the experiments.

4.1 Equipment and Procedures

The meniscus information was gathered using equipment assembled at Stanford University to study the sloshing of liquid in circular cylinders under weak gravity and strong capillary forces. The equipment consisted of a high speed 16-mm movie camera, * a front surface mirror, a 375-w reflector photoflood lamp, a mirror/scale/light assembly, and a black-light mask.

The specimens were fabricated from lucite blocks approximately 2 by 2 by 4 in. Different diameter holes were machined in the blocks from end to end, and the cylinder walls were given a high polish. The holes in the six specimens were 0.900, 0.750, 0.629, 0.500, 0.375, and 0.285 in. in diameter. Separate top and bottom pieces, each with an O-ring seal, were fastened to the blocks with small screws. The experimental setup is shown schematically in Fig. 4. The mirror/scale/light assembly and the light mask are not shown in the figure. This assembly was mounted to one side of the specimen so the image of a scale appeared in the object plane. The light mask surrounded the specimen and admitted light only through a 0.25-in. horizontal slit in line with the meniscus. This was to cause the light to enter the back of the specimen as undirectionally as possible. This lighting technique produced an excellent black shadow profile of the meniscus shape except at the very ends of the meniscus.

*A movie camera was used because the data reported here were part of a larger project to obtain low-gravity sloshing data at Stanford.

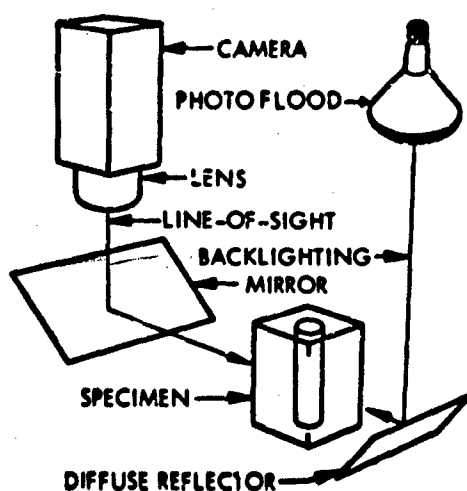


Fig. 4 Interface Profile Measuring Equipment

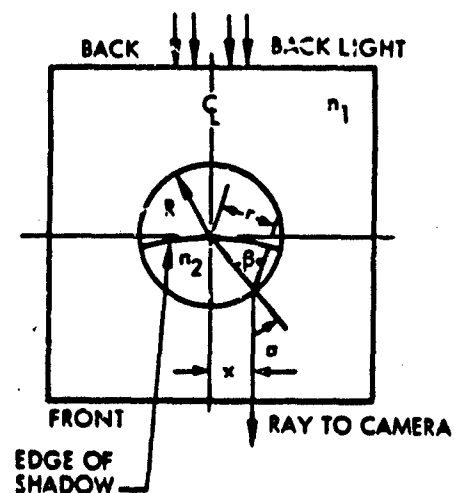


Fig. 5 Correction for Refraction Used in Reducing Meniscus Shape Data

The liquids used were water, methanol, and carbon tetrachloride. The water was obtained from an ion-exchange purifier and exceeded reagent grade in purity. The carbon chemicals used were of reagent grade.

The experimental procedure was simply to take relatively slow-speed movies of the specimen partially filled with liquid. The movie films were examined on a 16 \times magnification Vanguard film reader. Information on the x-y coordinates of points along the meniscus were tabulated and entered in punch cards for later correction for refraction error.

The cylindrical hole filled with liquid acts as a lens; therefore, a correction had to be made for the error introduced by the difference in refractive index of the plastic specimen and the liquid. The nature of the correction is shown in Fig. 5. The image of a point on the edge of the shadow of the meniscus appears closer to the centerline of the

tube than it really is. The distance from camera lens to subject, although small, was large enough that rays entering the camera lens were assumed parallel, considering the size of the largest meniscus. Shell's law, then, provided a correction factor

$$\frac{x}{r} = \frac{n_2}{n_1} \quad (38)$$

where n_1 and n_2 are the indices of refraction for the plastic and the liquid, respectively. The correction of the x-y coordinates of the menisci to r-y coordinates was facilitated by use of a small digital computer program.

The correction was tested by reading the photographs of bearing balls and applying the correction factor. The results agreed with the known shape of the ball very well except at the very ends of the curve where the profile is not as distinct as in the center of the tube. The bearing ball experiment provided experience that facilitated interpretation of the images of the liquid menisci.

Two methods were used to measure the contact angle. The first involved passing a quadratic through the coordinates of the last three points on each end of the meniscus. The second made use of the known relation between the zero-g meniscus rise height at the cylinder wall with contact angle [Eq. (15)].

The former method invariably yielded contact angles greater than those visually observed for the measurements using methanol and carbon tetrachloride. The latter method yielded values that agreed with the results of visual examination of the specimens. Therefore, values of the contact angle obtained in zero-g drop tests were used in theoretical calculation of meniscus shape, even though the meniscus shape experiments were performed under normal-gravity conditions. The contact angles measured for methanol and carbon tetrachloride were about 4.5 deg, and that for water was about 60 deg.

The uncertainty in contact angle determinations was examined using the root-sum-square of error contribution technique described by Kline and McClintock.* Uncertainty in contact angles for methanol and carbon tetrachloride (i.e., small contact angles) was estimated at 2 deg, and that for water was about 8 deg.

4.2 Results and Comparison with Theoretical Calculations

Representative data obtained for the free-surface shape of liquids in cylindrical containers are compared with the calculated results in Figs. 6, 7, and 8. Figure 6 compares the corrected experimental data for carbon tetrachloride with the meniscus shapes obtained by the exact solution for three different values of contact angle. It can be seen that the shape very near the wall is sensitive to the value of the assumed

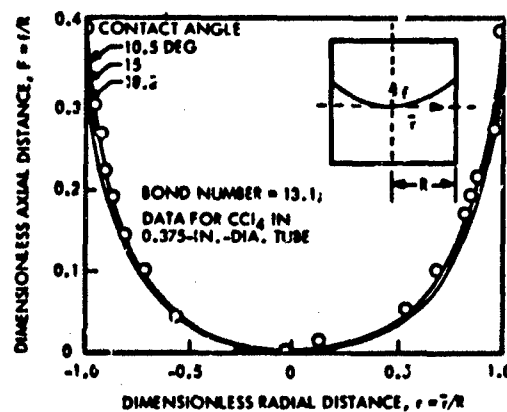


Fig. 6 Comparison of Exact Solutions with Meniscus Shape Data

contact angle. Figures 7 and 8 compare the experimental meniscus shape with that obtained by the exact solution and from the ellipsoidal approximation. The results from the exact solution are seen to agree very well with the data, whereas the results from the ellipsoidal approximation are satisfactory only for low Bond numbers ($B \leq 10$).

In Fig. 9, experimental data for the meniscus height are compared with theoretical predictions. The failure of the rise height of the low-contact-angle liquids to agree well with the theoretical rise heights is attributed to the difficulty experienced in reading the vertical coordinates

*S. J. Kline and F. A. McClintock, "Describing Uncertainties in Single Sample Experiments," *Mech. Eng.*, Jan 1953

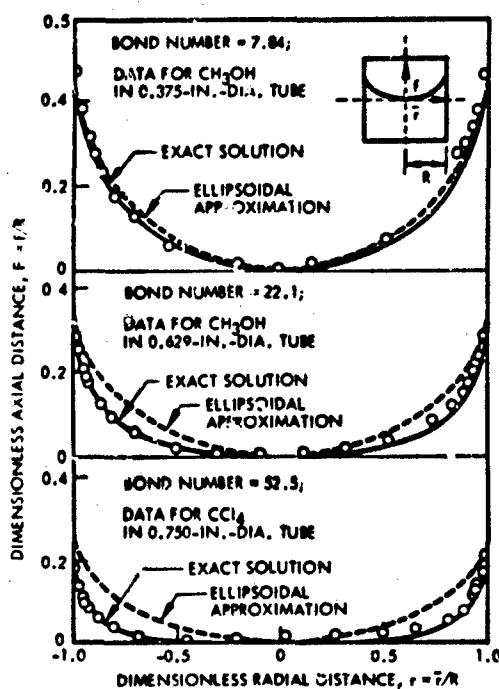


Fig. 7 Comparison of Exact and Approximate Solutions with Meniscus Shape Data (Various Bond Numbers)

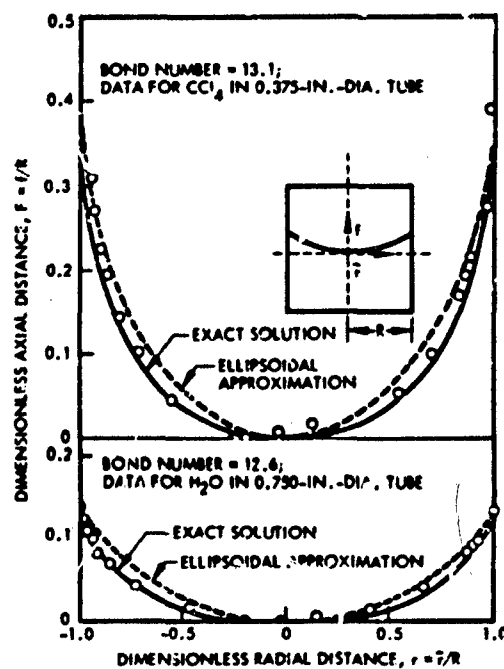


Fig. 8 Comparison of Exact and Approximate Solutions with Meniscus Shape Data (Two Contact Angles)

of the meniscus close to the cylinder wall. Elsewhere, the measured coordinates agree very well with the theoretical shape. The rise heights of the water menisci are in better agreement with theory.

5 CONCLUSIONS

The derivation of the differential equation for free-surface shape of liquid in a cylindrical container has been presented. This equation was integrated exactly by two numerical methods: the integral method and the Runge-Kutta method. The integral method yields a solution at low Bond numbers (e.g., $B < 10$) but presents divergent

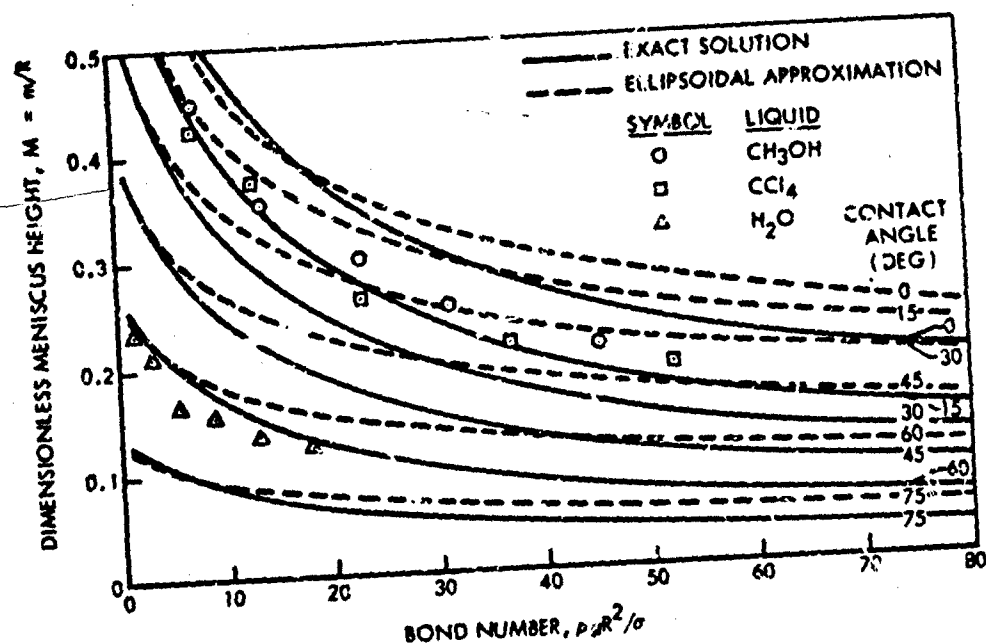


Fig. 9 Meniscus Rise Height Ratio as a Function of Bond Number and Contact Angle

results at large Bond numbers. In the Runge-Kutta method, the iteration converges for all Bond numbers. An approximate solution, based on an ellipsoidal meniscus shape, is also presented. The dimensionless semimajor and semiminor axes of the ellipsoid of revolution, together with the dimensionless volume above the meniscus and the dimensionless free surface, are expressed graphically as a function of Bond number and contact angle. The approximate solution agrees quite well with the exact solution for small Bond numbers ($B \leq 10$). The graphs calculated by the approximate solution are therefore useful for engineering purposes.

Experimental procedures reported here are satisfactory for determining the shape of menisci in transparent cylinders except for points very near the wall. There, lighting and refraction difficulties combine to obscure the precise contact point when the contact angle is small.

Experimental data, on meniscus shape, obtained with different liquids and different size containers (which correspond to a range of Bond numbers and contact angles simulating liquid in a rocket tank under reduced gravities) are found to agree with the results obtained by the exact solution, generally, and with the results obtained by the ellipsoidal approximation for small Bond numbers.

ACKNOWLEDGEMENTS

The analytical work presented here was supported by NASA under Contract NAS 8-11525. The experimental work was accomplished at Stanford University under NSF Grant G-20090. The authors acknowledge the help of L. W. Gallagher in the computer codes.

DISCUSSION

I. C. Statler, Cornell Aeronautical Laboratory

How do your results agree with W. E. Jahsman's series expansion for small Bond number and asymptotic expansion for large Bond number?

Satterlee

Comparisons have been made in the past. Although we did not include such comparisons in the paper, the methods do agree.

PAPER 14

LIQUID SETTLING IN LARGE TANKS

By **T. E. Bowman**
MARTIN COMPANY

ABSTRACT

The problem of propellant settling (repositioning from forward to aft orientation) in large orbiting tanks, in which the liquid-vapor interface is initially flat, has been studied experimentally using scale models in a 75-foot drop tower. Accelerations up to 0.025 g, test cylinders up to one foot diameter, and Bond numbers up to 390 have been investigated within the limitation of a 2.16-second drop test. Several different types of flow were observed, not normally encountered in settling from a meniscus-shaped (zero-gravity configuration) surface; all can be explained on the basis of the initial Taylor instability. Except for certain secondary phenomena, Bond number was found to be a valid scaling parameter within the range studied.

Although initial flow characteristics were studied rather extensively, no conclusions can be drawn (from these drop tower studies) about long-term aspects of settling, such as the time required before quiescent conditions are attained.

NOMENCLATURE

a	acceleration
a _r	acceleration ratio, model to prototype
g	acceleration due to normal gravity, 980 cm/sec ²
\bar{j}	unit vector in vertical direction
L _r	ratio of typical lengths, model to prototype
p	pressure
\bar{q}	velocity
R	tank radius
t	time
t _r	ratio of time scales, model to prototype
ρ	liquid density minus gas density
σ	surface tension

$$\text{Bond number} = \frac{\rho a R^2}{\sigma}$$

LIQUID SETTLING IN LARGE TANKS

1 INTRODUCTION

The general problem of interest concerns a large tank of liquid hydrogen coasting in low earth orbit, subject to a small aerodynamic drag. The carrier vehicle is oriented parallel to its velocity vector (nose first) at all times. Part of the hydrogen has been consumed, leaving the tank slightly more than half full. During the zero-thrust coast periods, Bond number in the hydrogen tank* is probably somewhere between 4 and 20, based on tank radius. In the absence of large perturbations to the vehicle attitude or motion, the hydrogen would be located in the forward end of the tank, with a generally flat free surface. Since the static shape of a free surface is determined entirely by Bond number and contact angle at the wall, it can be shown by scaling on the basis of Bond number that the free surface of the hydrogen is similar to the interface between water and air in a clean glass cylinder, 1.0 to 2.5 cm diameter, subject to normal gravity.

Because of the nature of liquid hydrogen and of the tank insulation, it is necessary to vent the tank to keep the ullage pressure within design limits. One venting technique involves periodically firing small ullaging rockets to accelerate the vehicle forward, settling the hydrogen in order to clear a vent at the forward end of the tank. The investigation described here was concerned in particular with the fluid behavior following application of this ullaging thrust.

*Bond number in this case is defined as the dimensionless ratio $(F_{ll} - F_{lg})/F_s$, where F_{ll} and F_{lg} are the inertial forces in the liquid and gas, respectively, and F_s is the surface tension force at the interface between liquid and gas. Inertial forces arise from vehicle/tank deceleration caused by aerodynamic drag. Thus, the Bond number can be expressed as $\rho a R^2/\sigma$, where ρ is the difference in density between liquid and gas, and a is the deceleration. The range of values of Bond number indicated here reflects the range of values of the drag-inducing particle density which might be encountered in a low orbit.

2 HYDRODYNAMICS OF LIQUID SETTling

Ignoring surface tension effects, the interface between two stationary, superposed fluids has long been known to be unstable if the upper fluid is more dense than the lower one (Ref. 1, pp. 370-372, 458-461). Only in the past two decades, however, has the logical extension of this stability criterion, from fluids in a stationary system under the influence of gravity to fluids in an accelerating system, been explicitly spelled out.

On the basis of the well-known equivalence* between uniformly accelerating systems and systems at rest in a gravitational field, G. I. Taylor in 1950 extended this stability criterion to the case of accelerating systems by stating that the interface between the two fluids should be stable if the systems are accelerated (relative to free fall) in a direction from the more dense to the less dense fluid, and unstable (again neglecting surface tension effects) if the acceleration is in the opposite direction (Ref. 2). This observation, along with Taylor's theoretical treatment of initial growth rates of the predicted instabilities, has given rise to the term "Taylor instability" which is

*Consider, for example, the transformation of the equations of motion of an ideal fluid to a moving system of coordinates. If \vec{f} is the external body force per unit mass, and primed variables refer to a coordinate system translating (without rotation) relative to the fixed (unprimed) coordinate system with a velocity \vec{v}_0 , then Euler's equation transforms from

$$\frac{\partial \vec{q}}{\partial t} + (\vec{q} \cdot \nabla) \vec{q} = -\frac{1}{\rho} \nabla p + \vec{f}$$

to

$$\frac{\partial \vec{q}'}{\partial t} + (\vec{q}' \cdot \nabla') \vec{q}' = -\frac{1}{\rho} \nabla' p + \vec{f} - \frac{\partial}{\partial t} (\vec{v}_0)$$

and the exercise has demonstrated that, in a system which is being accelerated by a constant amount

$$\frac{\partial}{\partial t} (\vec{v}_0) = \vec{a}_0$$

the fluid motion relative to coordinates fixed in the accelerating system is the same as it would be if the system were at rest and the gravitational body force $\vec{f} = -g\vec{j}$ were replaced by $-g\vec{j} - \vec{a}_0$. (The result is the same if the Navier-Stokes equation is used.)

commonly applied to instabilities of an interface between two stationary liquids of different density. In a companion paper to Taylor's, Lewis performed a series of experiments in which test vessels were accelerated downward for short distances at high (50 g) accelerations; the results confirmed Taylor's observations (Ref. 3).

Perhaps the most interesting of the many extensions of Taylor's theory which have appeared in the intervening years is the work of Bellman and Pennington (Ref. 4) who found that the effect of surface tension is to remove the Taylor instability for sufficiently small wavelengths, and that viscous effects, while never removing the instability, reduce the growth rate of the amplitude of the disturbance for all wavelengths. Also of interest is the work of Fermi (Ref. 5), and Fermi and von Neumann (Ref. 6), who attempted to extend the analysis of the growth of Taylor instabilities beyond the initial growth period—that is, beyond the point where the amplitude becomes comparable to the wavelength.

If the hydrodynamic theory reviewed above is now applied to the physical situation described in Section 1, the general nature of the initial fluid flow in the hydrogen tank can be predicted to a certain extent. Immediately following application of the settling acceleration, the interface is flat except for possible waves on its surface and a relatively large meniscus adjacent to the walls. The more dense fluid (liquid hydrogen) is "on top of" the less dense fluid (hydrogen vapor mixed with some gaseous helium). Ullage pressure would be sufficient to support the liquid if the interface were rigid; since the interface is not rigid, the problem is initially one of interfacial equilibrium and stability. For certain low values of the Bond number, there exists a curved interface which is a position of stable equilibrium; the interface therefore assumes this shape and settling does not occur.* In practical problems associated with settling, however, Bond numbers based on the vehicle acceleration are always greater than the critical value, and there is no stable equilibrium position for the interface with liquid above and gas below. Perturbations of the interface will therefore grow if their wavelengths are

*For the case of vertical, cylindrical walls and zero contact angle, analyses of this hydrostatic stability condition have been made by Bretherton (Ref. 7) and Gluck and Gille (Ref. 8). In each case, numerical solution gave the result $\rho a R^2 / \sigma < 0.842$ for stability. Experimental investigations by Masica et al (Refs. 9, 10) verify this result.

sufficiently large, even though amplitudes might initially be microscopic. For this reason, a meniscus grows when subjected to a settling acceleration, so that wetting liquids are observed to flow down the walls of their containers if the settling acceleration is large enough. In addition, when the Bond number is somewhat greater than the critical value, there is a possibility of liquid settling in the central region of a tank as well as along the walls. As a result of the initial Taylor instability, waves on the liquid surface are expected to grow, forming (for example) a liquid spike along the tank centerline, a broader, rising liquid dome in the center of the tank, a hollow cylinder around the centerline of a cylindrical tank, or even a number of concentric hollow cylinders. In addition to these flows in the central part of a tank, in the case of wetting liquids, the initial meniscus is always expected to result in flow along the walls. If for some reason the liquid is initially in the zero-gravity configuration where the entire surface is a meniscus, extending from wall to wall with uniform curvature, it is to be expected that the entire flow would be along the walls, since there would be no flat region on the interface from which other flows, separate from the flow along the walls, could grow.

Once the liquid begins to flow, there are at least two other stability considerations which must be taken into account. First, as the dense liquid flows past the less dense gas, the interface is subject to Helmholtz instability, as pointed out by Fermi and von Neumann. The effects of this instability would be especially pronounced in the case of a thin spike, which would tend to break up into discrete masses of liquid as a result of the surface pinching in at regular intervals. Second, the base of a spike (where the spike is attached to the bulk of the liquid) would be attracted to the walls of the tank by surface tension. The centerline of the tank would in this case be a location of unstable equilibrium for the base region of the spike. If the base were to move toward one side of the tank, the tank ullage pressure acting on the remaining lower part of the interface, where ullage pressure is higher than pressure in the liquid, would be expected to deform the bulk of the liquid in the direction of the moving spike, causing the major portion of the settling flow to occur along the side of the tank toward which the spike moved.

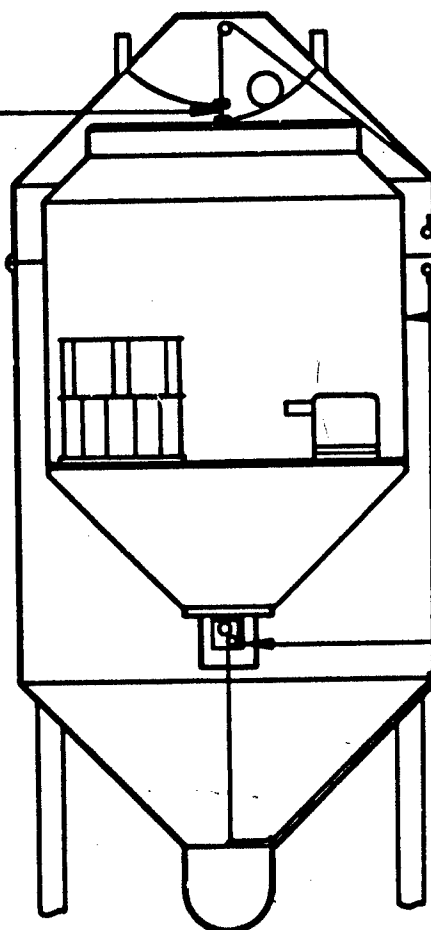
This description of the hydrodynamics of liquid settling is intentionally based entirely on abstract analysis and previous theoretical work, rather than on the experimental results of the present investigation. The purpose of such approach is to emphasize its physical reasonableness. The description was originally formulated, nevertheless, on the basis of the experimental results. The remainder of this paper describes the experimental program which was carried out, and presents results of that program which substantiate the physical description developed above.

3 EXPERIMENTAL PROGRAM

Experiments were performed in Martin-Denver's 75-foot drop tower, using constant force springs or cables from constant torque motors, extended between the experimental package and the outer capsule, to accelerate the experimental package downward relative to free fall. The device is shown in Fig. 1 and described in more detail by Paynter (Ref. 11). Test vessels were transparent cylinders with inside diameters of 2.3, 4.7, 7.6, 9.5, 12.8, 13.2, 15.2, 16.7, and 29.2 cm, arranged in various combinations inside the experimental package. The 12.8, 15.2, and 29.2-cm cylinders were Plexiglas because of the breakage problem encountered with glass specimens of this size. The smaller cylinders were glass: the 13.2 and 16.7-cm cylinders were glass while they lasted. Initial accelerations ranged from 0.002 g to 0.027 g. Test liquids were carbon tetrachloride, chloroform, Freon TF (trichlorotrifluoroethane), and methanol, with the bulk of the work being done with Freon TF because of its low specific surface tension (σ/ρ) with air, and its desirable handling properties. Bond numbers, based on specimen radius and initial acceleration, ranged from subcritical to 390.

Data were recorded using a Milliken camera operating at 213 frames per second. Films used were Kodak Plus-X and Ektachrome MS; the color film was used for most tests because it facilitated visual identification of many aspects of the complex flow patterns. Minute amounts of dye were used for the same reason; it was found that if just enough dye was used to give a barely discernible amount of color in the laboratory, the pictures would show a quite satisfactory liquid color.

WIRE FUSED
TO RELEASE
EXPERIMENTAL
PACKAGE



EXPERIMENTAL
PACKAGE

OUTER CAPSULE

CONSTANT
TORQUE
MOTOR

Fig. 1 Experimental Apparatus

Experiment technique assured that the wire supporting the experimental package was fused immediately after release of the outer capsule. Otherwise, the liquid surface would have tended toward its usual free fall shape before the fusing of the wire, and the type of flow being studied would not have been able to develop. Since the interface is initially rather flat in the full-scale case being studied, it was essential that these settling experiments begin with a flat interface.

The Bond numbers and accelerations stated herein are valid only during the initial part of the drop, because the system did not actually accelerate the experimental package at a constant rate. Acceleration of the test package decreased with time after capsule release, apparently due to a velocity dependence of the force delivered by the "constant torque" motors. (The advertised constancy of the springs which make up the motor is with respect to extension rather than rate of extension.) This force variation was not felt to be a major disadvantage, however, since quantitative values of Bond number are of primary importance in this investigation only during the formation of the various flow features resulting from the initial instability. Indeed, the question of the physical significance of the Bond number arises as soon as the liquid begins to flow.

4 EXPERIMENTAL RESULTS

Results of the experimental program are summarized in Fig. 2, with some typical examples shown in Figs. 3 through 5.

All of the settling tests which have been performed to date are listed in Fig. 2a, according to Bond number at start of test. The horizontal position of the line corresponding to each Bond number indicates which of the five flow regimes described at the right side of the page applies to the observed phenomena. Each of the lines shown in Fig. 2a represents from one to six tests. The number of tests made at many of the listed Bond numbers is due in part to an attempt to find an influence, if any, of liquid filling level on the settling phenomena. No such influence was found. In several cases, the same Bond number (to two significant figures) was studied at two different acceleration levels, using test cylinders of different sizes or different test liquids. A more

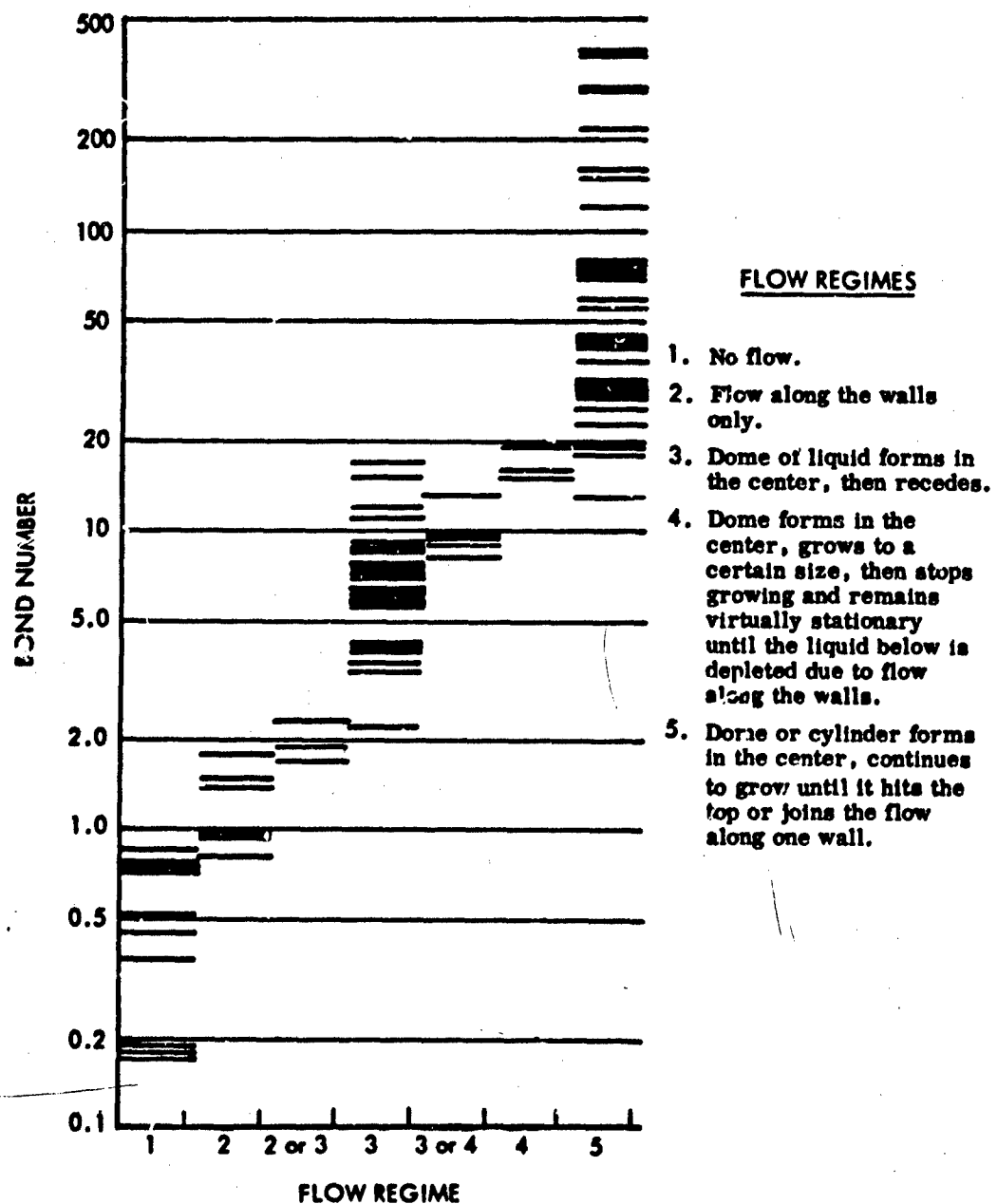


Fig. 2a Summary of Test Results; General Classification of the Observed Flows

common occurrence was for the Bond number studied in one test to be within the range of Bond numbers studied in tests of a different series.

Figure 2b presents more detailed descriptions of the rather wide range of fluid behavior which was grouped together as regime 5 in Fig. 2a. Analyses of only the best of the drop records have been included in Fig. 2b because of the more detailed flow features which distinguish the various sub-regimes defined below the graph.

Classifying a broad range of different flows as fitting one of a number of brief descriptions, as in Fig. 2, is obviously artificial. Nevertheless, a grouping such as Fig. 2 seems to be the most concise and understandable presentation of the experimental program results. Because of the large number of tests which were conducted and the quality of most of the photographic data, the groupings of Fig. 2 are presented with some confidence. Primary weaknesses in these groupings are at the boundaries between the different types of flow, as indicated in Fig. 2a.

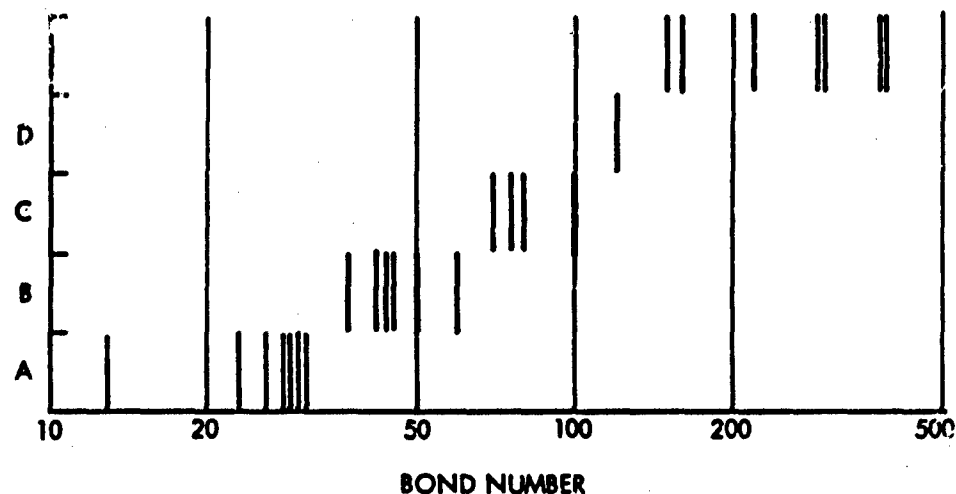
There is some uncertainty at the boundary between regimes 2 and 3 because many of these tests were made with the smallest (2.3 cm) test cylinders at relatively high acceleration levels. The liquid domes were present in these small cylinders only for extremely brief intervals of time*, if at all; in addition, photographic resolution was not as good as in the large cylinders.

As can be seen in Fig. 2a, the range of Bond numbers from 13 to 20 includes various types of behavior interspersed with each other. At Bond numbers 13, 15, and 19,

*Time scale is given by the acceleration level and physical dimensions of the test vessel,

$$t_r = (L_r/a_r)^{1/2}$$

so that higher accelerations and smaller physical dimensions in the experimental model both result in things happening faster.



- A. The liquid dome grows into a thin spike which eventually extends to the top of the tank. Effects of Helmholtz instability are seen if the spike L/D becomes large enough.
- B. A small depression forms in the center of the upper surface of the dome. Shortly after its formation, the depression "turns inside out," becoming a small protuberance on the top surface of the dome. The protuberance grows rapidly in amplitude and diameter relative to the original dome until the two cannot be distinguished from each other. Together they form a column up the center of the cylinder, as in A.
- C. A depression forms in the center of the upper surface of the dome, similar to the depression observed in B but somewhat larger. The depression is present only temporarily, leaving behind a bubble or cavity inside the dome. No protuberance is seen to form following the breakup of the depression.
- D. In its formative stages, the cylinder has a complex upper surface characterized by concentric waves whose amplitudes become large with time. The eventual result is a broad dome with protuberance growing on its upper surface as in B.
- E. Same as D, except that the eventual result is a hollow cylinder.

Fig. 2b Summary of Test Results; Additional Features of the Central Flow Observed in Certain Regime 5 Flows

different tests gave different types of behavior. Spikes were formed in some tests, while in others the dome did not grow past a certain maximum height. Once a dome attained a spike-like shape, the spike always continued to grow.

Figures 3 through 5 show some specific examples of the various types of flow described as regions 3 through 5 in Fig. 2. Each of these illustrations is a series of still photos reproduced from the motion picture record of a typical drop test. All three examples were chosen from a series of drops made with Freon TF and an initial acceleration of 0.016 to 0.017 g.

Figure 3 shows a test specimen containing two cylinders with inside diameters of 7.6 and 9.5 cm. Bond numbers immediately following capsule release are consequently 20 and 31.

At 0.53 seconds (Fig. 3a) the liquid is "climbing" the walls of each tank. In addition, Taylor instability is manifested in the formation of domes rising in the central portion of each tank. In the smaller tank, the dome is already moving toward the right-hand side of the tank, apparently as a result of surface tension.

At 1.06 seconds (Fig. 3b) the first thin layer of liquid flowing up the walls has reached the top of each tank and is beginning to flow radially inward along the top. The dome in the smaller tank has reached the wall on the right side, with the result that the major part of the flow is being established along that wall. Since the dome in the smaller tank has moved away from the central region of the interface, the interface is free to assume a curved shape, as it might in the case of a bubble or in a static "zero-gravity" situation. In the larger tank, the spike is growing almost vertically. In addition, Helmholtz instability is beginning to manifest itself in a "pinching off" of the flowing column of liquid about 1-1/2 diameters below the top.

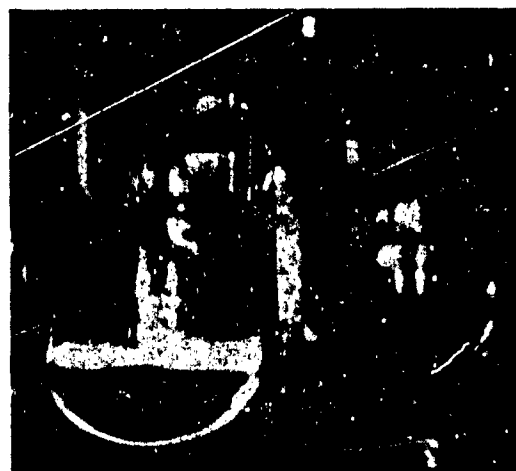
At 1.58 seconds (Fig. 3c): In the smaller tank, the major flow up the right-hand side has reached the top of the tank, proceeded across the top, and is beginning to "splash"



A. 0.53 SEC



B. 1.06 SEC



C. 1.58 SEC



D. 2.11 SEC

Fig. 3 7.6 and 9.5 cm Cylinders at 0.016 g; Freon Tt

back down. The column of liquid in the larger tank has almost reached the top and at the same time its base is beginning to move to the left, taking a large amount of liquid below with it. The Helmholtz instability has resulted in a sphere of liquid being almost separated from the remainder of the column; in some tests, this sphere is seen to separate completely. Ripples moving down the walls result from the initial thin layer which flowed up the walls, hit the top, rebounded, and is now setting up interference with the continuing flow up the walls.

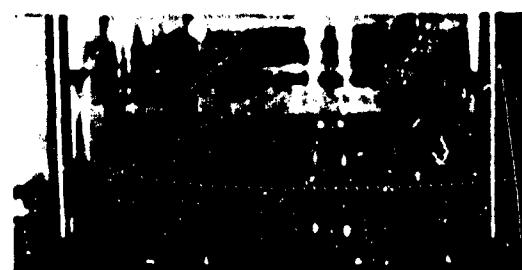
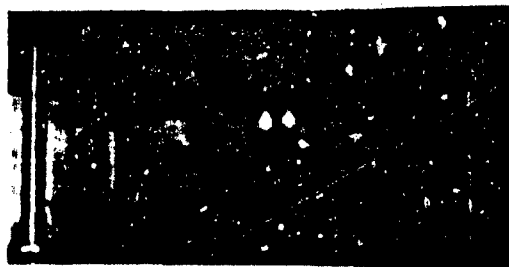
At 2.11 seconds (Fig. 3d): In the smaller vessel, the interface has reached the bottom of the tank. Considerable turbulence is present at the top of the tank, along with some flow down the left side and interference ripples where this downward-moving flow meets the upward-moving layer along the wall. In the larger tank, the remainder of the column which was formed as the result of Taylor instability is seen in the upper left corner. The top of the column has rebounded from the tank top. The bulk of the liquid is beginning to flow up the left side of the tank, following the Taylor instability.

In Fig. 4, the test specimen consists of four cylinders whose inside diameters are 2.3, 4.7, 13.2, and 15.2 cm. Bond numbers immediately following capsule release are consequently 1.8, 7.6, 60, and 80.

At 0.27 seconds (Fig. 4a) a dome has formed in the 4.7-cm cylinder and is already beginning to recede. Flow features are just beginning to form in the two larger cylinders.

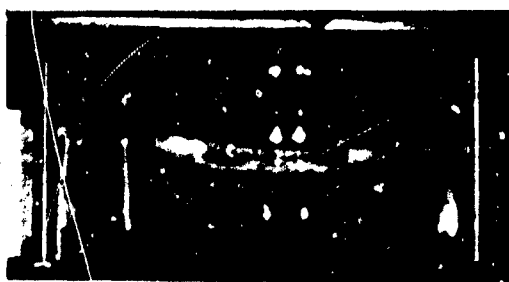
At 0.77 seconds (Fig. 4b) the dome in the 4.7-cm cylinder has receded into the downward-flowing liquid below. Broad domes have formed in the two larger cylinders; particular attention is called to the 13.2-cm cylinder, where the dome has a rather broad, flat upper surface on which a small depression can be seen.

At 0.98 seconds, the depression mentioned immediately above has "turned inside out," becoming a small, rapidly-growing protuberance on the top surface of the dome. Most of the liquid flow is now moving into this protuberance.



A. 0.27 SEC

B. 0.77 SEC



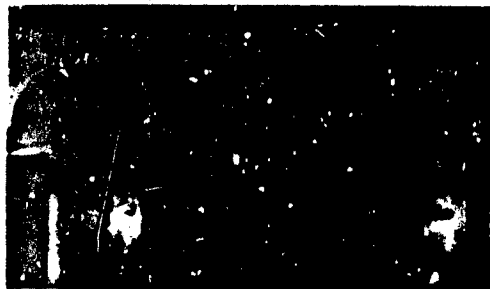
C. 0.98 SEC

D. 2.16 SEC

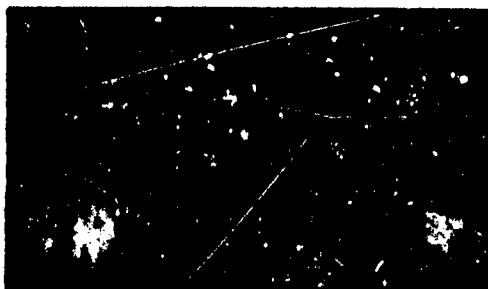
Fig. 4 2.3, 4.7, 13.2, and 15.2 cm Cylinders at 0.016 g; Freon TF

At 2.16 seconds, the flow in the two larger cylinders is dominated by columns which have formed for the entire length of each cylinder. Very turbulent liquid, mixed with considerable gas, is collecting at the top of each of these cylinders. Liquid has also collected at the top of each of the smaller cylinders. In the 4.7-cm cylinder, considerable liquid which had collected at the top of the cylinder has splashed back down as a single coherent ball, seen moving down near the center of the cylinder.

Figure 5 shows the largest test cylinder used, 29.2 cm. Bond number is 280. Still photos probably do not show as convincingly as the motion picture that the entire length of the cylinder of liquid becomes hollow by the end of the test. It was found that motion picture projection was extremely helpful in the analysis of all of the flows of sub-regime 5E, whereas flows at lower Bond numbers could be studied more advantageously frame by frame.



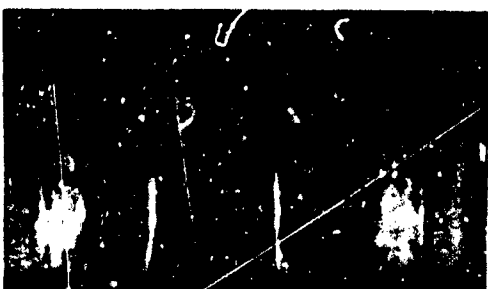
A. 0.54 SEC



B. 1.08 SEC



C. 1.62 SEC



D. 2.16 SEC

Fig. 5 29.2 cm Cylinder at 0.016 g; Freon TF

It should be noted that the understanding of liquid settling which has been gained in the course of this investigation applies only to the flow up to the time when it reaches the aft end of the tank. After liquid has reached the end of the tank, its motion generally becomes quite turbulent, with liquid and gas phases becoming rather well mixed. Interference occurs between this fluid and the liquid which has not yet reached the aft end of the tank. In some cases, quantities of liquid are seen to splash back to the forward portion of the tank. Even if sufficient time were available to study this later phase of settling to any extent, it is doubtful that any means of scaling the experimental results to a full-scale vehicle tank could be found. The data would probably be of a statistical nature at best.

CONCLUSIONS

The results discussed in the preceding section have shown that primary aspects of the settling flow can be validly scaled by using Bond number, at least within the range covered by this investigation. Liquid level in the test vessel was not found to have an effect on the initial settling flow. Secondary flow characteristics such as viscous effects are of course not scaled by the Bond number. However, except for the tendency of a liquid spike to move to one side of the tank, these secondary flow features are of limited importance in understanding the basic nature of the flow.

The physical explanation of the fact that Bond number was found to describe primary aspects of the settling flow for a wide range of vessel sizes, acceleration levels, and test liquids rests on the discussion of Taylor instabilities presented in Section II. Basic characteristics of the settling flow observed in the experiments are in general the same characteristics that were predicted on the basis of the Taylor instability. Within this general class of flows, differences between various specific types of flow have been shown by the experiments to depend on initial conditions at the interface. Since the interface is essentially static immediately following capsule release (or application of ullaging thrust, in the full-scale case), the conditions on which the initial flow behavior is based are determined by the ratio of inertial to surface tension forces,

or Bond number. Thus the basic characteristics of the entire flow should depend on the initial Bond number, as was found experimentally.

Although uncertainty is inherent in extrapolating from a series of small-scale tests to tanks which are more than an order of magnitude larger, there is no apparent reason, on the basis of the understanding gained from these tests, why the qualitative results could not be scaled to the full-size tank, using Bond number.

C REFERENCES

1. H. Lamb, Hydrodynamics, 6th ed, Cambridge: Cambridge University Press, 1932; New York: Dover Publications, 1945
2. G. I. Taylor, "The Instability of Liquid Surfaces When Accelerated in a Direction Perpendicular to Their Planes," I, Proc. Roy. Soc. A, 201, 1950, pp. 192-196
3. D. J. Lewis, "The Instability of Liquid Surfaces When Accelerated in a Direction Perpendicular to Their Planes," II, Proc. Roy. Soc. A, 202, 1950, pp. 81-96
4. R. Bellman, and R. H. Pennington, "Effects of Surface Tension and Viscosity on Taylor Instability," Quart. J. Appl. Math., 12, 1954, pp. 151-162; also Princeton University Report, 1952
5. E. Fermi, "Taylor Instability of an Incompressible Liquid," AEC memorandum, Sept. 4, 1951; Part 1 of "Taylor Instability of Incompressible Liquids," AECU-2979, Nov. 1955
6. E. Fermi, and J. von Neumann, "Taylor Instability at the Boundary of Two Incompressible Liquids," AEC memorandum, Aug. 19, 1953; Part 2 of "Taylor Instability of Incompressible Liquids," AECU-2979, Nov. 1955
7. F. P. Bretherton, "The Motion of Long Bubbles in Tubes," J. Fluid Mech., 10, 1961, pp. 166-188

8. D. F. Gluck, and J. P. Gille, "Fluid Mechanics of Zero-g Propellant Transfer in Spacecraft Propulsion Systems," Paper 862A, SAE-ASME National Air Transport and Space Meeting, April 1964
9. W. J. Masica, D. A. Petrash, and E. W. Otto, "Hydrostatic Stability of the Liquid-Vapor Interface in a Gravitational Field," NASA TN D-2267, May 1964
10. W. J. Masica, J. D. Derdul, and D. A. Petrash, "Hydrostatic Stability of the Liquid-Vapor Interface in a Low-Acceleration Field," NASA TN D-2444, August 1964
11. H. L. Paynter, "The Martin Company's Low-g Experimental Facility," Symposium on Fluid Mechanics and Heat Transfer Under Low Gravitational Conditions, Palo Alto, California, June 1965

7 ACKNOWLEDGEMENTS

The author wishes to thank Dr. B. K. Larkin, Mr. J. L. McGrew, Mr. E. A. Mossman, Mr. R. F. Fearn, and other personnel of the Propulsion Research Department for their continuing assistance and suggestions.

The help of Mr. H. L. Paynter and the other personnel of the Advanced Technology and Development Section responsible for operating Martin-Denver's drop tower has been invaluable.

Special thanks are extended to Dr. R. G. Fledderman of Martin-Denver's Technical Staff for valuable discussions of the Taylor instability.

The work described in this paper was sponsored by NASA, Marshall Space Flight Center, under Contract NAS8-11328.

DISCUSSION

A. Lytle, Bell Aerosystems Company

Your experimental results show quite different types of flow at higher settling Bond numbers than at lower ones. How do you explain the fact that for one range of Bond numbers the experiments show thin "spikes" of liquid flowing up the center of the tank, whereas for another, higher range of Bond numbers the flows are in the form of hollow cylinders of liquid?

Bowman

Perhaps the easiest way to explain the differing nature of the flows obtained at different Bond numbers is through consideration of the dynamics of the initial interface, which is very nearly a plane.

At Bond number 40, for example, only the lowest axi-symmetric vibrational mode is unstable and all higher axi-symmetric modes are stable, so that a wave would grow at the tank centerline and result in liquid flow in the form of a spike. At Bond numbers around 200 or higher, on the other hand, the first four axi-symmetric modes are all unstable. A rather simple, linearized examination of the exponential time dependence of each mode indicates that the second and third modes are more unstable than the first (that is, initially they grow faster than the first), so that some sort of wave concentric with the cylinder would grow to form a hollow cylinder of flowing liquid.

BLANK PAGE

PAPER 15

THE MARTIN COMPANY'S LOW-g EXPERIMENTAL FACILITY

By N. L. Payater
MARTIN COMPANY

ABSTRACT

The Martin Company 75-ft drop-test facility is described. This facility provides repeatable and controllable low-g conditions of 10^{-4} to 10^{-2} g for 2.1 sec. The test cell falls inside an evacuated drag shield while being accelerated at constant g-levels. Both indirect and planar lighting techniques are used for 16-mm photographic documentation of test results.

NOMENCLATURE

English Symbols

A	Area, ft ²
a	Acceleration, ft/sec ²
C _D	Drag coefficient
g ₁	Gravitational acceleration (local), ft/sec ²
g'	Acceleration ($g_1 - a_d$), ft/sec ²
g''	Acceleration ($g_1 + a_c$), ft/sec ²
K	Drag parameter, lb _m /ft
m	Mass, lb _m

t Time, sec
 v Velocity, ft/sec

Greek Symbols

Δv Differential velocity ($v_c - v_d$), ft/sec
 y Vertical distance, ft
 Δy Differential vertical distance ($y_c - y_d$), ft
 ρ Mass density, lb_m/ft³

Subscripts

c Test cell
 d Drag shield

THE MARTIN COMPANY'S LOW-g EXPERIMENTAL FACILITY

1 INTRODUCTION

The Martin Company's free-fall facility was developed during 1963 to experimentally support various zero-g* fluid investigations (Refs. 1 through 4). The facility's zero-g testing capability is described in Ref. 4. An additional test capability providing low-g conditions during the 2.1-sec free-fall duration was developed during 1964. A relatively simple method employing constant-force NEG'ATOR** springs is used for providing controllable and repeatable accelerations during free fall. The low-g capability is required for providing quantitative low-g experimental data, i.e., correlation of model and prototype Bond numbers. Acceleration levels to 0.019 g are obtained for the full free-fall duration while higher g-levels can be provided for shorter durations (less than 2.1 sec). This low-g capability was used extensively in support of the propellant settling study discussed in Ref. 5.

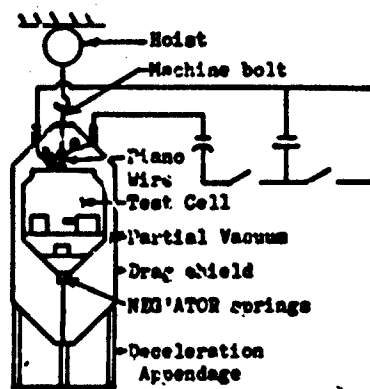
This paper describes the unique low-g testing technique, testing procedures, and instrumentation used in the drop tower at Denver, Colorado.

2 LOW-g TEST PRINCIPLE

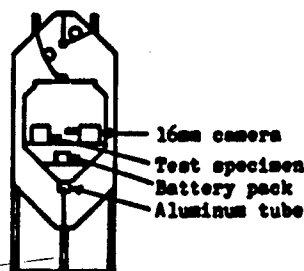
The test principle used for providing low-g conditions during free fall is illustrated in Fig. 1. The test cell is balanced prior to each test to assure that the NEG'ATOR spring force acts through its center of mass. The space between the test cell and drag shield is evacuated to assure that the only substantial force acting on the test cell during free fall is provided by the NEG'ATOR spring arrangement, as shown. The test cell and drag shield fall unguided, and are independent (except for the NEG'ATOR springs). The capsules fall at different rates because of the spring force

*The term zero-g is used herein to denote a condition of zero acceleration.

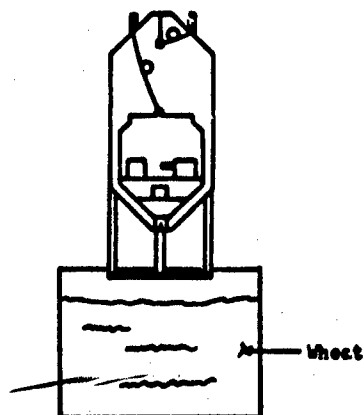
**Trade name, Hunter Spring Company, Hatfield, Pennsylvania.



- 1) Drop capsule package is pictured just prior to initiation of free-fall. The drop sequence is to charge the 2CK μ fd capacitor bank to 260 volts; stabilize the capsule package; turn camera and test cell lighting system on, and then sever machine bolt. The test cell is separated from the drag shield almost instantaneously (within 13 milliseconds). A microswitch, sensing downward motion of the drag shield, activates the capacitor bank to supply the energy for fusing the piano wire.



- 2) The capsule package is shown during free fall. The NEUTATOR springs are accelerating the test cell (downward with respect to the drag shield). The length of the aluminum tube is sized to provide the proper relative travel distance between capsules during the 2.1 sec free-fall.



- 3) Termination of free-fall is shown. The NEUTATOR spring force has bottomed the test cell in the drag shield (milliseconds) before the capsule package penetrates the wheat bin. The camera and lighting system are turned off by an impact switch during deceleration.

Fig. 1 Low-g Test Principle

and also because of air drag acting on the larger capsule. Neglecting buoyancy, the velocity of the drag shield can be calculated from:

$$v_d = \sqrt{\frac{mg'}{K}} \tanh \left(\sqrt{\frac{Kg'}{m}} t \right) \quad (1)$$

where

$$K = \frac{1}{2} (C_D \rho A) \quad (2)$$

$$g' = g_l - a_d \quad (3)$$

and where a_d is the acceleration (constant) provided by the NEG'ATOR springs.

The velocity of the test cell is simply:

$$v_c = g'' t \quad (4)$$

where

$$g'' = g_l + a_c \quad (5)$$

and where a_c is the constant acceleration provided the test cell by the spring force.

The drag-shield and test-cell accelerations, a_d and a_c , are calculated from the Newtonian force-mass relationship using the constant force supplied by the NEG'ATOR springs and by the drag shield and test cell individual masses, respectively. The springs are calibrated and the test cell is accurately weighed prior to each test. (There is no need to weigh the drag shield with each test since it is a constant mass.)

Differential capsule velocity is simply the difference between Eqs. (1) and (4):

$$\Delta v = g'' t - \sqrt{\frac{mg'}{K}} \tanh \left(\sqrt{\frac{Kg'}{m}} t \right) \quad (6)$$

and integration of Eq. (6) yields capsule relative travel (vertical):

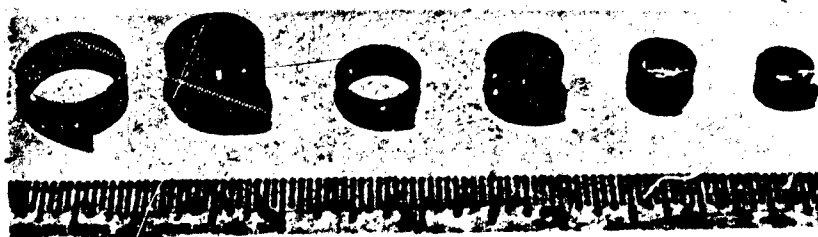
$$\Delta y = \frac{1}{2} g'' t^2 - \frac{m}{K} \ln \cosh \left(\sqrt{\frac{Kg'}{m}} t \right) \quad (7)$$

The maximum acceleration obtainable using this low-g testing method is limited by the capsule relative travel distance, Δy . Zero-g is, of course, the lower limit obtained by omitting the NEG'ATOR springs.

3 APPLICATION OF NEG'ATOR SPRINGS

The unique feature of this testing principle is the application of NEG'ATOR springs for providing the constant force required. Other acceleration techniques, such as choked gas jets, were also considered but were not as attractive from simplicity and cost considerations. Some of the other methods considered had specific shortcomings as well. For example, a choked nozzle would not permit evacuation of the space between the drag shield and test cell.

The NEG'ATOR springs, made of stainless steel or high-carbon spring steel, are pre-stressed to provide a constant resisting force incrementally, rather than cumulatively, as with conventional springs. Individual NEG'ATOR springs are pictured in Fig. 2a; constant-torque motors are shown in Fig. 2b. The latter consist of individual springs, as shown. The motors are preferred for low-g tests since they provide working deflections up to 6 ft while individual springs are limited to only about 1 ft. Both the springs and motors are reusable (2500 cycles or more).



a. CONSTANT-FORCE SPRINGS (STAINLESS STEEL). SPRINGS PICTURED VARY FROM 0.6 l_b TO 4.0 l_b .

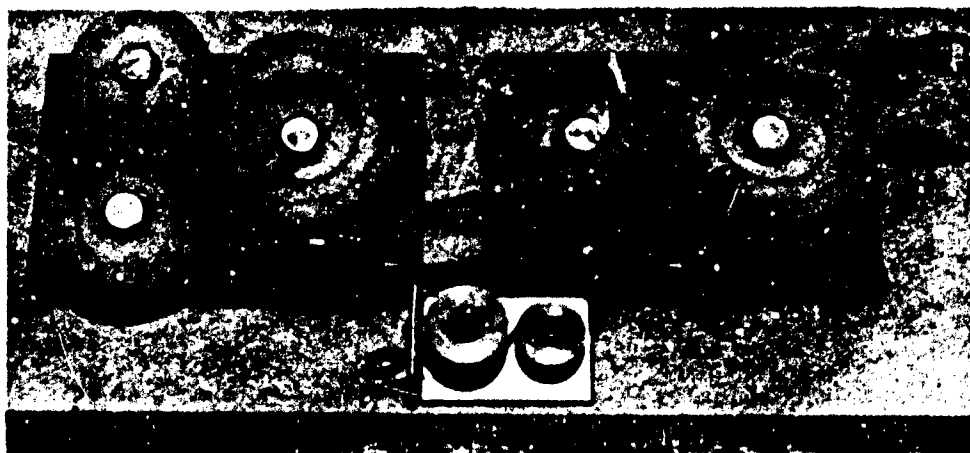


Fig. 2 Standard Open-Stock NEG'ATOR Springs and Motors

Different NEG'ATOR spring arrangements are possible for providing low-g test conditions. The simplest is shown in Fig. 1, i.e., a single unopposed motor, or spring. At extremely low acceleration levels (10^{-4} g or so), opposed springs, or motors, are more desirable. This opposed arrangement permits the use of fairly rugged springs while still providing the small differential force required.

The single, unopposed, constant-torque motor arrangement was used for the majority of the settling tests reported in Ref. 5. Standard open-stock NEG'ATOR motors ranging from 0.375 to 5.0 l_b (nominal) were used.

Typical force-versus-deflection calibrations for the constant-torque motors are presented in Fig. 3. The force deviation, as seen, is usually less than 10 percent for the open-stock motors. The calibration data are representative of the actual test usage in that the force presented in Fig. 3 is obtained during recoiling of the motor.

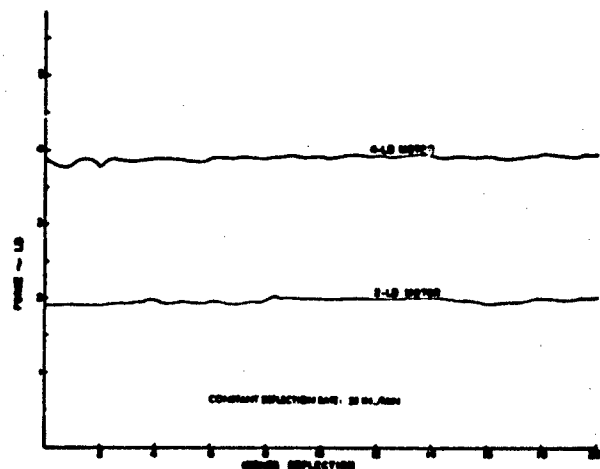


Fig. 3 Standard Open-Stock NEG'ATOR Constant-Torque Motor Calibrations

4 LOW-g TESTING CAPABILITY

The drop tower is housed in the Titan Vertical Test Facility at Denver. A schematic of the facility is presented in Fig. 4. The maximum drop height (75 ft) affords 2.16 sec of free-fall. The test duration is slightly less, about 2.10 sec, since the test cell is arrested in the drag shield prior to termination of free fall.

The present testing capability is limited to a maximum acceleration level of 0.019 g. This maximum level is obtained with the drag shield (Fig. 5) and the smaller of the two test cells (Fig. 6). The larger test cell is pictured in Fig. 7. The present test capability is limited to a negative direction only, as shown in Fig. 1. A positive low-g capability is being developed and will be operational by July of this year. In addition, a larger drag shield (Fig. 8) is being developed to increase the g-level upper limit to 0.10 g.

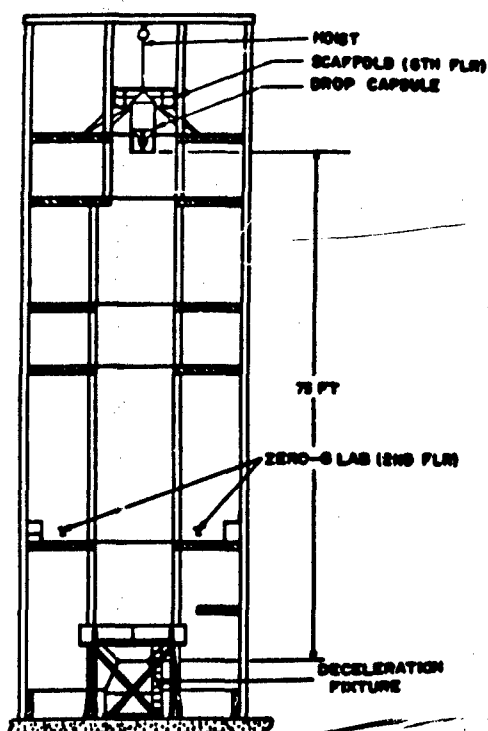


Fig. 4 Schematic Drawing of the Low-g Test Facility at Martin-Denver



Fig. 5 Drag Shield (3-ft Diameter by 10 ft; 1425 lb_m)

5 DATA DOCUMENTATION

Data are photographically documented to provide a chronological record. The 16-mm Milliken DBM 3A camera provides film speed to 400 fps; the 16-mm Fairchild HS 401 camera has a film speed up to 7000 fps. Tests are usually conducted with the Milliken camera at 200 fps. Both are powered by 28 vdc supplied by battery packs during free fall.

Two lighting techniques are used. An indirect method, common to drop tower investigations, is used along with a second technique, which focuses a narrow plane of light

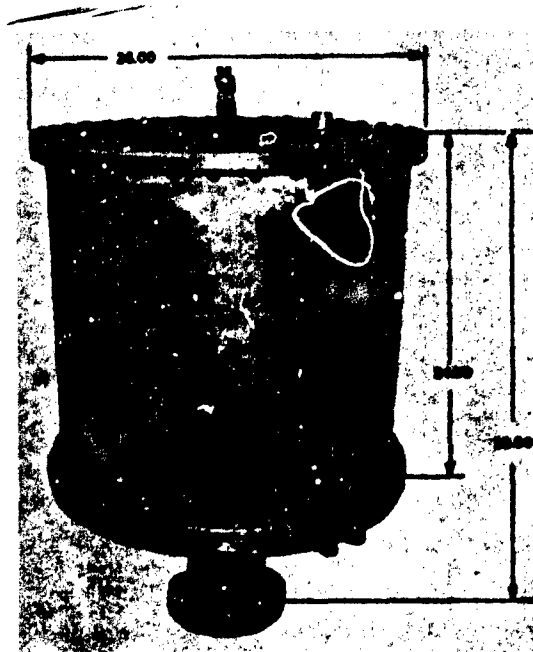


Fig. 6 Smaller of the Test Cells (128 lb_m Empty)

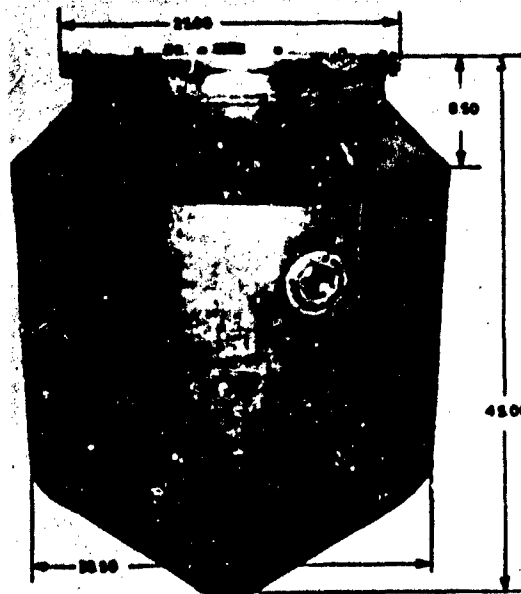


Fig. 7 Larger of the Test Cells (160 lb_m Empty)



Fig. 8 Drag Shield Under Development
(42-in. Diameter by 130 in.;
1600 lb_m)

(1/8-in. thick) through the test specimen, as shown in Fig. 9. The specimen is housed in a plexiglass box, and the space between the two is filled with water to reduce light dispersion and optical distortion effects. The camera is focused on the plane of light to provide a two-dimensional photographic record. This method is particularly attractive for quantitative documentation of fluid migration and liquid-vapor interface phenomena during low-g. Colloidal suspension techniques are also used with this planar lighting method for documenting flow patterns.

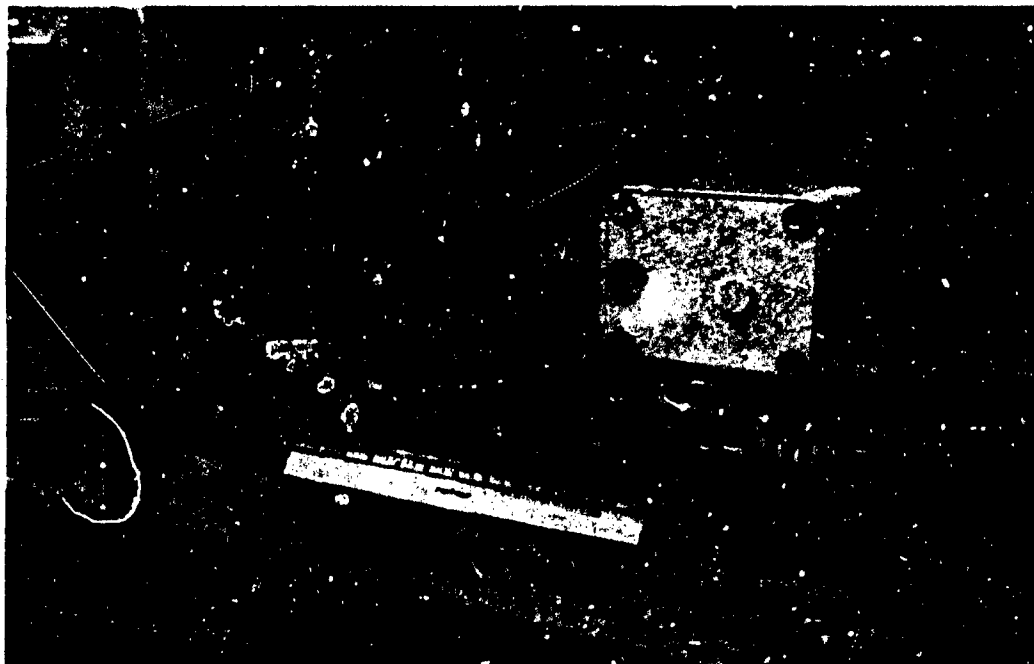


Fig. 9 Planar Lighting System. Test specimen (not shown) is positioned within the plexiglass box.

Data, other than photographic, can also be provided. Cables attached to the drop-cap-sule package fall with the package during test to provide pressure and temperature data, which are recorded by stationary readout equipment positioned at the third level of the facility.

6 TEST PROCEDURE

Laboratory work is performed at the second level of the facility. The test specimen is positioned in the test cell and the test cell is balanced. The cell is sealed and a 6-in.-diameter frangible aluminum tube (with 0.058-in. wall thickness) is attached to its bottom. The length of the tube is sized to provide the required capsule relative travel for the particular low-g test. The NEG'ATOR spring motor is then mounted to the cell (Fig. 10).

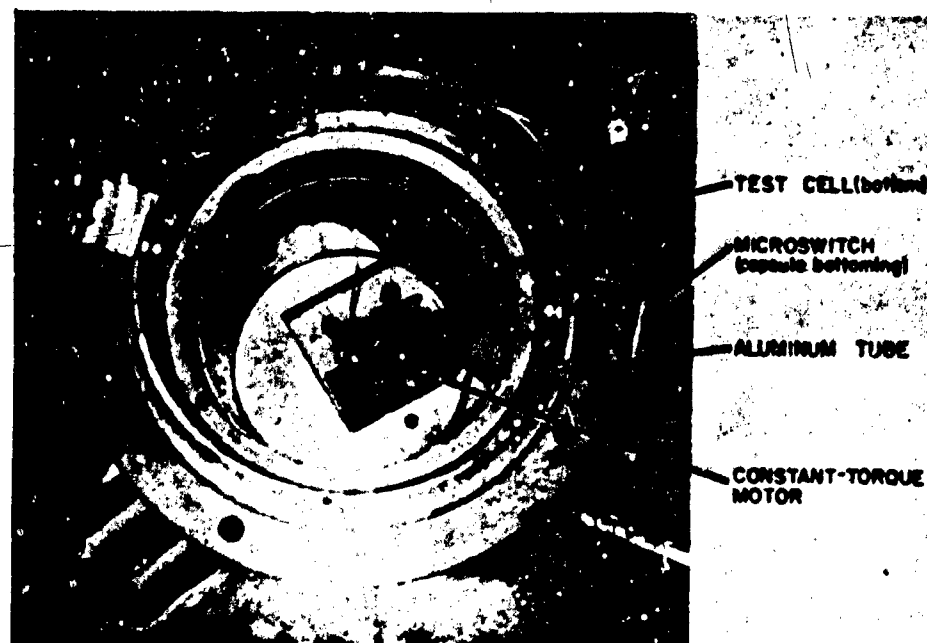


Fig. 10 NEG'ATOR Motor Mounted to Bottom of Test Cell

The test cell is attached to the upper segment of the drag shield by the single-piano-wire arrangement (Fig. 11). This package is then lowered into the drag shield to a position permitting attachment of the NEG'ATOR motor cable to the bottom segment

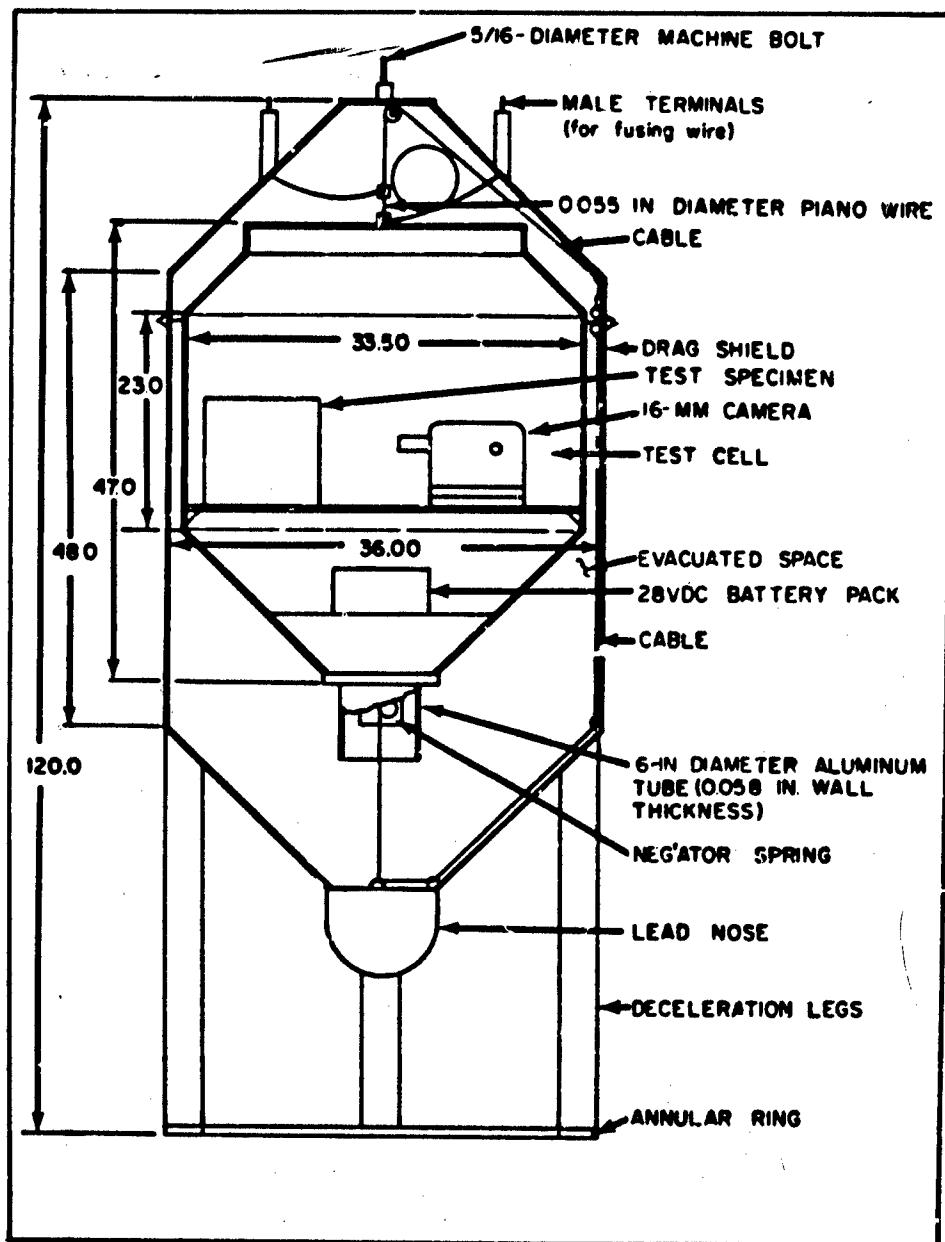


Fig. 11 Schematic Drawing of Drop-Capsule Package in Test Condition (Prior to Initiation of Free Fall)

of the drag shield. The latter is sealed and the space between the two capsules is evacuated. (The drag shield now used provides a vacuum level of 3.0 mm Hg; the larger drag shield being developed will provide a level less than 1.0 mm Hg.)

The package is hoisted to the scaffold at the sixth level of the drop tower (Fig. 12), and the 20K μ fd

capacitor bank, used for fusing the piano wire and separating the two capsules, is then charged. The capsule package is stabilized, and the camera and internal lighting system are activated.

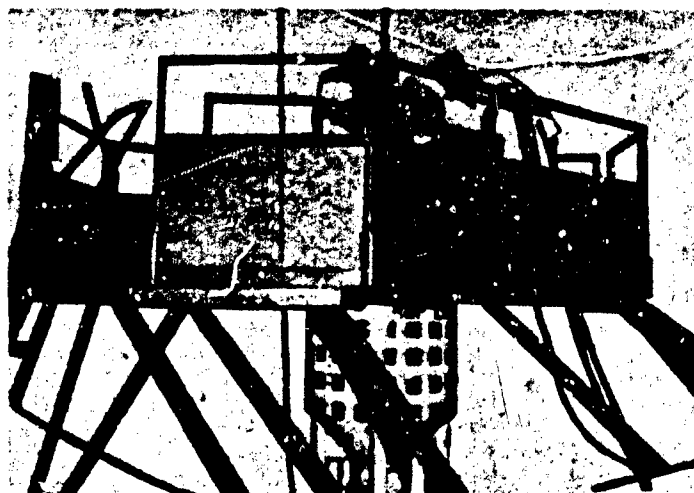


Fig. 12 Drop-Capsule Package at its Maximum Drop Height (75 ft)

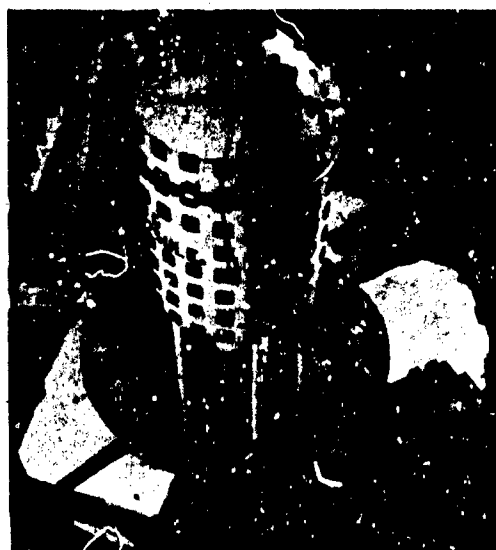


Fig. 13 Drop-Capsule Package Entering Wheat Bin

The drop test is initiated by severing a 5/16-in.-diameter machine bolt that suspends the package from a 2-ton overhead hoist. A microswitch, sensing downward motion of the drag shield, activates a relay that discharges the capacitor bank. The piano wire is fused within 13 msec of the drag-shield release.

The capsule package falls unguided. The test cell is arrested in the outer capsule just prior to termination of free fall. The package is decelerated in a large conical bin filled with 13,000 lb_m of wheat (Fig. 13). Peak g-level

is less than 25 g, and penetration is about 62 in. The 120,000 ft-lb are dissipated in approximately 0.15 sec (Fig. 14).

The chronological photographic documentation is terminated by an impact switch during capsule deceleration.

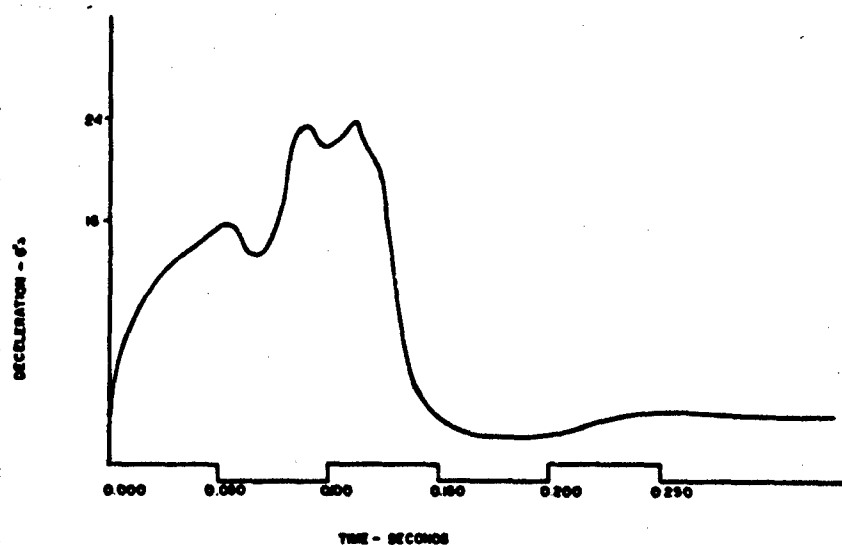


Fig. 14 Typical Energy Dissipation During Deceleration of Drop-Capsule Package in Wheat Bin

7 REFERENCES

1. Rocket Propellant and Pressurization Systems, Chapter 13, Prentice-Hall, Englewood Cliffs, N.J., 1964
2. H. Paynter, "Capillary Devices for Providing Positive Expulsion of Liquid Propellant in Zero-g" (paper presented at Symposium on Positive Expulsion Propellant Systems for Space Vehicles, Aerospace Corporation, Los Angeles, California, Mar 1964)

3. -----, "Time for a Totally Wetting Liquid to Deform From a Gravity-Dominated to a Nulled-Gravity Equilibrium State," AIAA Journal, Sep 1964
4. H. Paynter, R. Marsh, V. Tyler, and C. Mackenzie, "Zero-g Liquid Propellant Orientation by Passive Control," Paper 862D, SAE/ASME National Air Transport and Space Meeting, New York, Apr 1964
5. T. Bowman, "Liquid Settling in Large Tanks" (paper presented at Symposium on Fluid Mechanics and Heat Transfer Under Low Gravitational Conditions, Lockheed Missiles & Space Company, Palo Alto, California, 24 - 25 Jun 1965)

ACKNOWLEDGMENTS

The following personnel, members of the Advanced Technology and Development Section, Propulsion and Mechanical Engineering Department, made significant contributions during the development of the low-g facility: Larry D. Cameron, Dennis E. Gilmore, Ralph Z. Marsh, John N. Smith, and Robert W. Winks.

K. P. Timmons, Manager of the Propulsion and Mechanical Engineering Department, and T. R. Heuton, Chief of the Advanced Technology and Development Section, provided valuable assistance in this development effort.

DISCUSSION

H. M. Satterlee, Lockheed

You described two lighting techniques: the planar method and the colloidal method. Your planar lighting technique is quite different from our backlighting method. Ours gives a very sharp picture of the interface except in cases where it is double valued. The colloidal technique you mentioned is useful principally in flow visualization.

Paynter

The two lighting techniques we use are the indirect and planar methods. The colloidal technique is used with the latter method for obtaining two-dimensional flow patterns.

Satterlee

How do you measure accelerations as low as 10^{-3} and $10^{-4} g_0$?

Paynter

We obtain a chronological record of test acceleration by recording relative travel between the test cell and a steel ball (0.875-in dia) housed within the test cell during the 2.1-sec test duration. The ball is constrained to move freely in a vertical direction only and its travel is recorded chronologically by an equi-spaced photodiode network. The system's sensitivity is 0.1-in travel. Graphical differentiation of this relative travel yields test cell acceleration as a function of time. The acceleration profile reflects the variation in calibrated spring force, Figure 3.

BLANK PAGE

PAPER 16

THE APPLICATION OF HYDROPHILIC AND HYDROPHOBIC SURFACES FOR PHASE SEPARATION IN A LOW-g ENVIRONMENT

By J. M. Smith, R. M. Cima, and Yi-Sheng Li
LOCKHEED MISSILES & SPACE COMPANY

ABSTRACT

The separation of liquids and gases under low-g conditions is an important function in many spacecraft systems. In this paper the authors describe the use of hydrophobic (nonwetting) and hydrophilic (wetting) surfaces to control the water and gas phases in certain life-support equipment.

The theoretical basis for the phase separation process is described, the principles involved are demonstrated, a humidity-control system embodying these principles is described, and performance test data are presented for this system.

THE APPLICATION OF HYDROPHILIC AND HYDROPHOBIC SURFACES FOR PHASE SEPARATION IN A LOW-g ENVIRONMENT

1 THEORETICAL APPROACH

Theoretical consideration of two capillary phenomena supported the design of the phase-separation equipment described in this paper. These processes are: (1) the pressure differential existing across a stable liquid-gas interface in a porous material, and (2) the velocity which will cause a liquid droplet, striking a porous hydrophobic surface, to penetrate that surface.

The porous material of interest is a fine-mesh stainless steel screen. This material is used in the uncoated form as a hydrophilic surface; coated with Teflon, it behaves as a hydrophobic material. The liquid of interest is water.

Analytical models available for prediction of the low-gravity phase separation capabilities of woven screens are far from exact. For this reason a fairly simple model was used, recognizing that inaccuracies in performance predictions would result. The variance between predicted and actual performance described in this paper shows that the analytical model chosen can be used at least to estimate the order of magnitude of performance.

1.1 Stability of the Liquid-Gas Interface

The conditions for stability of a liquid-gas interface in a porous material (as shown in Fig. 1) are of interest for low-gravity phase separation applications described here. For example, if liquid droplets on the gas side of the porous plate shown in the illustration reach the stable liquid-gas interface they will enter the liquid phase. In this way liquid is extracted selectively from a two-phase medium with a hydrophilic screen mesh surface.

The model used for predicting the pressure differential existing across a stable gas-liquid interface is shown in Fig. 1. The analytical expression for the pressure differential across the interface is given by the capillary pressure rise equation attributed to Laplace:

$$p_g - p_l = \sigma \left(\frac{1}{r_1} + \frac{1}{r_2} \right) \quad (1)$$

where

p_g = pressure on gas side

p_l = pressure on liquid side

σ = surface tension

r_1 and r_2 = principal radii of curvature of the liquid-gas interface

For a cylindrical hole as shown in the model, the principal radii of curvature are identical and equal to

$$\frac{r}{\cos \theta}$$

where

r = radius of cylindrical hole

θ = contact angle

Substituting $r_1 = r_2 = r/\cos \theta$ in Eq. (1) gives

$$p_g - p_l = \frac{2\sigma \cos \theta}{r} \quad (2)$$

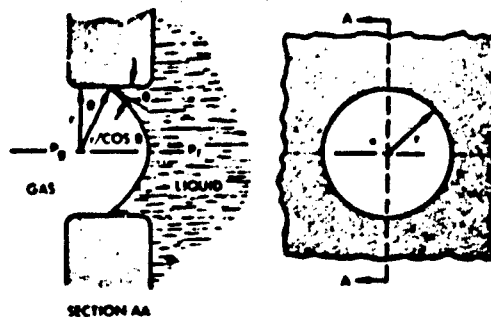


Fig. 1 Stability of Liquid-Gas Interface in a Cylindrical Hole

The geometry of interest, a woven screen, is roughly approximated by the square opening shown in Fig. 2; for the lack of a better model this approximation was used.

To apply the solution for the round opening to the square configuration, the hydraulic radius, r_h , was substituted for the term $r/2$ in Eq. (2), giving

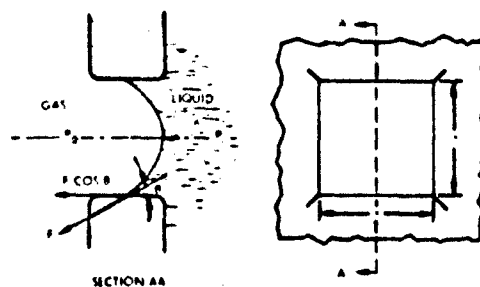


Fig. 2 Stability of Liquid-Gas Interface in a Square Hole

$$p_g - p_l = \frac{\sigma \cos \theta}{r_h} \quad (3)$$

where r_h = area/wetted perimeter. This approach appears to be justified on the basis of a force balance on the liquid surface as depicted in Fig. 2. The sum of the forces acting parallel to the axis of the opening contributes to the pressure difference:

$$(p_g - p_l) = \frac{\Sigma F}{A} = \frac{4\sigma x \cos \theta}{x^2} = \frac{4\sigma \cos \theta}{x} \quad (4)$$

The hydraulic radius of the square opening is:

$$r_h = \frac{x^2}{4x} = \frac{x}{4}$$

Substituting in Eq. (4) gives an expression identical to Eq. (3).

Using Eq. (3), pressure differential calculations were made for the hydrophilic (uncoated stainless steel) screen with $\theta = 45$ deg, and for the hydrophobic (Teflon-coated) screen using $\theta = 105$ deg. The results of these calculations, for water in contact with several mesh sizes, are presented in Table 1.

Table 1

**THEORETICAL WATER PRESSURE DIFFERENTIAL
ACROSS HYDROPHILIC AND HYDROPHOBIC SCREENS**

Screen Type	Screen Mesh Size	Wire Diam. (in.)	Pressure Differential (in. H ₂ O)
Hydrophilic	400	0.0010	20.9
Hydrophilic	325	0.0014	18.4
Hydrophilic	200	0.0021	10.8
Hydrophobic	325	0.0014	-7.6

Experimental values of pressure differential determined in subsequent experiments are compared with these theoretical values in Section 2.

1.2 Droplet Penetration Velocity

For a hydrophobic screen it is interesting to note that if gas with entrained liquid droplets were to flow to the screen, it would be possible to stop the liquid droplets from passing the screen mesh while the air was allowed to continue through. One requirement for this type of separation is that the droplet must be larger than the screen porosities. Additionally, when the liquid droplet contacts the hydrophobic screen, a liquid stagnation pressure will develop at the region of impact. As long as the pressure difference developed across the screen results in a stable interface, the liquid droplet will not pass through the screen.

To estimate the maximum velocity that a droplet may have and still be stopped by a hydrophobic screen, consider the schematic diagram of Fig. 3. With the liquid droplets approaching the hydrophobic screen at a velocity V , the difference between the stagnation and static pressures of the liquid drop is

$$p_{\text{stag.}} - p_{\text{static}} = \frac{\rho V^2}{2g_c}$$

where

ρ = liquid density

V = approach velocity

g_c = gravitational constant

If the radii of the droplets are large compared with the screen openings, then the static pressure of liquid in a drop will be equal to the pressure of the gas surrounding it; that is $p_{\text{stat.}} = p_g$. Hence, the difference between the stagnation pressure of the moving liquid droplets and the gas-stream pressure may be expressed by

$$p_{\text{stag.}} - p_g = \frac{\rho V^2}{2g_c}$$

If, as shown in Fig. 3, the angle between the normal to the screen surface and the direction of the gas-liquid droplet flow stream is ϕ , then only a fraction of the stagnation pressure will be developed on the hydrophobic screen as a liquid droplet impinges. The difference between liquid and gas pressures at the point of impact may be expressed by

$$p_l - p_g = \frac{\rho V^2}{2g_c} \cos \phi$$

The maximum stable pressure difference ($p_l - p_g$) that can be supported across a hydrophobic screen can be estimated from Eq. (3), thereby allowing calculation of the impingement velocity below which penetration should not occur.

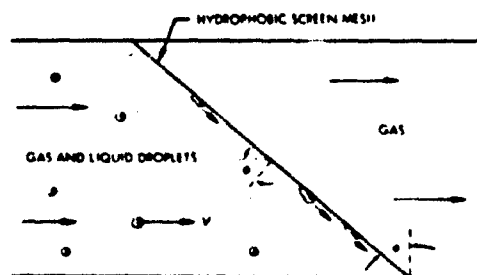


Fig. 3 Separation of Liquid Droplets From a Gaseous Stream by a Hydrophobic Surface

2 DEMONSTRATION OF PRINCIPLES

Devices have been constructed and tested to demonstrate (1) the ability of a hydrophilic screen to allow the selective transfer of water from a two-phase (water-gas) supply, and (2) the ability of a hydrophobic screen to allow the flow of gas with very little resistance, but to retain water.

These devices consist of:

- A hydrophilic screen on the end of a fitting equipped with a delivery tube (Fig. 4)
- A tube fitted at one end with a hydrophobic screen

A brief description of the experiments conducted with these devices follows.

2.1 Hydrophilic Screen

A sequence of three photographs demonstrates that the hydrophilic screen, subjected to a controlled* pressure differential, will provide a substantial liquid flow when it is fully covered with water** (Fig. 4), that it will flow water selectively when exposed to both the gas and liquid phases (Fig. 5), and that it will not allow gas to pass when it is exposed only to the gas phase (Fig. 6).

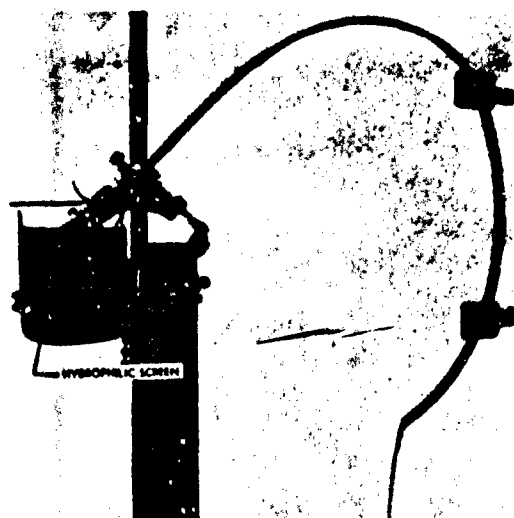


Fig. 4 Hydrophilic Screen - Liquid Flow When Exposed Only to Liquid Phase

From Eq. (3), the pressure difference which can be supported by such a screen without breaking the water-screen bond can be estimated. Experimental values

*Less than or equal to the pressure differential required to produce a stable liquid-gas interface.

**Colored slightly to clarify the picture.

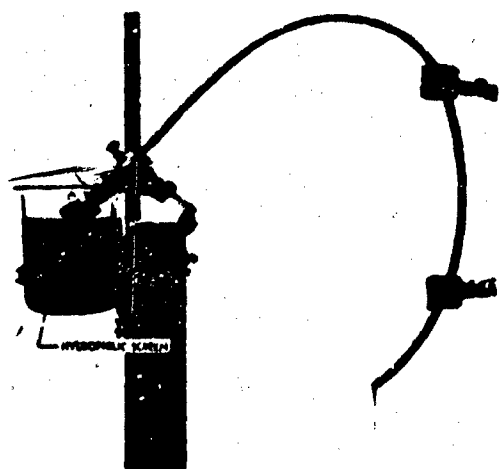


Fig. 5 Hydrophilic Screen – Selective Liquid Flow When Exposed to Both Gas and Liquid Phases

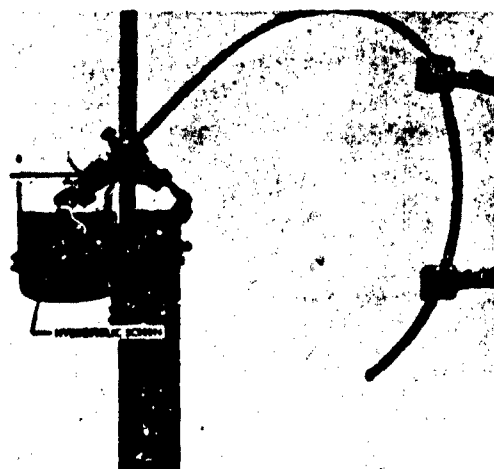


Fig. 6 Hydrophilic Screen – Prevention of Gas Flow When Exposed Only to Gas Phase

for this pressure difference were determined using an apparatus similar to that shown in the photographs.

The pressure differential across the screen was varied by raising or lowering the end of the delivery tube. In this manner the pressure differential required to break the water-screen bond was determined for three mesh sizes. Table 2 shows the experimental values and the percent of the theoretical values estimated by means of Eq. (3).

It is probable that the differences between experimental and theoretical pressure-difference values are due to the significant deviation of the woven-screen geometry from the square-hole model used, variations in screen pore dimensions, and uncertainties in the contact angle, θ . This reduction in differential is not a serious problem in the application of the principle; care is taken to maintain a pressure differential across the screen which will not cause instability in the liquid-gas interface, and sufficient screen area is provided to handle the desired flow rate at the reduced pressure differential.

Table 2

**PRESSURE DIFFERENCE REQUIRED TO BREAK WATER-SCREEN BOND
FOR THREE SCREEN MESH SIZES - HYDROPHILIC SCREEN***

Mesh Size	Wire Diam. (in.)	Pressure Difference (in. H ₂ O)	Percent of Theoretical Value
400	0.0010	15	72
325	0.0014	13	71
200	0.0021	6	57

2.2 Hydrophobic Screen

As shown in Fig. 7, a piece of tubing was fitted with 325-mesh stainless steel screen coated with Teflon. The dry screen passed air with negligible resistance. The tube, with the screen at the bottom, was immersed in a water bath to a depth of 5.5 in. before water flow through the screen was observed.

The theoretical water column weight was estimated at 7.6 in. from Eq. (3). Again, the difference between theoretical and actual performance is probably due to the geometrical complexity of the woven screen and uncertainty in the value of the water-Teflon contact angle. For a number of applications of interest, however, the actual performance is entirely adequate.

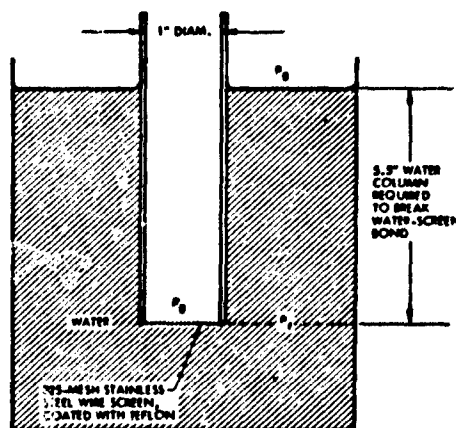


Fig. 7 Hydrophobic Screen Test Device

3 APPLICATION OF PRINCIPLES TO LIFE-SUPPORT SUBSYSTEMS

Many life-support processes involve the separation of gases and liquids under low-g conditions; primary examples are (1) the extraction of condensed moisture from an airstream to control humidity, (2) the collection of urine and other liquid wastes, (3) the distillation of liquid wastes to obtain usable water, and (4) the management of liquid supplies of expendable materials such as water and oxygen.

The authors have engaged in laboratory development activities to explore the use of hydrophobic and hydrophilic surfaces in devices to carry out some of these processes. Principles have been described and demonstrated in the previous sections; here, application of these principles to the control of space-cabin humidity will be described.

3.1 Humidity Control System

A basic space-cabin atmosphere-control problem is the maintenance of a physiologically satisfactory humidity. This is normally accomplished by reducing the temperature of the atmosphere, at some point in the system, to the desired dew-point; the moisture condensed in this process is then separated from the atmosphere and removed for storage, processed for re-use, or vented overboard.

The process by which liquid is removed from the separator must allow a minimum of atmosphere to be entrained in the water - for two reasons: (1) if the water is vented overboard this atmosphere is lost, and (2) if the liquid is stored, the storage tank will have to be large enough to store both the liquid and the entrained atmosphere.

Based on the principles described earlier, a humidity-control system has been built and tested at Lockheed; theoretically, this system will perform satisfactorily in the weightless condition, although proof awaits zero-g testing. The design concept for this system is described in the following paragraphs, while laboratory test results are described in Section 4.2.

The humidity control system comprises six primary parts; a heat exchanger, a coalescer, a hydrophobic liquid-separator, a hydrophilic sump, a pressure-control unit, and a bladdered tank.

Figure 8 depicts (1) how the heat exchanger cools the atmosphere to the desired dew-point, creating a mist or fog, (2) how the coalescer (a woven metal mat) creates droplets larger than the mesh size of the hydrophobic screen, and (3) how the droplets collect in larger globules at the base of the hydrophobic screen. The hydrophilic sump is equipped with a suction system to maintain a controlled pressure differential across the screen. The tube leading away from the sump must remain full of liquid to maintain the water-screen bond which prevents gas from passing through the hydrophilic sump.

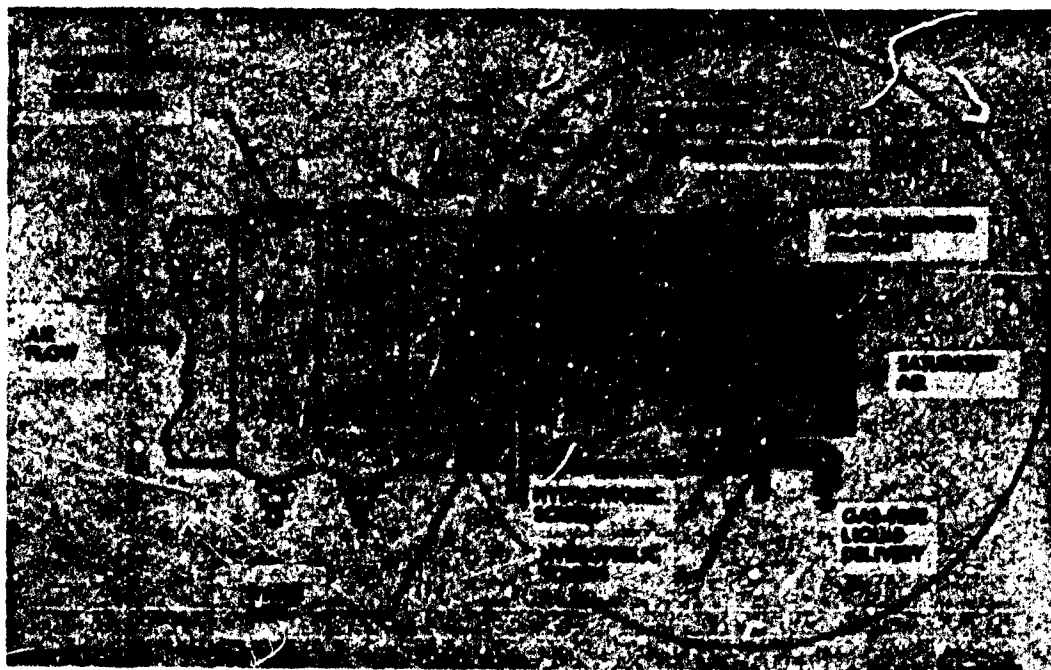


Fig. 8 Basic Concept of Hydrophobic/Hydrophilic Water Separator

The process may be described in the following manner:

- Dew-point control is maintained by controlling the temperature of the coolant supply to the heat exchanger.
- The atmosphere, saturated with water at the desired dew point and containing entrained moisture in the form of a fog or mist, passes through the coalescer, where sizeable droplets are formed.
- The droplets are carried by the airstream to the hydrophobic cone but do not pass it for two reasons: (1) their diameter is larger than the openings in the screen, and (2) the impact pressure is less than or equal to the pressure required to maintain a stable liquid-gas interface in the screen openings.*
- The separated liquid collects in the low-pressure region around the base of the cone. If there were no sump or collector tube, the liquid would form a body of revolution around the axis of flow, due to aerodynamic forces.
- The hydrophilic sump draws out any water in contact with it, causing an unsymmetrical liquid volume. Under such a condition, aerodynamic forces will cause liquid to flow around the base of the cone to the sump.
- The pressure-control system maintains the desired pressure differential across the hydrophilic sump — i. e. , sufficient to support the desired flow rate but insufficient to cause instability in the liquid-gas interface.
- The bladdered tank provides the necessary liquid storage volume. Liquid is drawn into this tank by reducing the pressure on the dry side of the bladder in response to the pressure controller. When it is desired to discharge this water for use, a three-way valve is sequenced and the bladder is pressurized from the dry side.

A test model for demonstration of the cone, sump, suction control, and storage tank is shown in Fig. 9.

*See the theoretical discussion of droplet penetration velocity in Section 1.

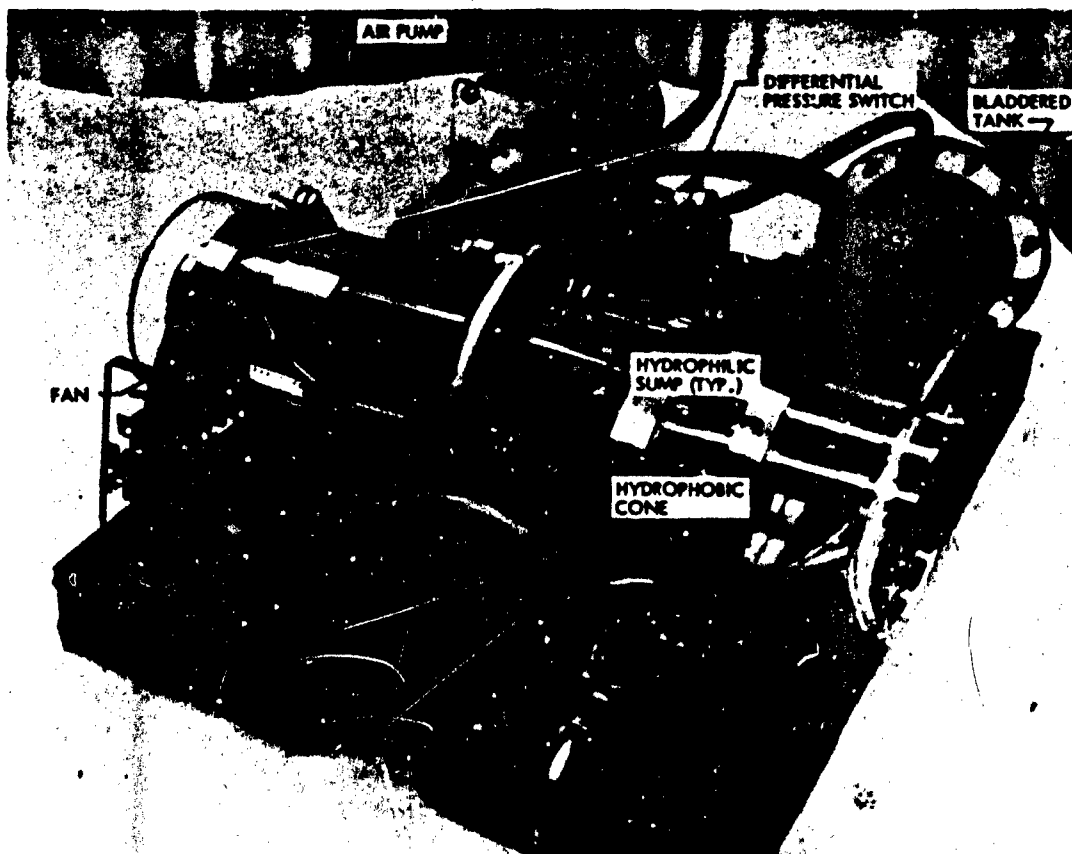


Fig. 9 Test Model of Zero-g Water Separator

3.2 Additional Applications

The principles described earlier in this paper are being applied also to the problems of collection, measurement, and distillation of urine.

A hydrophobic cone will separate urine and other liquids from an airstream. The use of an air flow to transport the liquid, combined with the separator for isolating the liquid at a desired point, appears to be a very effective way of collecting liquids in the weightless condition. The collection, measurement, and storage of urine for biological and chemical analysis is a potential area of application for the processes described.

One concept, that of a hydrophobic screen container to hold liquid urine while water vapor is allowed to pass, is being explored in a urine-distillation apparatus. Another approach to this problem, also under study, is that of holding the liquid in the boiler by means of a "minimum-energy" geometrical configuration and using the hydrophobic screen only to prevent liquid carryover. The condenser for the distillation device uses a cold hydrophilic surface to condense the water vapor and to collect it for subsequent filtration and ultimate use as drinking water.

In advanced life-support systems, it is desirable to reclaim oxygen from carbon dioxide. Promising concepts for this process involve the hydrogenation of CO_2 to water and carbon, or to water and methane. In each of these systems, it is necessary to separate the water from the process stream. Lockheed is constructing such a system using a hydrophobic-hydrophilic water separation technique similar to that described for humidity control.

4 SYSTEM TEST RESULTS

4.1 Water Separator and Sump

A simple test showing the ability of the conical hydrophobic screen to separate water from a flowing air stream is illustrated in Fig. 10. In this test, a water jet* impinges on the screen without passing through. The water, thus separated from the air stream, flows through the hydrophilic sump until the sump runs dry; as shown in Fig. 6, no air passes through the dry sump.

*Colored to provide contrast in the photograph.



Fig. 10 Test Model in Operation, Showing Liquid-Gas Separation

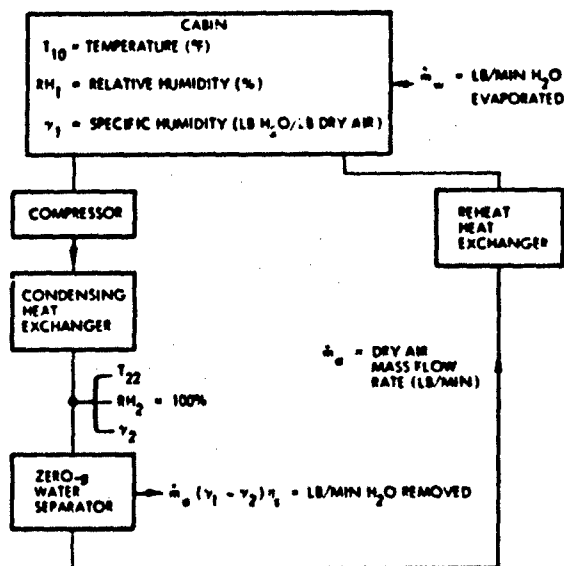


Fig. 11 Schematic Diagram of Humidity Control System

In a 1-g condition, the sump is located in the bottom of the duct; under the low-g condition, the sump location is not critical.

4.2 Humidity Control System

Similar components, included in a prototype life-support system under development at Lockheed, are used to control cabin humidity. In these tests, water is evaporated into the atmosphere at a controlled rate to simulate the space-cabin humidity load. Cold fluid, supplied to a condensing heat exchanger, effects water condensation. The separator removes nearly 100 percent of the condensed moisture, as will be shown by subsequent analysis of the data obtained.

Figure 11 shows schematically how the humidity-control system functions, while Table 3 shows data from a humidity-control test. The variation in humidity with time is due primarily to variations in the water introduction rate, and in the cabin

Table 3
DATA FROM HUMIDITY CONTROL SYSTEM TEST

Time (A. M.)	Cabin Temp. T_{10} (°F)	Cabin RH. RH_1 (%)	Condens. Temp., T_{22} (°F)	Dry Air Flow Rate, \dot{m}_a (lb/min)	Cabin Specific Humidity, γ_1 (lb H ₂ O/lb air)	Condens. Pt. Specific Humidity γ_2 (lb H ₂ O/lb air)	Water Condensed, $\dot{m}_a (\gamma_1 - \gamma_2)$ lb/min
10:40	81.0	56.0	50	4.9	0.0127	0.0077	0.0245
10:42	81.0	58.5	53	4.9	0.0133	0.0086	0.0239
10:44	81.2	59.0	48	4.9	0.0134	0.0072	0.0304
10:46	81.5	56.0	49	4.9	0.0128	0.0074	0.0265
10:48	82.0	63.0	52	4.9	0.0148	0.0083	0.0318
10:50	82.0	56.0	52	4.9	0.0129	0.0083	0.0225
10:52	82.0	58.0	48	4.9	0.0133	0.0072	0.0299
10:54	82.0	64.5	50	4.9	0.0149	0.0077	0.0353
10:56	81.0	58.0	53	4.9	0.0133	0.0086	0.0230
10:58	81.0	62.0	50	4.9	0.0146	0.0077	0.0328
11:00	81.0	62.0	48	4.9	0.0146	0.0072	0.0363
11:02	81.0	57.0	50	4.9	0.0128	0.0077	0.0250
11:04	81.0	62.5	54	4.9	0.0146	0.0080	0.0313
11:06	81.0	55.0	49	4.9	0.0120	0.0074	0.0225
11:08	81.0	56.0	48	4.9	0.0120	0.0072	0.0225
11:10	81.0	57.0	48	4.9	0.0121	0.0072	0.0240
Average Rate of Water Condensation							0.0277

and condensing temperatures. The system was designed to maintain relative humidity between 30 and 70 percent over the entire range of load conditions expected. Under the conditions prevailing in this test, humidity varied from 53 to 63 percent, as shown in Fig. 12.

The water separator efficiency—i.e., the percent of entrained moisture removed from the atmosphere as it passes through the separator—can be determined from Eq. (5), assuming that cabin humidity is constant:

$$\eta_s = \frac{\dot{m}_w}{\dot{m}_a (\gamma_1 - \gamma_2)} \times 100 \quad (5)$$

where

- η_s = separation efficiency (percent)
- \dot{m}_w = water introduction rate (lb H₂O/min)
- \dot{m}_a = air flow rate (lb dry air/min)
- γ_1 = specific humidity in cabin (lb H₂O/lb dry air)
- γ_2 = specific humidity at exit of condensing heat exchanger (lb H₂O/lb dry air)

Table 3 represents data taken over a 30-min period with the humidity-control system in operation. Cabin humidity and various temperatures in the system vary continuously; therefore, average values of the pertinent variables were calculated for this period.

If the nominal value of water introduction rate is used, the separation efficiency is calculated as 98.6 percent. Since the water introduction rate was subject to a possible measurement error of ± 5 percent, a corresponding error may exist in the calculated removal efficiencies shown in Table 4.

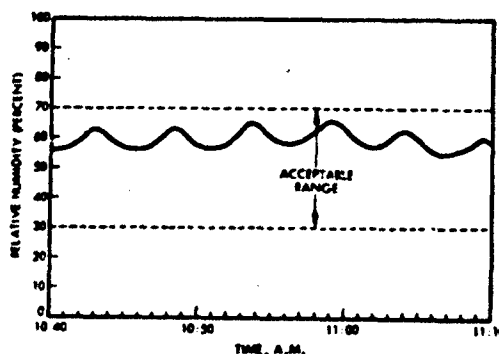


Fig. 12 Relative Humidity vs. Time for Conditions Presented in Table 3

Table 4
SEPARATION EFFICIENCY BASED ON MINIMUM, NOMINAL, AND
MAXIMUM WATER INPUT RATES

Water Input, \dot{m}_w (lb/min)	Ave. Water Condens. Rate, $\dot{m}_a (\gamma_1 - \gamma_2)$, (lb/min)	Separation Efficiency, η_s (%)
0.0260 (minimum)	0.0277	93.8
0.0273 (nominal)	0.0277	98.6
0.0288 (maximum)	0.0277	>100

5 CONCLUSIONS AND RECOMMENDATIONS

The application of hydrophobic and hydrophilic materials to low-g liquid-gas phase separation has been demonstrated in 1-g tests of the humidity-control system described here, as well as in other elements of life-support equipment where phase separation plays an important role. While the tests were not conducted under low-g conditions, there is no reason to suspect that the equipment would not function properly under such conditions; aircraft low-g flight experiments are planned to confirm that it will.

As with any new development, these techniques are not without their potential problems; several areas where further work is needed are as follows:

- Analytical work to allow better prediction of the performance of complex geometrical shapes - e.g., woven screens
- Improvement in Teflon-coating techniques to ensure complete and uniform coverage of a screen or other support structure
- Development of perforated and/or foamed Teflon to eliminate the need for coating a support structure
- Investigation of hydrophobic materials other than Teflon
- Laboratory tests of extended duration to explore possible degradation of the system - e.g., changes in the contact angle of the hydrophobic surface due to adsorption of liquids and/or impurities, and clogging problems encountered with the fine-mesh hydrophilic sump
- Determination of the effects of coalescer porosity and thickness on the water-separation efficiency (The coalescer pressure drop can be significant.)
- Investigation of the effect on separation efficiency of hydrophobic cone size and angle, and screen mesh size.

DISCUSSION

Unknown questioner

Have you tried your scheme with other liquids than water or with other nonwetting coatings?

Smith

We have been concerned only with urine. It is satisfactorily separated by the hydrophobic materials we've used. Urine particles will eventually coat the screen and cause problems. We've investigated no other nonwetting materials (than teflon) however.

Milton Rogers, AFOSR

The effectiveness of your nonwetting teflon surfaces might be increased by using polarized teflon as opposed to nonpolarized teflon. Which did you use?

Smith

We used commercial Dupont teflon. I'm not sure which it is.

Milton Rogers, AFOSR

How do you make the collected material potable?

Smith

It's easy to separate urine from an airstream as we've shown. Purifying the urine is another matter. In principle, it is possible to hold a bit of urine by capillary action in these nonwetting materials and evaporate the water by adding heat. The concentrations of salts and urea increase with time, however, and cause fouling problems.

J. M. Robinson, TRW Space Systems Group

I was involved in the design of some of the boilers and condensers used on the Apollo which you mentioned. The wicking materials (Refrasil and fritted glass) used in these were hydrophilic materials. Their wetting characteristics change with time, and this is a function of the solid material used and the purity of the water used.

Robert Johnson, NASA Langley

Have you had a cleaning problem once the system has been wetted?

Smith

We have had no problem of this sort with the hydrophobic. We have occasionally experienced plugging of the hydrophilic screens. This situation can usually be cleared up by back-purging water through the screens. The hydrophilic screens are also easily replaced.